NASA Contractor Report 178152

CHANGES IN THE TURBULENT BOUNDARY LAYER
STRUCTURE ASSOCIATED WITH NET DRAG
REDUCTION BY OUTER LAYER MANIPULATORS

N. Rashidnia and R. E. Falco

MICHIGAN STATE UNIVERSITY
East Lansing, Michigan

NASA

National Aeronautics and
Space Administration

Langley Research Center
Hampton, Virginia 23665

ABSTRACT

A specially designed wind tunnel was used to examine the effects of tandemly-arranged parallel plate manipulators (TAPPMs) on a turbulent boundary-layer structure and the associated drag. Momentum balances, as well as measurements of the local shear stress from the velocity gradient near the wall, were used to obtain the net drag and local skin friction changes. Two TAPPM's, identical except for the thickness of their plates, were used in the study. Results with .003" plates were a maximum net drag reduction of 10% at $5\delta_0$ (using a momentum balance).

At $20\delta_0$, simultaneous laser sheet flow visualization and hot-wire anemometry data showed that the Reynolds stress in the large eddies was significantly reduced, as were the streamwise and normal velocity components. Using space-time correlations the reductions were again identified. Furthermore, quantitative flow visualization showed that the outward normal velocity of the inner region was also significantly decreased in the region around $20\delta_0$. However, throughout the first $130\delta_0$, the measured sublayer thickness with the TAPPMs in place was 15-20% greater.

On the whole, the data showed that the skin friction, as well as the structure of the turbulence, was strongly modified in the first $35\delta_0$, but that they both significantly relaxed toward unmanipulated boundary layer values by $50\delta_0$.

Acknowledgements

TABLE OF CONTENTS

LIST OF FIGURES

LIST OF TABLES

LIST OF SYMBOLS

A   Coles (1968) "law of the wall" parameter = 5.61

B   Coles (1968) "law of the wall" constant = 5.0

C_{fa} Skin friction coefficient = $\tau_w/(1/2\rho U^2\infty)$
         where a=c ; τ_w is obtained from Clauser plot,
             a=n ; τ_w is obtained from $d\bar{U}/dy_w$, (Newtonian)
             a=Θ ; τ_w is obtained from momentum balance

G   Equilibrium shape factor

h   Height of manipulator plates away from wall

H   Shape factor = δ_d/Θ

k   Von Karman's constant = .41

1   Chord dimension of parallel plate manipulator

R_Θ Reynolds Number = $\rho U_\infty\Theta/\mu$

s   Streamwise spacing between tandem manipulator plates

$R_{p'q'}$ Space-time correlation of functions p' and q' where
         p' is used as the reference function

TAPPM   Tandem arrayed parallel plate manipulator

T_B Time period between wall burst events ("Pockets")

U   Streamwise velocity component = $\bar{U} + u'$

u'   Fluctuating velocity component in the x direction

⟨u'⟩   Ensemble averaged of u' in the large scale motions (LSM)

$\bar{U}$ Time-averaged mean of streamwise velocity component

U_∞ Time-averaged freestream velocity

u^+ $\bar{U}/u_\tau$

$u_{\tau a}$ Wall shear velocity = $(\tau_w/\rho)^{0.5}$
         where a=c ; τ_w is obtained from Clauser plot,
             a=n ; τ_w is obtained from $d\bar{U}/dy_w$, (Newtonian)
             a=Θ ; τ_w is obtained from momentum balance

u'v'   Fluctuating Reynolds shear stress

$\langle u'v' \rangle$	Ensemble average of $u'v'$ in the large scale motions (LSM)
v'	Fluctuating velocity component in the y direction
$\langle v' \rangle$	Ensemble average of v' in the large scale motions (LSM)
x	Cartesian coordinate in streamwise direction; origin at leading edge of test plate
x_0	Downstream distance between leading edge of the test wall and turbulence manipulator
y	Cartesian coordinate taken normal to test wall (flat plate); origin at wall surface
y^+	$\rho u_\tau y/\mu$
z	Lateral cartesian coordinate taken parallel to flat plate; origin along test wall centerline
δ	Boundary layer thickness = y value where $\bar{U}$ equals 0.99 U_∞
δ_d	Displacement thickness = $\int_0^\infty \left[1 - \bar{U}/U_\infty\right] \, dy$
δ_0	Boundary layer thickness at the leading edge of upstream plate of the TAPPM
Θ	Momentum thickness = $\int_0^\infty \bar{U}/U_\infty\left[1 - \bar{U}/U_\infty\right] \, dy$
Δ	Energy thickness = $\int_0^\infty \bar{U}/U_\infty\left[1 - (\bar{U}/U_\infty)^2\right] \, dy$
ξ	Distance downstream of manipulator where measurements were taken = $(x - x_0)/\delta_0$
π	Wake strength coefficient
ρ	Fluid density
τ	Non-dimensionalized time delay in temporal correlation calculations = $(t - t_0)U_\infty/\delta$
τ_w	Wall shear stress
μ	Dynamic viscosity

CHAPTER 1

INTRODUCTION

During the past thirty years, it has been known that fully-developed turbulent flows contain coherent flow patterns (often called eddies) imbedded in what appears to be more random, less organized ambient fluctuations. The transport resulting from these organized motions is large compared to that of the "background" fluctuations, but they are surprisingly difficult to detect (although there are definable families of such motions). Reasons for the difficulty in detection include; a) the large variability in the flow fields they produce; b) the unsteady nature of the motions; and c) the three-dimensionality of the eddy. Eddies develop, evolve, and decay and the usual point detecting techniques yield no information about the point in their development at which they passed over the probe (i.e., the probes do not know where in the flow field they are located). These problems can be alleviated somewhat by using flow visualization to locate the eddies' positions and to give information about their histories. Many studies have been made, each with a scheme to detect and quantify at least one of the coherent motions in the turbulent boundary layer. No schemes have been able to account for all of the problems mentioned above, hence experimental results have led to varying interpretations of the role and importance of the coherent motions. The large eddies of the boundary layer, those identified as being associated with the large scale outer layer intermittency, have received the most

attention. Although all studies (known to the authors) that have searched for them have found them, their relative importance varies among investigators. In the fifties, using spatially separated long-time-averaged correlations, Townsend interpreted the large eddies as weak but important features in controlling transport. In the sixties and early seventies, using space-time correlations conditionally sampled to detect the large eddies, many investigators, notably Kovasznay and Laufer, reinforced earlier guesses, derived from free shear layer spectral measurements that the strength of these large scale motions was as high as eighty percent of the total. More recent studies using simultaneous flow visualization and multiprobe hot-wire anemometry to circumvent some of the problems mentioned above have been made by Falco and colleagues. These studies have identified two important types of coherent motions. The large eddies were identified and quantified, with results showing that they are responsible for about one half of the transport in the outer region. The other coherent motion, which is a microscale motion, was found to have contributed most of the remaining transport. The interaction among these scales has also been examined (Falco, 1983). In brief, the interaction between the large eddies and the microscale eddies further helps the large eddies to control transport within the boundary layer, and in particular transport in the wall region, which is directly relevant to the production of turbulence, and hence the creation of drag.

Over the past decade interest has been growing in the manipulation of the large eddies for technological applications. These applications include turbulent drag reduction, separation delay, and reduction of

noise and vibration (Bushnell, 1983). Moreover, the shortage of energy resources (petroleum resources in particular) has increased efforts to improve the efficiency of transportation systems, particularly aircraft. Research toward the development of techniques for reducing viscous drag on aerodynamic bodies has become more and more crucial in recent years. An example of the magnitude of the viscous drag contribution for aircraft given by Hefner et al. (1980) indicated that "typical values of skin friction drag range from 25% of the total drag for supersonic fighters to 50% for long-haul transports and 54% for general aviation executive jets."

It has been shown that the viscous drag created by turbulence in a boundary layer can be changed (reduced or increased) by placing a pair of thin flat ribbons, or airfoil devices, in tandem in the outer part of the layer. Net drag reductions of more than 7%, in smooth flat plate turbulent boundary layers, have been reported by the group at NASA Langley. Another group at the Illinois Institute of Technology reported the highest net drag reductions, ranging from 10-28% with very slow relaxation (Plezniak and Nagib, 1985). Most studies at the time of the initiation of the present work did not extend beyond 70 boundary layer thicknesses downstream of the manipulators, therefore, the question of the duration of the effects had not been addressed. Other studies have reported local skin friction reductions for about $55\delta_0$; typically these investigations did not measure net drag reductions. Attempts made by NASA Langley researchers to reproduce the results of the IIT group's larger drag reductions were not successful.

Most of the investigations have used only one method to measure the

skin friction drag -- either indirect measurements from momentum balance, (e.g., IIT group since 1978, Anders, 1984 and 1985), or direct measurement using skin friction balance. The results generated by these independent techniques have not, to date, been compared. In addition to skin friction balance measurements, Lemay et al. (1985) used a Preston tube to measure skin friction. Although the universality of the "law of the wall" might not hold in the manipulated turbulent boundary layers, they did, however, show similar local wall-friction reduction and evolution in the manipulated boundary layers. A number of recent investigations have made direct skin friction measurements (Hefner et al., 1983; Westphal, 1986; Lynn and Sreenivasan, 1985; Lemay et al., 1985; and Mumford and Savill, 1984). These have all shown similar reductions, which we will discuss later.

Flow visualization studies at first appeared to show dramatic changes in the large eddy structure (Corke 1981). However, he (Corke) used the smoke-wire technique which was first used by Wille (1972, Cambridge University, unpublished). This technique adequately marks the boundary of a turbulent flow, but does not give useful information in the interior. Marking the boundary can be very misleading when the plate wakes are present (Falco 1983). Volume smoke marking does give good detail about the interior structure, but requires a tunnel that can exhaust the contaminant, which has usually not been available. It was used by Mumford and Savill (1984) to study modifications made by various manipulator plate and rod combinations. Their studies were at very low Reynolds number and only qualitative. The primary difficulty with visual studies at very low Reynolds numbers is that there isn't adequate

separation between the two dominant coherent motions; one of which is the large eddies and the other the microscale eddies (see Falco 1977). At the Reynolds numbers present in aircraft operation, the scales would be well separated. Thus, it was not possible to determine whether a particular scale was being significantly altered, and therefore, largely responsible for the overall drag changes.

Thus, in two important areas the research on turbulence manipulation by tandem outer layer plates needs additional work: 1) simultaneous measurement of local and net skin friction changes--to determine the effects of three-dimensionality (inherent in all tunnels) on two-dimensional momentum balance estimates; and 2) quantitative volume flow visualization combined with quantitative measurements of the observed flow structures. A third aspect, the downstream extent of the modifications, or the relaxation time of the boundary layer, also needed study. This is a report of experiments designed to fill these gaps. For the drag measurement, we used a local technique--direct measurement of the local mean velocity gradient near the wall--to complement our drag measurements made using a momentum balance. To uncover the mechanistic changes we used simultaneous flow visualization and hot-wire anemometry to conditionally sample the large eddies both with and without the manipulators. This technique enabled us to compare changes in the scale presumed to be responsible for the changes in drag. To determine the downstream extent of the effects, we designed a wind tunnel that allowed both of the above objectives to be met, and allowed measurements to be made over more than 150 δ_0.

The manipulator configuration used in the present research was

close to one arrived at through optimization trials conducted at NASA by Anders, Hefner and Bushnell (1979), and IIT by Corke (1981). Our initial objective was to set up a known drag reducing configuration, confirm by a momentum balance that we had achieved it, and then proceed with the objectives mentioned above.

CHAPTER 2

DESCRIPTION OF EXPERIMENTAL FACILITIES AND TECHNIQUES

2.1 Facilities

This chapter presents a discussion of the experimental apparatus and techniques used for data acquisition and reduction.

2.1.1 Wind Tunnel

Preliminary studies were performed in the 2' x 4' x 24' low-speed boundary layer wind tunnel in the Turbulence Structure Laboratory (TSL) at Michigan State University. The inability to study layers sufficiently thick to determine changes in the turbulence structure, while at the same time develop a boundary layer whose length was a sufficient number of boundary layer thicknesses to explore relaxation lengths, led to the design and construction of a new boundary layer tunnel with a test section 56' long by 4' wide and nominally 2' high. The top and one side wall are made of 3/8" plexiglass to allow visualization from both directions. The top wall is adjustable to produce different pressure gradients if necessary. For the present experiments, the top wall was diverged .25 degrees over the entire test section length. The bottom and the second side wall are made from 3/4" thick plywood. These walls are sanded so that they are hydraulically smooth and painted black for background flow visualization purposes. Special attention was paid to the fit and smoothness of the joints between each 8 foot section. The tunnel is of the open-circuit suction

type. It is positioned in the center of a 60' x 100' x 20' laboratory area, which acts as the return circuit for high-quality probe measurements. The suction is provided by a low-noise axial fan (Chicago Blower Corporation, 44½" diameter, W9, Class 1, with a 10 HP, 1200 RPM TEFC 3/60/230-460, T-FRAME electric motor). The speed is kept constant using an Eaton Model 4000 eddy current speed controller. The fan is located between a 2:1 axial diffuser, and the 2:1 radial diffuser. Flexible joints reduce transmission of vibration from the fan assembly to the test section. For flow visualization experiments, the radial diffuser can be exchanged with an axial diffuser which connects to an exhaust section that ultimately empties outside into the atmosphere, allowing the continuous flow of the smoke visualization marker (for further details of this technique see Falco 1980). The exit section consists of a wind-baffled passage which was built outside the laboratory. It contains a 1/2" x 6" Hex-cell honeycomb, followed by a fine grid screen attached to one end of the exit section. This combination of honeycomb and screen in the exit section reduces the possible effects of atmospheric wind pressure variations on the flow in the test section. BUNA-N rubber seals are used along the entire test section to allow the experiments with oil-fog contaminants, and a design which will allow future extension or modification of the wind tunnel test section divergence or general shape.

The lower wall of the tunnel was used as the test plate. It had adjustable bracing every 4 feet along its length to allow accurate adjustment and leveling of the test wall. This wall is carefully adjusted horizontally to a flatness within 0.001 inch per foot in both

streamwise and spanwise directions. Figure 2.1 is a schematic of the wind tunnel.

2.1.2 Measurement Stations, Probe Support, Traverse Mechanism, and Positioning Instrument (Cathetometer)

The test wall downstream of the manipulators was divided into 10 stations. The distance between stations was nonuniform. The nonuniform spacing resulted from an iterative procedure in which preliminary results of velocity measurements and flow visualization were assessed and additional data stations were added to obtain the resolution needed to allow a curve fit of the momentum thickness variations in the region of relaxation. The final positions between test stations represent the minimum number thought necessary to obtain accurate drag measurements under the test conditions in our tunnel. The distances of these stations from the leading edge of the test plate are shown in Figure 2.2. The boundary layer grew to approximately 10 inches at the last test station on the test wall. This very thick boundary layer allowed hot-wire measurements as close as one wall unit ($y+ = 1$) before heat transfer effects became important. To this end, a two-stage traverse mechanism (for movement normal to the wall) was designed. The first stage (one inch travel) was provided by a digital micrometer with ±0.0001 inch accuracy. After the first inch the second stage of travel was provided by a larger traverse mechanism with 12 inch capacity but lower resolution. To use this stage, the first micrometer was locked and the probe was moved higher by the second part of the mechanism up the center line of the tunnel into the freestream. All y (normal to the

test plate) movements of the probe were done manually. In order to keep the direction of probe travel perpendicular to the test wall and uniform for all the stations a liquid level was mounted onto the moving part of the traverse mechanism body and adjusted for each station. The traverse mechanism was mounted and rigidly fixed to 9" x 8"x 3/8" aluminum plates attached to the outside part of the test wall (floor of the wind tunnel) for each test station. The support of the probe was a 3/8" O.D., 1/4" I.D., 18"-long aluminum tube. The tube passed through a 3/8"-diameter hole in the test wall, and its lower end was fixed to the moving part of the mechanism. When a station was not in use, the holes were carefully plugged and smoothed to eliminate roughness. The sensing portion of the probe was always positioned 10 inches upstream of the supporting rod, in order to avoid any possible interference with the flow field under measurement.

A measurement of the closest position of the sensor to the test wall was carefully made using a short-range telescope (cathetometer). This instrument was used to find a reference point to compare the readings from the traverse mechanism and to obtain the actual distance of the probe from the wall. The cathetometer is capable of measuring the vertical distance within 0.01 mm with an error of ±0.001 mm. Thus the probe could be positioned, for all the stations of the test wall, as close as $y^+ = 1$ above the test wall surface. This allowed the velocity in the sublayer of the turbulent boundary layer under survey to be measured. This data allowed a second independent measurement of the drag to be made.

2.1.3 Tunnel Inlet

In order to achieve a high quality, two-dimensional, low turbulence intensity flow on the tunnel wall and, particularly, to avoid Taylor-Görtler vortices on the test wall, the decision was made not to use a traditional contraction for the inlet of the tunnel. Based on tests at low-velocity (less than 20 ft/sec) in a similar tunnel a flow management system was constructed. This consisted of a high precision 4 mm Hex-cell honeycomb (Figures 2.3 and 2.4) along with a series of fine mesh aluminum screens fitted in a section with the same area as the test section (contraction area ratio 1:1). A series of iterations with the distance and number of screen arrangements were made. For each iteration, smoke-wire flow visualizations and turbulence intensity measurements at various downstream stations were made. The final configuration of the inlet was obtained after a period of 6 months. The tunnel inlet adjustments were based on the work of Loehrke and Nagib (1977), and of de Bray (1967). A range of turbulence intensities (0.1-0.25%) for velocities 5-20 fps were obtained. The final inlet configuration is shown in Figure 2.5. Using this simple inlet configuration a large amount of space and design and construction effort was saved. Between 1/3 and 1/2 of the mass flux otherwise needed is saved (reducing tunnel size and fan, motor and power requirements). Furthermore, the installation of a plate and the associated support equipment is avoided. Streamwise vortices have also been observed to emerge from contractions quite far above the boundary layers. These might be associated with Taylor-Görtler vortices (Smith, 1955, Schlichting, 1979), generated on the concave surfaces of a contraction,

or as a result of nonuniformities generated in the contracting flow. Furthermore, an unsteadiness associated with separation in contractions is avoided. Use of the tunnel wall also avoids problems with the strong corner vortices resulting from the three-dimensional separated region and the resulting horseshoe vortex that is created at the plate/wall junction.

Two different screen arrangements were used for the experiments. The first consisted of a stack of 44 screens almost touching one another followed by a precision hex-cell honeycomb with 3/16" cells measuring 3" long (Cynamid, Blomingdale division, Havre De Grace, MD). Figure 2.3 shows the honeycomb with the carefully cut ends. The second inlet configuration, which was used for the final experiments, is also a combination of 6 screens of the same quality used in the original inlet arrangement but with different spacings between screens. This set of screens is followed by a honeycomb of the same precision with another screen placed downstream from it (Figure 2.5). The flow management section is made to allow modifications by either increasing or decreasing the number of screens for different turbulence intensity levels of the tunnel flow. The turbulence intensity level at the nominal test velocity (3 m/sec) (at several stations) is shown in Figure 2.6 for both configurations. Additional qualifying measurements are discussed below.

2.1.4 Exit Diffusers

The second stage of the diffuser (aft of the fan) was designed to be removable, allowing either a radial or axial configuration to be

installed. The axial diffuser was also used to discharge the smoke contaminated air resulting from flow visualization into the atmosphere outside the laboratory building. The radial diffuser was used when highest quality probe measurements were required and flow visualization was not being performed. Each diffuser was mounted on a supporting structure with four rollers. This roller arrangement provided the convenience of exchanging the two diffusers with minimal effort. The radial diffuser, which had been tested on the Lagrangian Wind Tunnel (LWT) in the Turbulence Structure Laboratory, has an area ratio of 2:1 (exit to inlet area). The axial diffuser also has a 2:1 area ratio (Figure 2.1).

2.2 Experimental Apparatus

The techniques and instrumentation used are described below.

2.2.1 Static Pressure Probes

In order to measure the variation of static pressure along the test wall, static pressure taps were flush mounted every 48 inches along the center line of the test wall. These pressure taps were designed according to Shaw's (1960) suggestion, and accurately machined from a 0.25"-diameter aluminum rod. The sensing hole of these taps had a 0.125" diameter. They were connected to 0.25" I.D. clear Tygon tubes 24" long (plugged when not in use). The static pressure was also measured using a 1/8"-diameter static L-shaped pressure probe (United Sensor PSC-12, 1/8", with four 1/32" holes) which was mounted on a movable support. The probe was positioned one inch (= 8d) above the

test wall surface and 12" upstream of its support. The probe was also used to measure the static pressure for spanwise Preston tube experiments, as explained in Section 2.2.2. The results obtained from the static wall taps were in excellent agreement with those obtained using the static pressure probe.

2.2.2 Traveling Preston Tube

In order to examine the two-dimensionality of the flow on the test wall the arrangement of a total pressure probe resting on the wall and the above mentioned static pressure probe was used. This arrangement of pressure probes, which is a modified version of the well-known Preston tube (J.H. Preston, 1954) with V.C. Patel's (1965) design version, was employed to measure the shear stress on the test wall. The measurements were made across the span of the test wall by moving the Preston tube, which was attached to a traverse mechanism with 36" travel. The sensor part of the probe was 12" upstream of the support thus avoiding any disturbance in the measurement. A schematic of the probe appears in Figure 2.8. In order to calibrate the Preston tube, the shear stresses (τ_w), were estimated from Clauser plots based on Coles' 1968 "law of wall" constants. The probe was only used in the unmanipulated turbulent boundary layer. The present calibration data were plotted on the empirical calibration curve (refer to Figure 3.2). The calibration relation $\tau_w d^2 \rho / 4\mu^2 = F(dP_p d^2 \rho / 4\mu^2)$ was suggested by Preston. The results of the above calculations were in good agreement with the curve-fit suggested by Patel (1965) for a much wider range of data. Therefore, the same curve-fit was used as the calibration of the present

measurements. Further calculation procedures are discussed in Section 2.4.1.

2.2.3 Boundary Layer Manipulators and Tripping Device

The manipulator device used was a tandem-arranged parallel plate manipulator (referred to hereafter by its acronym 'TAPPM'). It consisted of two plates of the same thickness. Two different plate thicknesses were employed during this research. For the first TAPPM, the plates were 48" x 3" x 0.03"; the second set had the same dimensions except for plate thickness which was 0.003". The first set was made of stainless steel shim stock, and the second set of manipulator plates were blue tempered spring steel shim stock (Type C-1095 from DE.STA.CO). These thin plates were clamped between two blocks of steel outside of the tunnel. The blocks were used for holding the TAPPM plates at the desired height above the test wall. Tension in the TAPPM plates was provided by an adjustable mechanism located outside the tunnel's vertical walls. In order to keep a uniform tension in the manipulator plates for different runs, a strain gage was mounted at the far end of each of the plates. The strain in the plates under tension was measured by a VISHAY electronic strain indicator. In this manner tension in the plates could be monitored and kept constant throughout the entire experimental procedure. There was no evidence of any vibration of the TAPPMs. This was confirmed by steady--non-moving--reflection observed from a light shining on the surface of the TAPPMs. These tests were conducted for 5, 10.5, and 15 fps freestream velocities in the tunnel. The non-dimensional geometry of these manipulators was similar to the

configuration suggested by Corke (1981) (refer to Figure 2.2).

The boundary layer flow was tripped by placing a .0625" (1.588 mm) diameter threaded rod at x = 19.5" (49.5 cm) from the leading edge of the test wall. Sand paper was also tried in the preliminary tests but resulted in larger spanwise nonuniformities of the Preston tube measurements and was abandoned in favor of the better defined transition position provided by the threaded rod. The leading edge referred to in this experiment is the downstream edge of the honeycomb where it attaches to the test section. Note that all the streamwise distances referred to are from this reference point.

2.2.4 Hot-wire Anemometry and the Data Acquisition System

2.2.4.1 Single Wire Hot-wire Probe

Most of the velocity profile measurements were made with a single wire mounted perpendicular to the flow and parallel to the wall (called a U-wire). The axis of this wire was in the z direction (refer to Figure 2.2 for the coordinate system used throughout this study). It was made from 5 μm tungsten wire, with 30 μm sleeves. The active length was 1mm and the sleeves were 1mm. The sleeves were soldered to broaches that extended 20mm in front of their epoxy supporting base. U-wires were used for near-wall mean velocity and intensity measurements and sometimes for overall velocity and intensity profiles. In every case the U-wire was calibrated before a measurement and this calibration was checked after each measurement.

2.2.4.2 Twin X-wire Probe

A four-element hot-wire array was employed to measure streamwise and normal velocity components at two points. This array consisted of two x-wire probes. The two x-wire probes were independently mounted on a 3/8"-diameter aluminum rod using similar fixtures which allowed for the adjustment of x-wire number one with respect to x-wire number two (Figure 2.9) which was held stationary. These fixtures were mounted to the traverse mechanism allowing adjustment perpendicular to the test wall. These probes, as well as the U-wires, were fabricated in the Turbulence Structure Laboratory at Michigan State University.

The twin x-wire probe is shown in Figure 2.9. Each wire of the x-wire probe was in the x-y plane, enabling measurement of the streamwise velocity component 'u', the component in the y direction 'v', and, therefore, the product of the fluctuations (the instantaneous Reynolds Stress u'v').

The twin x-probes were used at two stations downstream of the TAPPM location. The geometry of their relative positions is shown in Figure 2.9. The four element hot-wire probe was operated using four DISA type 55M10 constant temperature standard bridge anemometers. The four anemometer signals were digitized by a simultaneous sample and hold 12 bit analog-to-digital (A/D) converter and stored on a 10mb RLO2 disc connected to a DEC PDP11/23 microcomputer. The four anemometer signals were simultaneously sampled and then digitized. In addition, experiments using simultaneous hot-wire anemometry and flow visualization were performed using the technique similar to that discussed in detail by Falco (1980), Lovett (1982), and Signor (1982).

For this experiment a more powerful laser light source was used (a Copper Vapor Laser with 40 watts at 514 nm and 578 nm). (This laser power is five times greater than the Argon Ion laser used by the three researchers mentioned above thus the flow visualization was clearer and provided better resolution, allowing more accurate visual information to be obtained).

2.2.5 Flattened Pitot-tube

The first part of the velocity survey was conducted using a flattened Pitot-tube (shown in Figure 2.10). The pitot-tube was constructed in the TSL shop. A wall tap which was usually located below the tip of the total pressure tube, was used to measure static pressure. The results were checked against a United Sensor Pitot static tube (PSC-12, 1/4") with very very consistent test results. The difference between the total pressure tube and the wall tap was used for our velocity profiles which were made along the center line of the test wall. The total pressure tube was mounted on the same traverse mechanism used for hot-wire anemometry. Several Pitot tube displacement corrections were applied to the data obtained from near the wall. Little difference was found; in light of the insignificance of these empirical corrections no correction in Pitot static tube measurements was made.

2.2.6 Flow Visualization

2.2.6.1 Smoke Fog

The volume flow marking technique used in this work provides good detail within the turbulence but requires a wind tunnel that is "open return". A sheet of laser light was used for definition of the side view of the flow field. The boundary layer was visualized by introducing a fog of oil droplets (droplet diameters ranged from .5 μ to 5 μ) into the flow through a closely spaced row of holes in the test wall located at $x = 13.5"$. A small overpressure was used so that the laminar boundary layer above the holes remained stable. The laminar boundary layer with the oil fog in the lower part was then tripped. The turbulent boundary layer resulting from this process was almost completely filled with the oil fog (hereafter referred to as smoke). This visualization technique and its use with hot-wire anemometry is explained by Falco (1980). The side view of the flow, along with the counter (LED clock) which displayed the number of digitized data points from the hot-wire array being stored in the computer, was recorded by a LOCAM high-speed 16 mm pin registered movie camera on 7250 Kodak film. This data was used to conditionally sample signals corresponding to the large eddies in both regular and manipulated turbulent boundary layers.

2.2.6.2 Smoke-Wire

This technique is also well known (refer to Corke et al (1977) for a complete description of the technique). A stainless steel wire of .04 mm diameter was used with a manually-controlled variable DC power

supply. Three 1000-watt floodlights were used as the light source with the 16 mm Red Lake Locam movie camera and Kodak 7250 Video News Film, mentioned above, to record the visualization data at two stations (x = 210" and x = 520").

2.2.6.3 Titanium Tetrachloride ($TiCl_4$) Studies

Titanium tetrachloride ($TiCl_4$) is very difficult to use because it is extremely corrosive to metals and the resulting fumes are dangerous to laboratory personnel. Its use in transient flow visualization, however, is of great value. $TiCl_4$ was used in three different experiments: 1) to observe the possible separation of the flow on the surface of the TAPPMs, 2) to provide evidence of the coherence and persistence of coherence of the TAPPM wakes, and 3) to study the mass transport and lift-up of the fluid from the sublayer into the outer region of the boundary layer downstream of the TAPPM device and compare it to the unmanipulated boundary layer. The use and safety aspects of the technique are discussed by Freymuth et al. (1983).

2.3 Experimental Procedure

All three phases of the experimental procedure, including the tunnel preparation, are discussed in this section.

2.3.1 Visual Data Acquisition

After the main structure of the wind tunnel was built, a series of smoke fog flow visualization tests were conducted in order to check possible leaks. The first step was to run the tunnel fan at a very low

speed, which produced a steady one foot/sec freestream velocity in the test section. The boundary layer that developed over the entire length of the test wall (56 feet) was laminar. This could be seen by observing the smoke, which remained stable and attached to the test wall from x = 13.5" where it was introduced into the boundary layer, to the end of the test section (x = 672"). This was a candidate for the longest laminar boundary layer ever produced in a laboratory and showed the quality of the rectilinearity of the flow that was created. During this experiment no serious leaks were detected. At higher speeds, up to 20 ft/sec, smoke was used to detect possible leaks close to the joints of the sections from outside the tunnel. Observation of the flow through the clear plexiglass walls of the test section made this detection procedure possible. This technique was used until all the leaks were sealed. The inlet configuration (Figure 2.4) was used on the tunnel during this phase of the work. Based on a rough estimate of turbulence intensity (0.8%) by hot-wire anemometry the tunnel was used for the next task: to examine the pressure gradient, the two-dimensionality of the flow, and, eventually, the velocity survey of the test wall.

2.3.1.1 Tunnel Preparation by Visualization

It was later found that the turbulence intensity level could still be improved by removal and rearrangement of the screens in the inlet box frame. The screen box, 6 inches in length, was replaced by one 30 inches in length. This allowed flexibility in the rearrangement of screens so that the number of screens and the distance between screens could be easily altered. A series of smoke-wire visualizations for each

arrangement was conducted. For each modification a series of still 35 millimeter photos was taken and studied. It took a period of more than six months to obtain a reasonable improvement in the turbulence intensity of the flow in the freestream region. The final configuration is shown in Figure 2.5. The mesh and cell size of the screens and honeycomb is provided in Section 2.1.3. An example of the smoke-wire visualization of the freestream and the boundary layer flow at station A ($x \simeq 240''$) is provided in Figure 2.7.

A very interesting phenomenon was observed near the center line of the tunnel when smoke was being introduced continuously into the tunnel's core region. Careful real-time visual observation of the smoke streaklines showed an apparent 'jumping' of these lines which left the impression that a new problem in the tunnel had been encountered. Note that this could not be detected by the 35mm still photos. The high-speed films were taken at two stations ($x = 240''$ and $x = 520''$). For $U_\infty = 10.5$ ft./sec. the 16mm film, framing at 100 frames/sec., showed that passage of "large eddies" in the bottom and the top wall boundary layers of the tunnel were responsible for this phenomenon. When a large eddy was in view on the bottom wall boundary layer a 'bending' was observed in the streaklines in the potential region of the flow. This distortion had a finite amplitude at the centerline of the tunnel. This phenomenon was amplified when a valley between two large eddies on the top boundary layer was present. This result was more clearly seen in the 16mm films taken at $x = 520''$ station because the boundary layers of both the top and the bottom were somewhat thicker at this station (boundary layer thickness, $\delta = 8''$ at $x = 520''$). The

amplitude of this wavy movement of the streak lines was measured and found to be on the order of 0.01-0.02 boundary layer thickness. Figure 2.15 shows an example of the phenomenon. Thus, it was concluded that, the apparent unsteadiness was not due to the wind tunnel fan but to the passage of the large eddies in the turbulent boundary layer. The observations also clearly showed that the boundary layers on opposing walls always had a well defined irrotational region between them even at the 520" station.

2.3.1.2 TAPPM Wake and Wall-Layer Visualization

As discussed in Section 3.3.1 below, the results of the velocity profile survey, in the relaxation region of the skin drag, combined with known results of low Reynolds number airfoil stall characteristics led to a suspicion that the flow around the TAPPM's was separated. To obtain a definitive answer regarding the separation around these plates a series of flow visualizations using $TiCl_4$ as the flow marker was conducted. The visualization experiment was performed at three spanwise locations on both plate surfaces of the TAPPM (U_∞ = 5, 10.5, and 15 fps), (drag tests were performed at a nominal 10 fps). Examination of more than 200 snapshots of these experiments did not show any evidence of separation (see Figure 2.17).

A series of TAPPM wake and wall layer flow visualizations at station A (ξ = 20) were conducted. These visualization experiments were quantifiable and resulted in conclusive findings in terms of the correlation of drag reduction and the structural changes in the turbulent boundary layer.

A volume of 2 cc $TiCl_4$ was applied, using a 5cc syringe for each 39-frame roll of film taken (the syringes became plugged after each application and were not used again), along a line that always started at the same x-position. For each case (manipulated and regular boundary layer) snapshots were taken at intervals of 0.5 second. For each run a fresh strip of TiCl4 (70 cm by 1 cm) was laid on the test wall under similar overall conditions. The experiments were recorded on 35mm films (Kodak Tri-X pan, ISO 400) and later were quantized on the film analyzer. An estimate of the difference in mass transport from sublayer region into the outer region for the two cases of manipulated and regular turbulent boundary layers was obtained. The difference in the level of sublayer fluid lifted up and ingested into the outer layer was correlated with the changes in C_f for the two boundary layer cases. Figure 2.11 gives the dimensions and the geometry of the region under investigation in this experiment. The portion of the films of the flow field which was quantized appears in the central portion of the view. After a series of similar trials the last rolls of film, which contained 39 frames in each case, were selected for final data acquisition and analysis. Twenty six data points (y values) were measured from each frame. These values represent the highest points that the marked sublayer fluid reached into the outer region. The distance between the two points selected for measuring y values (from wall surface to the top boundary of the marker) was based on the smallest sized structures observed in the flow in this region. In this manner each eddy structure seen in the flow, on the average, had two y values in the data obtained from these films. In each case 1014 y-values were recorded. These

values were statistically analyzed using a TSL program called RATHIS which created an equal interval histogram and used the mean and standard deviation of the sample to fit a theoretical distribution over the histogram. The histogram and the theoretical distribution were plotted using a routine called RATPLT on the TSL computer. Final results of this part of the experiment will be discussed in Section 3.3.1.

2.3.1.3 Wall Layer "Pocket Module" Event Visualization

Flow visualization of the footprint of the bursting process, which creates a "pocket" of high speed fluid in the sublayer, was performed at the station (x = 340" (8.64 m)) where the local skin friction $C_{f\theta}$ (based on the momentum balance calculation) showed the largest change due to manipulation of the boundary layer. This technique was used by Falco (1980) and Lovett (1982). The experiment consisted of the introduction of smoke through a shallow angle slit in the test wall, which provided a dense sheet of smoke on the wall in the x-z plane, to mark the occurrence of the "pockets". The slit was 12 in. (30.5 cm) long in the z-direction with a 0.07" (1.18 mm) gap in the y direction and an injection angle of 9 degrees. Immediately downstream from the slit smoke was highly concentrated in the region of the boundary layer very close to the test wall surface. As the turbulent motions of the smoke free region above the wall enter the smoke-filled wall region at the surface their interaction is demonstrated by a "footprint". This footprint is referred to by Falco (1980) as the "pocket module" (also refer to Lovett, 1982). These footprints were illuminated using two 300-watt floodlights mounted above the tunnel shining on the test wall,

and were photographed using the Locam 16 mm high-speed movie camera (500 frames/sec.). Because of the narrow depth of field of the f/.95 lens determination of the correct y plane to focus on for the sharpest image of the pocket was accomplished by trial and error.

2.3.2 Mean Velocity and Combined Hot-wire and Laser Visual Data Acquisition Systems

The first mean velocity profile data sets taken with the thicker TAPPM device (TAPPM No. 1, 48" x 3" x 0.03", in Experiment I) in place were collected using the flat Pitot-tube probe discussed in Section 2.2.5. This probe was made of a 3/8" diameter copper tube. The static probe part of this Pitot-tube was chosen to be the wall static pressure tap nearest to the tip of the total pressure probe (a schematic of this probe appears in Figure 2.10). The velocity profile voltages collected for this part of the experiment with TAPPM No. 1 were manually recorded from a digital voltmeter, then, using Bernoulli's equation, the corresponding velocities were calculated. These velocity profile data were later manually typed into a preformatted file and processed on the TSL computer to obtain the mean velocity profiles and their integral parameters. This program and procedure is discussed below. The steps in processing and plotting the various graphs of these profiles are shown in Figure 2.12.

An MKS Baratron, .01 TORR resolution, pressure transducer was used to measure pressures. Pressure related to voltages were averaged by a DISA integrator on the 100 second range; i.e. for each y position of the Pitot-tube probe the pressure transducer signal was time averaged

over a 100 second period. The instantaneous signals were monitored on an oscilloscope. Final averaged voltages were recorded from the TSI digital voltmeter and converted to velocities via the Bernoulli's equation. They were then interactively typed into a data file to be processed by a computer command file program called CALANL. The function this program performs is shown in Figure 2.12.

The next set of velocity profiles was obtained using a single u-wire hot-wire probe. This time the thinner TAPPM (TAPPM No. 2, 48" x 3" x 0.003") was used to manipulate the turbulent boundary layer. The hot-wire was used in order to obtain accurate information as close to the wall as possible and to obtain turbulence intensities.

The final mean velocity profile and rms fluctuation data were obtained using a constant temperature DISA hot-wire anemometer. Two TSI digital voltmeters were used to record the mean and rms fluctuations of the velocity profiles. The hot-wire was calibrated in the same wind tunnel before and after each velocity profile data collection. The hot-wire calibration consisted of collecting simultaneous average voltages from the hot-wire and pressure readings from the pressure transducer. The final velocity profile and respective hot-wire calibration data were collected using the two TSI digital voltmeters, a single hot-wire probe with a DISA 55M10 constant temperature anemometer, an MKS Baratron model 146H-0.1 pressure transducer, and a Keithly digital voltmeter.

The experiments using the twin x-wire probe array, and those which involved using the array combined with simultaneous visual data collection, required more sophisticated data acquisition. The signals

from the twin-x-wire probe were digitized using a simultaneous sample-and-hold 125 KHz analog to digital converter (hereafter referred to as "the A/D"), and a PDP-11/23 DEC computer, using the RT-11 operating system. The computer (hereafter referred to as "the data acquisition computer") had an RL02 disk drive for mass storage. The MKS Baratron pressure transducer (mentioned above) was used for calibration. A Plasma Kinetic 40 Watt Copper Vapor laser was used to produce a sheet of light parallel to the flow, normal to the wall, and in the plane of the probe array. Melles Griot cylindrical lenses and mirrors were used to produce the laser sheet which was 1/8" thick. Figure 2.16 is a schematic of the optical arrangement used for this part of the experiment. A digital counter (hereafter referred to as "the LED clock", or "counter"), triggered by the computer, registered a change for every digitized data point. This was recorded on the 16mm film simultaneously with the smoke-filled boundary layer. In addition, the hot-wire probe data was recorded by the data acquisition computer and stored on the RL02 disk. Each realization took 4.91 seconds, was separated into three portions, and was later saved in three separate data files. For each portion the LED clock was reset by the computer and indicated the changes in each separate portion of hot-wire data. The total time of data recording for each final case (regular or manipulated boundary layer) was 49.1 seconds.

The following equipment was used to record the structures in the flow passing the probe when the twin-x-wire was in use: 1) four DISA 55M10 constant anemometers, 2) the MKS Baratron pressure transducer and two TSI digital voltmeters, 3) the Keithly digital voltmeter, 4) the

smoke generator, and 5) the Redlake Locam high-speed movie camera (with the same lens at f/.95 and 16mm Kodak 7250 film). The two x-wire probes were calibrated using the standard TSL procedure (see Lovett, 1982). Two computers, an LSI-11/23+ with 1.0 MB memory running RSX-11M, and a Digital Equipment Corporation VAX running under the VMS, (Version 4.0) operating system were used for processing the data collected in this part of the experiment. A diagram of the main instrumentation and computer network appears in Figure 2.14.

2.4 Data Reduction and Analysis

Several techniques and experimental procedures used are described in the order of performance of the experiments.

2.4.1 Streamwise Pressure Gradient and Skin Friction Data

An important objective of the tunnel design was to achieve a streamwise zero pressure gradient on the test wall in a two-dimensional turbulent boundary layer without having to resort to an expensive jack-supported structure. The axial pressure gradient and spanwise uniformity of the tunnel design, with no contraction, and the 1/4 degree divergence was tested via a series of pressure measurements in streamwise and spanwise directions. The streamwise pressure measurements were conducted by recording the pressure difference between a reference static pressure wall tap (located at x = 25.5 in. (0.65 m) downstream of the leading edge of the test wall) and other static pressure taps located 48 in. apart along the center line of the test wall. Each measurement was taken for a period of 100 seconds and was

time-averaged with the DISA integrator described above. The same measurements were conducted using the United Sensor static pressure probe. No significant differences in the pressure readings were observed. Thus the quality of information from the 1/8" static pressure taps was confirmed. These pressure readings were substituted into Bernoulli's equation then non-dimensionalized to obtain $dCp/dx = 2dp/\rho U_\infty^2$ per foot. The streamwise pressure gradient of the flow in the tunnel will be discussed in Section 3.1.1.

Spanwise skin friction variation measurements were conducted using the movable Preston tube (Preston, 1954) described above. The pressure readings were again time-averaged by the DISA integrator for 100 second periods. This information was substituted into Patel's 1965 calibration. The calibration held for total pressure tubes with $d/D = 0.6$, where d is the inner diameter and D is the outer diameter of the total pressure tube used in the Preston tube probe. The diameter D of the total head tube was always less than the thickness of the logarithmic layer of the boundary layers ($D < 0.1\delta$) under survey (refer to Preston, 1954). The shear stress at the wall and the local skin friction coefficient C_f were obtained using the calibration equations, $x^* = \log_{10}(\rho dPd^2/4\mu^2)$ (which for our range of data resulted basically in the number $4.4 < x^* < 4.7$ for several stations under investigation) and $y^* = 0.8287 - .1381x^* + 0.1437(x^*)^2 - 0.006(x^*)^3$, (where y^* is defined as $\log_{10}(\tau_w d^2\rho/4\mu^2)$).

2.4.2 Mean Velocity Profile Data

Mean velocity profile data for the thicker TAPPM (the first set of

boundary layer velocity profiles) was calculated by hand from measured voltages using Bernoulli's equation. Further non-dimensionalization and plotting of the results were performed on the TSL computer (operated under the RSX-11M operating system). The mean and rms of velocity profile data of the thinner TAPPM experiment were processed using calibration and data reduction algorithms of the TSL. The single hot-wire was calibrated before and after the actual velocity profile data acquisition period (which was usually about 4 hours when data was collected with digital voltmeters). The temperature variations during this period were less than ±0.3°C. When the data was digitized by the A/D it took one hour to collect data for each complete velocity profile (which consisted of 50 probe positions). In this manner, potential variations of probe calibration, over the course of the measurements, could be accounted for. No noticeable variations due to drifting were obtained throughout the course of the experiments. Both sets of velocity profiles were analyzed and processed in the same manner using a number of computer programs which are summarized in Figure 2.12. The boundary layer parameters, obtained from velocity profiles, were determined from both sets of data to obtain the net skin drag and wall friction coefficient (C_f) and their variations along the center line of the test wall for the regular and manipulated boundary layers. Each profile consisted of 50 discrete data points, spaced normal to the test wall, which resulted result in high resolution near the wall and at the outer edge (to allow the sublayer edge and the overall boundary layer thickness to be accurately defined). In spite of this approach, it was considered valuable to smooth the velocity profiles by hand using the

following procedure: The data was plotted (y vs $\bar{U}$) by computer on a large sheet of graph paper (approximately 32 cm by 150 cm). Then, using a large french curve, sets of 5 to 10 points at a time were fitted on a curved line. In cases of a bad fit of a point to the curve, the velocity of that particular point was changed to fit the smooth curve. In cases where a deviation from a smooth curve in the velocity profile was observed the relative velocity difference was never more than 1% at any particular position. The smoothed profile was replotted and the data processing was continued on the computer. Profiles were taken at the streamwise stations shown in Figure 2.2.

The data from each profile were displayed on a series of plots which are described as follows: (1) y vs $\bar{U}$ for the data points which were very close to the surface of the test wall (0.0 to 0.1" (2.54 mm)). There were, on average, 10 data points in this graph which could normally be fitted on a straight line. This line, for most of the profiles, would pass through the origin of the axis (y vs $\bar{U}$). In some cases the line did not pass through zero (origin) and the error in reading the y value was not more than ±0.002". The error was corrected for y values of the particular velocity profile data and the graph was replotted. The slope of this line was used to obtain the shear stress at the wall. The friction velocity and other parameters obtained by this method will hereafter be referred to by a subscript "n" (such as friction velocity $u_{\tau n}$, local skin friction coefficient C_{fn}, and so on). (2) The second plot showed y vs $\bar{U}$ for the complete velocity profile. (3) Two Clauser plots produced by the program were used to obtain an estimate of C_f. One was based on Coles' "law of the wall" ($u^+ =$

5.61$\log_{10}y^+$ + 5.0) parameters (see Coles, 1968) and the other was based on Patel's "law of the wall" (u^+ = 5.5$\log_{10}y^+$ + 5.45) parameters (see Patel, 1965). We chose to use Coles' "law of the wall" for the final estimates of C_f because of its general acceptance (especially in the U.S.) and to make our results more easily comparable to the work of others. These parameters were used to obtain the Clauser plot and to estimate the skin friction coefficient for the particular velocity profile being processed (for further details of the method refer to Clauser, 1954).

(4) At this point of velocity profile data processing the information regarding slope at the wall and the C_{fc} from the Clauser plot were interactively typed into the TSL computer and processed. This complete velocity profile processing and plotting routine was performed by a command file referred to as CALANL. Its position in the data processing is shown in Figure 2.12. The responsibility of CALANL was to process and plot the data. The subprograms in CALANL are as follows:

VELPRO— can either calculate velocities from a calibrated single hot-wire or bypass this part and continue to process the data for Clauser plot.

MULPLT— plots data in desired format.

VELPR3— calculates the boundary layer profile parameters: freestream velocity U_∞, boundary layer thickness δ ($y = \delta$ at 0.99U_∞), displacement thickness δ_d, momentum thickness Θ, shape factor H, Reynolds number (based on the momentum thickness R_Θ), energy thickness Δ, Cole's wake coefficient (π) (based on C_{fn} and C_{fc}), and friction velocity (based on C_{fn} and C_{fc} estimated from the Clauser plot). In addition, this program non-dimensionalizes the velocity profile data to obtain the rest of the plots explained in Figure 2.12. All the above information is stored in one master data file.

Once this part of the velocity profile survey and analysis for both regular and manipulated boundary layers was completed, a plot representing the momentum thickness (Θ) vs distance from the test wall leading edge (x) was made using the calculated Θ. From this plot we obtained $C_{f\Theta} = 2d\Theta/dx$. This relation is obtained from the von Karman integral equation (Schlichting, 1979) ($d\Theta/dx$ was obtained by a graphical differentiation of the Θ curve plotted against x) when the pressure gradient along the x-direction in the boundary layer is equal to zero ($dp/dx = 0$). $C_{f\Theta}$ and C_{fc} were used in reprocessing the velocity profile data in the final non-dimensionalization (presented in Chapter 3). The momentum thickness variation was also used to determine the variation of the net drag of the manipulated with respect to the regular boundary layer from:

Net Drag Ratio = $(\Theta_x - \Theta_0)_{man.} / (\Theta_x - \Theta_0)_{reg.}$

where Θ_0 and Θ_x are momentum thicknesses of the boundary layers at the TAPPM and x-station locations where the corresponding net drag is calculated. This relationship is also the result of the von Karman integral equation, which represents a non-dimensional form of the net drag of the boundary layer flow on a flat plate of length x.

The results from the above equations led to the observation of crucial changes and the relaxation of the drag which developed downstream of the TAPPM device. Furthermore, these results were the key factors leading to the third phase of the experiments performed at stations where interesting changes in the structures of the flow were expected. This phase attempted to determine what structural changes result from the insertion of the TAPPMs into the boundary layer flow.

It involved flow visualization, hot-wire array anemometry, and simultaneous visualization and hot-wire measurements. Details of the experimental procedure, data processing, and analysis will be provided in the following sections of this chapter.

2.4.3 Twin X-wire Probe Data Processing and Analysis

Measurements to determine the structural changes in the turbulence were made in the boundary layers at two stations ($x = 240"$ and $x = 340"$). The data were collected at $x = 340"$ with the twin x-wire array only and with the x-wire array and visual technique simultaneously at $x = 240"$. These were processed on the TSL computer and, in part, on the MSU Engineering Computer Facility VAX-11/750 (using the VMS 4.0 operating system). The x-wire array data which were collected by the data acquisition computer system were transferred to the TSL computer and were processed from "raw" form (bits per millivolt) to velocities with the CONVOL program. CONVOL uses calibration information in Collis and Williams' (1959) parameter form and outputs the results of each wire (whether slant or straight) as velocities (if U-wire) or as pseudo-velocities (if a slant wire). The pseudo-velocities needed to be converted into u and v components. At the same time, a correction was made to compensate for possible errors in the angles of the x-wires. Two coefficients, CP and CN, were obtained via a calibration procedure detailed by Lovett (1982). These were calculated in a separate program called CPCN and were used as inputs to the TSL program VEL4 to account for the probe angle error corrections. In addition to data file names VEL4 program requires the following information to process the data:

sampling rate of the A/D, number of columns in the data files, format of the data files, and CP and CN values for both x-wires used in the array. The processed output files from VEL4 contain 12 columns of numbers. Six of these columns contain the fluctuating components (i.e., fluctuation = total – mean) of velocities and Reynolds stresses which are of interest in this experiment (the others are for storage of velocity gradient information). The fluctuating quantities which were examined in this experiment are u'_1, v'_1, $u'_1v'_1$, u'_2, v'_2, and $u'_2v'_2$ (subscript 1 refers to the top x-array probe located at $y = 0.6\delta$ and subscript 2 refers to the lower x-array at $y = 0.4\delta$ in the twin x-wire probe). Due to possible signal noise interference with A/D, a 5-point moving average smoothing routine was used in VEL4. The process of smoothing the data (which was performed by VEL4) is actually the same as that used by Signor (1982) in his data processing programs.

In order to obtain a visual sense of the velocity and Reynolds stress variations calculated in VEL4 the long-time records of these fluctuating quantities were plotted using a program (developed at TSL) called TIMPLT. TIMPLT is capable of plotting as many as 16 long-time series records of data, on 8 axes, for comparison purposes. These plots were studied to enhance and verify the visual data obtained from films taken in the simultaneous visual and x-array probe arrangement. This technique has been developed and successfully used over the past several years in turbulence studies at TSL.

The fluctuating velocities were further processed to obtain space-time correlations. A program called CORRELATE3 was used to process the data. Due to the massive amount of data recorded in this

experiment, a faster computer with a larger memory than the TSL computer proved to be a tremendous asset in performing the correlation calculations. These data were processed on the VAX-11/750 VMS system of the Engineering Computer Facility at MSU. The data for this part of the experiment were collected at two stations: $x = 240''$ ($\xi \simeq 20$) and $x = 340''$ ($\xi \simeq 51$). Since the space-time correlations at $\xi = 51$ did not show significant changes due to TAPPMs, it was decided to conduct simultaneous visualization and probe data acquisition only at $\xi \simeq 20$. These results will be discussed in the following chapter.

In order to obtain information about changes in the large eddies of the boundary layers studied in this experiment, space-time correlation analysis of such flows with large spatial separation of the probes was necessary. The correlations computed were $R_{u'_1 u'_2}$, $R_{v'_1 v'_2}$, $R_{u'_1 v'_2}$, and $R_{(u'v')_1 (u'v')_2}$. As is evident, the reference is the top x-wire probe (referred to as number 1).

The space-time correlation for functions p' and q' is defined as:

$$R_{p'q'} = \overline{p'(X_0, Y_0, Z_0, t_0) q'(X, Y, Z, t)}$$

where the overbar represents the time-average of the function. Subscript p' of R represents the reference signal, which in this experiment is defined as the velocity (or Reynolds stress) fluctuation at the top x-wire array position, and q' represents the velocity (or Reynolds stress) fluctuation at the lower x-wire array position. If functions p' and q' are statistically homogeneous in space and stationary in time, the correlation depends only on the differences $X_2 - X_1$, $Y_2 - Y_1$, $Z_2 - Z_1$, and $t_2 - t_1$. In the case of zero pressure gradients, such as the condition in this experiment, we expect the

functions to be homogeneous with respect to Z and stationary with respect to t. In the zero pressure gradient case the growth of the boundary layer thickness is slow (as has been shown). One can, therefore, scale the coordinates with the local value of boundary layer thickness. Although y/δ is held constant, homogeneity does not exist along the y axis. The space coordinates in this experiment for the two stations under survey were non-dimensionalized by the respective local boundary layer thickness and were kept constant as: $X_2 - X_1 = 0.5\delta$, $Y_2 - Y_1 = 0.2\delta$, $Z_2 - Z_1 = 0.0$, and $\tau = (t - t_0)U_\infty/\delta$ (which was the only variable in the correlation computation process for both stations).

The flow field for this experiment was stationary in time. Thus, based on Taylor's hypothesis for the stationary flow conditions, one can express:

$$R_{p'q'}(X_0, t) \simeq R_{p'q'}(X, t_0)$$

The validity of this relationship is well supported and documented by Favre (1965). Based on the above discussion, the correlations $R_{u'_1u'_2}$, $R_{v'_1v'_2}$, $R_{u'_1v'_2}$, and $R_{(u'v')_1(u'v')_2}$ have been calculated and normalized by their respective rms values of the signals and by the freestream velocity (U_∞). The results of this analysis will be discussed in the next chapter.

The program CORRELATE3, for processing data from this experiment, requires the output velocity files of the VEL4, the number of columns in the data file, the columns of velocity fluctuations to be processed for correlation, the sampling window size (the number of points before and after the moving reference), the correlation step size, and the name of the output file for each data set taken. The data sets for each case of

the experiment were ensemble averaged by the CORAVG program and plotted using the MULPLT.

2.4.4 Conditional Sampling of Probe Data Based Upon the Film Data

An understanding of the large-eddy structural changes, due to a TAPPM device, that resulted in net drag reduction was an important goal of this research. To gain some physical insight into the correlation of skin friction drag reduction (obtained in experiments with boundary layer manipulators (TAPPMs)) and large-eddy alterations, we sought significant changes in the large eddies. Many attempts have relied mainly on probe data and a sparingly detailed associated flow visualization to explain the large-eddy structure changes in the manipulated boundary layers. We feel that the speculations that have resulted may be misleading. Utilizing the unique TSL facility and experimental techniques allows a one to one correspondence between the visually marked large eddies and the velocity and Reynolds stress they contain. The study of the films from the high-speed movies of both regular and manipulated boundary layers, combined with the simultaneous probe data, therefore, can uniquely answer questions about changes in the strength of the large eddies.

The process of conditionally sampling the probe data to the large eddies using the films was as follows: The digital clock read-out appeared in the bottom portion of the frames. Those moments at which the probe entered and left the large eddies were recorded. Each pair of recorded numbers represented the beginning and the end of probe data

numbers to be conditionally sampled out of the complete record of a data take. Each data take period was 4.91 seconds. The rate of sampling was 5 KHz. Using these number pairs, it was possible to look at the plots of the probe data and observe the fluctuating velocities and the Reynolds stresses inside the sampled large eddies. This is actually one of the most attractive techniques available at the TSL for the study of the structure of turbulence. For further details on this technique refer to Falco (1983). Due to clearer visibility of the large-eddies' boundaries, at the position of the top x-wire in the hot-wire array (y/δ = 0.6), only the number pairs for this x-wire were recorded to be used in the process of conditionally sampling the data. Figure 2.18 displays an example of a large eddy passing the probe. The number which is printed in reverse on the lower portion of the picture represents the point number stored in this data take.

The criteria for choosing the large eddies to be sampled were: (1) shape, (2) size, and, (3) clearly defined smoke marked borders (versus the valleys (non-turbulent regions upstream and downstream of the large eddies)) as the eddies convected over the field of view. Each large eddy had to remain a coherent visual entity over the field of view (eddies that divided or coalesced were not accepted (these were few in number)). The quantitative signals obtained from the probe were selectively sampled in the manner described above. Then these samples, for regular and manipulated boundary layers, were ensemble averaged separately for each case. The ensemble averaged signals were then normalized by different boundary layer flow characteristic parameters and plotted by TIMPLT. The ensemble averaged signals of u', v', and

u'v' give an excellent representation of the flow dynamics inside the large eddies (refer to Falco, 1977, 1982, 1983). The long-time records of the fluctuating signals, plotted by TIMPLT, were of great help in the sampling process of the data. They showed that the conditionally sampled regions did, indeed, contain essentially all of the significant perturbation represented by the signals.

CHAPTER 3

RESULTS

First we will discuss the results of the documentation of the flow facility, the mean velocity profile surveys, and the integral parameters of these velocity profiles. Next the results of flow visualization, x-array hot-wire anemometry (both alone and combined with simultaneous laser sheet flow visualization), along with space-time correlations will be discussed. Finally, an analysis of the results for both cases of regular and manipulated turbulent boundary layers will be presented.

3.1 Flow Field Conditions

First, documentation of the flow conditions achieved in the experiments is presented: The ideal conditions sought for the wind tunnel were constant pressure along the test section (zero pressure gradient), a two-dimensional boundary layer flow with a low-level turbulence intensity, a long flat test wall to investigate skin friction drag and structural development in both the regular and manipulated boundary layers.

3.1.1 Pressure Gradient Along the Centerline of the Test Wall

Figure 3.1 shows the results of the pressure gradient measurements along the x-axis of the test wall. The differential pressure coefficient defined as dC_p/dx (where $C_p = dP/\rho U_\infty^2$, $dP =$ (downstream static pressure – upstream static pressure), and $dx = x_2 - x_1$) was used

to obtain the information plotted in Figure 3.1. It was observed that the coefficient, which is calculated at different streamwise stations, varies, on average, less than ±0.002 per ft about a mean value of -0.002. This value is considered very low for a pressure gradient that is experimentally obtained. Murlis, Tsai and Bradshaw (1982) consider a 0.02 value for this coefficient a negligible pressure gradient. The pressure gradient measurement was conducted for both regular and manipulated boundary layers with results indicating no difference between them. Thus, the zero pressure gradient condition required for this experiment was satisfactorily met. The small variation in this coefficient was believed due to the slightly bowed top of the 8 ft tunnel sections. The first point at x = 49.5" had the lowest value. This was due to the fact that it is closest to the tripping device which was located 6" upstream of the first wall pressure tap. The boundary layer growth rate is greatest at the leading edge consequently the wall divergence did not compensate as effectively in this region. One can see that the low value is relaxed to the average value farther downstream from the trip. The last point has a somewhat higher dC_p/dx value than the rest of the points, and is the result of the presence of the diffuser 24" downstream of the last wall pressure tap.

3.1.2 Two-dimensionality of the Boundary Layer

The two-dimensionality of the flow on the test wall was examined using the traveling Preston tube. The results of this experiment for two inlet configurations with two tripping devices are shown in Figures 3.2-3.5. Figure 3.3 shows the variation of the skin friction in a

spanwise direction at several stations when the boundary layer was tripped with grit 36 sandpaper as suggested by Corke (1981). The sandpaper was 30 cm wide in the flow direction and was cemented to the test wall. It protruded 0.8 mm above the wall. The upstream edge of the sandpaper was located 10 cm downstream of the leading edge of the test wall. Figure 3.4 shows an improvement of this variation using a 0.0625" threaded rod at $x = 19.5"$. Figure 3.5 shows further improvement of the skin friction variation from 10.3% to 4.6%. This was accomplished through the use of the second inlet configuration (which was discussed in Section 2.1.3). A point of interest here is that the change in C_f variations and the lower mean value of C_f were associated with the lower freestream turbulent intensity (from 0.8% to 0.15%). As we shall see, the free stream turbulence may also seriously affect the performance of the TAPPM's.

3.1.3 Turbulence Intensity of the Wind Tunnel

As explained above, two inlets were used in order to achieve a high quality flow. The streamwise turbulence intensity levels of both cases are shown in Figure 2.6. The higher intensity existed when the first set of TAPPM devices was installed (Experiment I) in the test section. Turbulence intensity was reduced when the screen and honeycomb arrangements were altered. This reduction was from approximately 0.8% to a value of 0.15%, which was sufficient for the present experiment.

3.1.4 Smoke Flow Visualization of the Laminar Flow on the Test Wall

Before the velocity profile survey on the test wall, the tunnel fan

was run at one foot per second and smoke was introduced into the boundary layer at x = 13.5" downstream of the origin of the test wall. The flow stayed laminar over the entire length (17 m) of the test wall. This was an excellent demonstration of the high quality flow obtainable with this tunnel configuration, particularly with respect to the lack of three-dimensionality either existing or developing in the tunnel (since forces and growth rates that are clearly too small to measure could result in significant displacements over this length).

3.2 Mean Velocity Profiles

In order to obtain an estimate of skin friction drag in regular and manipulated turbulent boundary layers a series of velocity profiles was obtained. With the first TAPPM device (TAPPM No. 1, thickness = 0.03") the velocity profile data were obtained using the Pitot probe (see Chapter 2). The velocity profile data were obtained for both regular and manipulated boundary layers (measurements using TAPPM No. 1 are hereafter referred to as 'Experiment I'). The second velocity profile survey was conducted using the .003" thickness TAPPM (TAPPM No. 2). For these a single hot-wire probe was used to obtain the velocity profiles (hereafter we refer to this as 'Experiment II').

3.2.1 Mean Velocity Profile and Integral Parameters in Experiment I

Each boundary layer profile for the first TAPPM device experiment was made up of 30-34 data points. These profiles were taken at the stations shown in Figure 2.2. The Reynolds numbers (R_θ) ranged from

1434 to 5648 (the data processing procedure is explained in Chapter 2).

Figures 3.6 to 3.10 show the non-dimensional mean velocity profiles in Experiment I for regular boundary layers at different stations. Figure 3.6 shows y/θ vs $\bar{U}/U_\infty$. This figure illustrates the overall similarity of profiles in the fully developed turbulent boundary layer. Figure 3.7 shows the Clauser plot of velocity profiles from which C_{fc}'s were estimated for the regular boundary layer case. The coordinates are $\bar{U}/U_\infty$ vs Rey, where Rey = $\rho y U_\infty/\mu$. The straight lines plotted in this figure represent various C_{fc} uniformly spaced (with 0.00025 between two consecutive lines) from 0.00100 to 0.00575. It is observed that the data in the log region are essentially parallel to the constant C_f lines. The C_{fc} is shown later (see Figure 3.44) to be in close agreement with $C_{f\theta}$ (calculated from the momentum integral equation for the two-dimensional regular turbulent boundary layers).

Figure 3.8 shows the log region plotted in wall units i.e. u^+ vs y^+. Note that the friction velocities which have been used in the non-dimensionalization were obtained by the momentum balance method (referred to as $u_{\tau\theta}$). They are also used to non-dimensionalize the rest of the velocity profiles unless otherwise stated. The solid straight line is Coles (1968) "law of the wall" ($u^+ = 5.61\log_{10}(y^+) + 5.0$); the line $u^+ = y^+$, which holds in the viscous-sublayer, is also shown. The figure shows that the log law region is consistent with the log law constants suggested by Coles. A similar plot using $u_{\tau c}$ is not shown, but, obviously, the fit will go through the center of Coles' line since it is forced.

In order to demonstrate the equilibrium condition of the boundary layers, as suggested by Clauser (1954), Figure 3.9 adopted from Rotta (1962), is presented (the coordinates are $(U_\infty - \bar{U})/u_\tau$ vs $yu_\tau/\delta_d U_\infty$). The match is very good, suggesting that we have a fully developed turbulent boundary layer. Figure 3.10 shows the wake function W vs y/δ. For comparison purposes, the wake function, $W = 2\sin^2(\pi y/2\delta)$ suggested by Coles (1968) is also plotted in the same figure. The scatter is representative of the best zero pressure gradient data known to the authors.

In Experiment I, with manipulators in position, a similar data reduction and display procedure was used. Corresponding velocity profiles are presented in Figures 3.11-3.15. The data in Figure 3.11 nearly collapse on each other, except for the first two stations (A and B) downstream of the TAPPM. This is the wake effect of the manipulator which is positioned at $0.8\delta_0$. From examination of Figures 3.12 and 3.13 it is obvious that the skin friction coefficients (C_{fc}, estimated from Figure 3.12 (Clauser plot)) no longer agree with the $C_{f\theta}$. Notice that the data appear to be linear in the log region, but that the slope deviates somewhat from that of the constant stress lines in the Clauser plot. The information from this plot cannot be used to infer the local skin friction coefficient because the Clauser plot technique only exploits mechanisms which govern regular turbulent boundary layers. It is clear that a universal 'law of the wall' does not exist for the manipulated layer. Figure 3.14 demonstrates the lack of equilibrium found in the manipulated layer. Figure 3.15 further shows that the wake region is severely distorted in a non-monotonic manner as distance from

the TAPPM is increased.

Using the calculated Θ from the velocity profiles at various stations for both the regular and manipulated boundary layers, a plot of Θ vs x was constructed (see Figure 3.16). It was used to obtain $C_{f\Theta}$ and $u_{\tau\Theta}$, which were then used to normalize the velocity profile data shown in this section. Figure 3.16 shows that the momentum thickness at station A ($\xi \simeq 24$) was significantly increased. This increase was due to the skin drag which the TAPPM's presence added to the regular boundary layer drag. As one moves farther downstream Θ stays higher than it does in the regular boundary layer. However, it has a lower gradient which leads to the lower local skin friction coefficient, up to station E (at $\xi \simeq 86.4$), where the resulting net drag is zero. After this station the momentum thickness overshot, produced a higher drag than that found in the unmanipulated layer, then relaxed back farther downstream where ξ values were higher than 150. The result of the net drag variation deduced from this process in a non-dimensional form is presented in Figure 3.45.

The deviation from Coles' log law in Figure 3.13 can be attributed to the momentum thickness gradients (obtained from Figure 3.16) at various stations. In contrast to Corke's (1981) results, no unique universal log law line for the manipulated boundary layer mean velocity profiles was obtained. Notice that the parameters A and B (refer to equation $u^+ = A\log_{10}(y^+) + B$) are obtained by fitting straight lines through the data in the log region. This line fit was normally covered by data at $30 < y^+ < 500$ for our Reynolds number range. Parameters A and B (at various stations) are shown in Figure 3.17.

3.2.2 Mean Velocity Profiles and Integral Parameters in Experiment II

Since no net drag reduction occurred in Experiment I (refer to Figure 3.44), the decision was made (based on the results of Anders et al. (1984)) to use the thinner plates (t = 0.003"; t/δ_0 = 0.00095) to construct TAPPM No. 2, and redo the experiment. Each velocity profile in Experiment II was made up of 50 discrete data points. These profiles were taken at several stations (refer to Figure 2.2). The data processing procedure is explained in Chapter 2. Table 3.2 contains some of the integral characteristics of the boundary layers in Experiment II. Figures 3.18 to 3.25 show the non-dimensionalized velocity profiles in Experiment II for the regular boundary layer at various stations. Figure 3.18 shows y/θ vs $\bar{U}/U_\infty$. Figure 3.19 displays the Clauser plot of velocity profiles from which C_{fc} were estimated for the regular boundary layer case. Information, the C_{fc}, from this figure is used in the results (to be presented in Section 3.2.3) for a comparison with momentum balance and skin friction coefficient results (obtained from the slope of the mean velocity profile close to wall, for "Newtonian fluid"). Figure 3.20 shows the profiles in wall-unit coordinates (u^+ vs y^+). Again, the solid straight lines are Coles' "law of the wall" (u^+ = $5.61\log_{10}(y^+)$ + 5.0), and $u^+ = y^+$. Once again, the wall shear stress velocity is obtained from the momentum balance. It is clear that the regular boundary results in this figure all fit the solid line in the "log law" region very well.

The equilibrium condition of the boundary layer is shown in Figure 3.21. Figure 3.22 displays the wake function W vs y/δ. For comparison purposes, the wake function $W = 2\sin^2(\pi y/2\delta)$ (suggested by Coles (1968))

is plotted in the same figure. Figures 3.23 to 3.26 show the non-dimensional streamwise component of fluctuating mean velocity profiles at different stations. Figure 3.23 shows $\text{rms}(u')/u_\tau$ vs y^+. Figure 3.24 shows $\text{rms}(u')/U_\infty$ vs y/θ for the mean velocity profile and Figure 3.25 shows "near wall" data normalized in the same way as for Figure 3.24. Due to the thick boundary layer in this experiment, velocities very near the surface of the wall could be measured using the single hot-wire probe. The probe could get closer than one wall unit ($y^+ = 1$) before heat transfer effects begin to be felt (refer to Figures 3.20, 3.26, and 3.27). This can also be seen in Figure 3.27, which shows the dimensional mean velocities close to the wall in the regular boundary layer at various stations. It is important to note that each profile has at least 10 points which fit a straight line passing through the origin ($y = 0.0$ and $U = 0.0$ in Figure 3.27). This confirms the linearity condition in the sublayer region of the mean velocity profiles. These results were also used to obtain the thickness of the sublayer region. Notice that the resulting local skin friction coefficients, from the slope of the velocity profiles, are different from both Clauser C_{fc} and from $C_{f\theta}$ presented in this experiment. Details of the discrepancies between local skin friction coefficients obtained by different methods are discussed in chapter 4.

In Experiment II, with TAPPM No. 2 in position, a similar set of data was obtained. Corresponding velocity profiles are presented in Figures 3.28-3.36 in the same order as for the regular boundary layer case discussed above. Figure 3.28 shows y/θ vs $\overline{U}/U_\infty$ at various stations. Only two profiles of stations A ($\xi = 19.3$) and B ($\xi = 34.81$)

show the effect of the wake of the manipulator plates. Figure 3.29 displays the data plotted on the Clauser plot. This figure is presented here to again demonstrate the inadequacy of the Clauser plot method for the manipulated boundary layer. Results of local skin friction coefficients obtained from this figure are discussed in the following section.

Using the friction velocity obtained via the momentum balance method, we present the manipulated profiles of Experiment No. 2, in inner coordinates, in Figure 3.30. The non-monotonic trend of the profiles with increasing distance follows the variation of $C_{f\theta}$ at different stations. Notice that the parameters A and B (refer to equation $u^+ = A\log_{10}(y^+) + B$) are obtained by fitting a straight line through the data in the log region. This line fit was normally located at $30 < y^+ < 500$. Parameters A and B (at various stations) are shown in Figure 3.39. $C_{f\theta}$ results are also discussed in the following section.

The equilibrium condition of the boundary layer is also shown in Figure 3.31. Like the results in Experiment I, this figure shows that at stations where the skin friction drag is reduced, the profiles demonstrate a deviation from the other profiles. This leads to a pressure gradient-like effect in the manipulated boundary layer (Clauser 1954). The wake function of the manipulated case is shown in Figure 3.32. In this figure there is a large profile deviation (similar to that found in Experiment No. 1) from the Coles' wake function.

Figures 3.33 to 3.36 show the non-dimensionalized streamwise component of the fluctuating velocities at different stations. Figure 3.33 of this group shows $\text{rms}(u')/u_\tau$ vs y^+. At low skin friction

stations there is higher $rms(u')/u_\tau$ in the inner region (also refer to Figure 3.36) and lower $rms(u')/u_\tau$ in the outer region of the manipulated boundary layer compared to their corresponding regular boundary layers. Figures 3.34 and 3.35 show similar effects when the $rms(u')$ and y are non-dimensionalized by the outer region parameters U_∞ and θ. Figure 3.36 shows that the breakdown in similarity extends to non-dimensionalization in wall coordinates in the near-wall region (compare with Figure 3.26).

Figure 3.37 shows the dimensional mean velocity profiles close to the wall in the manipulated boundary layer at various stations. Similar to the regular boundary layer, each profile has 10 points which fit a straight line passing through the origin (y = 0.0 and U = 0.0 in Figure 3.37). This confirms the linearity condition in the sublayer region of the mean velocity profiles and its persistence in the manipulated case. Notice that the resulting local skin friction coefficients, from the slope of the velocity profiles, are different from both Clauser's C_{fc} and the $C_{f\theta}$ obtained in this experiment (as in Experiment I). Details of the local skin friction coefficient results, obtained through different methods, are presented in the following section.

Figure 3.38 (θ vs x) was constructed using the θ calculated from the velocity profiles at various stations for both regular and manipulated boundary layers. It was then used to obtain $C_{f\theta}$ and $u_{\tau\theta}$, which were used to normalize the velocity profile data in this experiment. This figure shows that at station A (ξ = 19.3) θ overshoots (due to device drag) then relaxes back (with a lower θ gradient than the regular boundary layer). This θ gradient stays low, even after θ

reaches values less than those of the regular boundary layer. This reflects a net skin drag reduction (lower Θ). At about station D ($\xi >$ 60) the momentum thickness gradient increases sharply, then after $\xi \simeq 94$ it levels off with the regular boundary layer to almost no net drag reduction.

The results of Figures 3.37 and 3.27 were also used to obtain the thickness of the sublayer region. Individual near-wall velocity profiles for regular and manipulated boundary layers are shown in Figures 3.42 and 3.43. The resulting sublayer thickness variations, with streamwise position for both regular and manipulated boundary layers, are shown in Figure 3.40. In dimensional form, the manipulated boundary layer has, on average, a 17% thicker sublayer. For reference, the streamwise variation of the ratio of the non-dimensional sublayer thicknesses (normalized by $u_{\tau n}$ obtained from the slope of the mean velocity profile near the wall) is shown in Figure 3.41. Overall, this indicates a similar increase in sublayer thickness. On the other hand, when the sublayer thickness is normalized by $u_{\tau\Theta}$ (obtained from the momentum balance) it must show sharp variations, as seen in $C_{f\Theta}$ vs ξ.

3.2.3 Skin Friction and Net Drag Results of Experiment I

Using the information from Figure 3.16 (Θ vs x), the local skin friction coefficient ($C_{f\Theta}$) was obtained by a graphical differentiation; $C_{f\Theta} = 2d\Theta/dx$. Furthermore, the non-dimensional net drag (($\Theta_x - \Theta_{x_0})_{Man.}/(\Theta_x - \Theta_{x_0})_{Reg.}$) along the centerline of the test wall was calculated. These parameters, combined with the results discussed above, were used to obtain Figures 3.44 to 3.47. Figure 3.44 shows

$C_{f\theta}/C_{fc}$ vs ξ. The agreement shows the high degree of consistency between momentum balance $C_{f\theta}$ and the Clauser C_{fc} results in the regular boundary layer.

The net drag change due to the use of TAPPM No. 1 in Experiment I is shown in Figure 3.45 in the form $(\theta_x - \theta_{x_0})_{Man.} / (\theta_x - \theta_{x_0})_{Reg.}$ vs ξ. The net drag increase is at its highest value at $\xi \simeq 25$ (the closest point measured downstream of the TAPPM). This is reduced to zero at $\xi \simeq 80$ then increased to higher values (10%) at stations farther downstream. Thus, no net drag reduction was obtained in Experiment I (in fact, we obtained a net drag increase). More surprising still, we appear to have had a significant relaxation of the flow downstream to a high drag condition ($\xi \simeq 80$) (Rashidnia and Falco, 1983). Figure 3.46 is a replot of the same result showing, in addition, the streamwise normalized local skin friction variation $(C_{f\theta})_{Man.} / (C_{f\theta})_{Reg.}$ vs ξ. At $\xi < 80$, where net drag has increased, the local skin friction is reduced ($(C_{f\theta})_{Man.} / (C_{f\theta})_{Reg.} < 1.0$). The two curves cross ($\xi \simeq 80$) and the ratio $(C_{f\theta})_{Man.} / (C_{f\theta})_{Reg.}$ stays above 1.0. As a result of the sharp increase in gradient of θ in the range of $80 < \xi < 120$, $(C_{f\theta})_{Man.} / (C_{f\theta})_{Reg.}$ increases and reaches its peak of about 1.4. In addition, net drag increases from zero to 10% in the same range. The net drag increase tends to relax back to the regular boundary layer condition very slowly, while the ratio $(C_{f\theta})_{Man.} / (C_{f\theta})_{Reg.}$ sharply decreases to about 0.7 at $\xi = 188.4$.

In Experiment I the slope of the mean velocity profile, near the wall, was obtained by a single hot-wire probe at two stations: $\xi \simeq 44$ (a decreased local skin friction station), and at $\xi \simeq 121$ (an increased

local skin friction station). The result is shown in Figure 3.47 and is compared with the momentum balance $C_{f\theta}\%$ changes. The magnitude of changes in these two methods is not the same, yet they demonstrate similar trends of local skin friction variations.

3.2.4 Skin Friction and Net Drag Results of Experiment II

Using the information from Figure 3.38 (θ vs x) the local skin friction coefficient ($C_{f\theta}$) was obtained by a graphical differentiation (similar to Experiment I). The non-dimensional net drag (($\theta_x - \theta_{x_0})_{Man.}/(\theta_x - \theta_{x_0})_{Reg.}$), along the centerline of the test wall, was also calculated. These parameters, combined with previously explained results, were used to obtain Figures 3.48 to 3.53. Figure 3.48 shows $C_{f\theta}/C_{fc}$ vs ξ. For this experiment $C_{f\theta}$ is a few percent lower than C_{fc} but still exhibits (as noted in Experiment I) remarkable consistency between the two techniques.

The non-dimensional net drag changes (($\theta_x - \theta_{x_0})_{Man.}/(\theta_x - \theta_{x_0})_{Reg.}$ vs ξ) found in Experiment II are shown in Figure 3.49. The net drag was at its highest value at $\xi \simeq 20$ (the first measurement station downstream of the TAPPM). This was reduced to zero at $\xi \simeq 45$ reaching its minimum at $\xi = 58.2$; at this point a 10% net drag reduction was obtained. This net reduction relaxed back to normal boundary layer drag at $\xi \simeq 94$ and remained at its normal value (zero net drag change). Thus, if the plate had ended at $\xi = 58.2$ we would have achieved a 10% net drag reduction. Figure 3.50 is a replot of the same result with the addition of the streamwise normalized local skin friction variation (($C_{f\theta})_{Man.}/(C_{f\theta})_{Reg.}$ vs ξ). In the range of $\xi < 45$, where no net drag

reduction is obtained, there is still a significant reduction in the local skin friction coefficient ($C_{f\theta} \simeq 45\%$); i.e., $(C_{f\theta})_{Man.}/(C_{f\theta})_{Reg.} \simeq 0.55$). At $\xi = 58.2$, where the maximum net drag reduction is achieved, the local skin friction reaches its regular boundary layer value. The peak of the $C_{f\theta}$ increase is reached at $\xi \simeq 66$ where the momentum thickness gradient reaches its maximum in the manipulated boundary layer. The two curves meet again at $\xi \simeq 93$ where net skin drag and local skin friction coefficient changes are almost nonexistent. This condition (ratio $(C_{f\theta})_{Man.}/(C_{f\theta})_{Reg.} \simeq 1$) holds to the last measuring station.

In Experiment II the near-wall slope of the mean velocity profile was obtained by a single hot-wire probe at several stations. Figure 3.52 shows the percentage variation of the streamwise local skin friction coefficient ($[(C_{fn})_{Man.} - (C_{fn})_{Reg.}]/(C_{fn})_{Reg.}$) vs ξ. For purposes of comparison, similar parameters obtained from the momentum balance method ($([(C_{f\theta})_{Man.} - (C_{f\theta})_{Reg.}]/(C_{f\theta})_{Reg.}$) are also plotted in Figure 3.51. This figure does not show an overall correlation between the two curves but shows a reduced skin friction at all points measured. Figure 3.53 shows the ratio $(C_{f\theta})_{Man.}/(C_{fn})_{Man.}$ vs ξ. The similarity of the shape of this curve with that of $(C_{f\theta})_{Man.}$ vs ξ points out that variation in C_f differences ($([(C_{f\theta})_{Man.} - (C_{f\theta})_{Reg.}]/(C_{f\theta})_{Reg.}$) are a function of the flow development behind the TAPPM, with the $(C_{fn})_{Man.}$ first higher than $(C_{f\theta})_{Man.}$, then lower. Later we will estimate the net drag reduction based upon the local C_{fn} measurements.

3.3 Flow Visualization Results

This section discusses flow visualization results obtained with the second TAPPM configuratiocn (unless otherwise specified).

3.3.1 Flow Visualization on Manipulator Plates

The possibility of flow separation around the TAPPM plates which might increase the device drag, was examined. Careful flow visualization around the manipulator plates was conducted with no evidence of any flow separation observed. An example of this is shown in Figure 2.17. We foun no evidence of flow separation on the order of plate thickness (t = 0.003").

During the process of separation investigation, further flow visualization was conducted downstream from the plates. Figure 3.54 presents an example of the manipulated boundary layer with the wake of plates visualized by $TiCl_4$ and the boundary layer marked with smoke. These pictures precipitated a study of the spread and coherence of the plates' wakes. A combination of plate-wake and wall-region flow visualization, around $\xi = 20$ showed new evidence of wake interaction with wall region flow. More than 200 snapshots of this experiment were taken. A study of two cases (upstream plate alone and both plates in place) indicated that when two plates were in place the structures in the wake of the plates stayed coherent farther downstream than the one-plate case. The mixing of wall region flow and wake structure was also reduced in the region around $\xi = 20$. This is shown in Figures 3.55(a) and 3.55(b). Figure 3.55(a) shows the one-plate case and 3.55(b) shows the two plates case.

Quantitative results, regarding movement of the flow marker (TiCl4) normal to the wall, in the region around $\xi \simeq 20$, were obtained from several rolls of pictures taken of the mixing process. Under similar visualization conditions, the last two rolls, with 39 frames of film, were used for the final analysis. Figure 3.56 presents an example of the data obtained in measuring the normal movement of the marker as it is lifted up into the wall region. The maximum normal penetration, obtained from similar films, were statistically analyzed. The experimental setup is shown in Figure 2.11. The results of this analysis are presented in Figure 3.57. The mean value of y^+, averaged around $\pm 3.3\delta_0$, shows a 25% reduction in the manipulated case. Table 3.1 displays the mean characteristics of the boundary layers at $\xi = 19.3$ for this experiment. It is interesting to note that the flow marker ($TiCl_4$), which was originally painted on the test wall surface, travelled in the normal direction up to $y^+ \simeq 240$ in the regular case and $y^+ \simeq 180$ in the manipulated boundary layer.

3.3.2 Sublayer "Bursting" Results from (Falco's) "Pocket Flow Modules"

Information resulting from the interaction of "typical eddies" with the sublayer flow, leading to the "pocket" module, was obtained at the station $\xi = 51$, where the maximum $C_{f\theta}$ reduction occurred. Using this information, along with the length of the experiment and the frame rate of the movies, a calculation of the burst rate of wall events in both regular and manipulated boundary layers was possible. Figure 3.58 gives an example of the "footprints" of this interaction (referred to as the "pocket module"). This sublayer structure was originally observed by

Falco (1977, 1978, 1980) and is one of the strongest structural features of the turbulence production process in turbulent boundary layers. It was found that the frequency of occurrence of this footprint of the bursting process changed significantly. This frequency decreased in absolute value and increased from 0.6905 to 1.033 when scaled with outer variables $(T_B U_\infty / \delta)$. However, it decreased from 29.670 to 21.699 when scaled on inner variables $(\rho T_B u_\tau^2 \Theta / \mu)$. The regular boundary layer value compares very well with the data of Falco (1983). An increase, corresponding to fewer pockets per unit time, would be expected if the skin friction was reduced in an equilibrium situation. This expectation is based on the assumption that the pockets remain at a given strength.

3.4 Correlation of Fluctuating Component Results

Based on the skin friction results and the wall bursting results, obtained through "pocket" flow module visualization at station C ($\xi = 51$), the decision was made to do a space-time correlation analysis of the fluctuating components obtained from the twin x-wire array. A similar correlation analysis was conducted at station A ($\xi = 20$). These results were obtained for both regular and manipulated boundary layers in Experiment II.

3.4.1 Correlation of Fluctuating Components Normalized with Their Respective RMS Values

Results of the analysis on u', v', and u'v', when normalized with their respective rms values, are presented as follows. Figures 3.59 to 3.62 represent the results at $\xi = 51$ while Figures 3.63 to 3.66 show similar results at $\xi = 20$. Notice that all the peaks in these figures are shifted to the right side of $\tau = 0$ (where $\tau = (t - t_0)U_\infty/\delta_{Reg.}$). This is the result of the streamwise separation ($0.5\delta_{local}$) of the two x-wire arrays.

Figure 3.59 shows the rms normalized correlation of vertical velocity components ($R_{v'_1 v'_2}/rms(v'_1)rms(v'_2)$ vs τ, at .6δ and .4δ). Signals from the top x-array (subscript 1) are used as the reference in the correlation calculation. Note that the peak values for both cases were positive. There was a slight change in the peak of the normal fluctuations (8.75% reduction). No other significant differences are indicated in this figure.

Figure 3.60 shows the rms normalized correlation of streamwise fluctuations for both regular and manipulated boundary layers ($R_{u'_1 u'_2}/rms(u'_1)rms(u'_2)$ vs τ). There is a 10.8% reduction in this correlation and the peak is narrowed a small amount due to the TAPPM. Therefore, a relatively small change appears in the large-scale motions (LSMs) at $\xi = 51$ as a result of the presence of the TAPPM in the boundary layer. At about one δ_{local} to the left of the peak the correlation is closer to the zero value. This may be a sign of an alteration of the flow in the valleys between the two consecutive LSMs at this station. In Figure 3.61, from the same station, cross

correlation of the signals, $R_{u'_1 v'_2}$ with a negative peak, shows almost no change in the peak value $(R_{u'_1 v'_2}/rms(u'_1)rms(v'_2)$ vs $\tau)$. This correlation, on the left-hand side of the peak, shows a minor positive correlation in the manipulated case which could be an indication of the manipulator's wake.

A correlation reduction of 9.4% occurred in the peak of Reynolds stress signature $(R_{(u'v')_1(u'v')_2}/rms((u'v')_1)rms((u'v')_2)$ vs $\tau)$. This reduction was of the same order as the normal and streamwise components previously indicated. Figure 3.62 shows the correlations with positive peaks.

In the rms normalized form at station C $(\xi = 51)$ results of temporal correlations did not reveal significant changes. The decision was made, therefore, to conduct the same analysis on the data obtained at $\xi = 20$, where the effect of the manipulator was expected to be more pronounced. Using the same procedure applied to the data at $\xi = 51$, Figures 3.63 to 3.66 were obtained. Figure 3.63 indicates a 6.4% reduction (neligible) in the peak of normal velocity correlations. However, the streamwise fluctuating temporal correlations are significantly changed. Figure 3.64 $(R_{u'_1 u'_2}/rms(u'_1)rms(u'_2)$ vs $\tau)$ indicates a 28% decrease in peak value along with a 30% narrower peak in the manipulated than the regular boundary layer case.

The cross-correlation at this station $(R_{u'_1 v'_2}/rms(u'_1)rms(v'_2)$ vs τ, at $\xi = 20)$ shows a 13% reduction and a 25% narrower peak (see Figure 3.65). This effect is more pronounced in the Reynolds stress correlation $((R_{(u'v')_1(u'v')_2}/rms((u'v')_1)rms((u'v')_2)$ vs $\tau)$, shown in Figure 3.66, which indicates a 48% lower and 30% narrower peak when

compared with the regular boundary case.

3.4.2 Correlation of Fluctuating Components Normalized with Freestream Velocity (U_∞)

Although the traditional normalization of space-time correlations, based on rms fluctuations, showed the presence of some structural changes in the manipulated boundary layers, it was not easy to observe a clear picture of flow alterations due to the TAPPM. For an alternative picture of the changes, that is not tied to the local value of the point fluctuations, (the LSM's are not) the aforementioned fluctuating correlations were non-dimensionalized with the freestream velocity (U_∞) (which was held constant for all cases).

Results of the analyses on u', v', and u'v' will now be presented, Figures 3.67 to 3.70 represent the results at $\xi = 51$, while Figures 3.71 to 3.74 show similar results at $\xi = 20$. Notice that all the peaks are again shifted to the right of $\tau = 0$, as was the case in Section 3.4.1. This was explained as the result of the fixed streamwise separation of the x-wire arrays.

Figure 3.67 shows the correlation of vertical velocity components ($R_{v'_1 v'_2}/U_\infty^2$ vs τ) at $.6\delta$ and $.4\delta$. The subscripts used are the same as those in the previous section (as explained above). There are no significant differences in the temporal correlations at station C

Figure 3.68 shows the correlation of streamwise fluctuations ($R_{u'_1 u'_2}/U_\infty^2$ vs τ) for both regular and manipulated boundary layers. A small amount of correlation reduction is observed in the peak value shown in Figure 3.68. In general, no significant change is indicated in

that correlation. In Figure 3.69, at the same station, cross-correlation $(R_{u'_1 v'_2}/U_\infty^2$ vs $\tau)$ of the signals $(R_{u'_1 v'_2}/U_\infty^2$ manipulated and regular with a negative peaks, shows little change. For Reynolds stresses, the only apparent difference in the correlations at this station $(\xi = 51)$ are shown in Figure 3.70 with a 7.5% peak increase and a 30% peak width increase. The average Reynolds stress correlation farther outside the peak also stayed above the regular boundary layer. Thus, the correlation functions, when normalized by the freestream velocity at station C $(\xi = 51)$, again, showed no significant change.

Similar normalization was applied to the signatures at station A $(\xi = 20)$. Figures 3.71 to 3.74 display these results. Figure 3.71 $(R_{v'_1 v'_2}/U_\infty^2$ vs $\tau)$ shows a 48% reduction in the peak correlation of normal fluctuating velocities. A 60% reduction in the streamwise correlation of u' signals (Figure 3.72, $R_{u'_1 u'_2}/U_\infty^2$ vs $\tau)$ was obtained. This major difference was not so obvious in the rms normalized correlations in the previous section. Cross-correlation results at this station are shown in Figure 3.73 $(R_{u'_1 v'_2}/U_\infty^2$ vs $\tau)$. This figure shows a 54% reduction in peak value and a similar reduction in width. It is interesting to note that the correlation function is, for the most part, very flat, at values $\tau < 0$ for the manipulated boundary layer, in comparison to the regular case which has a strong positive value for a relatively long range of negative τ values $(-0.6 > \tau > -2.0)$.

The most striking change in the entire correlation occurred in the Reynolds stress signatures (Figure 3.74, $R_{(u'v')_1 (u'v')_2}/U_\infty^4$ vs $\tau)$. The major changes in these correlation results are an 84% reduction in the peak value and a 97.2% reduction for the rest of the function. It is

clearly evident that this result demonstrates the fact that there is a dramatically reduced correlation between the two Reynolds stresses at .6δ and .4δ. In other words, in addition to the results in previous figures, one might be convinced that u' and v' signals are decoupled across this .2δ. These results need to be compared with those at $\xi = 51$ to gain a sense of how fast the large scale motions have recovered from the TAPPM. This will be further explored by conditionally sampling the large-scale motions.

3.5 Conditionally Sampled Large-Scale Motions (LSMs)

Conditionally sampled measurements of the u', v', and u'v' signals, corresponding to the large-scale motions (LSMs), have been made and the ensemble averaged signatures of the LSMs, for both regular and manipulated boundary layers, have been constructed. The conditions corresponded to those of Experiment II. Data were obtained by simultaneous hot-wire anemometry and laser flow visualization at station A ($\xi = 20$). Because of the better visibility of the top x-wire array in the smoke filled turbulent boundary layer, the data from both probes were sampled in sync with the signals of the top probe (which was located at y=0.6δ). The lower x-wire array was located at .4δ and was .5δ downstream of the top array. In order to find the upstream and the downstream border of the signals, related to the averaged LSMs passing by the probe (located at y=.4δ), a simple geometrical analysis on an ideal LSM was performed. To this end, a sketch of the side view of a LSM was plotted and, using the suggested 33° angle (Falco, 1974) of the upstream side of an ideal large eddy structure and the average

convective velocity of a typical LSM at the probe position, the approximate location of front and back of the averaged scales was estimated. A schematic of the LSM used for the above procedure is shown in Figure 3.75.

In order to determine the changes in the large eddy structures, when the turbulent boundary layer was manipulated, the above mentioned signals from both regular and manipulated layers were conditionally sampled as explained in Chapter 2. The sampled data were then scaled to a unit length, averaged, and plotted. Data within the LSMs, and a few δ upstream and downstream, were included in order to obtain information on the flow in the "valleys", where the high speed sweeps originate (refer to Falco, 1977 for further details of this technique). Only one boundary of the valleys is scaled properly so the ensemble averaged signatures of the valleys lose accuracy as we move away from the LSM boundaries. The average large eddy in the turbulent boundary layer is assumed to look, in a laser sheet slice perpendicular to the wall and parallel to the flow, like the structure shown in Figure 3.75 (with the flow moving from right to left). When viewing the ensemble averaged signatures it is helpful to keep this picture in mind. The two vertical axes in the middle portion of the signals represent the boundaries (upstream = right side of the large eddies sampled in this experiment. Therefore, the distance between these two vertical axes represents a normalized streamwise length of the LSMs at the probe location. The signals outside these two lines indicate the average activity of the flow upstream and downstream of the LSMs in this experiment. For each signal the horizontal line with vertical 'ticks' is the ensemble

averaged value, the dashed line is the zero value of the signal, and the line made of spaced dots represents one rms deviation from the ensemble average of the regular boundary layer signature. For comparison, signals of the top x-wire probe for both regular and manipulated boundary layers are shown in the same figure. Although the velocity scale of the large eddies should properly be the rms of the turbulent energy spectrum of the component studied, in equilibrium turbulent boundary layer studies the velocity scale of the outer flow, U_∞ and u_τ, have both been argued to be appropriate scales. Because of the non-equilibrium nature of the manipulated layer, the data have been normalized using four velocity scales: $u_{\tau\theta}$ in Figures 3.76 and 3.77; U_∞ in Figures 3.78 and 3.79; rms u,v, and uv in Figures 3.80 and 3.81; and $u_{\tau n}$ in Figures 3.82 and 3.83.

Regardless of the normalization used, some overall differences are apparent. When the signals were normalized by their respective rms values, they appeared similar to the comparisons with $u_{\tau\theta}$. When the signals normalized by the friction velocities $u_{\tau n}$, they appeared similar to those normalized by U_∞. Surveying the data within the eddies there is, on the whole, a reduction of streamwise velocity defect, a reduction of outward normal velocity, and a reduction of Reynolds stress at both y/δ = .6 and .4 when the TAPPM is present. Upstream of the LSMs the magnitude of the high speed fluid (in the valleys) is reduced and the wallward normal motion is reduced. At y/δ = .6 the Reynolds stress changes depend upon the normalization used but at y/δ = .4 the Reynolds stress is generally reduced with the TAPPM in place. Downstream of the LSMs there is, on the whole, a higher magnitude of high speed fluid at

y/δ = .6 but at y/δ = .4 the high speed fluid in the valley is no longer present (with the TAPPM in place). The wallward motion and the Reynolds stress are reduced at y/δ = .6 (again, dependent on the normalization used), and are reduced even further at y/δ = .4. On the whole, the changes are greater at y/δ = .4 than at .6. The changes at y/δ = .4 are surprisingly large and reflect the fact that the manipulators have a somewhat stronger effect on the flow dynamics closer to the wall. Finally, we observe that the distribution of $\langle u'\rangle$ and $\langle v'\rangle$ signatures inside the LSMs show more symmetry in the manipulated layer.

3.6 Accuracy

In this section a brief discussion of the maximum errors resulting from instrumentation and calculation will be presented. Errors resulting from the conditional sampling (670 samples in each case) technique have not been calculated. The errors due to sampling, however, are assumed to be small. This assumption is based on a comparison with similar results in regular boundary layers obtained by Falco (1983) from his LSMs. It appears that Falco's ensemble averaged signals at $y = .75\delta_{local}$ are consistent with the signatures obtained at $y = .6\delta_{local}$ in this experiment. It has been shown that the ensemble averaged signatures in LSMs do not depend on R_θ over a range of $730 < R_\theta < 3116$. This was substantiated for $R_\theta = 2542$ in the present experiment.

The A/D was tested with a 3.75-volt input with the output being 3.75 ± .002 volts, or ± .006% in converted anemometer voltages. This error converts to 1.1% and .6% error in the streamwise and normal velocity components respectively. The pressure transducer contributed a

maximum of 1% error to the freestream velocity. The error of the A/D, due to sampling rate, is about .01%, which is negligible. The error due to the calibration curve (using the Collis and Willams parameters) were .002% in velocity. The sum of the above errors is at most 2.4 and 1.9 for the streamwise (u') and normal (v') velocity components respectively. This amounts to a 2% error for components. Based on the above error in u' and v', the error in $u'v'$ was estimated to be less than 4%.

The error in local skin friction measurements, obtained from the slope of the mean velocity profiles at the wall, was calculated. The error bars on the most important factors which influence the measurement of the slope of the mean velocity profile at the wall were determined as follows:

1) measurement of probe position resulted in a 3% change in C_{fn}

2) hot-wire wall effects for the insulating test wall showed up only below $y^+ \simeq 2$ (in excellent agreement with the work of Bhatia et al, 1982), and therefore did not affect the measurements in this experiment

3) the accuracy of the calibration, from day to day, of a burned-in hot-wire resulted in $\pm$ 1.5% changes in C_{fn}; temperature changes during a run, $\pm$ .2% (C_{fn}); and the accuracy of the curve fit, $\pm$ .3% (C_{fn}). Thus, the overall measurement accuracy of the wall slope technique is estimated to be $\pm$ 3.5%. In an attempt to eliminate the effect of changes in wire calibration in the C_{fn} calculation, a procedure was devised in which a calibration was made when a profile were taken. The wire was recalibrated after the profile data was taken. Minute changes in the calibration constants were always noted. However, by using this

procedure the overall error reduced by another 0.5% to $\simeq \pm3\%$ at the expense of much time and effort.

CHAPTER 4

DISCUSSION

In Chapter 3 flow conditions and the consequences of manipulating the outer layer flow structures in turbulent boundary layers were presented. In this chapter these results will be examined and interrelated in an attempt to gain further insight into the manipulation of the boundary layer and to understand the effect of the manipulation on the physical mechanisms of the turbulence structures of the boundary layer.

4.1 Effects of Plate Thickness, Free Stream Turbulence, and Skin Friction Measurements on the Overall Picture of Regular and Manipulated Boundary Layers

The two major changes in Experiment II (freestream turbulence level and thickness of the TAPPM plates) played an important role in changing the net drag reduction from zero, in Experiment I, to 10%, at ξ = 58.2 in Experiment II. The lower turbulence intensity (refer to Figure 2.6) is the key to the improved two-dimensionality of the turbulent boundary layers (Bradshaw, 1965) which developed on the test wall (refer to Figure 3.4). This, plus reduction in thickness of the plates suggested by other investigators (Corke, 1981; Hefner et al., 1983; Anders et al., 1984; Plesniak et al., 1984), resulted in the successful net drag reduction mentioned above. We were not able to perform the additional experiment needed to isolate the two parameters to determine which was the major contributor to the improved situation. It does appear that the momentum balance is reasonably accurate in the regular boundary

layer case, because of the good agreement between the C_f obtained from it and that obtained using the Clauser plot technique. This was true for both Experiment I and Experiment II. Despite the relative crudeness of our curve fitting (θ vs. x), we found that for a reasonable range of curve fits only a few percent variation in net drag was obtained. Similar trends of local skin friction reduction, overshoot, and relaxation were obtained by Anders et al. (1984) who also used a momentum balance.

Figure 4.1 shows a comparison of the streamwise variation of $C_{f\theta}$ vs ζ for several investigators. Clearly there is a lack of consistency in skin drag results between different laboratories trying to reproduce the same flow with the manipulators in place. These differences could be due to the three-dimensional flow produced by the presence of the manupulators while the momentum balance used in their calculations assumes a two-dimensional flow. One may, therefore, speculate that, when the TAPPM is in place, the manipulated boundary layer could develop three-dimensional flow due to some very small irregularity (e.g., angle of attack, spanwise and/or streamwise ripples, burrs at upstream/downstream edges of the plates) in the device which, in turn, can cause a separation around it. The skin friction drag evolution for similar flow conditions of several investigators has also been discussed by Anders (1985). To determine if this hypothesis is correct, we could examine the skin friction determined by a technique which is not sensitive to three-dimensional effects. If there is consistency between such measurements, and if they result in similar skin friction reductions for the manipulators of different investigators, we will have

determined that the effect on the surface is not sensitive to the previously mentioned influences, and will only have to determine whether the device drag is highly sensitive to irregularities of the device itself or to low Reynolds number device separation effects. It is thus necessary to examine and compare our results to the skin drag direct measurements made with different independent techniques available today (e.g., Westphal, 1985; Lemay et al., 1985; Mumford and Savill, 1984; Lynn and Sreenivasan, 1985). Our skin friction measurements obtained from the mean velocity gradients near the wall indicated a 30% lower local skin friction than that of the momentum balance in the regular boundary layers. It could be argued that this is a consequence of the wall heat transfer effects on the probe measurements. However, the ratio of manipulated to regular boundary layer measurements should not, and, indeed, do not, show the presumed wall heat transfer effects. The change in C_{fn} is shown in Figure 4.2. For comparative purposes, results obtained by other investigators are displayed in the same figure. Note that they were obtained through different measurement techniques: skin friction interferometer (Westphal 1985), two different types of floating point balances (Mumford and Savill 1984, Lemay et al 1984), sublayer fence (Lynn and Sreenivasan, 1985). The scatter is within 10% and if Lynn and Sreenivasan's data are removed (since their TAPPM was at an angle of attack) it is even better. All the results indicate lower skin drag in the manipulated boundary layers with maximum reductions near ξ = 25 to 35, and a relatively rapid relaxation followed by a more gradual one. This consistency suggests that it may be useful to reanalyze wind tunnel TAPPM data based on local skin friction measurements. A

preliminary attempt to do this is made below. In support of this point of view, it is of interest to note that our spanwise C_f results, from Preston tube measurements, indicated rather similar perce age variations in their peaks (about their averages) for the manipulated layer case. Thus, one suspects that the two-dimensionality of the flow near the wall is preserved (at least in our experiments). These results were not presented here because interpretation of their magnitude depends on the 'universal' law of the wall constants which appear to change at each streamwise station in the manipulated flows.

Of course, it may still be the case that the device drag for 'low Reynolds number' wind tunnel experiments is high due to low Reynolds number effects. However, the visualization results presented in Chapter 2, at very low chord Reynolds numbers (refer to Figure 2.18), did not show separation (note, however, that the resolution of this technique is not high enough to detect long, thin separation regions of thickness on the order of a few thousandths of an inch). Momentum balances around the devices for a range of parameters would be helpful in settling the issue. These, combined with the local skin friction measurements made downstream, could give net drag changes which would not be sensitive to the development of three-dimensionality downstream of the devices.

Our examination of the overall structural changes in both the inner and wall regions showed the dramatic effects of the TAPPM on the inner region. The mass transfer visualization experiment indicated that the sublayer fluid moved 25% less into the outer layer region (reduced from $y_{Reg.}^+ = 240$ to $y_{Man.}^+ = 179$, over a range of $\pm 3.3\delta_0$ around $\xi \simeq 20$). Estimates of the change in bursting frequency, made by counting visually

observed pockets at $\xi \simeq$ 51, indicated that the burst frequency in absolute value was reduced. Furthermore, the sublayer thickness increased from 15-20% (refer to Figure 3.40) over the entire downstream region where changes were measured. The increase in sublayer thickness was hypothesized by Corke (1981) but not supported by direct data. Corke's estimate was that sublayer thickness increased by 17%. From the present experimental results, it is now strongly evident, for the first time, that the sublayer thickness in the manipulated boundary layers does, indeed, increase (refer to Figures 3.40 and 3.41). Thus, although there is a decrease in the normal outward velocity component, in the log region, there is a corresponding increase in the thickness of the sublayer. This is consistent with a picture of fewer bursts. Evidence clearly shows that the number of burst footprints (pockets) decreases.

Falco (1983) has demonstrated that increasing the local thickness of the sublayer will result in fewer bursts, even if no change occurs in the structure of the turbulence in the boundary layer up to the position of sublayer increase. The thickened sublayer makes the interaction of typical eddies with the sublayer significantly less chaotic (Falco 1983). This leads to reduced bursting, or weakened bursting, and hence local skin friction reduction. Note that the thickened sublayer persists beyond the point where the momentum balance shows the rapid rise in skin friction, but, that the skin friction measured from the wall slope remains lower in the manipulated layer over the range of measurement, this is consistent with a thick sublayer.

4.2 Large Eddy Characteristic Changes Associated with Drag
Reduction in Manipulated Boundary Layers

A comparison of ensemble averaged fluctuating components indicated that distinct changes occurred in the LSMs when TAPPMs were present. Temporal correlations at $\xi = 20$ were significantly modified. Farther downstream, at $\xi = 51$, the correlations returned closer to their normal turbulent boundary layer level. This indicates that the LSMs regained most of their strength. Our measurements of the turbulent intensity distribution showed a similar relaxation back to regular boundary layer levels (see Figures 3.33 and 3.34). The downstream relaxation of fluctuating components was also investigated by Guezenec et al. (1985). Their results showed that at $\xi = 45$ (close to station C in the present experiment) u', v', and $u'v'$ had a small amount of overrelaxation. This, interestingly, supports the mean velocity and space-time correlation results at $\xi \simeq 51$. There is, however, a significant difference in the net drag reduction and its relaxation farther downstream. The IIT research team's net drag results (in particular, refer to Plesniak, 1984), on the whole, did not show a sharp relaxation to normal boundary layer values when the manipulators were present. Although this is not the place to make a complete analysis, there were many differences between the experiments, the most intriguing to us being the very large spanwise increases in momentum thickness as an observer moved away from the centerline. It is, therefore, tentatively concluded, in accord with Hefner et al. (1983), that the resultant relaxation disturbances become significant by about 40-80 boundary layer thicknesses downstream of the manipulators. This conclusion refers to the three-dimensional effects discussed earlier and suggests the

development length needed before they become important.

A detailed study of the ensemble averaged signals in the LSMs indicates a significant reduction in the sweeps at .4δ at both their upstream and downstream boundaries and a large reduction in the Reynolds stress inside bulges at both heights (.4 and .6δ) when the TAPPM was in place. Despite these large signal changes, it is not hypothesized that the large scale motions lose their identity. Relative to the local fluctuation velocities, the eddies retain most of their $\langle u' \rangle$ and $\langle v' \rangle$ signatures, as do the valleys both upstream and downstream. It is true, however, that they lose most of their Reynolds stress signature (see Figures 3.80 and 3.81). Further work is needed to understand the decoupling or dephasing suggested by this result. Thus, characterizing the TAPPM as a large eddy breakup device depends upon one's point of view. If the reference point is the absolute change in the large eddies due to the presence of a TAPPM, then we can certainly agree. But, if we look at the large eddies as only one part of the turbulence energy spectrum, then, relative to the reduced energy in the spectrum, the large eddies have remained an approximately constant fraction. This would not be true of the Reynolds stress spectrum. Considering the role that the large eddies play in the production of turbulence in the boundary layer, the maintenance of velocity defect and normal velocity at its boundaries is the key (see Falco 1983). Thus, the reduction of these, for the same overall length and velocity scales of the boundary layer, means that we will have reduced turbulence production and we can characterize the TAPPM as a large eddy intensity reduction device. However, the fact that their intensity is reduced in proportion to the

overall intensity reduction may simply suggest that a TAPPM is an overall turbulence intensity reduction device. In any case, this reduction appears to go away by $\xi = 51$, as does the reduction in the overall intensity.

Based on the sublayer flow visualization and the mass transport experiment, in the region $\xi \simeq 20$, the large-scale motion data, at $\xi \simeq 20$, the space-time correlation data, at $\xi = 20$ and 51, and the wall event visualization at $\xi \simeq 51$, and their correlation with the C_f data of Figure 3.51 (which shows that both methods result in a sharp decrease in C_f reduction by $\xi \simeq 50$) the following is concluded: a strong inhibition in the interaction of the inner and outer layer flow structures is created by the TAPPM and is the key mechanism responsible for the skin friction drag reduction in manipulated boundary layers. The deterioration of this condition is associated with the spread of the TAPPM wake to the wall. This has been supported by the evidence that the wake of the TAPPM maintains a strong coherence at $\xi = 20$ (see Figure 3.55), but, by $\xi = 51$, is distributed throughout the turbulent boundary layer and reaches the wall. In other words, the relaxation of the skin friction drag in the manipulated boundary layer to normal conditions by about $50\delta_0$ for TAPPMs at $y/\delta = .8$ is essentially unavoidable, unless the TAPPM is redesigned to generate a more coherent wake which will not spread as rapidly. The rapid rise is noted in all of the local skin friction measurements in Figure 4.2. It occurs at slightly different positions because the position of the wake/wall interaction obviously depends on the height of the TAPPM in the boundary layer.

The effects of the interaction of a turbulent wake with a laminar

boundary layer have been described by Falco (1978). It was observed that a stable laminar boundary layer could be destabilized, with the formation of pockets clearly evident. These evolved and led to transition of the layer. As mentioned earlier these pockets have also been identified as key elements of the turbulence production process in regular turbulent boundary layers. It appears that as the TAPPM wake nears the wall it will have a similar effect on the sublayer by increasing the wall interactions of the turbulent boundary layer. When pockets were counted at $\xi = 51$ and normalized by the local skin friction velocity, based upon the momentum balance $\rho T_B u_{\tau\theta}^2/\mu$ was 21.7, a 27% increase in the number of pockets over that in a regular boundary layer was found. This strongly supports the above hypothesis.

4.3 Preliminary Attempt to Obtain Net Drag Reduction Using the Wall Friction Velocity ($u_{\tau n}$) Obtained by Local Means Combined with a TAPPM Drag Estimate

We had enough data to attempt a crude drag estimate of our TAPPM device for Experiment II and, thus, could combine this with estimates of the drag on the wall obtained using the slope of the velocity profiles. A 2% net drag reduction was observed (the procedure is shown in Appendix). Notice that a linear extrapolation was made to estimate θ at the trailing edge of the second plate of the TAPPM and to calculate the device drag. The resultant net drag from momentum balance and the local skin friction integration are shown in Figure 4.3. The difference between momentum balance results and direct skin friction drag measurements plus device drag measurement, seems to support the suggestion that downsteam three-dimensionality develops in the

manipulated boundary layer, thereby invalidating the applicability of the two-dimensional momentum balance. However, the results of this section are subject to significant error due to the need to extrapolate to positions not measured. The analysis was performed only in the interest of completeness, but further investigation is needed in order to answer the question.

CHAPTER 5

CONCLUSIONS

The results and conclusions presented in the previous chapters address several interrelated subjects of this experimental investigation. First, a flow facility was designed and constructed. The objective was to come up with a wind tunnel capable of producing a thick two-dimensional boundary layer (up to 10") with low intensity freestream turbulence to be used for visualization, and high-quality hot-wire measurements. Next, net drag reduction in the manipulated boundary layers was obtained. This supported the ongoing research activities of others in the field, yet revealed sharp skin drag relaxation back to the unmanipulated case. Last, the detailed investigation of structural changes, which were presented in the space-time correlations and the conditionally ensemble averaged large scale motions, were discussed.

The major findings of the three phases of this experimental project can be summarized as follows:

1) A high-quality flow wind tunnel with a unique (no-contraction) inlet, long enough to study the relaxation of manipulated turbulent boundary layers, was constructed.

2) Two sets of very thin tandemly-arranged parallel plate manipulators (TAPPMs), were used in an attempt to reproduce the results of other net drag reduction investigations and to study the downstream evolution of the drag changes. It was

C-2

found that the thickness of the manipulator plates was of importance to both the skin friction change and the device drag. Also, the experiment with thinner plates (.003") resulted in a 10% net drag reduction at $58.2\delta_0$ downstream of the TAPPM, which relaxed back by $100\delta_0$. In each of the two separate experiments (I and II), a similar drag evolution was obtained, although the thick plates (.03") did not reduce the net drag. The local skin friction coefficient ($C_{f\theta}$) was reduced by 30-45% for up to $50-85\delta_0$ downstream of the manipulators in both experiments. The local skin friction obtained from the mean velocity gradient, near the wall, was reduced by 10-20%, but did not show a sharp overrelaxation as it did when calculated from the momentum balance. A 2% net drag reduction was obtained from C_{fn}, taking the device drag into consideration.

3) No separation of flow was detected (to within the order of a few thousandths of an inch) over the manipulator plate surfaces. A laminar boundary layer was developed on both plates, which were parallel to the test wall in the experiments.

4) The Coles' constant in the "law of the wall" also underwent a sequence of changes. It increased in the region of $C_{f\theta}$ reduction, then decreased, and finally relaxed back to the normal value (B = 5.) after $90\delta_0$.

5) The "law of the wake" portion of the mean velocity profiles also incurred some changes which were similar to the

variations in the Coles' constant, B.

6) The sublayer thickness increased 15-20% throughout the length of the test wall for the manipulated layers.

7) At $\xi \simeq 20$:

a) The outward normal distance that the sublayer fluid travelled into the logarithmic region decreased 30% or 11.4% around $\xi \simeq 20$, when it was normalized by $u_{\tau\theta}$ or $u_{\tau n}$ respectively.

b) The dynamics of the large-scale motions changed, but they did not lose their uniqueness in geometry nor the flow patterns within. The Reynolds stress of the LSMs was reduced significantly.

c) The space-time correlations changed at $\xi = 20$, with significant reductions in the Reynolds stress and the streamwise components of temporal correlations.

At $\xi \simeq 50$:

a) The large-eddy motions regained most of their strength by $51\delta_0$ downstream of the manipulators.

b) The burst frequency in the sublayer decreased by 38% (in absolute value). It increased by 27% when normalized by the inner variables (μ/ρ, $u_{\tau\theta}$).

The structure of the boundary layer turbulence appears to have relaxed back to unmanipulated values by $\xi \simeq 50$, and the TAPPM wake appears to have spread across the boundary layer by this distance. These changes correlate well with the skin friction relaxation measured by the two

independent techniques in the same experiments.

FIGURES
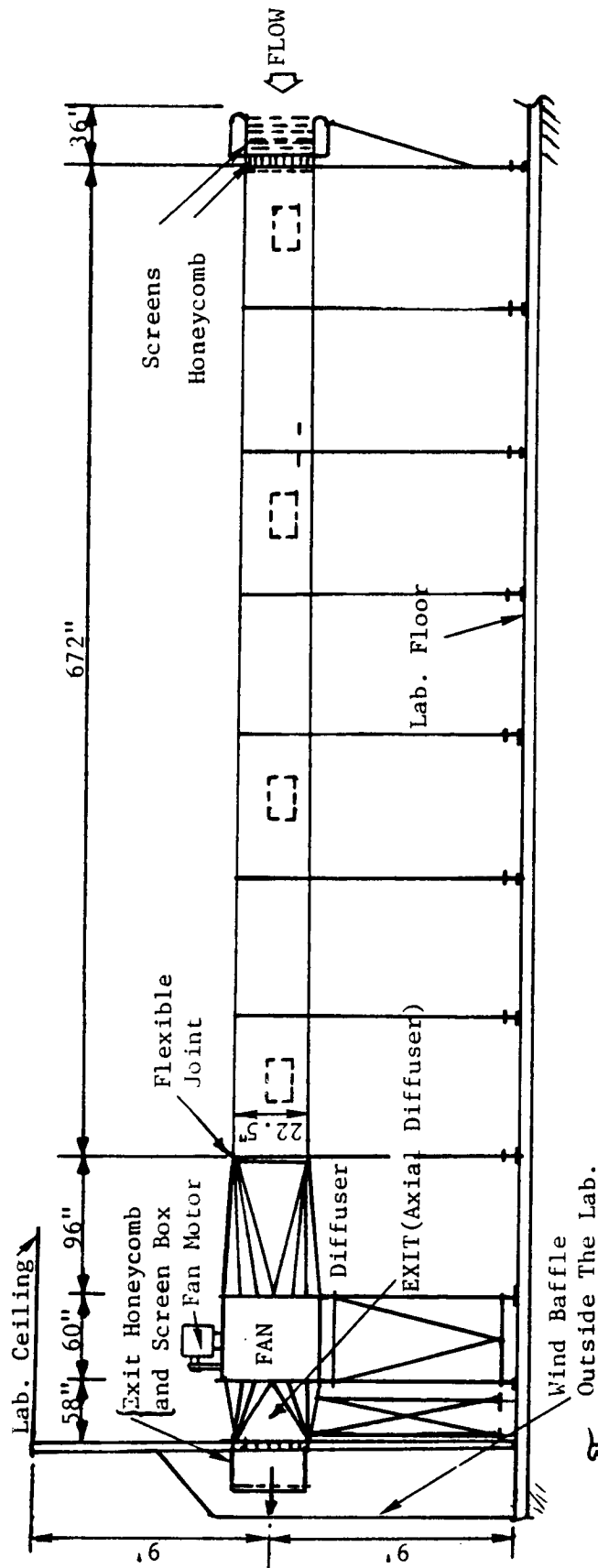
SIDE-VIEW: Schematic of the wind tunnel (with axial exit diffuser)
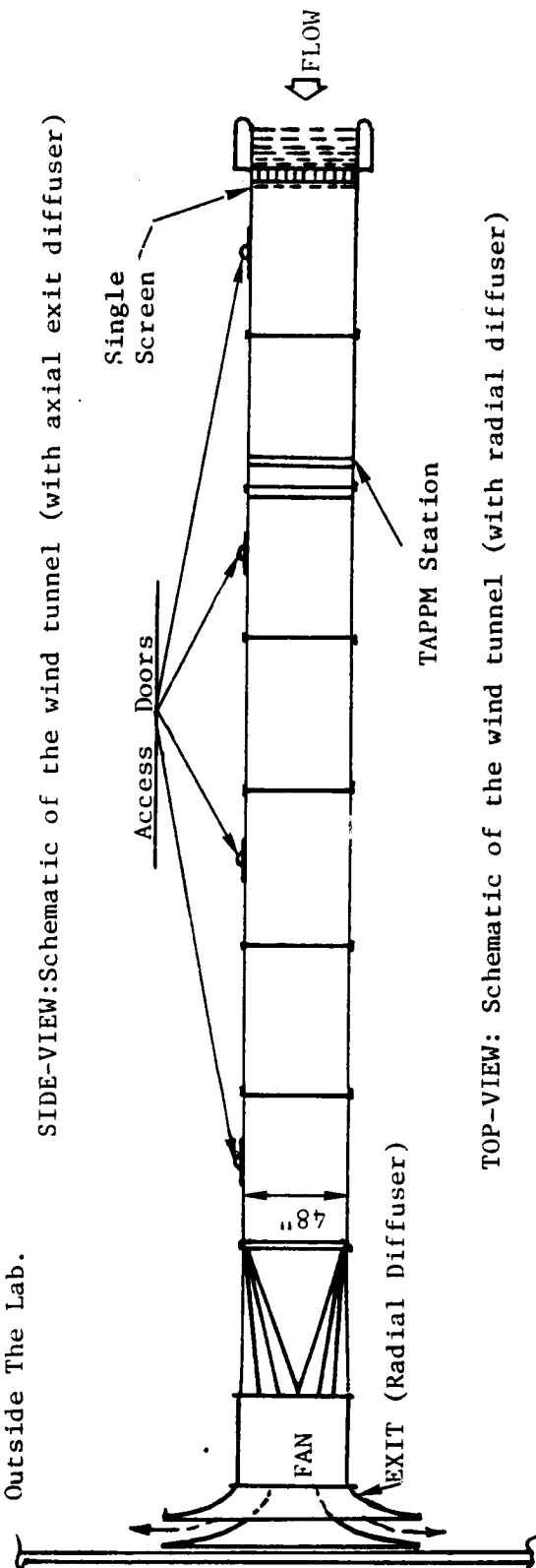
TOP-VIEW: Schematic of the wind tunnel (with radial diffuser)

Figure 2.1 Schematic of the low-speed wind tunnel

Experiment I   Experiment II

STATION	x (IN)	$\xi = (x-x_0)/\delta_0$	x (IN)	$\xi = (x-x_0)/\delta_0$
0	178.8	0.0	174.5	-1.43
A	240.0	24.7	238.5	19.30
B	293.0	46.0	289.0	34.81
C	340.0	65.0	337.5	50.16
D	367.0	75.9	363.0	58.23
E	393.0	86.4	388.3	66.22
F	410.0	93.2	405.5	71.52
G	444.0	106.9	440.0	82.59
H	480.0	121.5	475.8	93.59
I	521.0	138.0	516.8	106.88
J	594.0	167.4	594.3	131.41
K	646.0	188.4	642.0	146.52
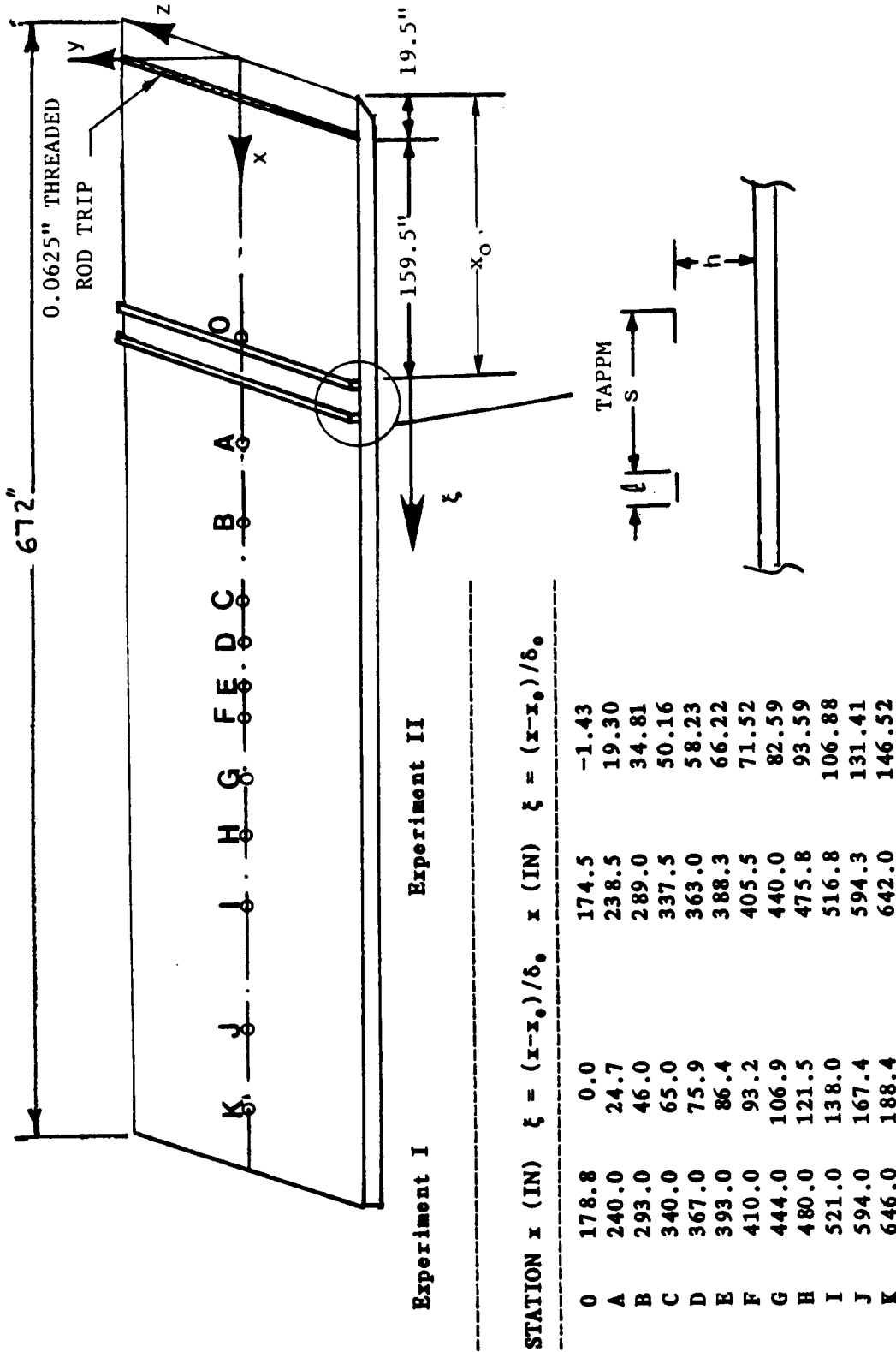
EXPERIMENT I, $h = 0.86_0$, $l = 1.216_0$, $S = 7.746_0$, $t = 0.01216_0$, $R_{\theta_0} = 1450$

EXPERIMENT II, $h = 0.86_0$, $l = 0.956_0$, $S = 6.16_0$, $t = 0.000956_0$, $R_{\theta_0} = 2150$

Figure 2.2 Schematic of boundary layer test wall showing the TAPPM and measurement stations.
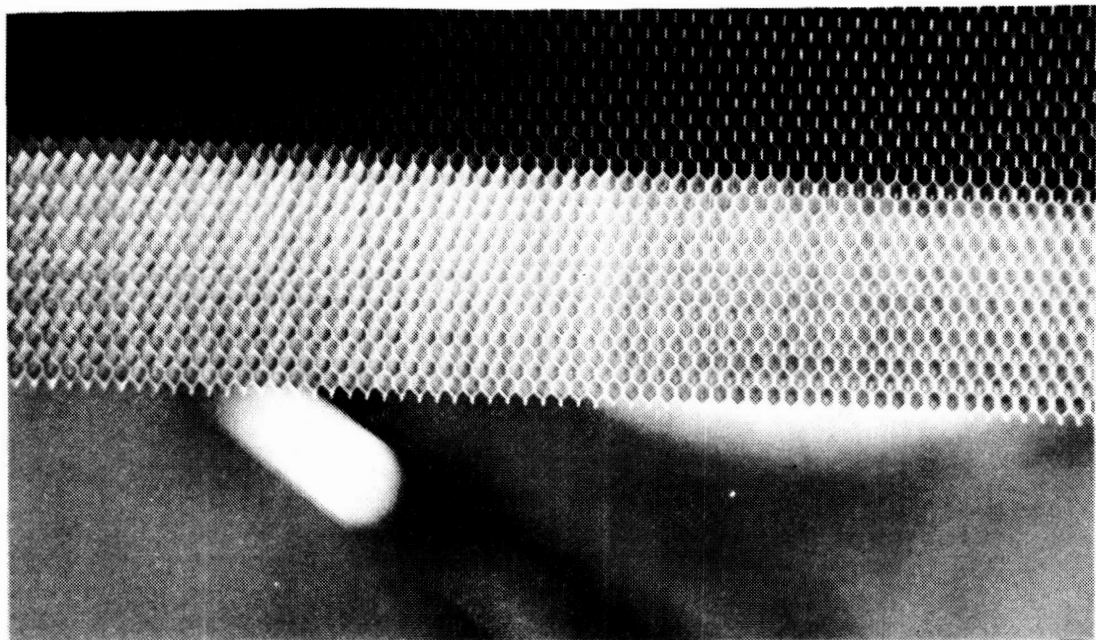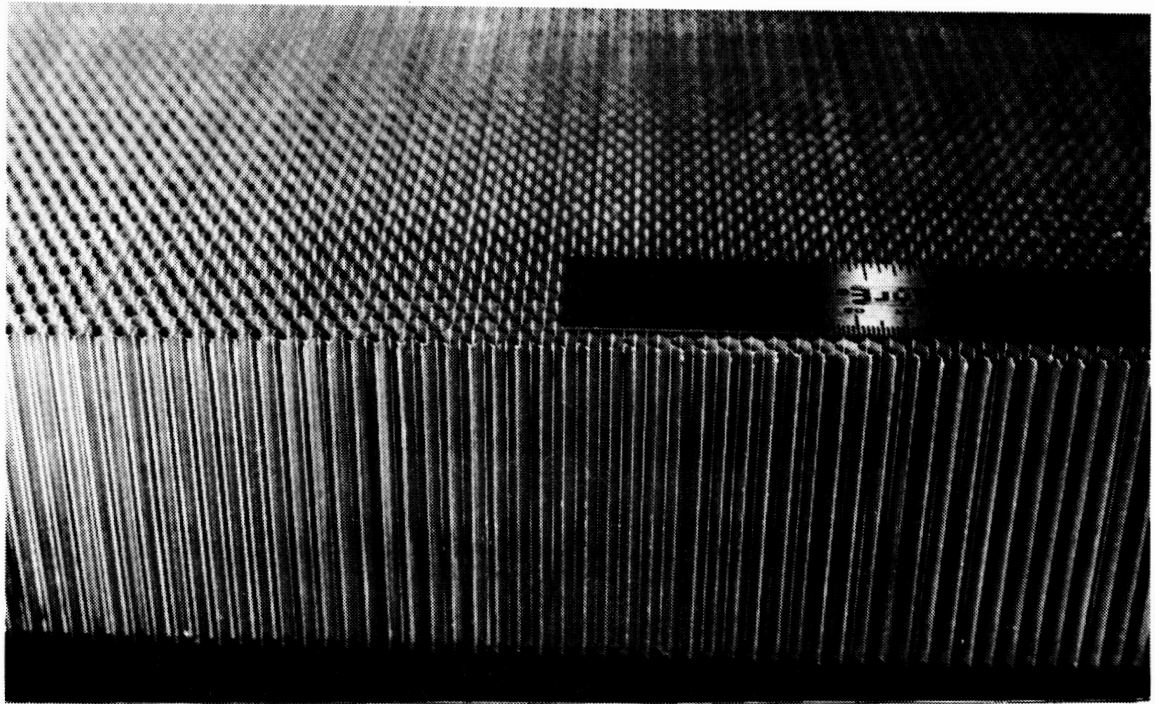
Figure 2.3 Honeycomb; Top picture shows the cell size, Bottom picture shows the uniformity of the lower edge of cells.
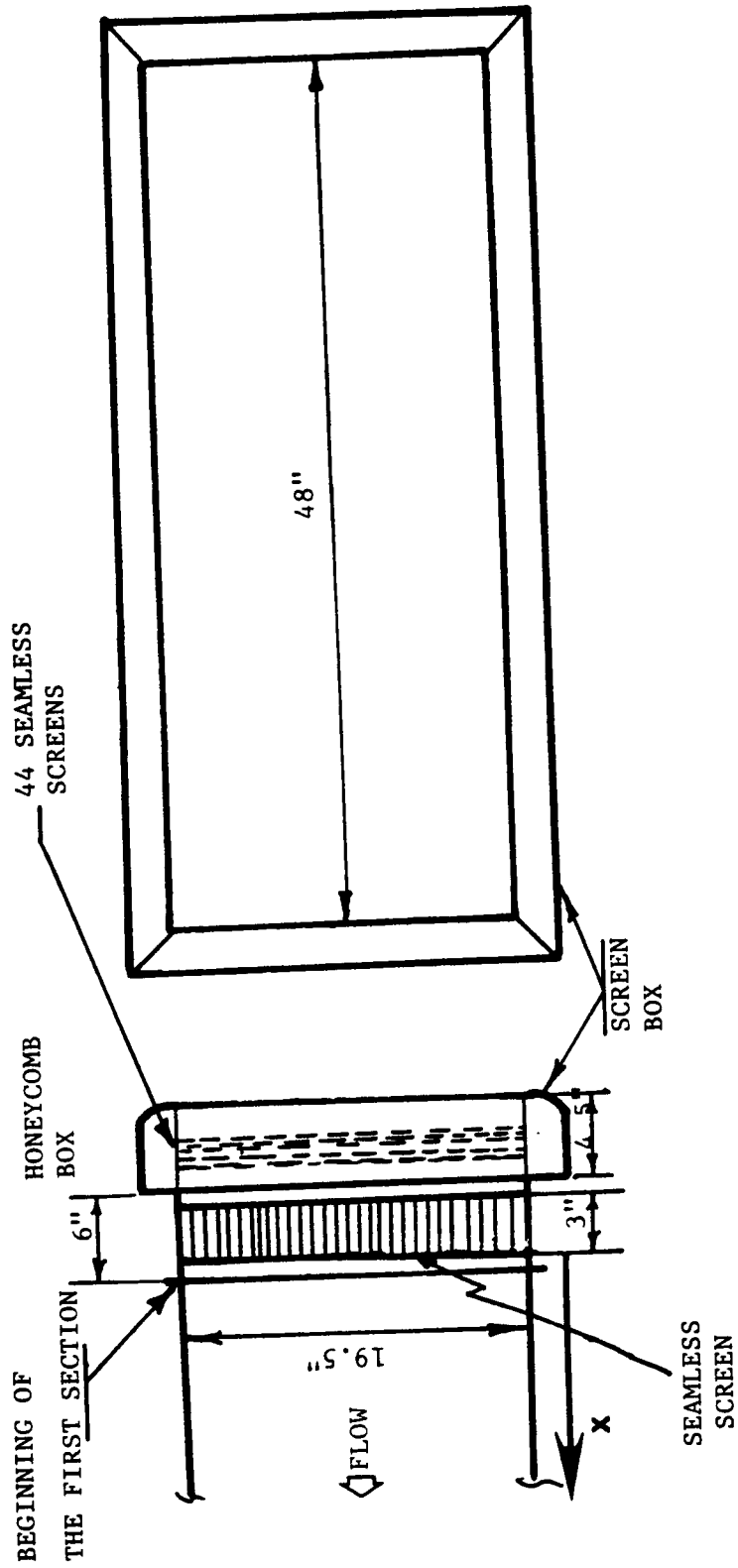
Figure 2.4 Schematic of honeycomb-screen arrangement used for experiment I.
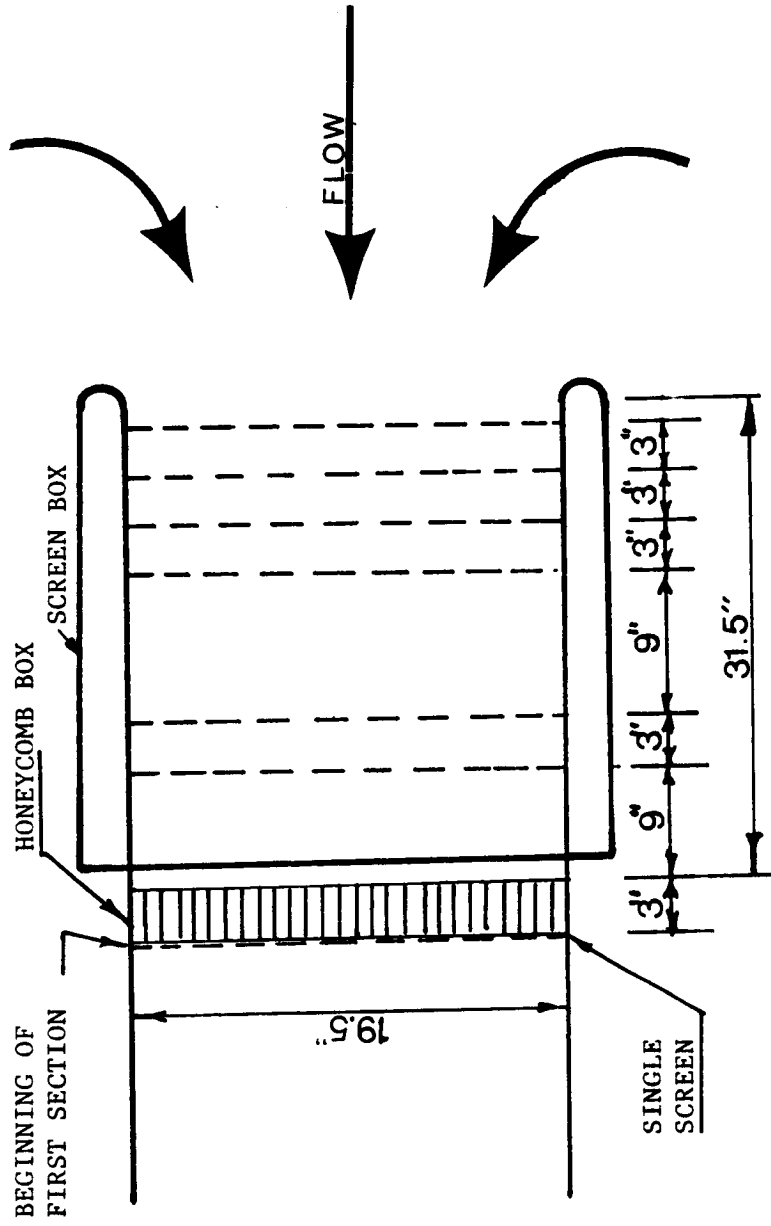
Figure 2.5 Schematic of honeycomb-screen arrangement used for experiment II.

[Inlet I <+>, Inlet II <x>]
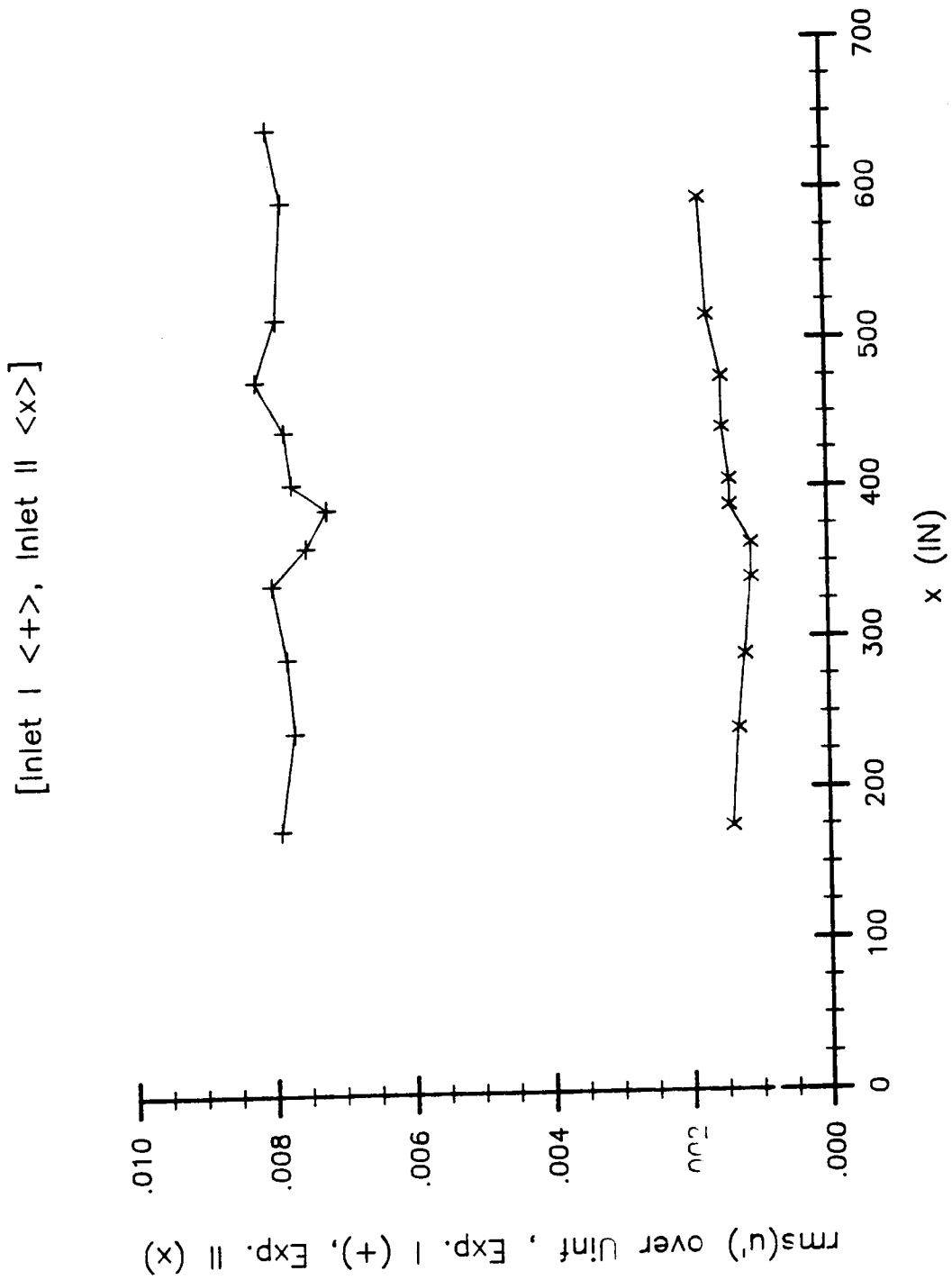
Figure 2.6 Variation of freestream turbulent intensity rms(u')/U_∞ versus x for both experiments: I (+), II (x).
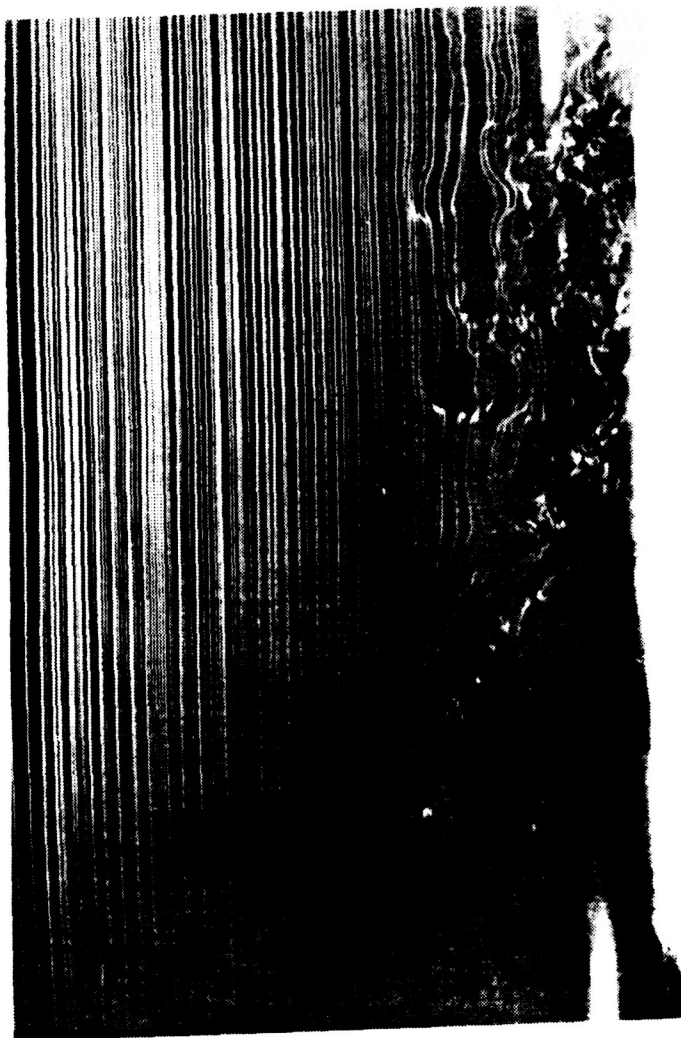
Figure 2.7 A snap-shot of the freestream and the boundary layer smoke-wire flow visualization around x = 210", (flow is from right to left).
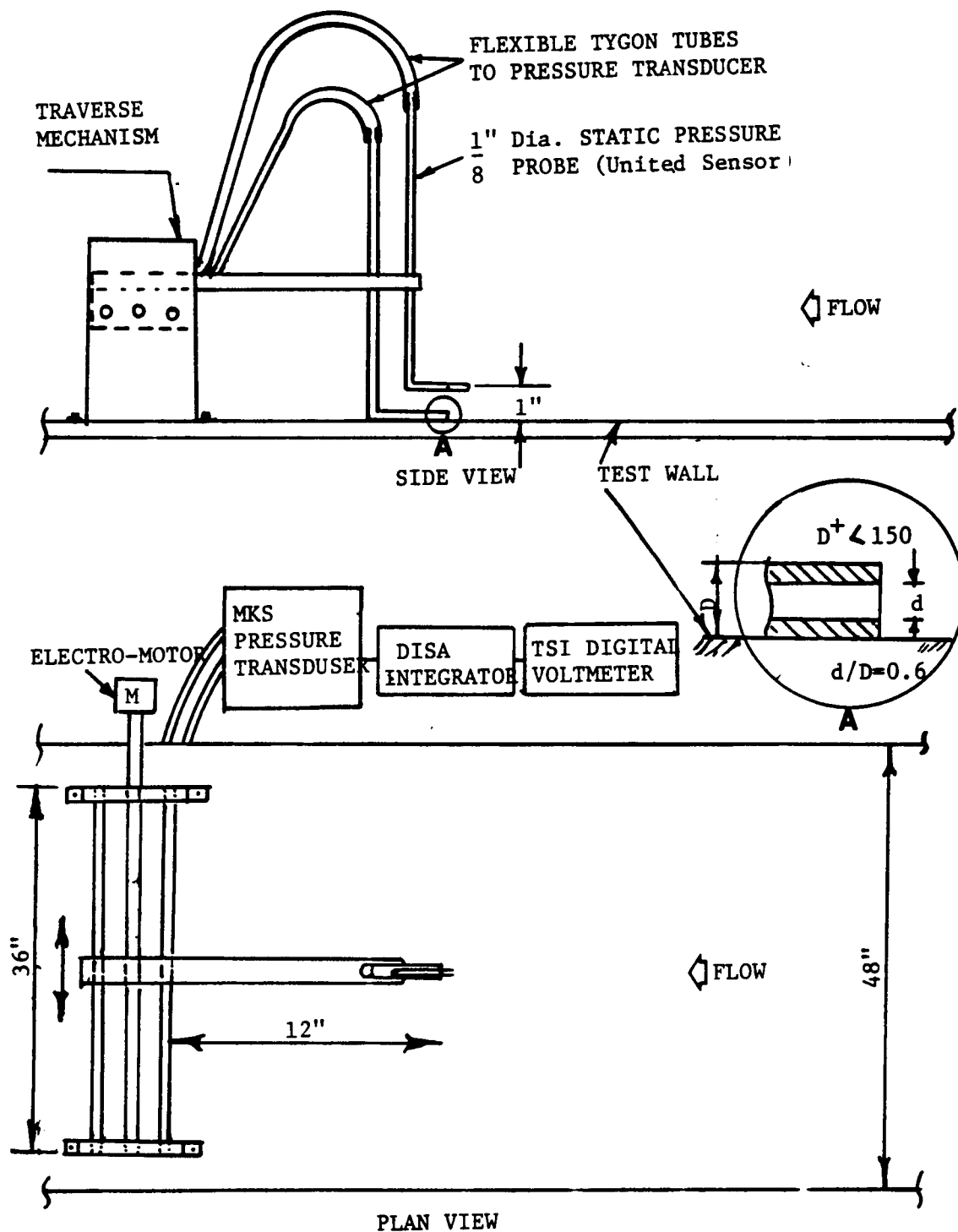
Figure 2.8 Schematic of the movable (modified) Preston tube probe.

93
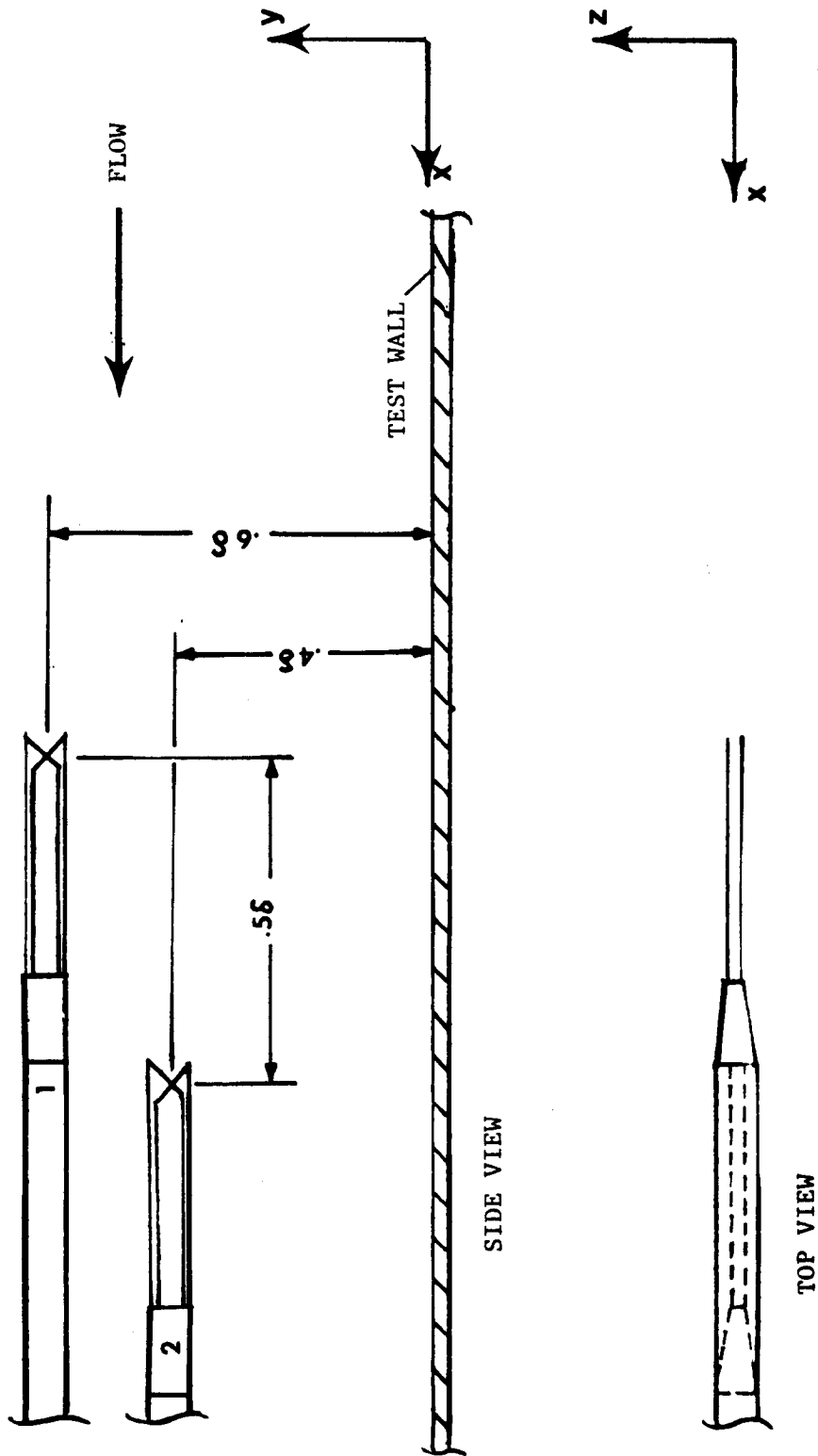
Figure 2.9 Schematic of twin-x-wire array probe.
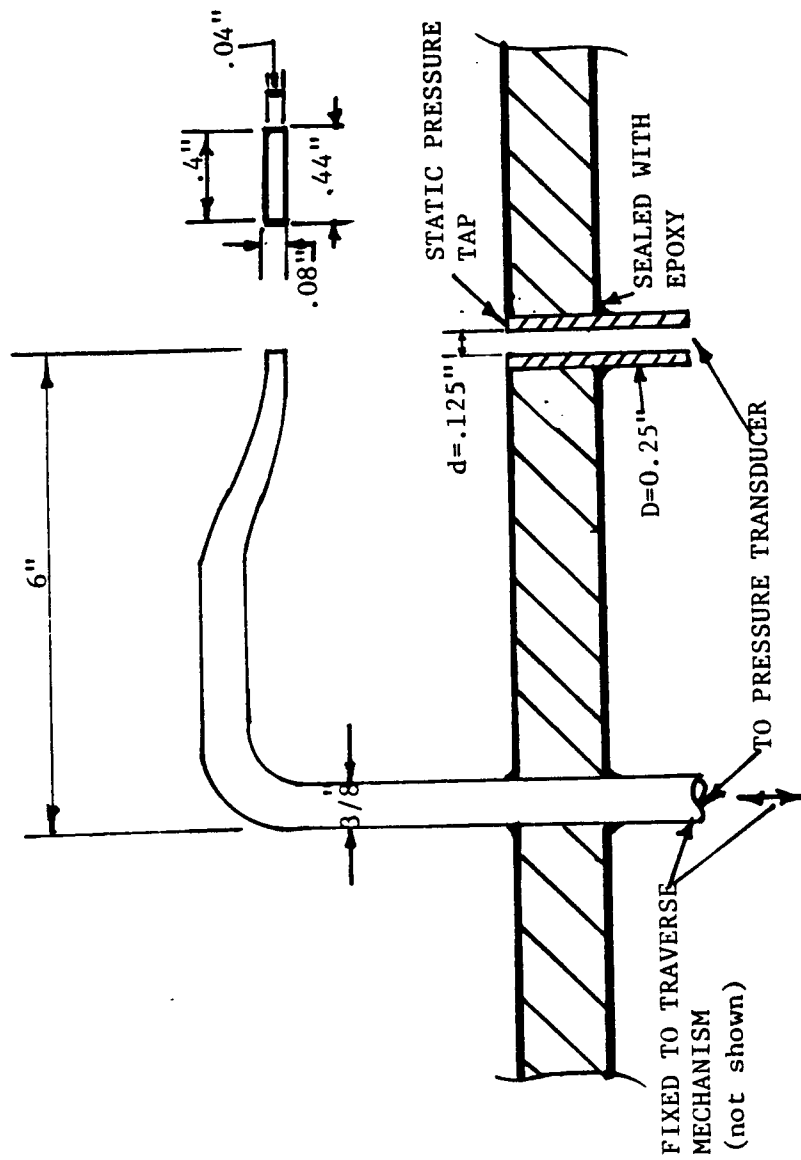
Figure 2.10 Schematic of Pitot static tube used in velocity profile survey in experiment I.

95
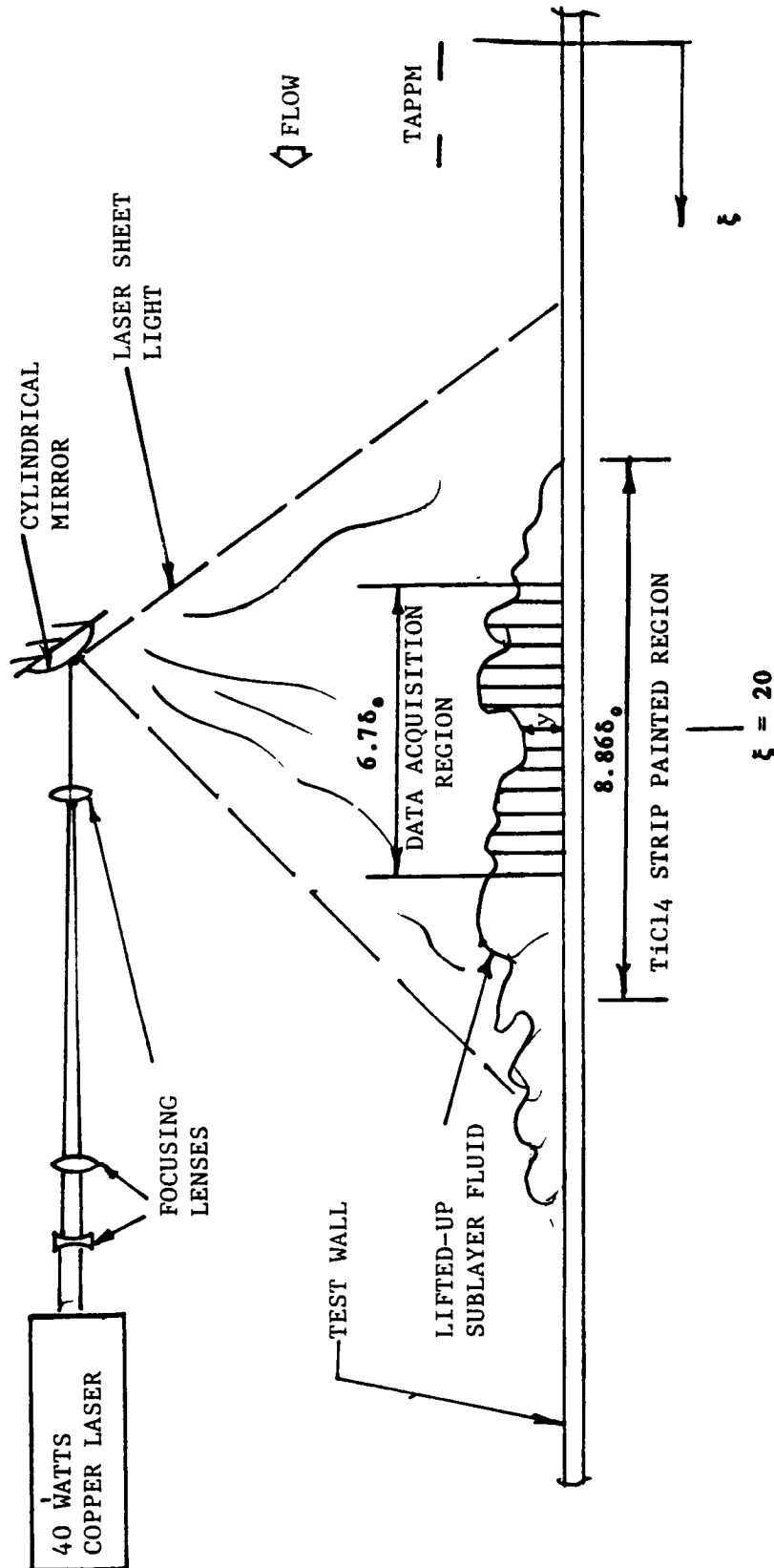
Figure 2.11 Schematic side view of laser optics and data acquisition streamwise region of inner wall flow visualization with Titanium tetrachloride (TiCl₄) flow marker.

CALIBRATION PROGRAMS
  Data Acquisition

  ALEX2   computer and A/D synchronization
  RUNTST   collects u-wire and pressure trasducer calibration data

Data Reduction

  CONVOL   converts bits/millivolt to voltages

Data Analysis

  CAL1WIRE   determines Collis and Williams parameters
  MULPLT   plots calibration data for a visual check of the result

MEAN VELOCITY PROFILE PROGRAMS
  Data Acquisition

  ALEX2   computer and A/D synchronization
  RUNTST   collects velocity profile data

Data Reduction

  CONVOL   converts bits/mollivolt to voltages (mean and fluctuations)
                 and merges with probe positions in one data file

Data Analysis in Batch Form:

  CALANL   command file for analysis and plotting programs

    VELPRO   converts voltages to velocities and processes the velocity
                 profile for four plots
    MULPLT   plots the output of VELPRO as follows:
                 1) mean velocity profile close to the wall in the sublayer
                    region (y vs U) for velociy slope estimation at the wall
                 2) y vs U of the entire velocity profile
                 3) Clauser plot to obtain C_{fC} based on Coles "law of the
                    wall" parameters

    VELPR3   analyses the data and calculates the boundary layer velocity
                 profile parameters, non-dimensionalizes the velocity profile
                 based on two different estimations of the wall shear stress
                 ($d\bar{U}/dy$ at wall ($C_{\tau n}$), and C_{fc} or $d\theta/dx$), and finally stores
                 them with the rest of the information in one master data file

    MULPLT   plots the output file of VELPR3:
                 4) y/θ vs $\bar{U}/U_{\infty}$
                 5) u^+ vs Y_+ based on both $u_{\tau\theta}$ and $u_{\tau c}$
                 6) $(U_{\infty} - \bar{U})/u_{\tau}$ vs $yu_{\tau}/\delta_d U_{\infty}$
                 7) Wake part of the velocity profile   vs y/δ
                        8) $rms(u')/u_{\tau}$ vs y^+, also for near wall region
                 9) $rms(u')/U_{\infty}$ vs y/θ, also for near wall region

Figure 2.12 Velocity profile and calibration data acquisition, reduction,
            and analysis program sequence

CALIBRATION PROGRAMS
Data Acquisition

ALEX2	computer and A/D synchronization
RUNTST	collects twin-x-wire and pressure trasducer calibration data

Data Reduction

CONVOL	converts bits/millivolt to voltages

Data Analysis

CALFIT	determines Collis and Williams parameters
MULPLT	plots calibration data for a visual check of the result

TWIN-X-WIRE PROBE PROGRAMS
Data Acquisition

ALEX2	computer and A/D synchronization
RUNTST	collects twin-x-wire probe data

Data Reduction

CONVOL	converts bits/mollivolt to velocities
CPCN	calculates the CP and CN parameters for the x-wires
VEL4	calculates the long time record of fluctuating quantities
TIMPLT	plots long time records of fluctuating quantities
CORRELATE3	computes space-time correlations of fluctuating quantities
CORAVG	averages the space-time correlation output files of CORRELATE3
MULPLT	plots the space-time correlations
ENSMBL	selects, scales and averges the segments of the data records produced by VEL4 which correspond to large eddies striking the twin-x-wire array probe
NORMALIZE	non-dimensionalizes the long records of data

Figure 2.13 Twin-x-wire probe calibration, data acquisition, reduction, and analysis program sequence
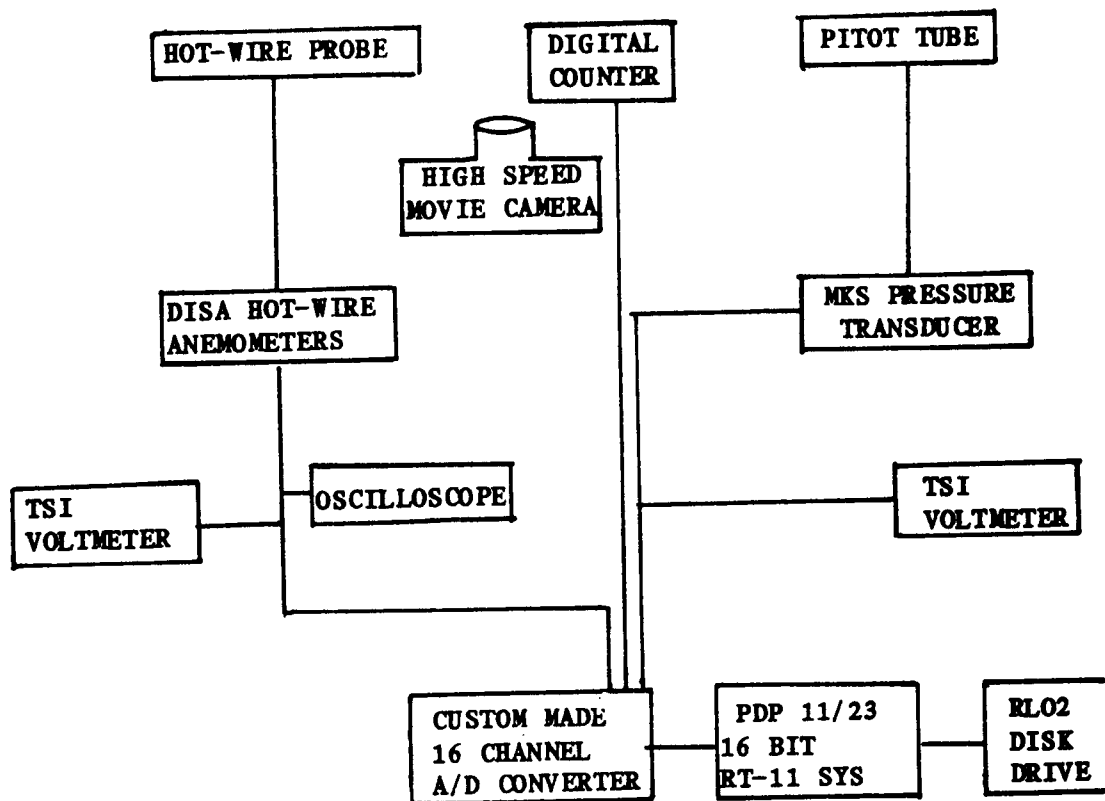
Arrangement of instruments used for hot-wire anemometry and simultaneous visual data acquisition.
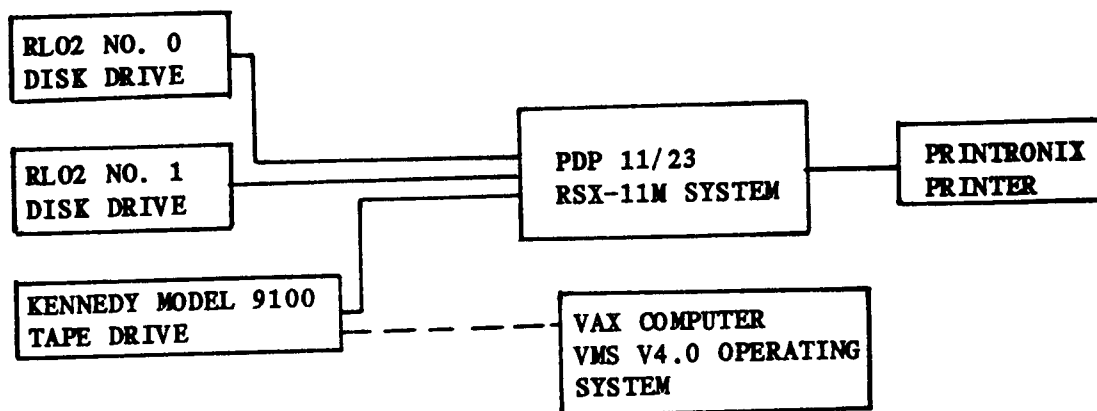
Figure 2.14 Block diagram of data acquisition and processing system.
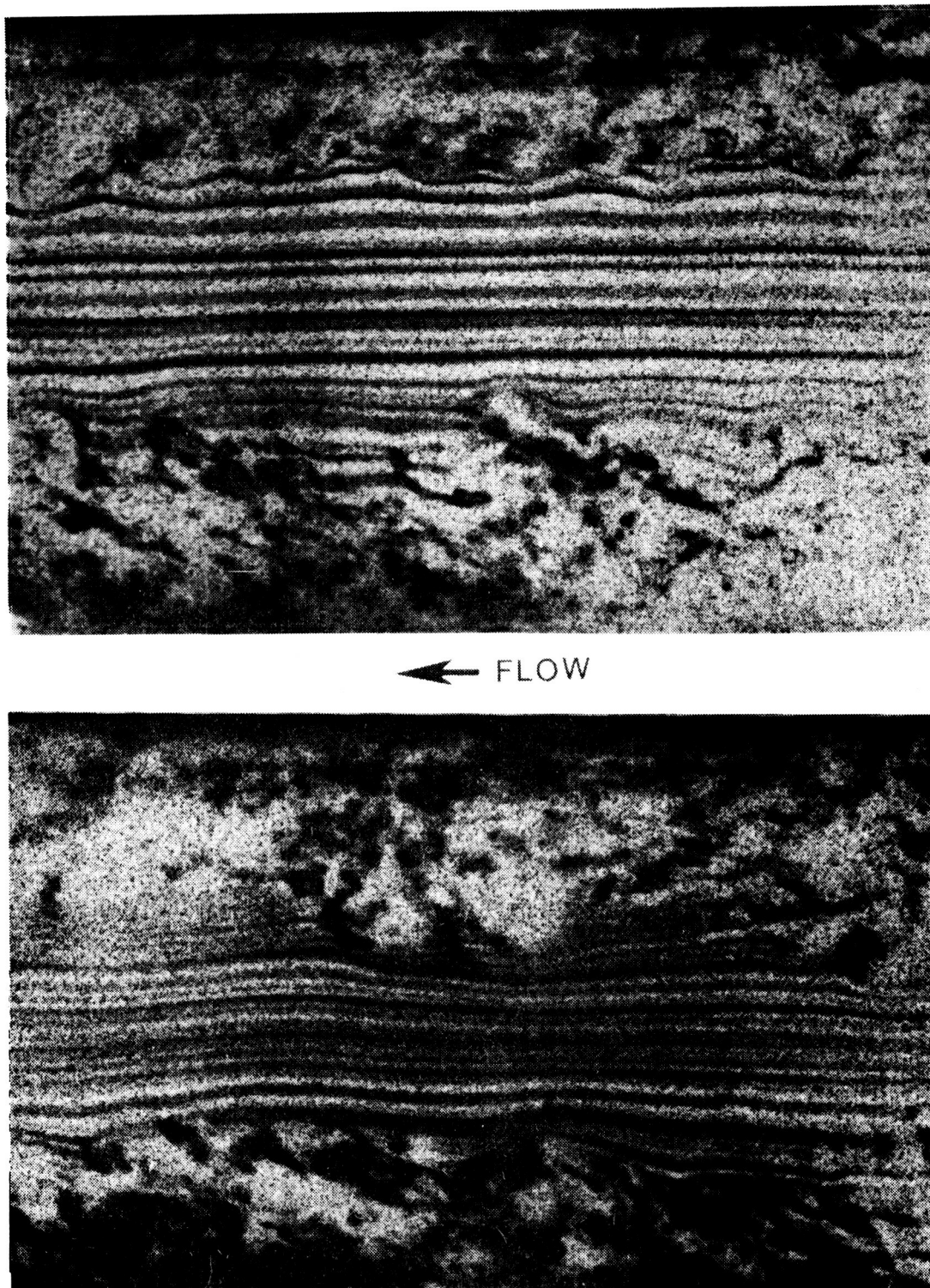
← FLOW

Figure 2.15   Smoke-wire flow visualization with high-speed movie camera
at x = 520" (13.2m); straight streaklines (top); wavy
streaklines in the freestream flow due to passage of large
scale motions.
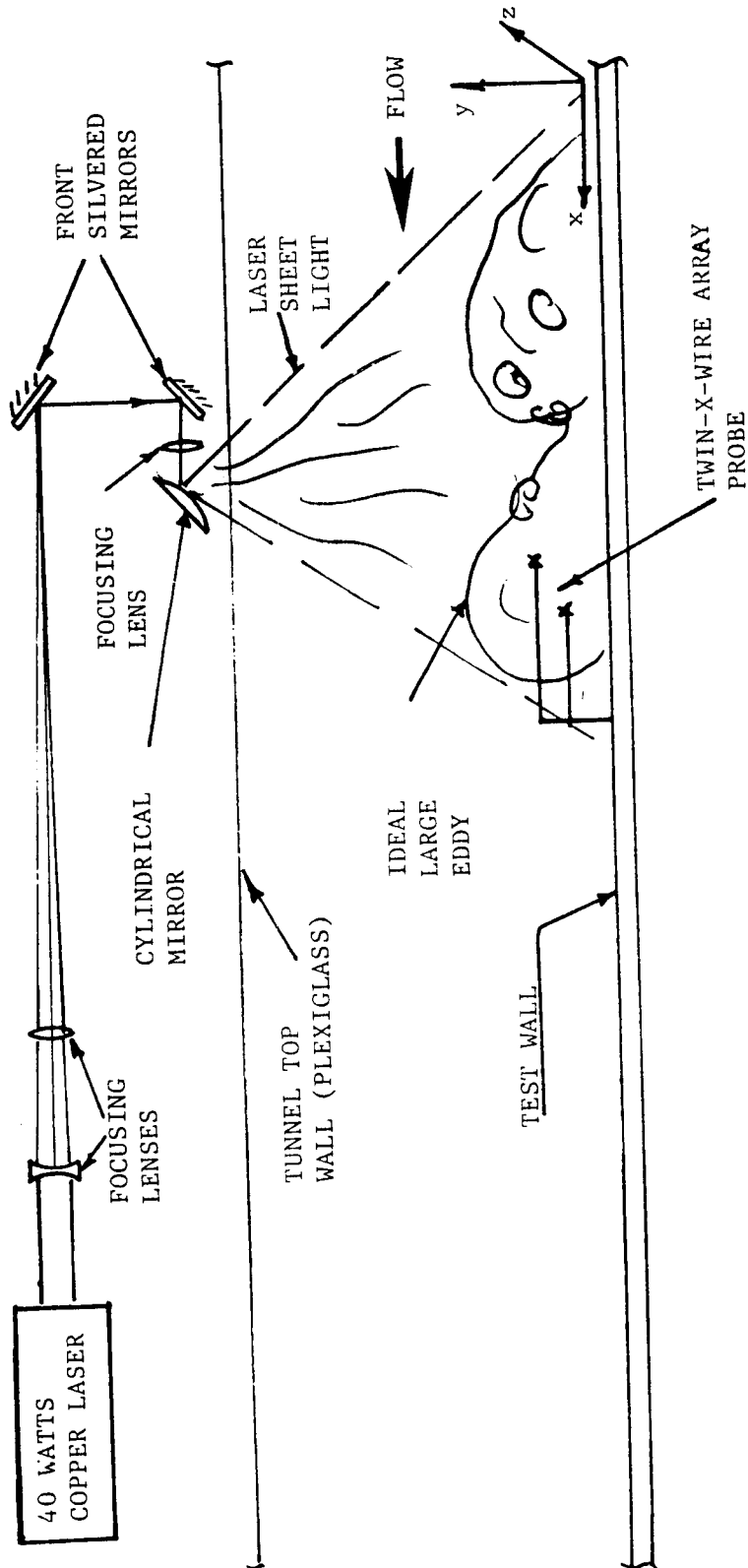
Figure 2.16 Schematic of laser optics and x-wire array probe arrangement used in simultaneous visualization and anemometry at 206₀.

Figure 2.17 Smoke flow visualization around the downstream plate of TAPPM device $(h = .8\delta_0)$ at $z = 0$ (top); $z = 30.5$cm in the turbulent boundary layer.

Figure 2.18 An example of a large eddy structure striking the probe in a turbulent boundary layer.
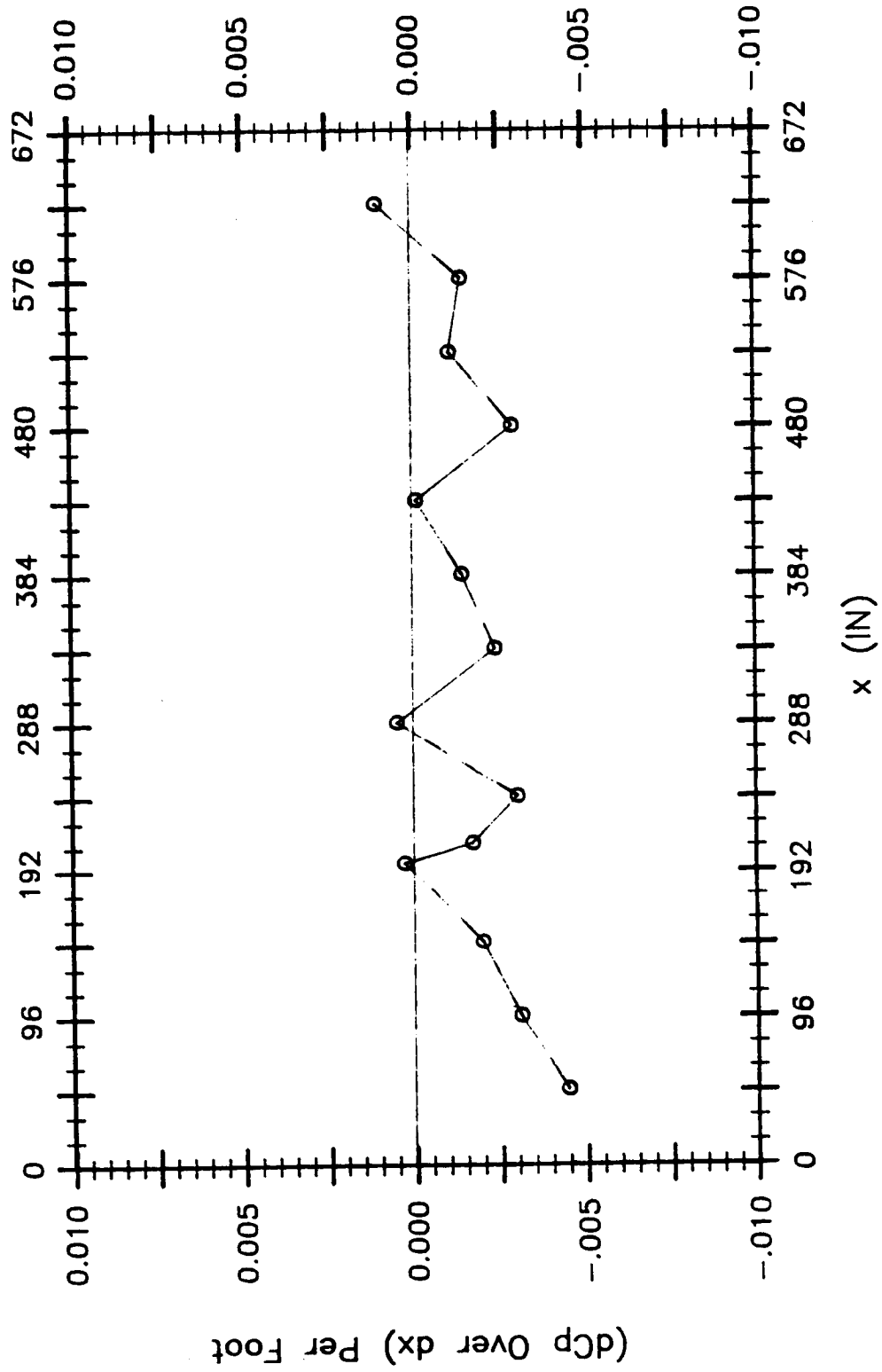
Figure 3.1 Variation of differential pressure gradient dC_p/dx per foot vs x.

$X* = \log_{10}[(DPp)\ (d\ Sq.)\ Over\ 4(rou)(noo\ Sq.)]$
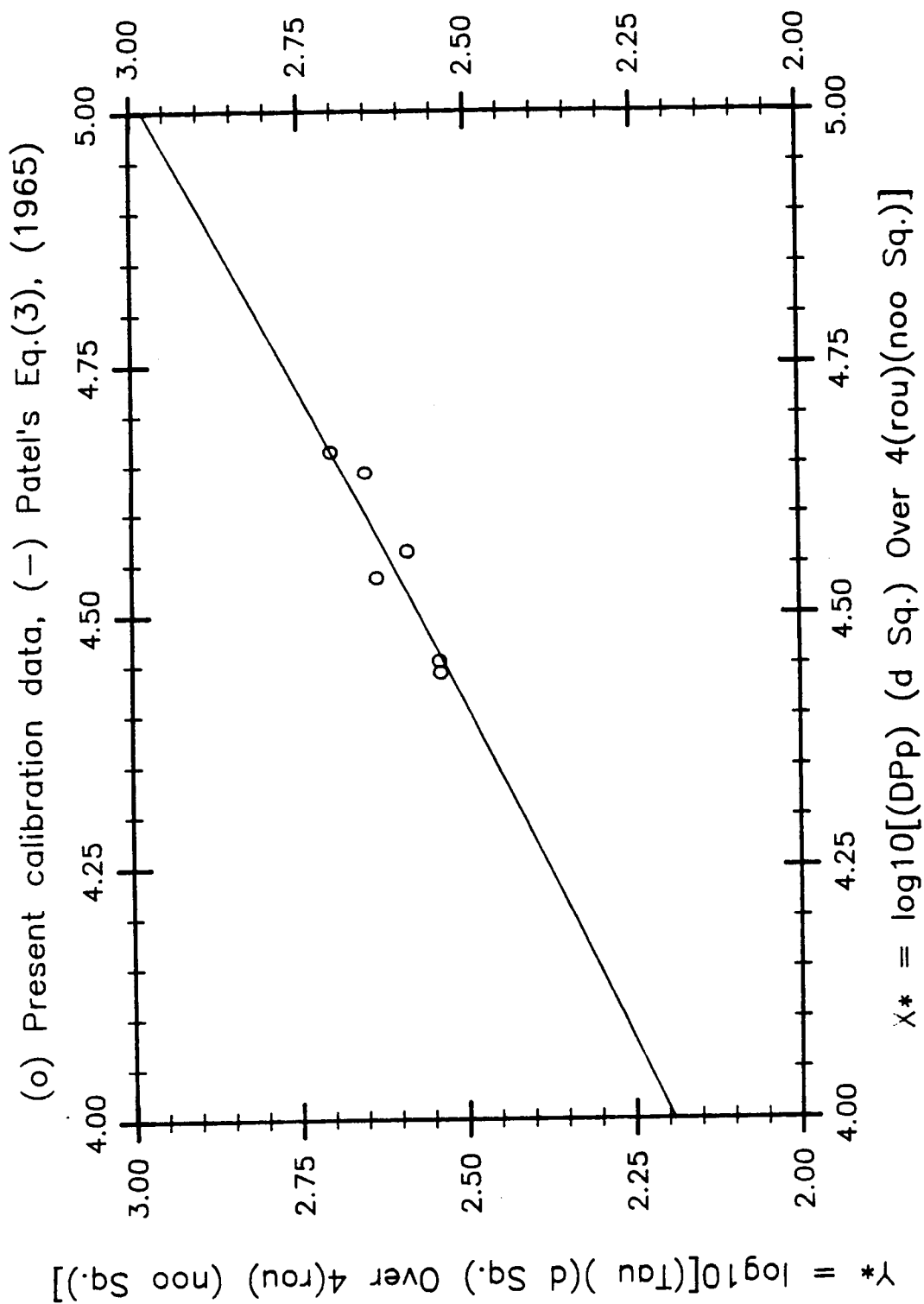
Figure 3.2 Preston tube calibration data (o), compared to Patel's (1965) empirical relation: $y* = 0.8287 - 0.1381x* + 0.1437x*^2 - 0.0060x*^3$ (solid line).
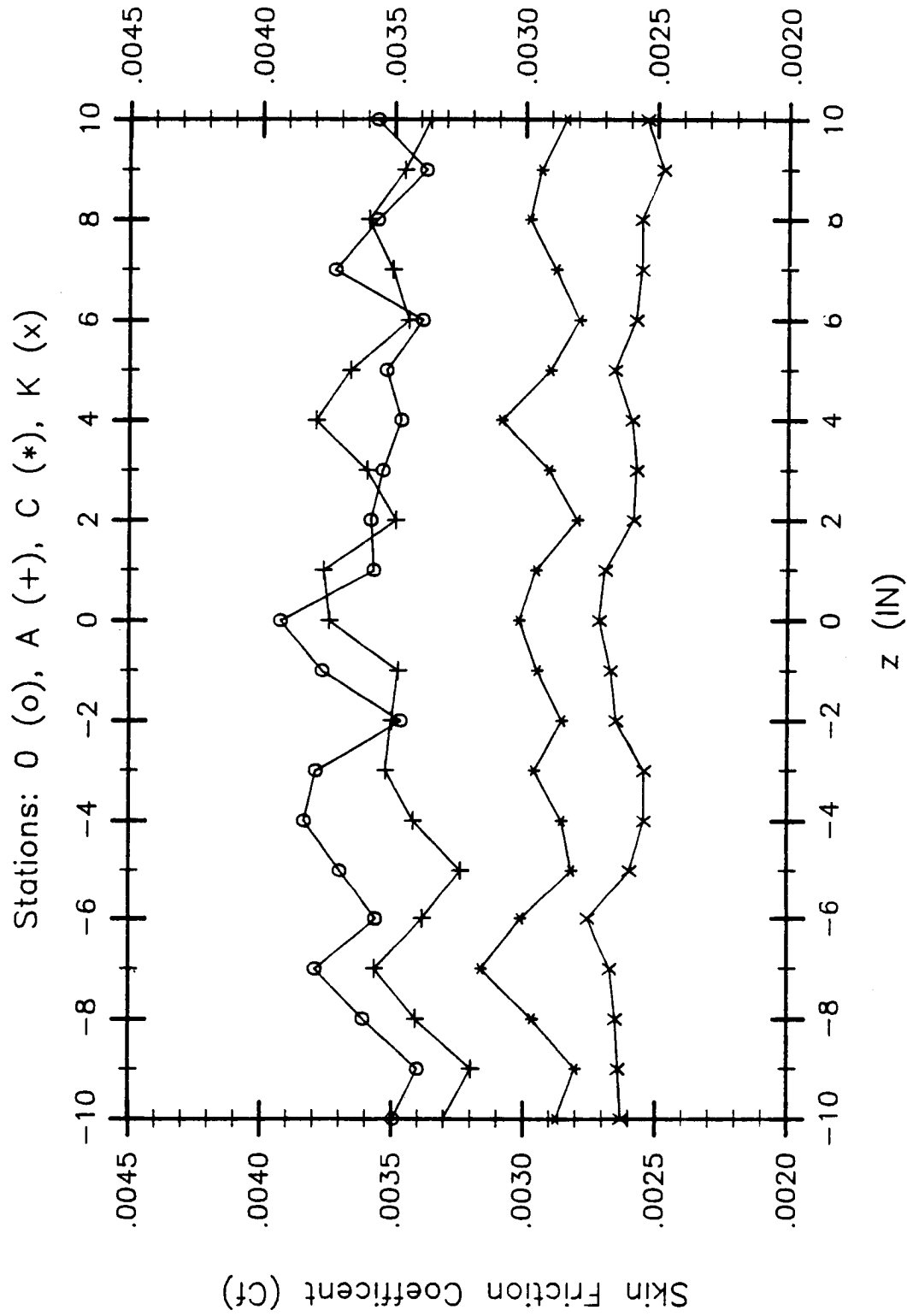
Figure 3.3 Spanwise variation of the local skin friction measured by Preston tube at different streamwise stations: O (o), A (+), C (*), and K (x), with a sand paper (36 grit) tripping device and inlet No. 1 configuration.

Reg. B. L., Stations: O (o), K (x)

Skin Friction Coefficient (Cf)

Z (IN)
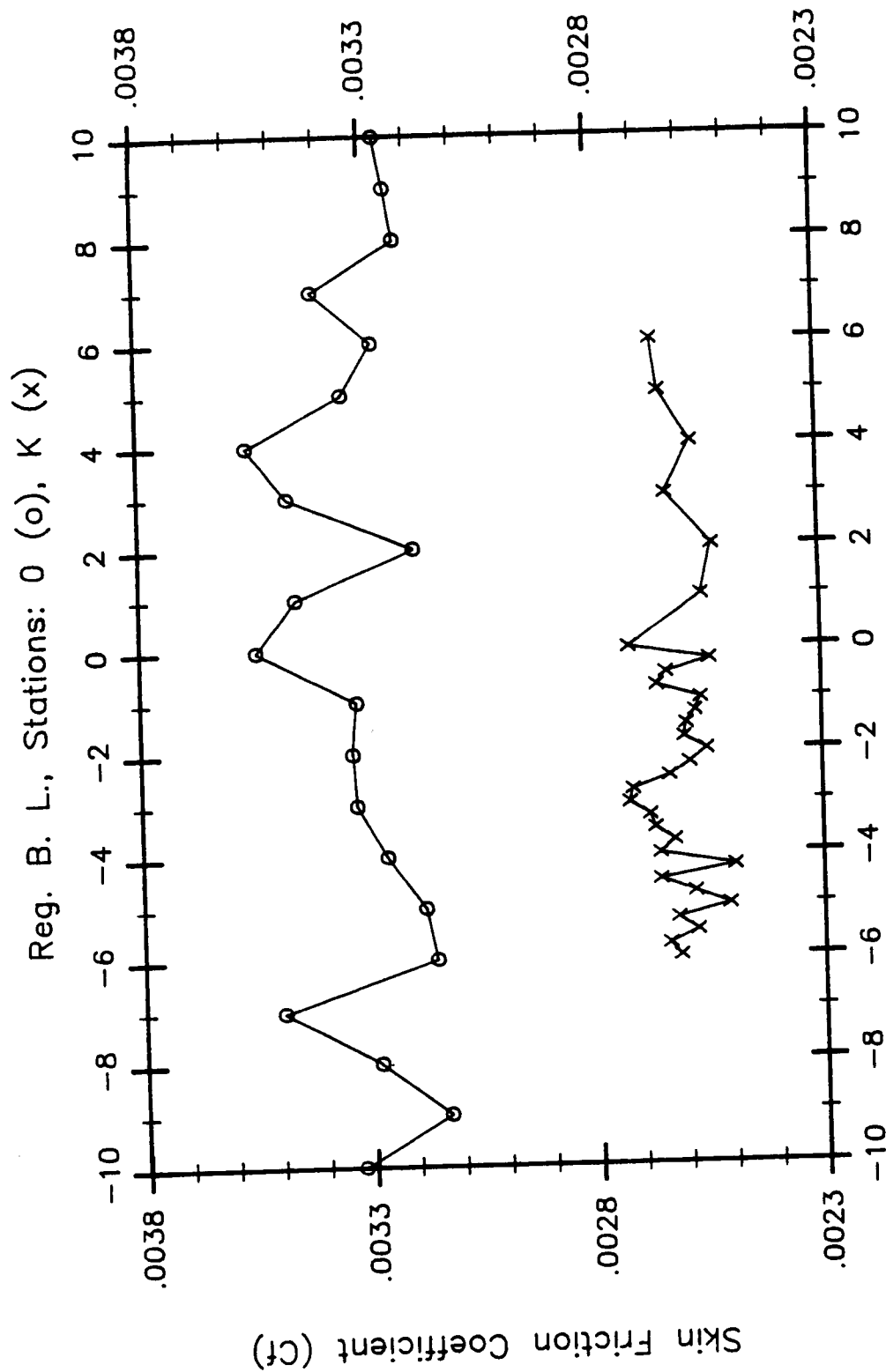
Figure 3.4   Spanwise variation of the local skin friction measured by Preston tube at different streamwise stations; O (o), and K (x), with a 1/16" threaded rod tripping device for inlet No. 1 configuration.
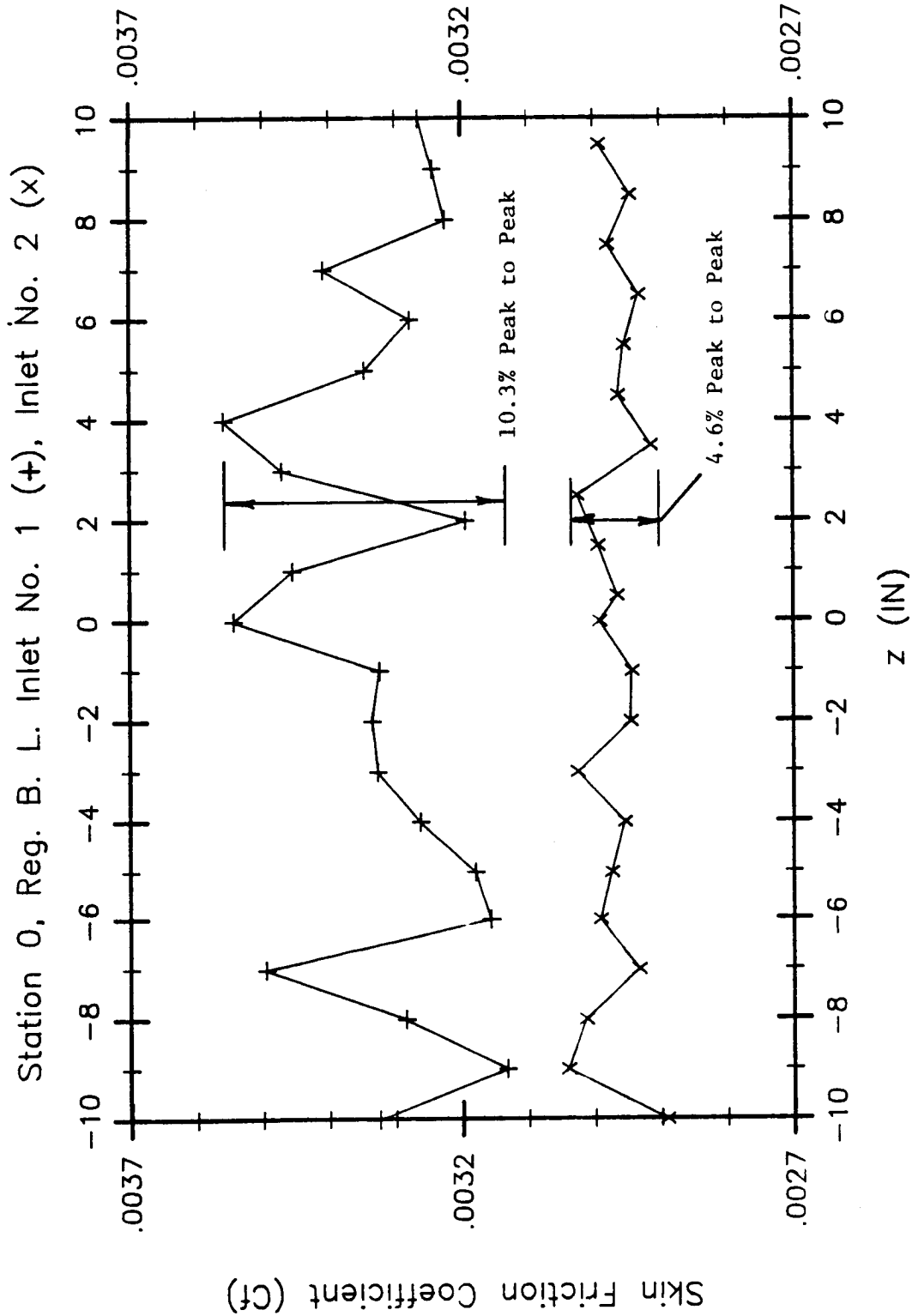
Figure 3.5 Comparison of spanwise variation of the local skin friction measured
by Preston tube at station 0 (x = 179") with a 1/16" threaded rod tripping
device (at x = 13.5") for inlet No. 1 (+) and inlet No. 2 (x) configurations.
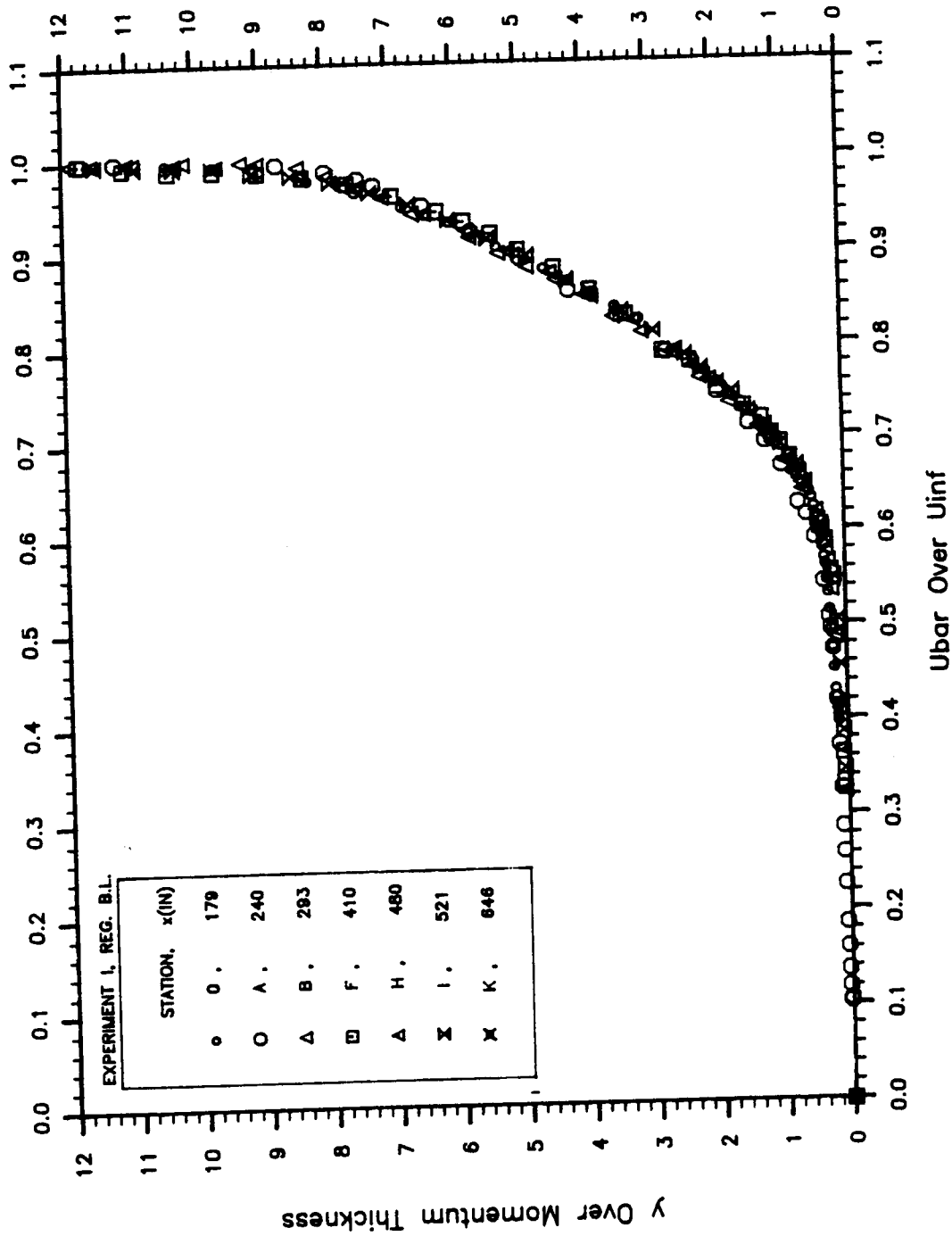
Figure 3.6 Non-dimensional mean velocity profiles (y/θ vs $\overline{U}/U_\infty$) at various streamwise stations in regular boundary layer from experiment I.
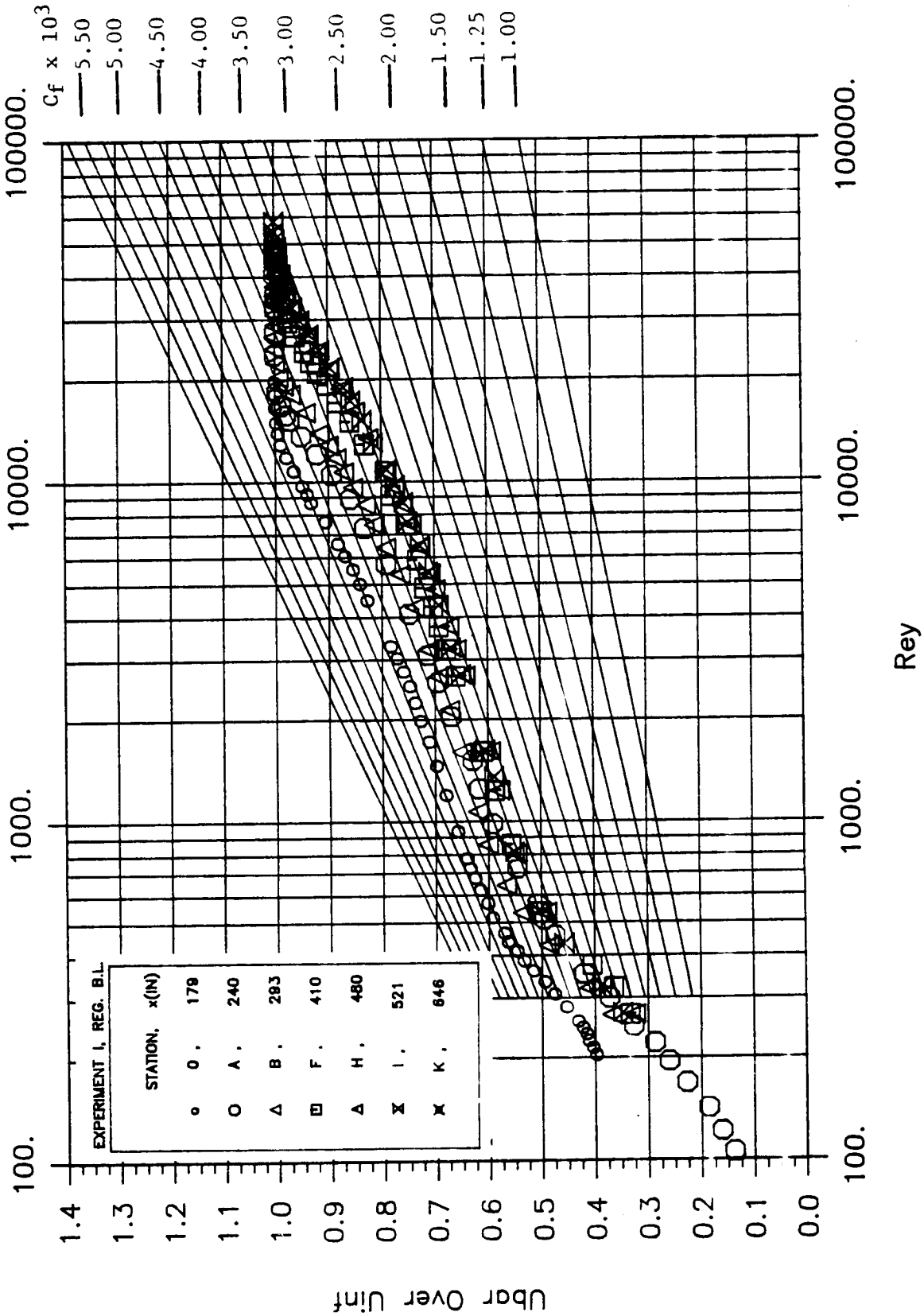
Figure 3.7 Clauser plot for mean velocity profiles (U/U_∞ vs $\rho U_\infty y/\mu$) at various streamwise stations in regular boundary layer from experiment I.
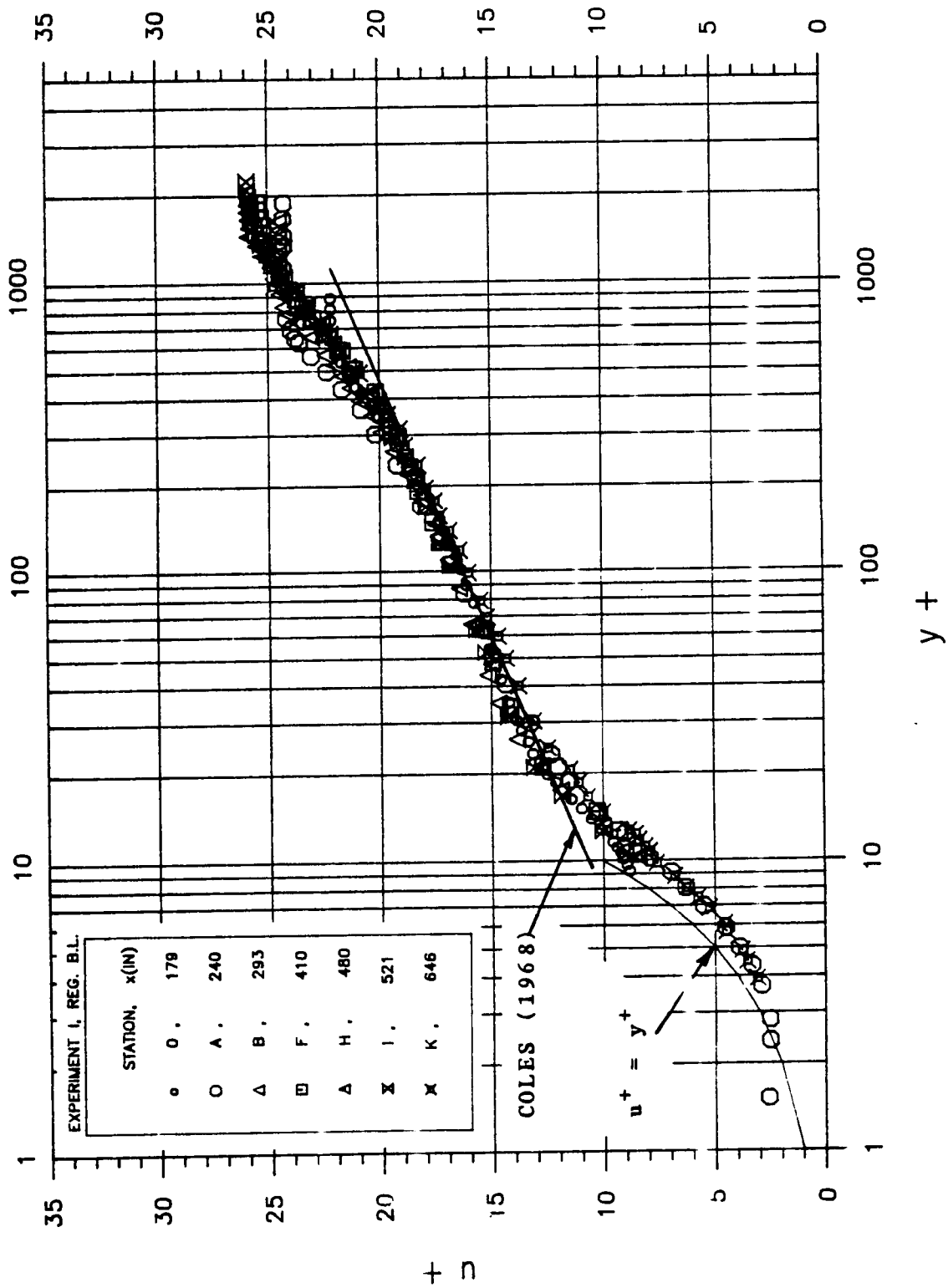
Figure 3.8 Wall-unit non-dimensionalized mean velocity profiles ($\overline{U}/u_\tau\theta$ vs $\rho y u_\tau\theta/\mu$) at various streamwise stations in regular boundary layer from experiment I.
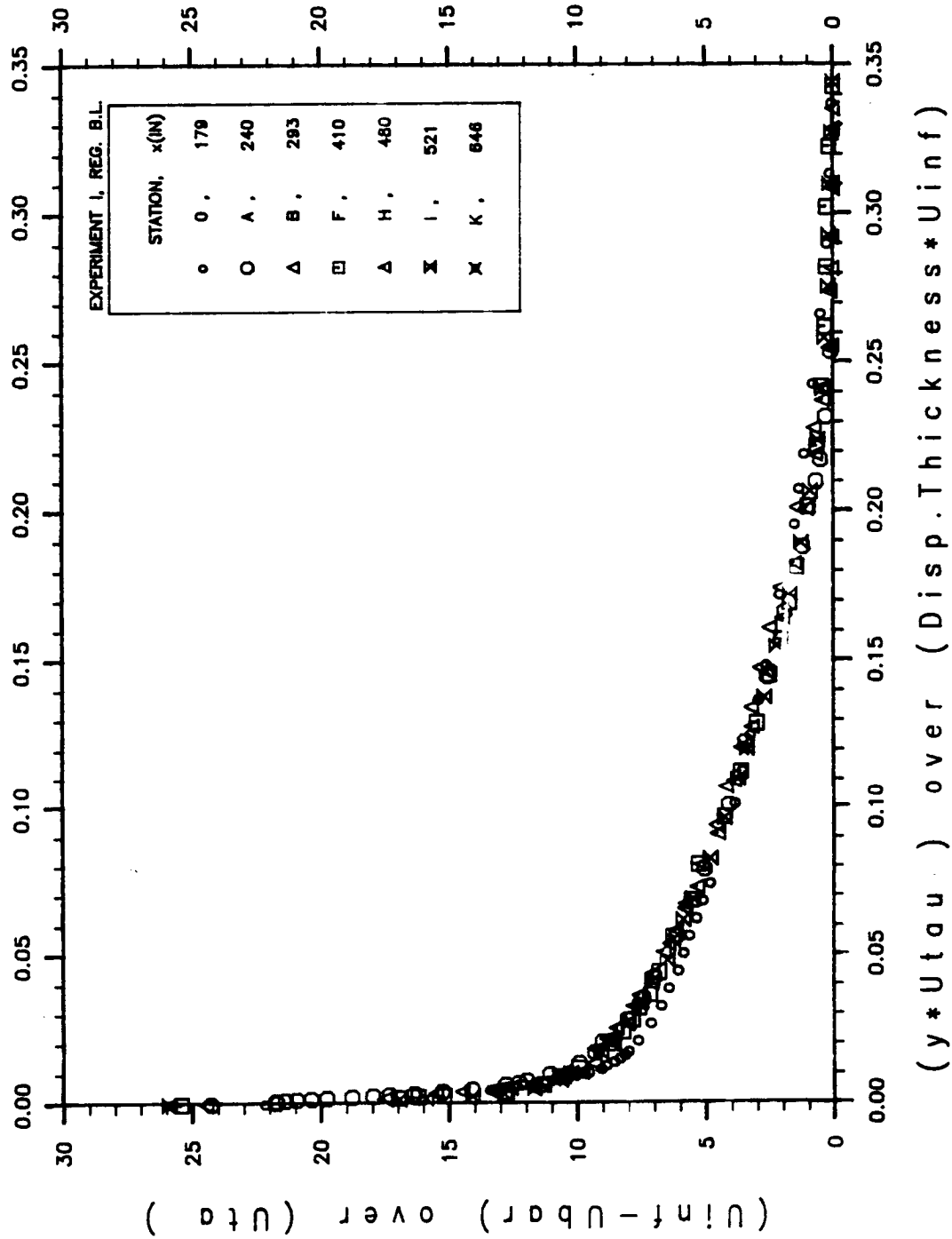
Figure 3.9 Variation of $(U_\infty - \bar{U})/u_{\tau\theta}$ vs $(yu_{\tau\theta}/\delta_d U_\infty)$ at various streamwise stations in regular boundary layer from experiment I.

112
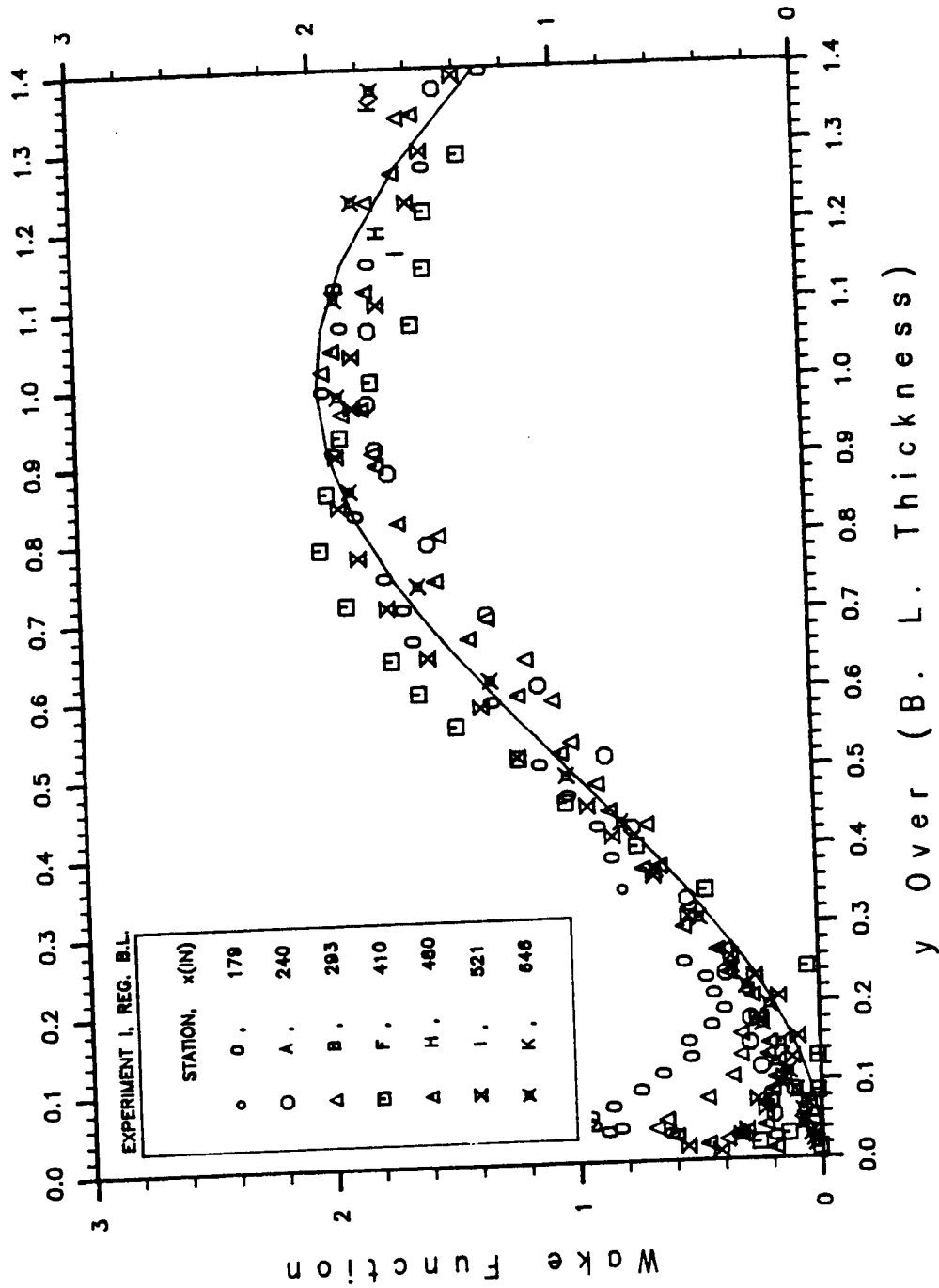
Figure 3.10 Wake function profiles (W vs y/δ) at various streamwise stations in regular boundary layer from experiment I. (Solid line : $W = 2\sin^2(\pi y/2\delta)$)
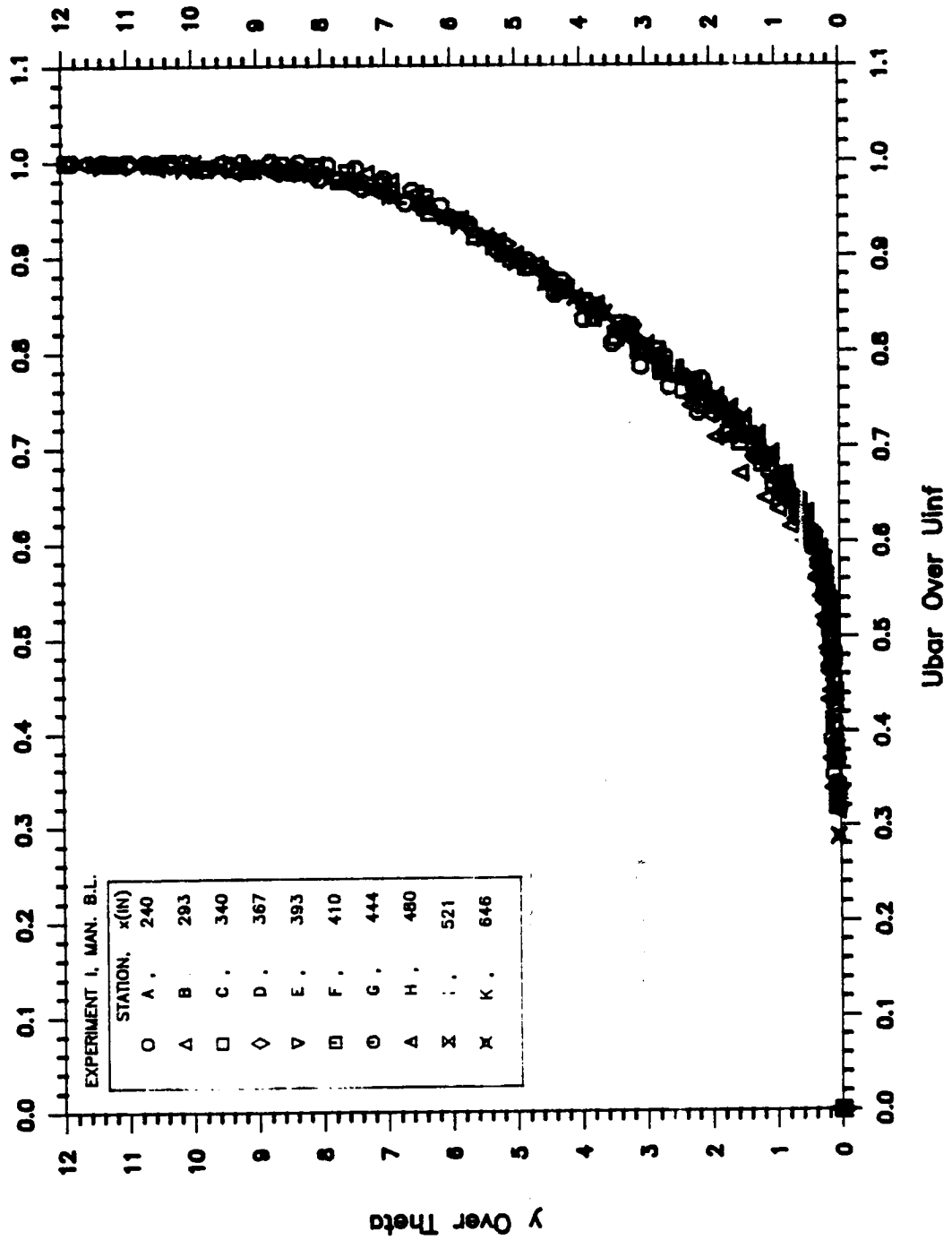
Figure 3.11 Non-dimensional mean velocity profiles (y/Θ vs $\bar{U}/U_\infty$) at various streamwise stations in manipulated boundary layer from experiment I.

114
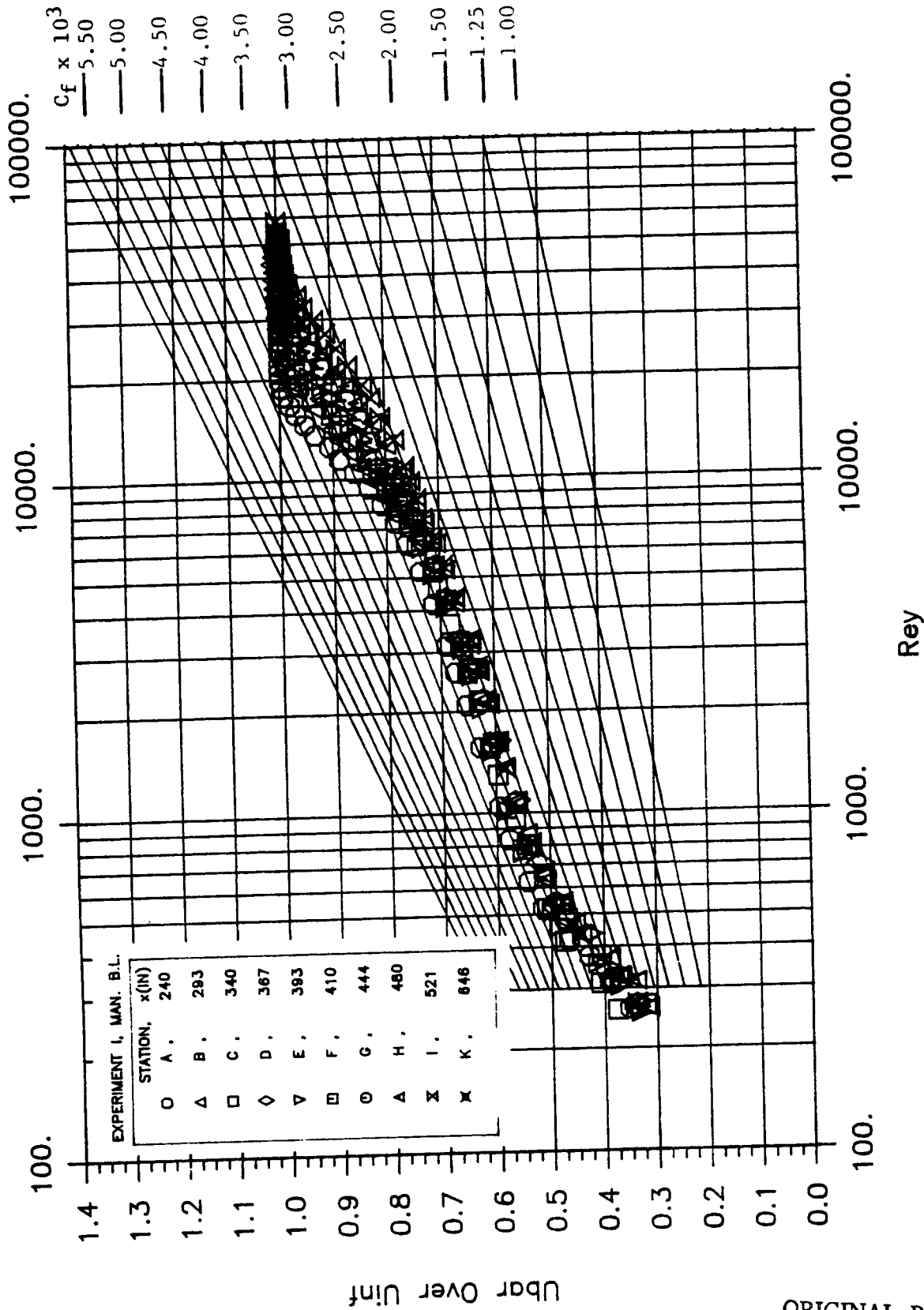
Figure 3.12 Clauser plot for mean velocity profiles ($\overline{U}/U_\infty$ vs $\rho U_\infty y/\mu$) at various streamwise stations in manipulated boundary layer from experiment I.
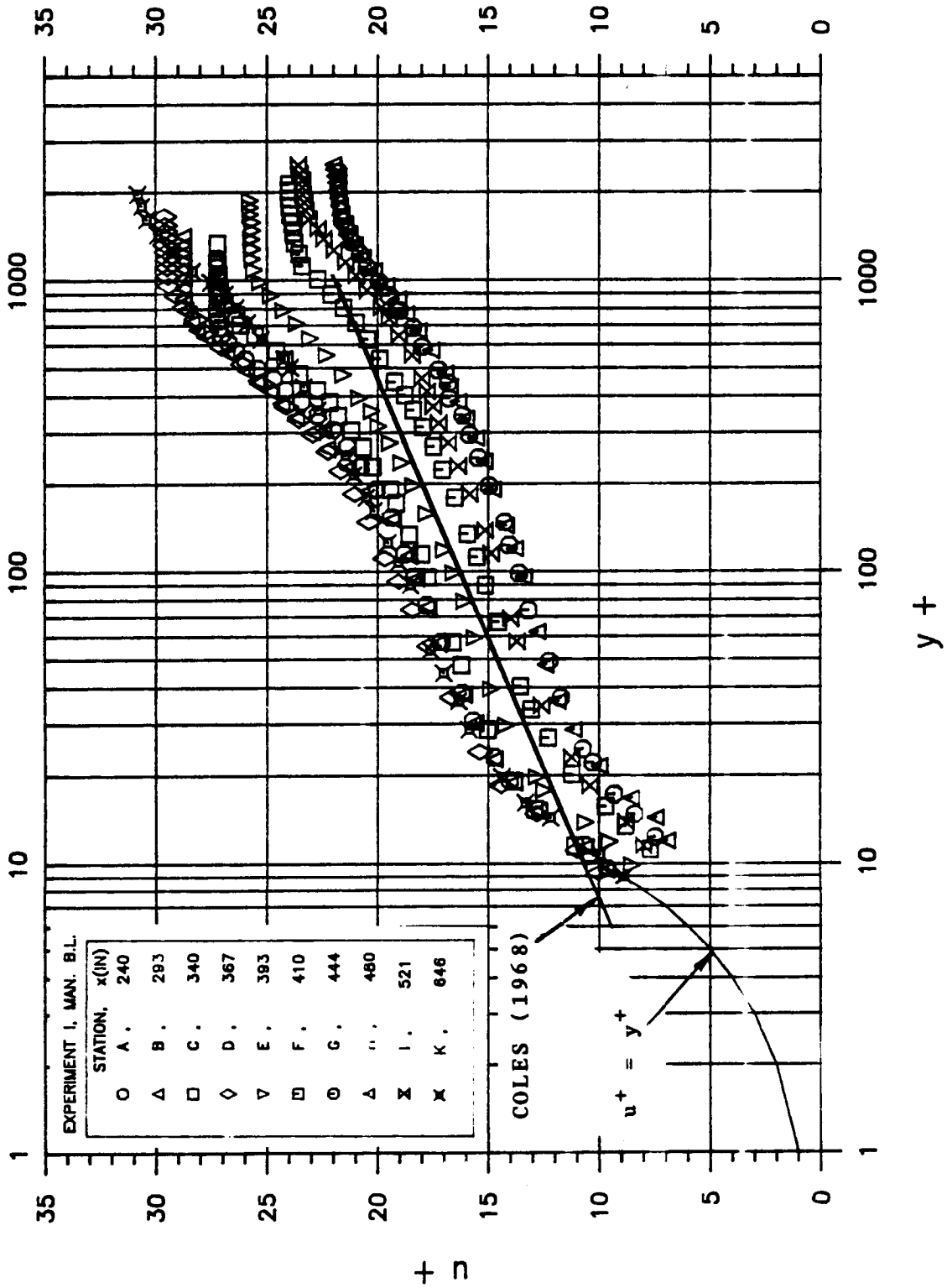
Figure 3.13 Wall-unit non-dimensionalized mean velocity profiles ($\bar{U}/u_{\tau\theta}$ vs $\rho y u_{\tau\theta}/\mu$) at various streamwise stations in manipulated boundary layer from experiment I.
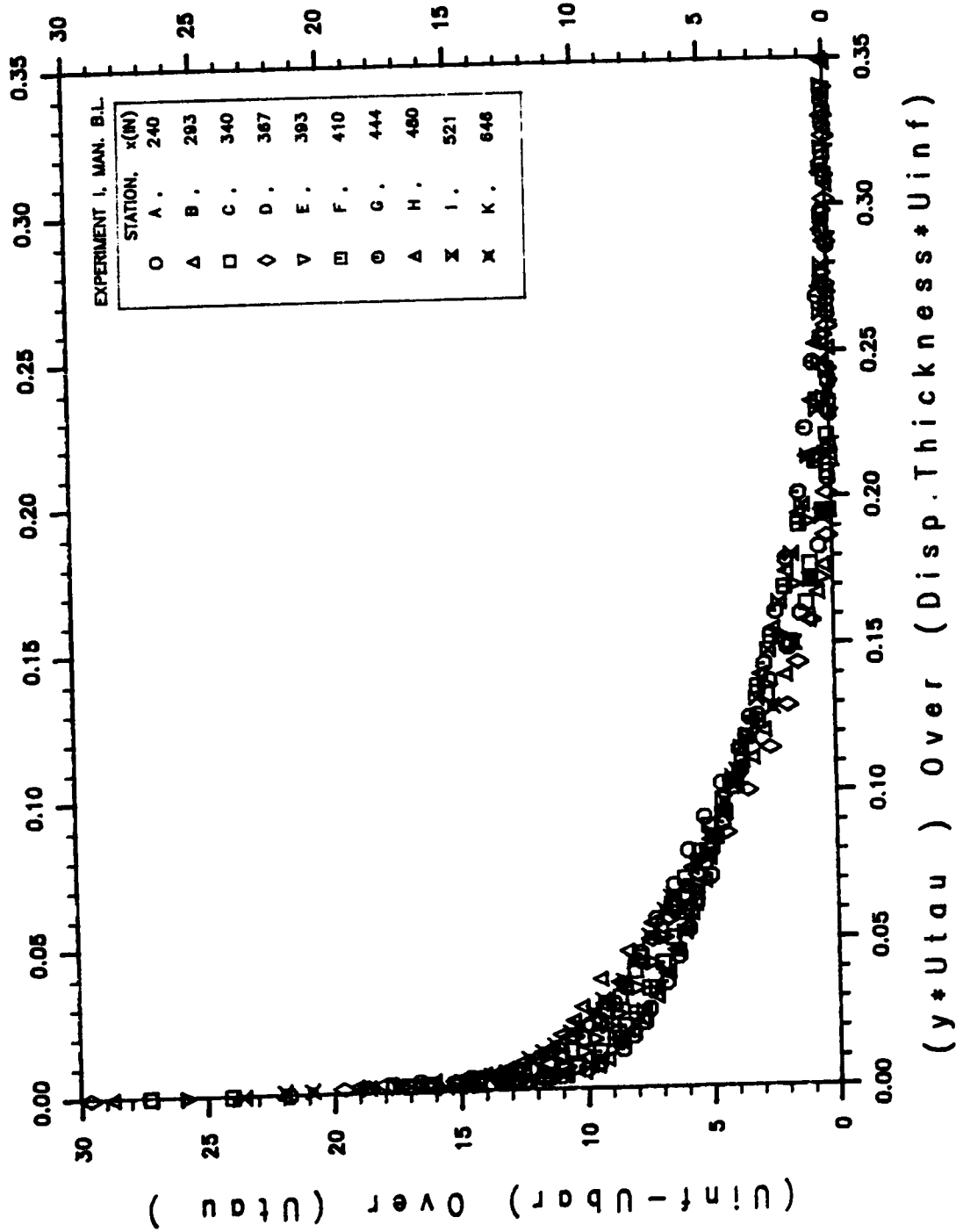
Figure 3.14 Variation of $(U_\infty - \bar{U})/u_{\tau\theta}$ vs $(yu_{\tau\theta}/\delta_d U_\infty)$ at various streamwise stations in manipulated boundary layer from experiment I.

117
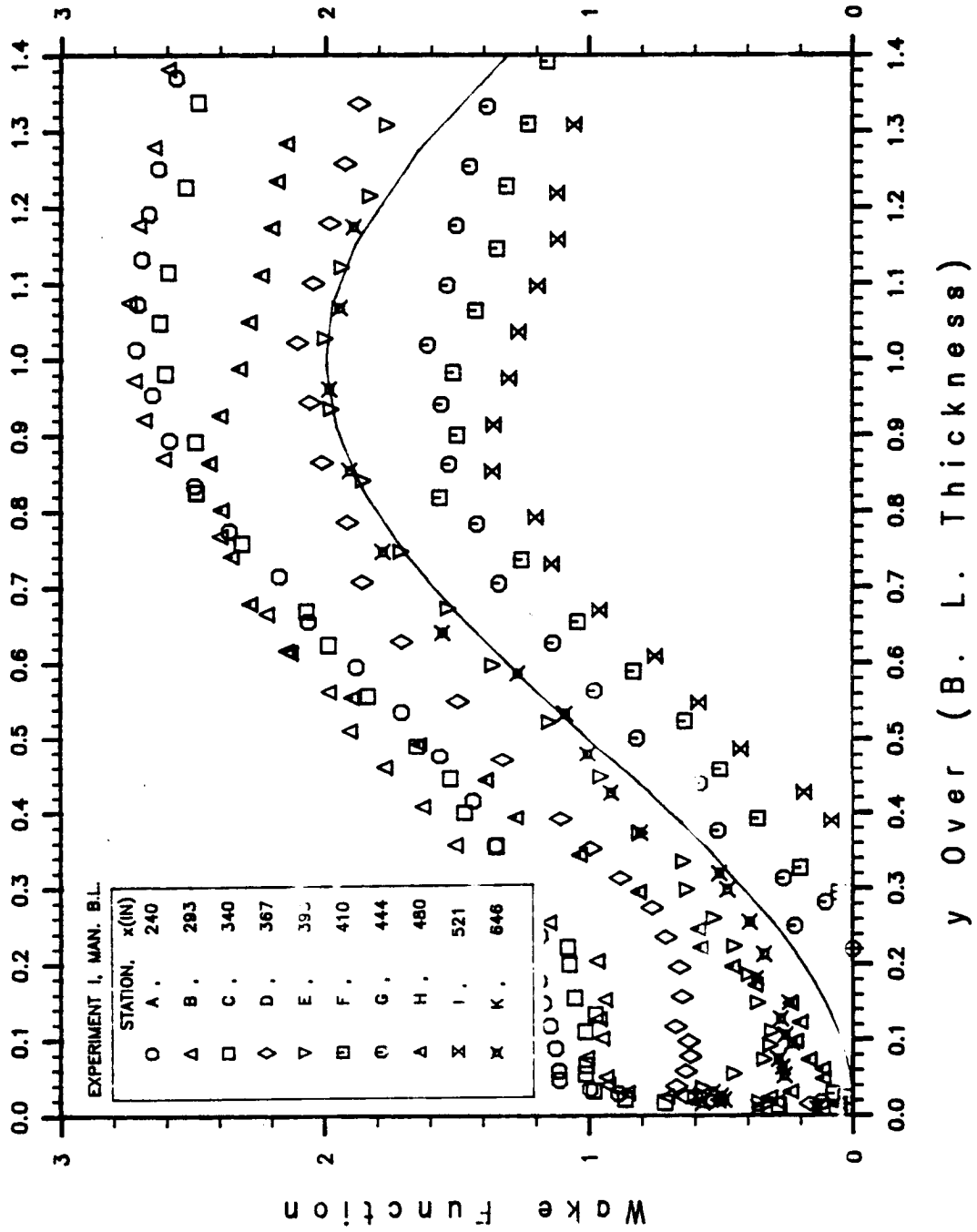
Figure 3.15 Wake function profiles (W vs y/δ) at various streamwise stations in manipulated boundary layer from experiment I. (Solid line : W =2Sin²(πy/2δ))
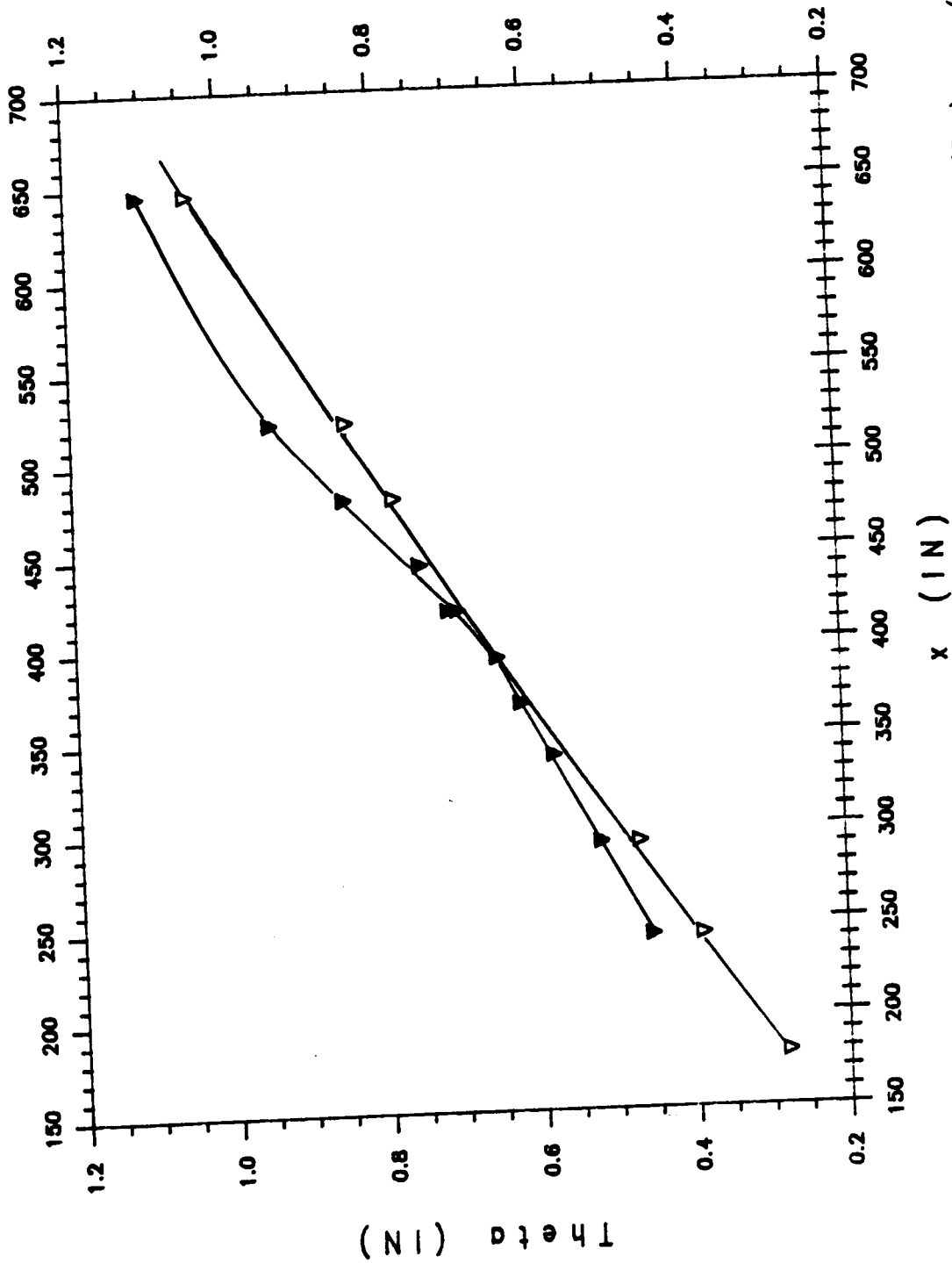
Figure 3.16 Comparison of streamwise momentum thickness distributions (Θ (In.) vs x (In.)) for regular (open) and manipulated (filled) boundary layers from experiment I.
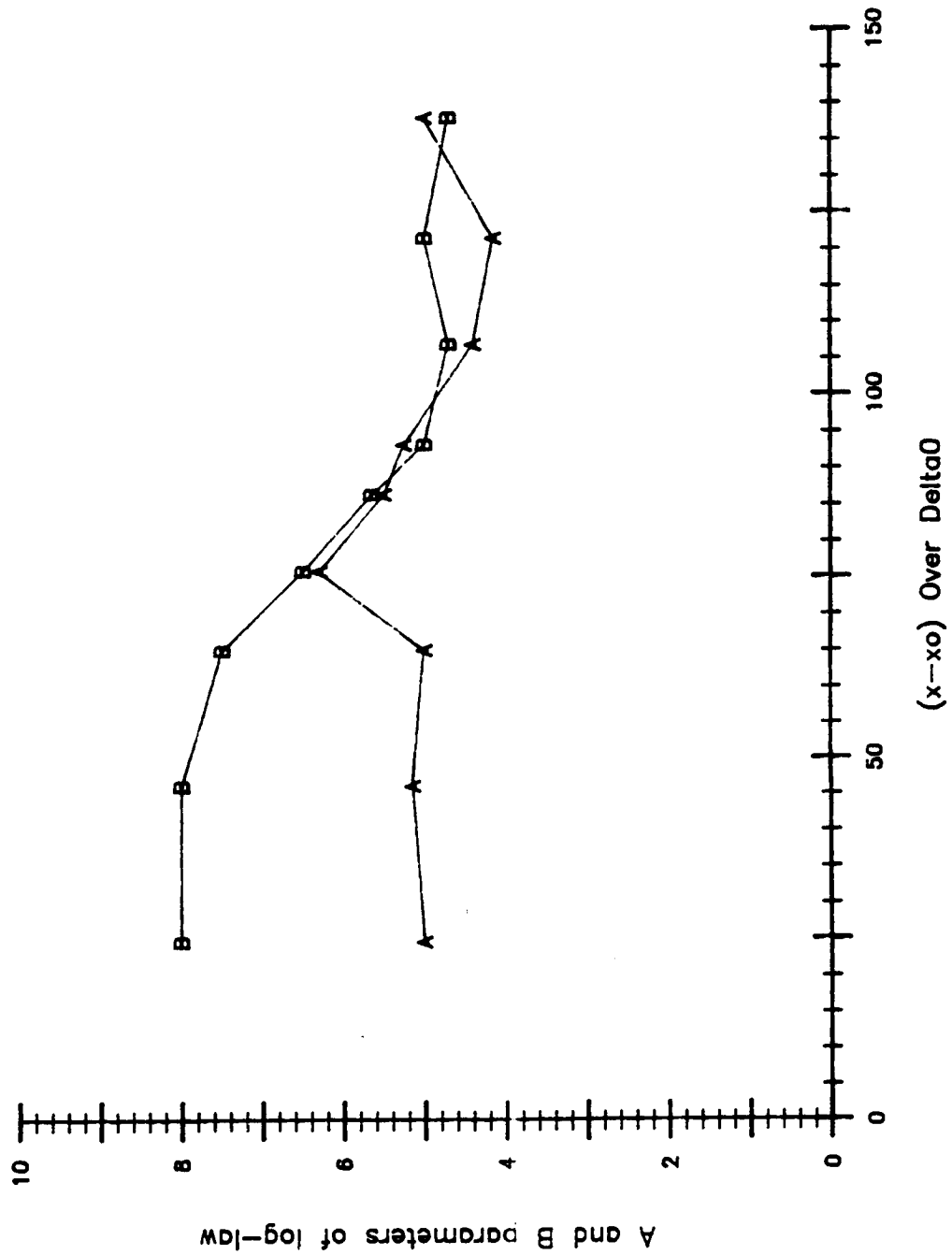
Figure 3.17 Streamwise variation of "law of the wall" ($u^+ = A\log_{10}(y^+) + B$) parameters (A and B) in manipulated boundary layers from experiment I.
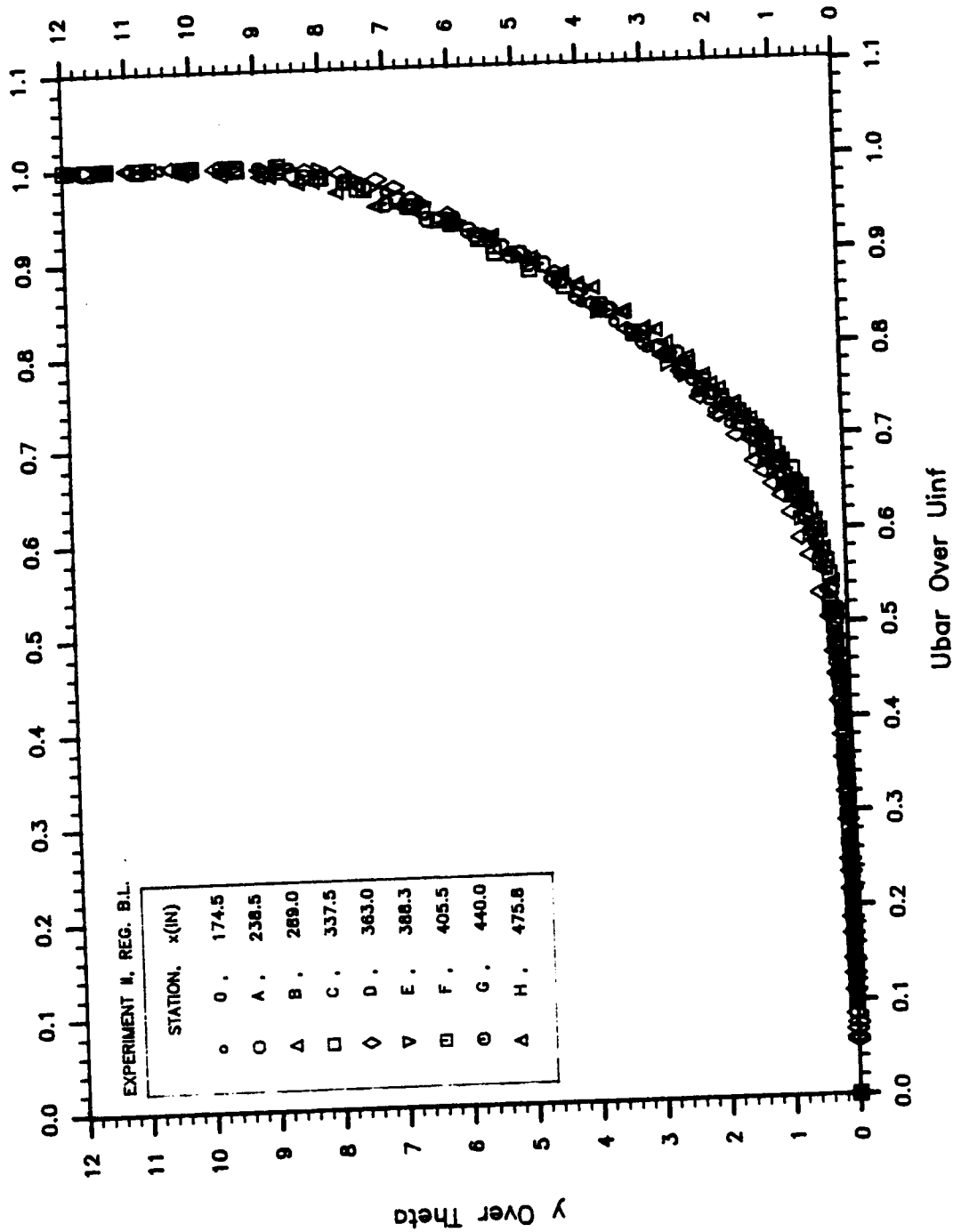
Figure 3.18 Non-dimensional mean velocity profiles (y/θ vs Ū/U∞) at various
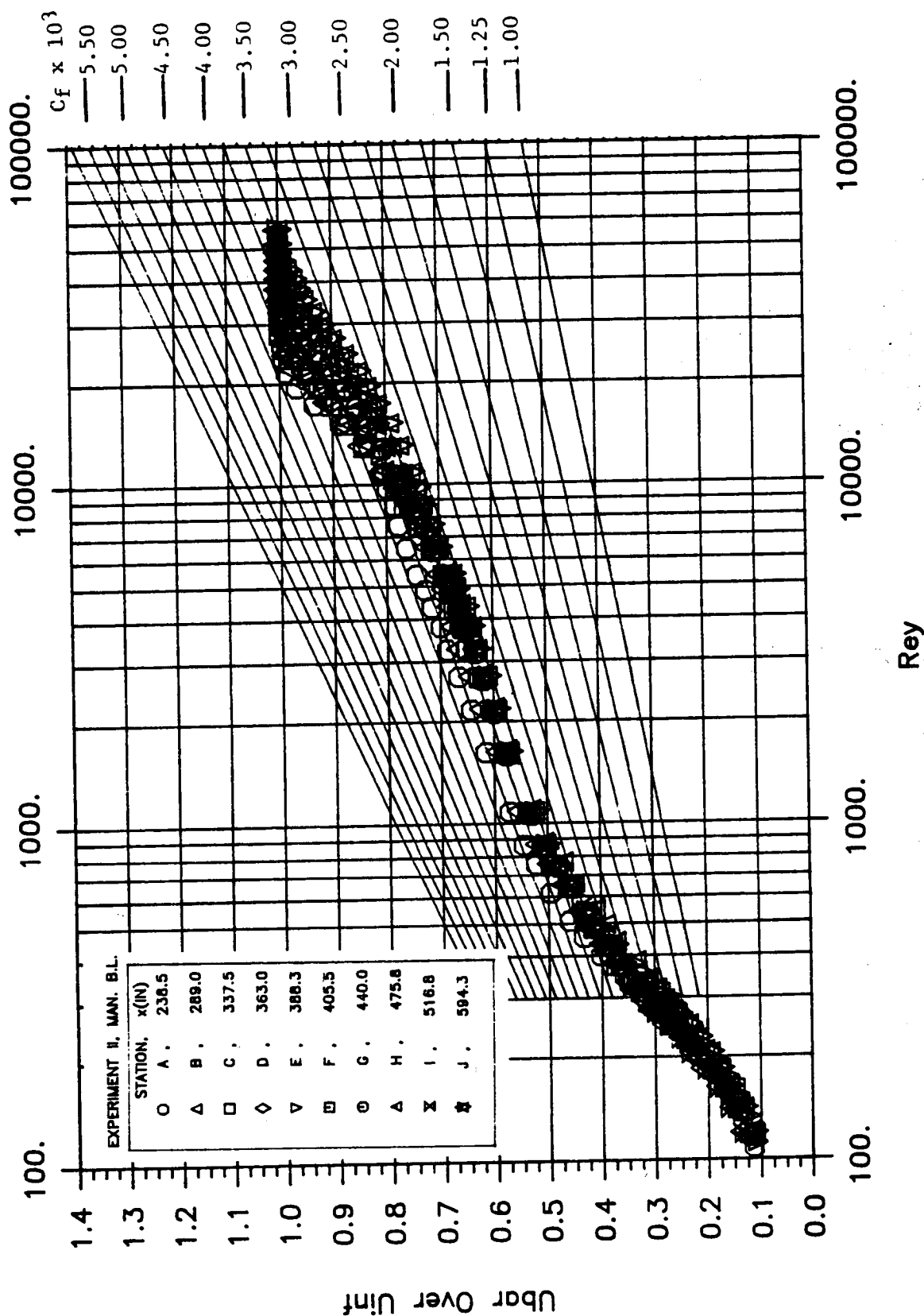streamwise stations in regular boundary layer from experiment II.
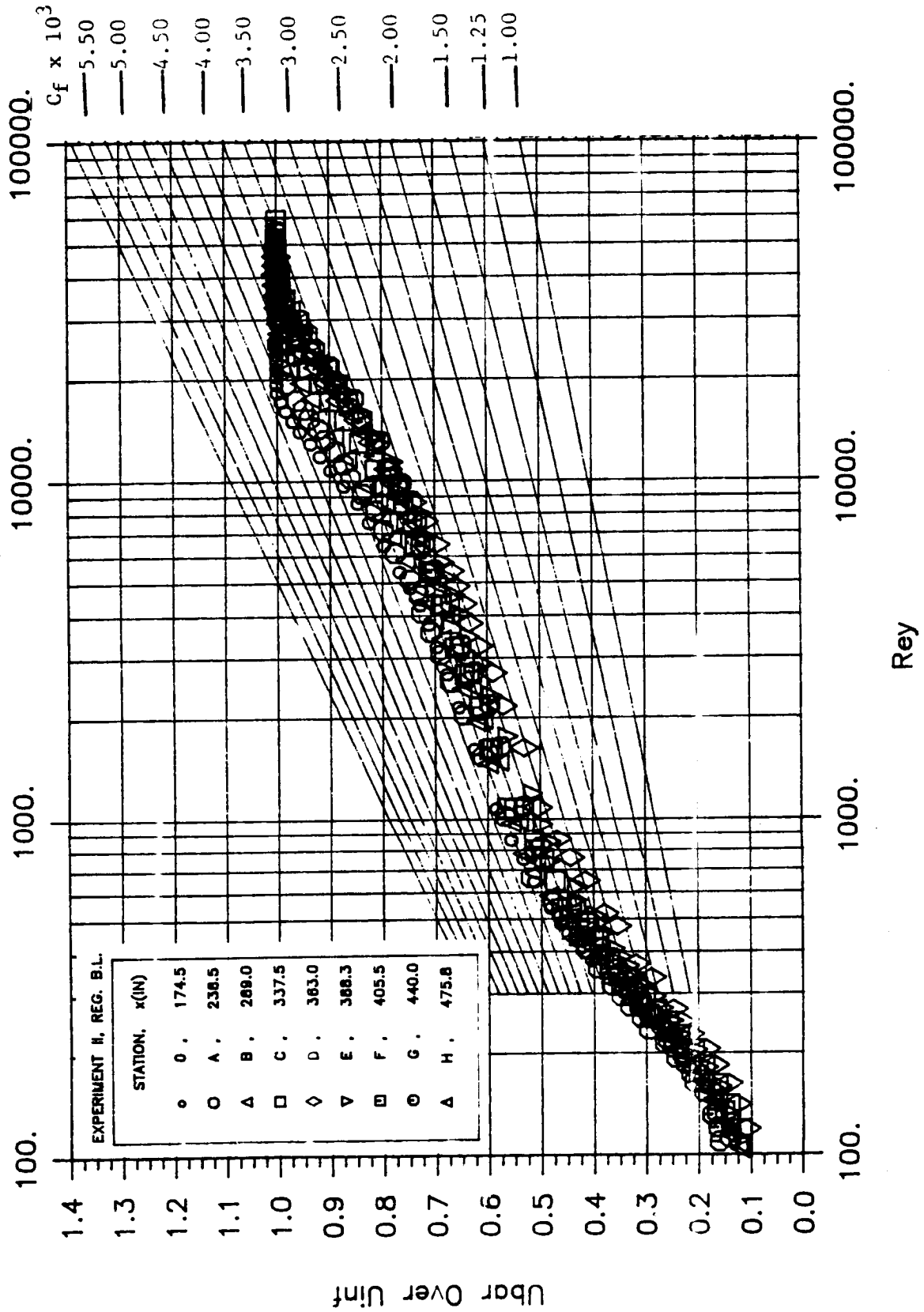
Figure 3.19 Clauser plot for mean velocity profiles (U/U_∞ vs $\rho U_\infty y/\mu$) at various streamwise stations in regular boundary layer from experiment II.
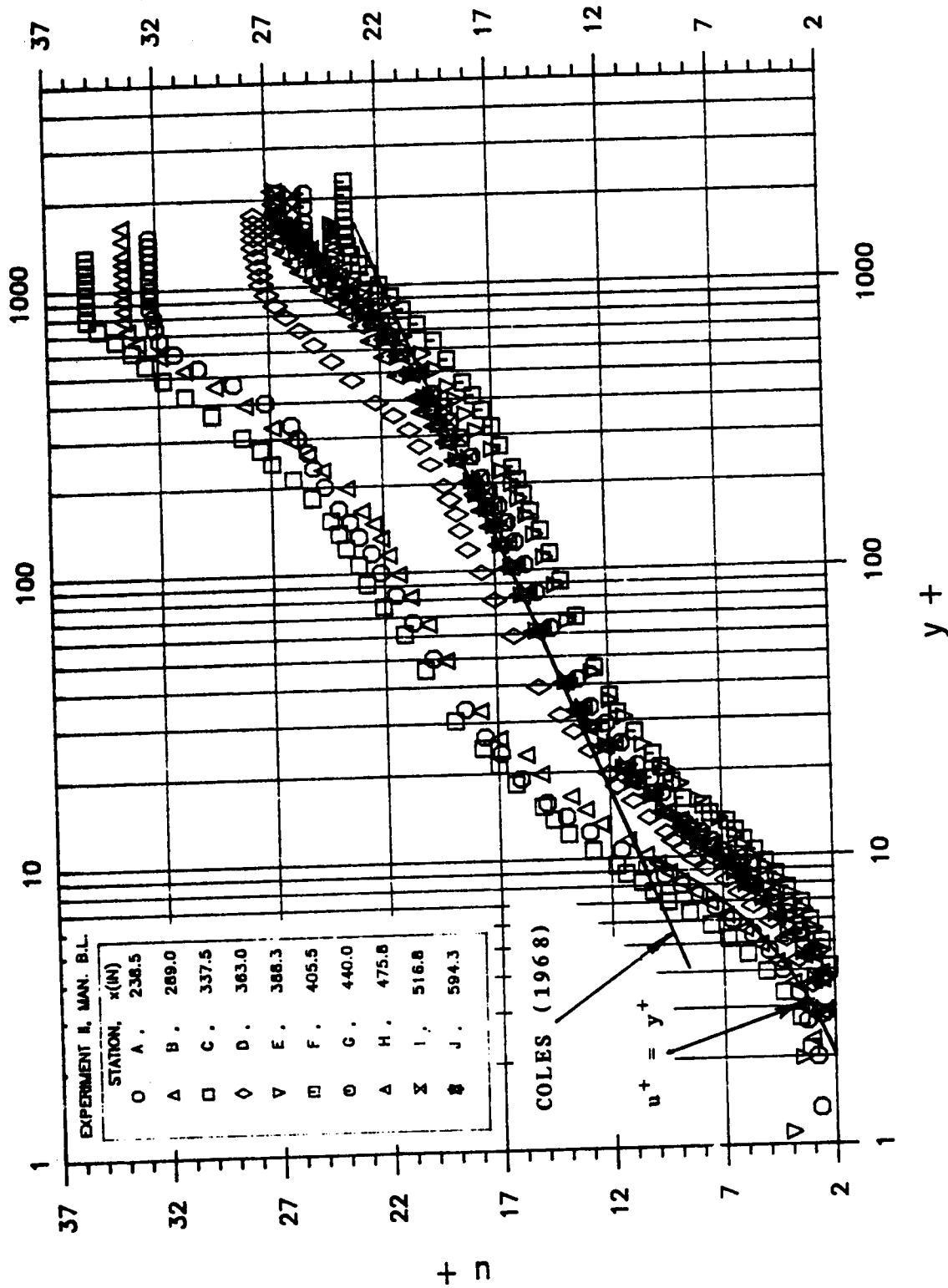
122
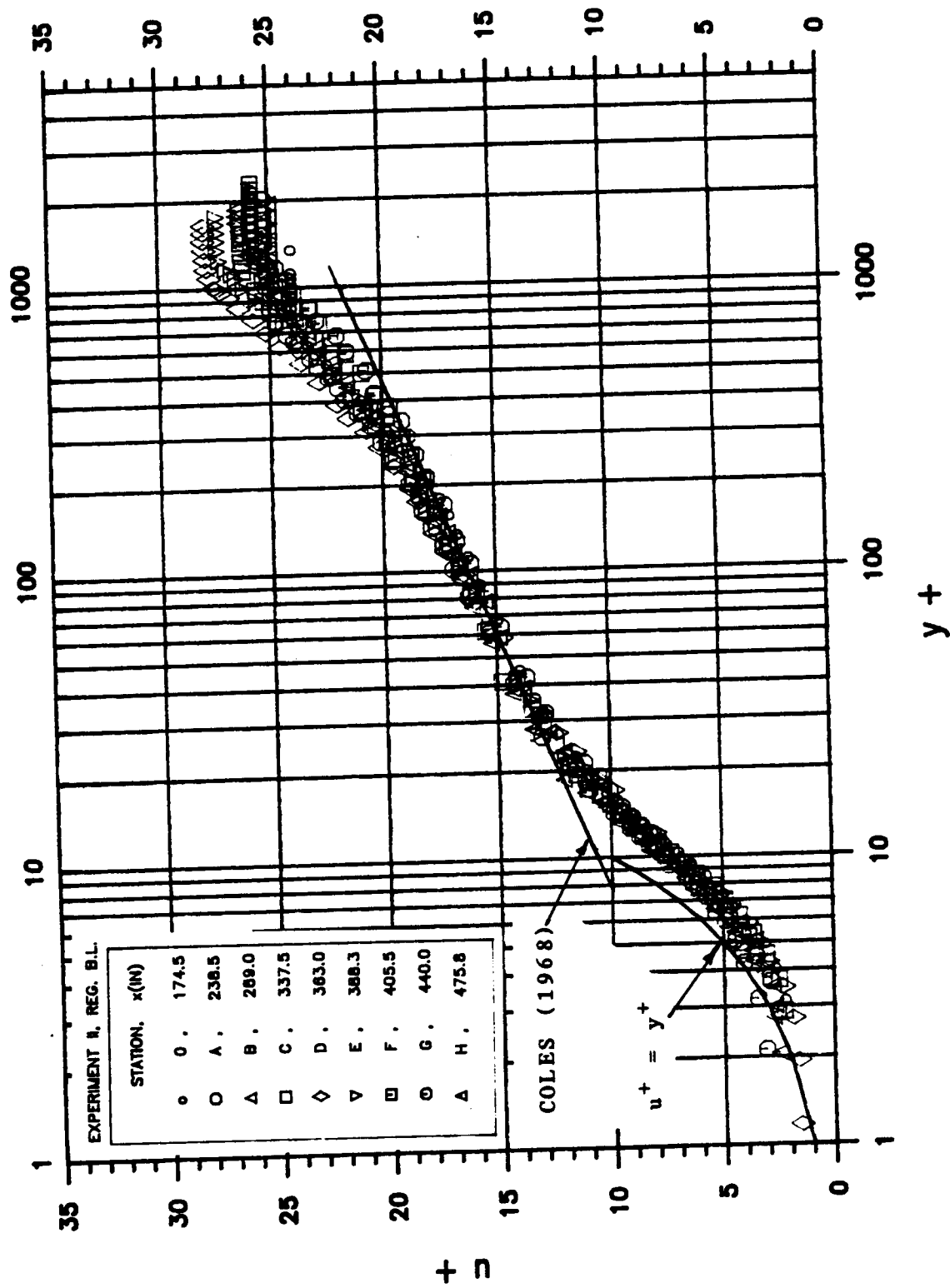
Figure 3.20 Wall-unit non-dimensionalized mean velocity profiles ($\overline{U}/u_{\tau\theta}$ vs $\rho y u_{\tau\theta}/\mu$) at various streamwise stations in regular boundary layer from experiment II.
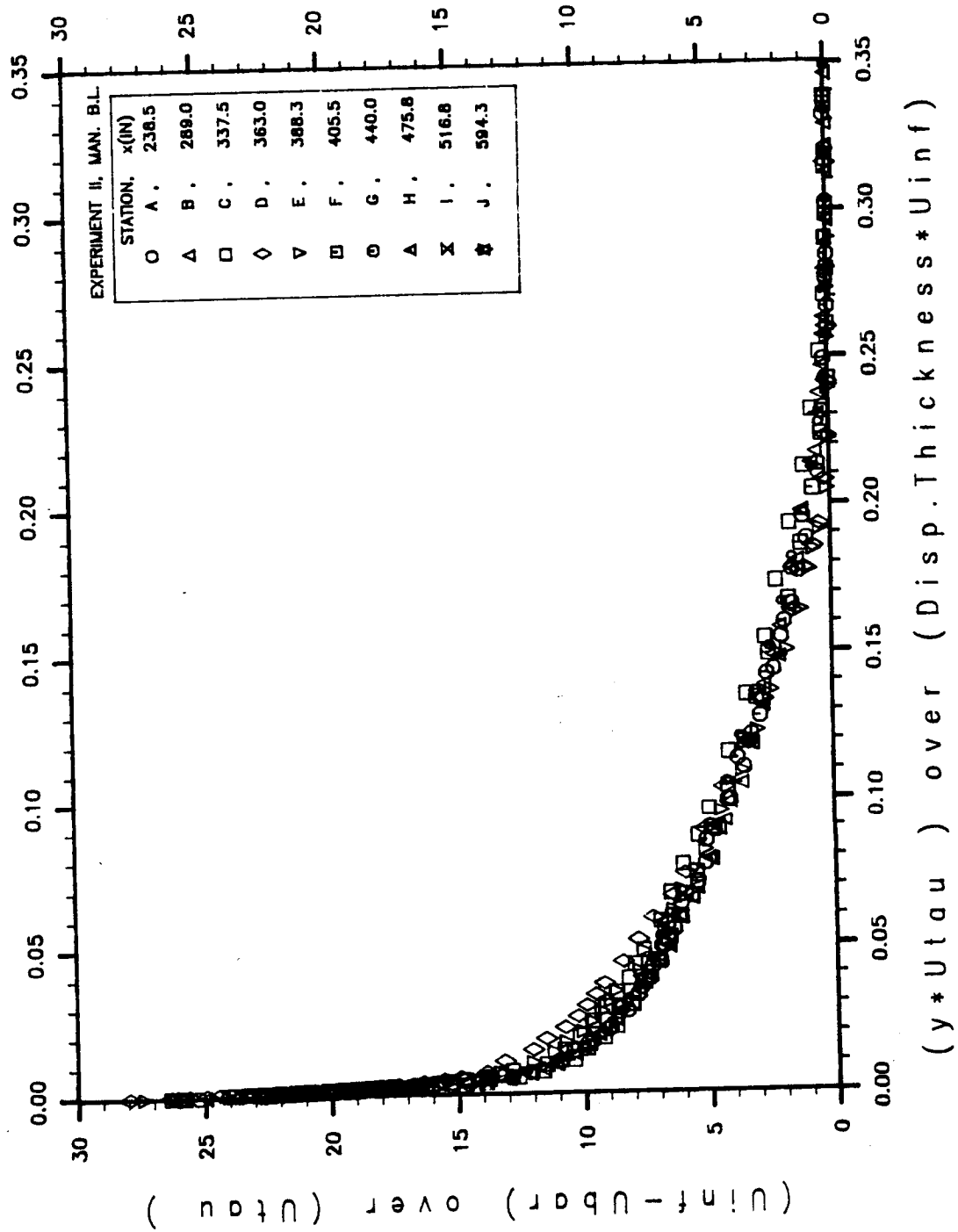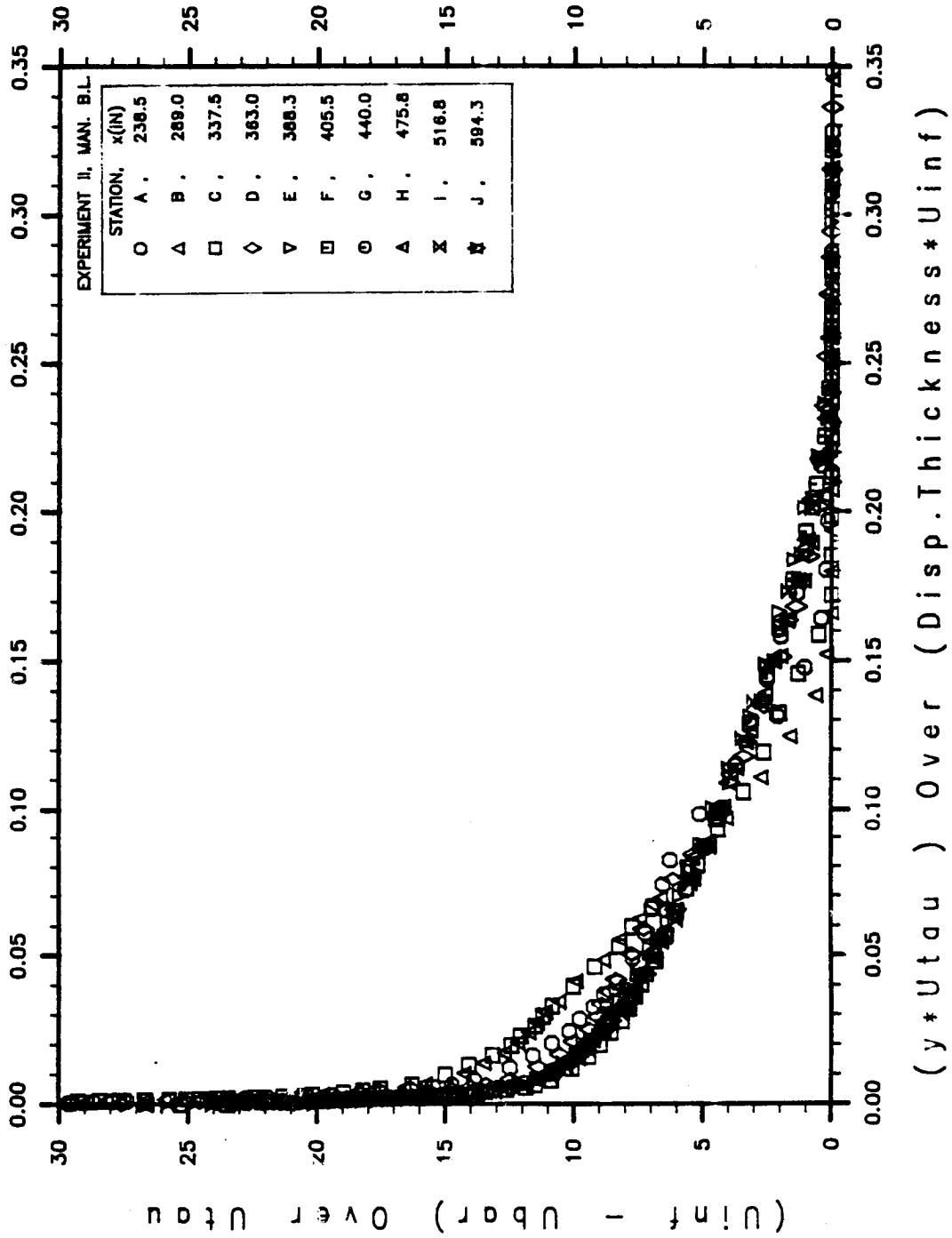
Figure 3.21 Variation of $(U_\infty - \bar{U})/u_{\tau\theta}$ vs $(yu_{\tau\theta}/\delta_d U_\infty)$ at various streamwise stations in regular boundary layer from experiment II.
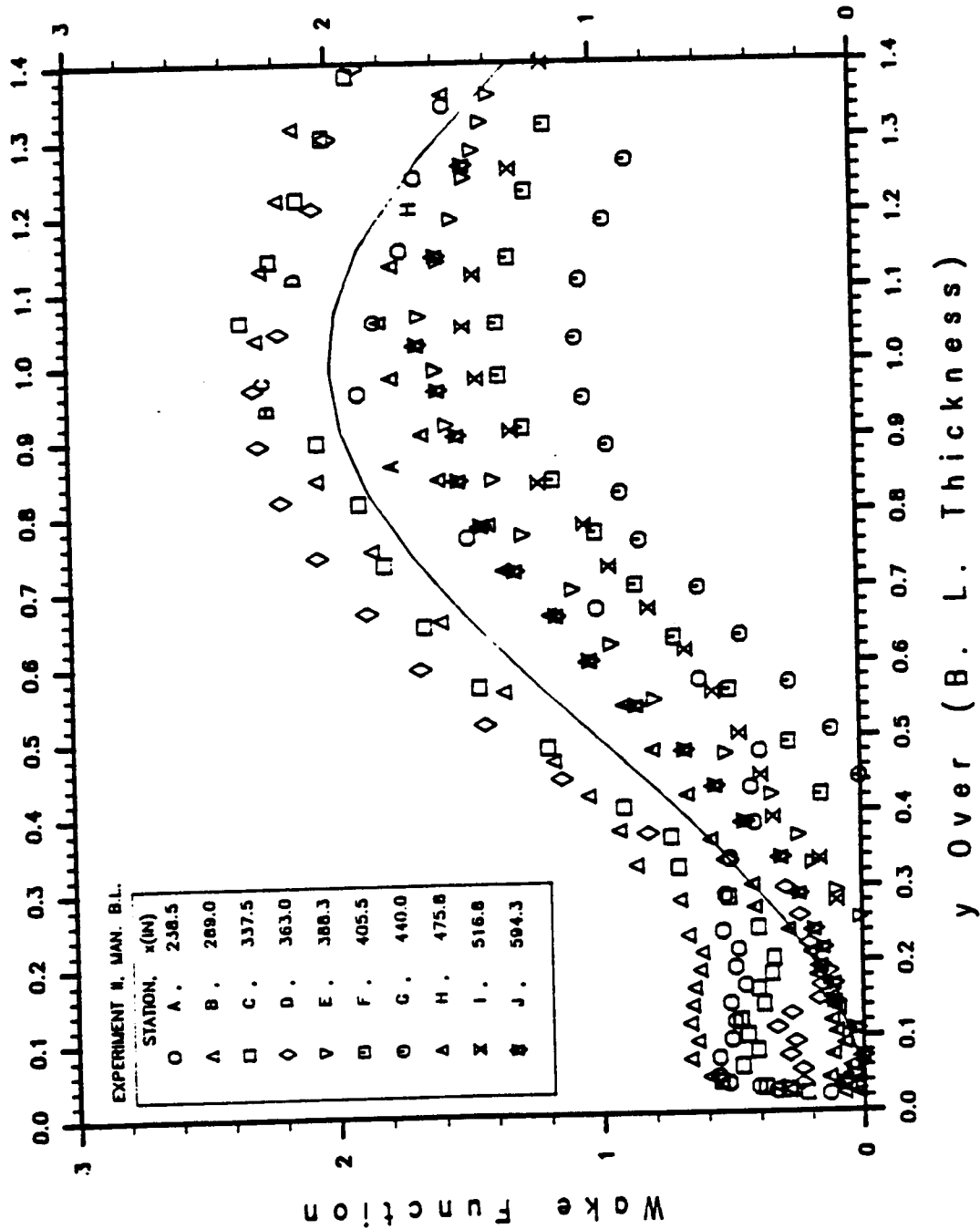
124
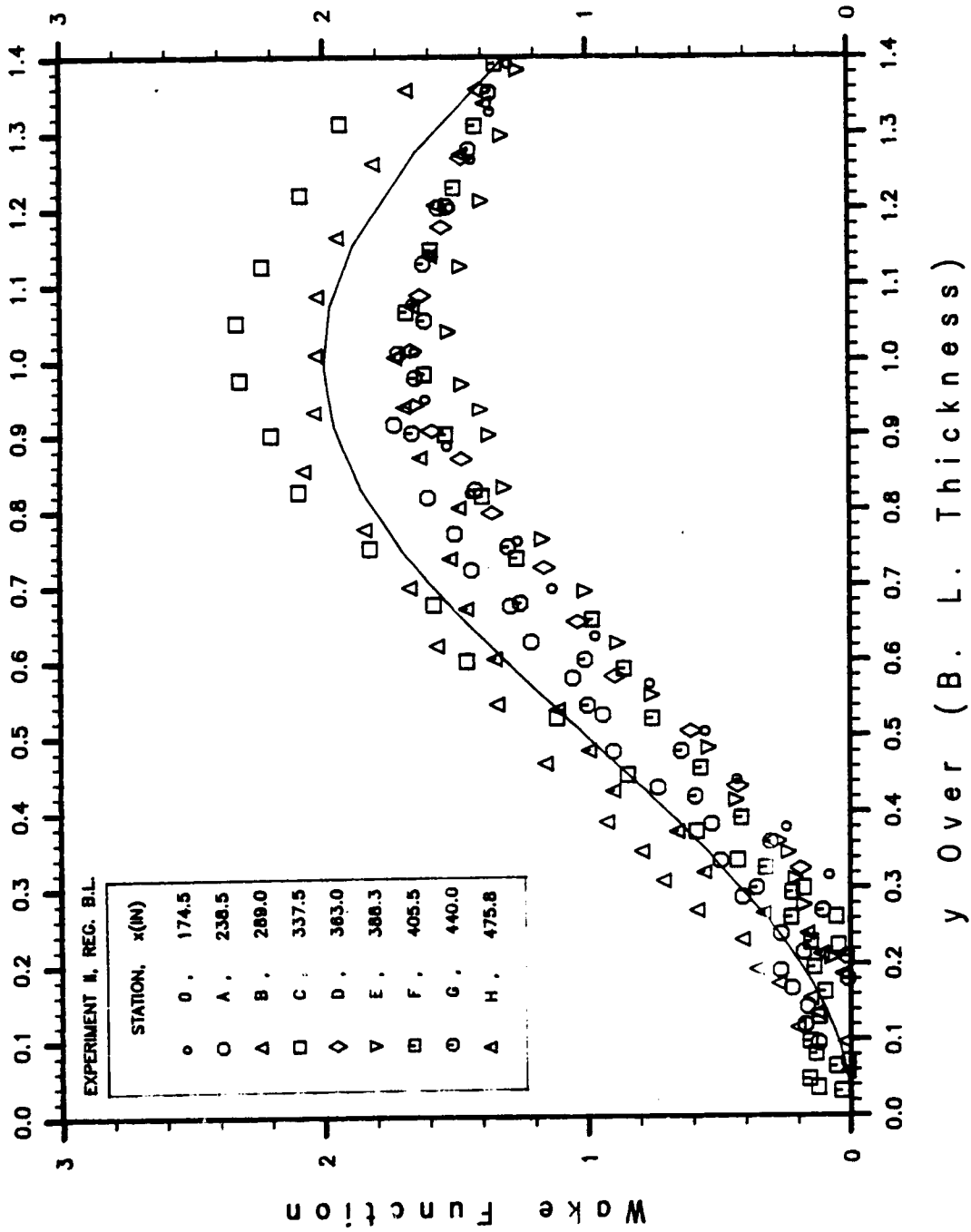
Figure 3.22 Wake function profile (W vs y/δ) at various streamwise stations in regular boundary layer from experiment II. (Solid line : W =2Sin² (πy/2δ))
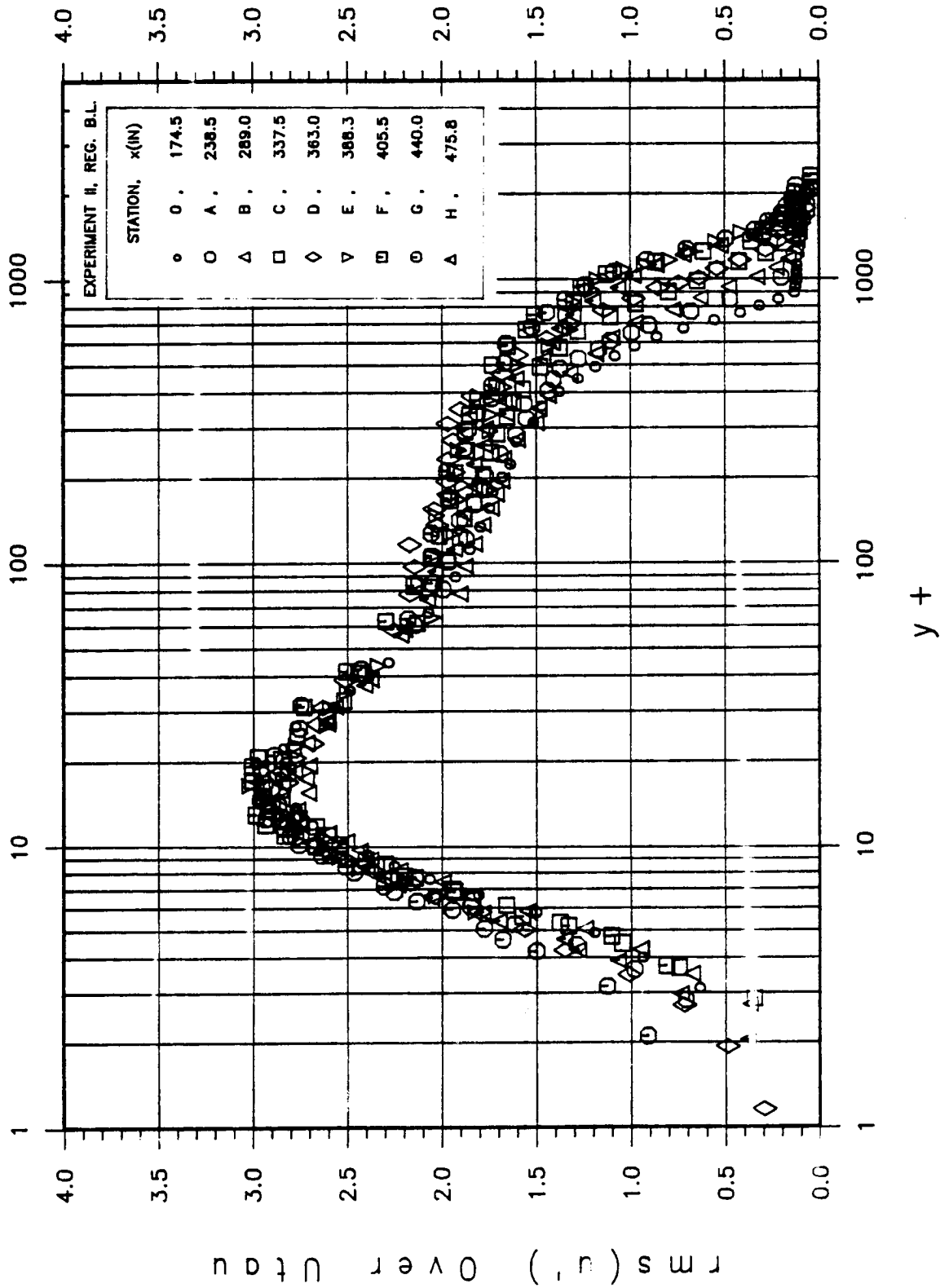
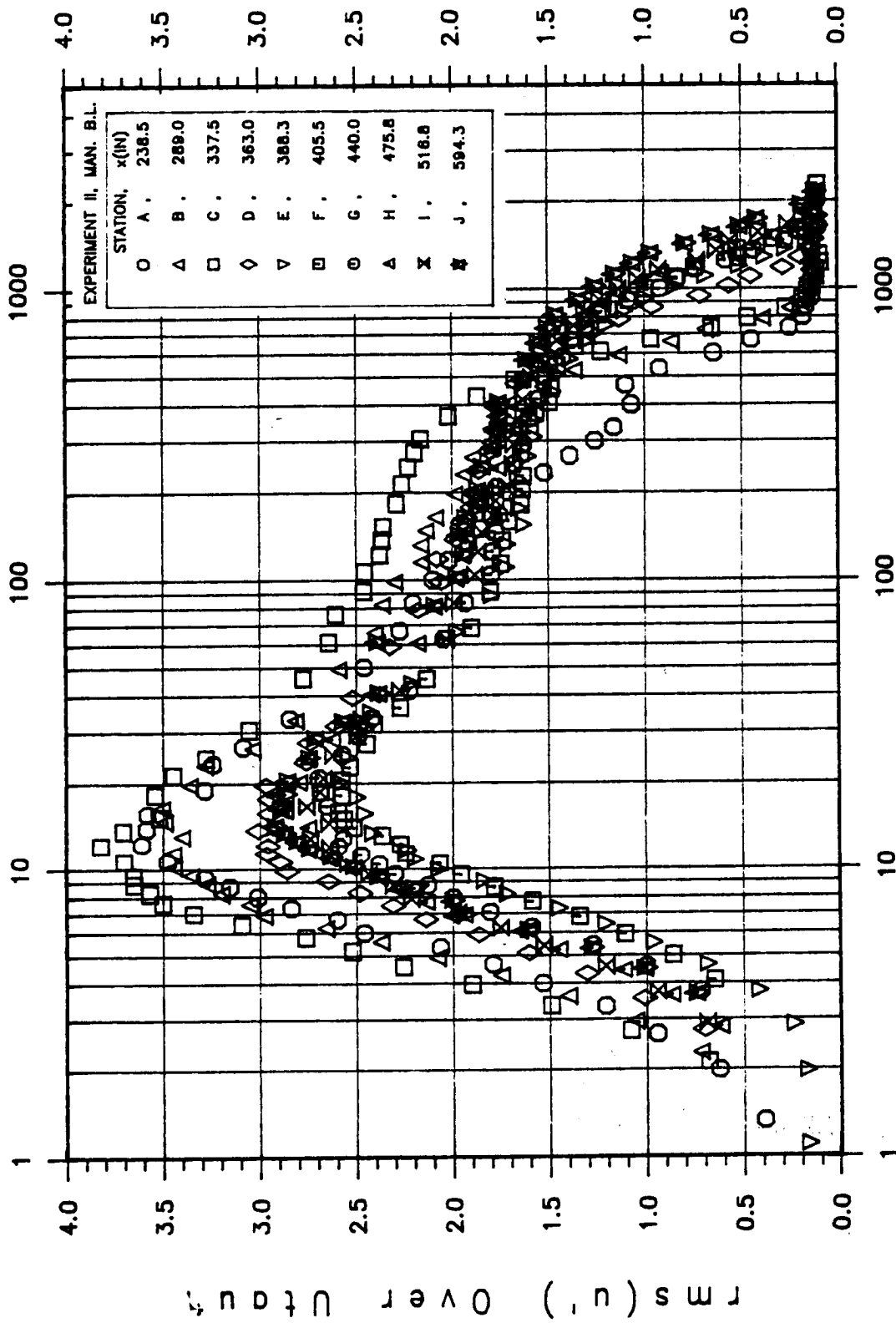**Figure 3.23** Wall-unit non-dimensionalized fluctuating velocity profile (rms(u')/$u_{\tau\theta}$ vs $\rho y u_{\tau\theta}/\mu$) at various streamwise stations in regular boundary layer from experiment II.
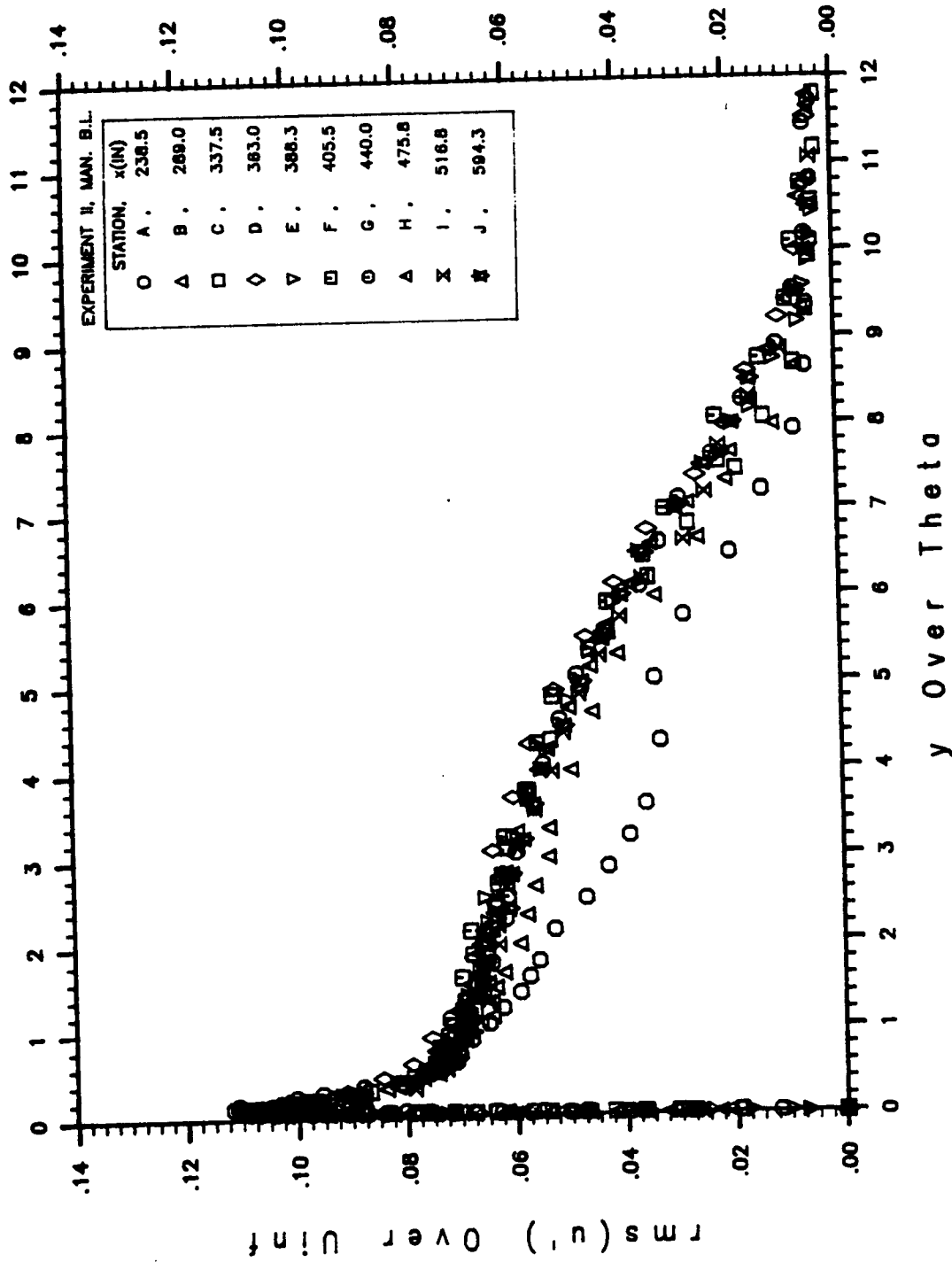
126
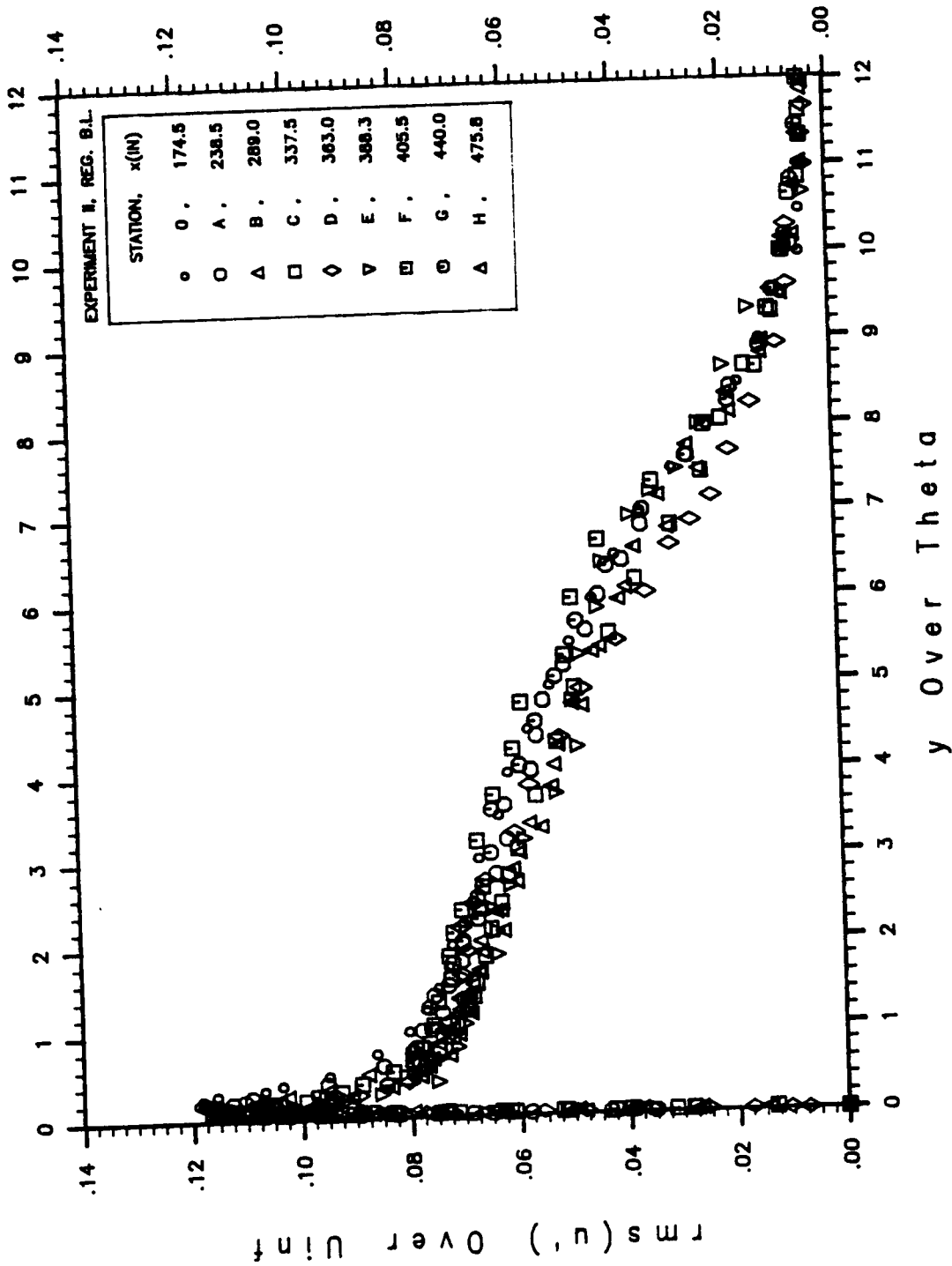
Figure 3.24 Variation of rms(u')/U_∞ vs y/θ at various streamwise stations in regular boundary layer from experiment II.
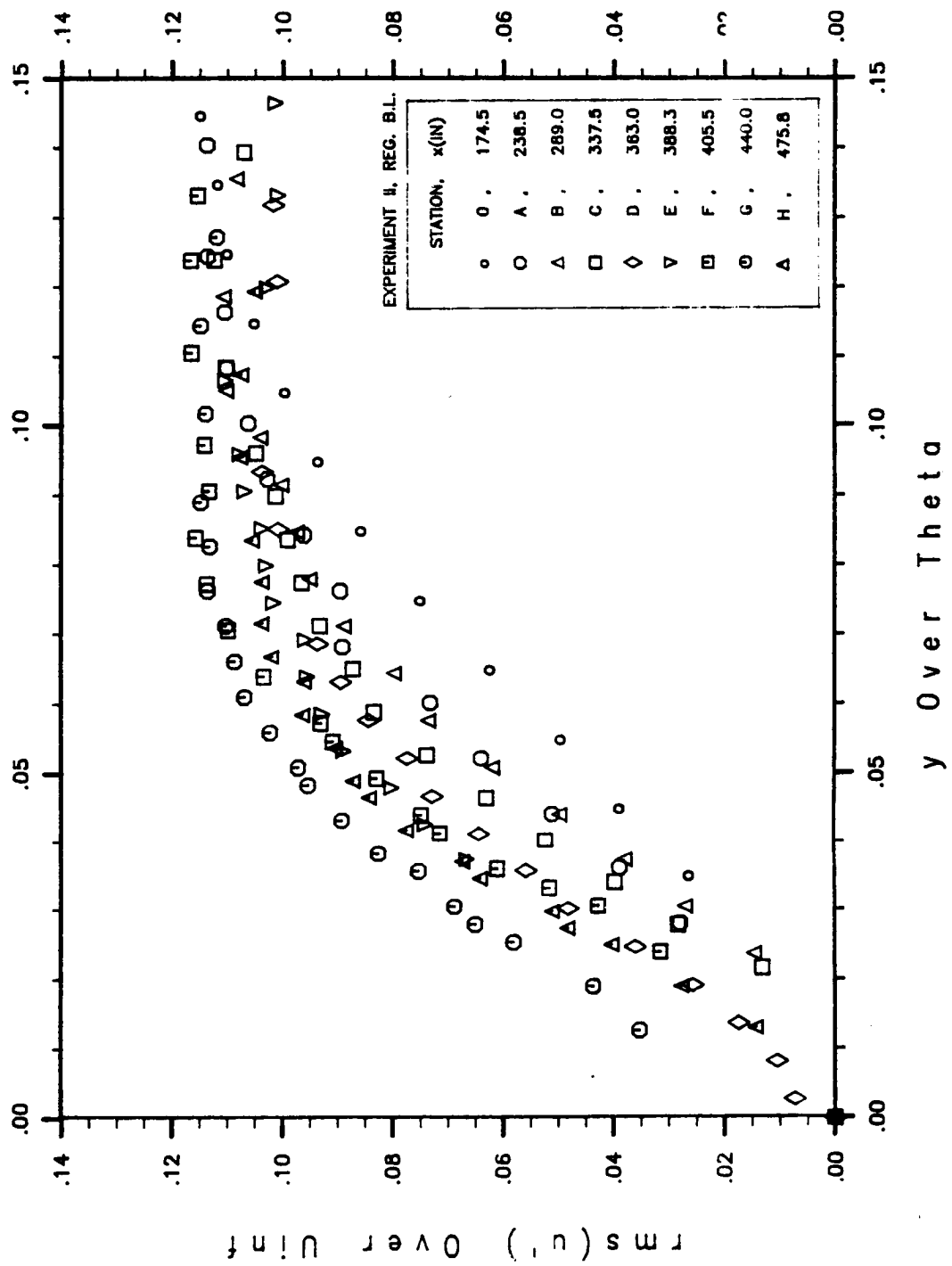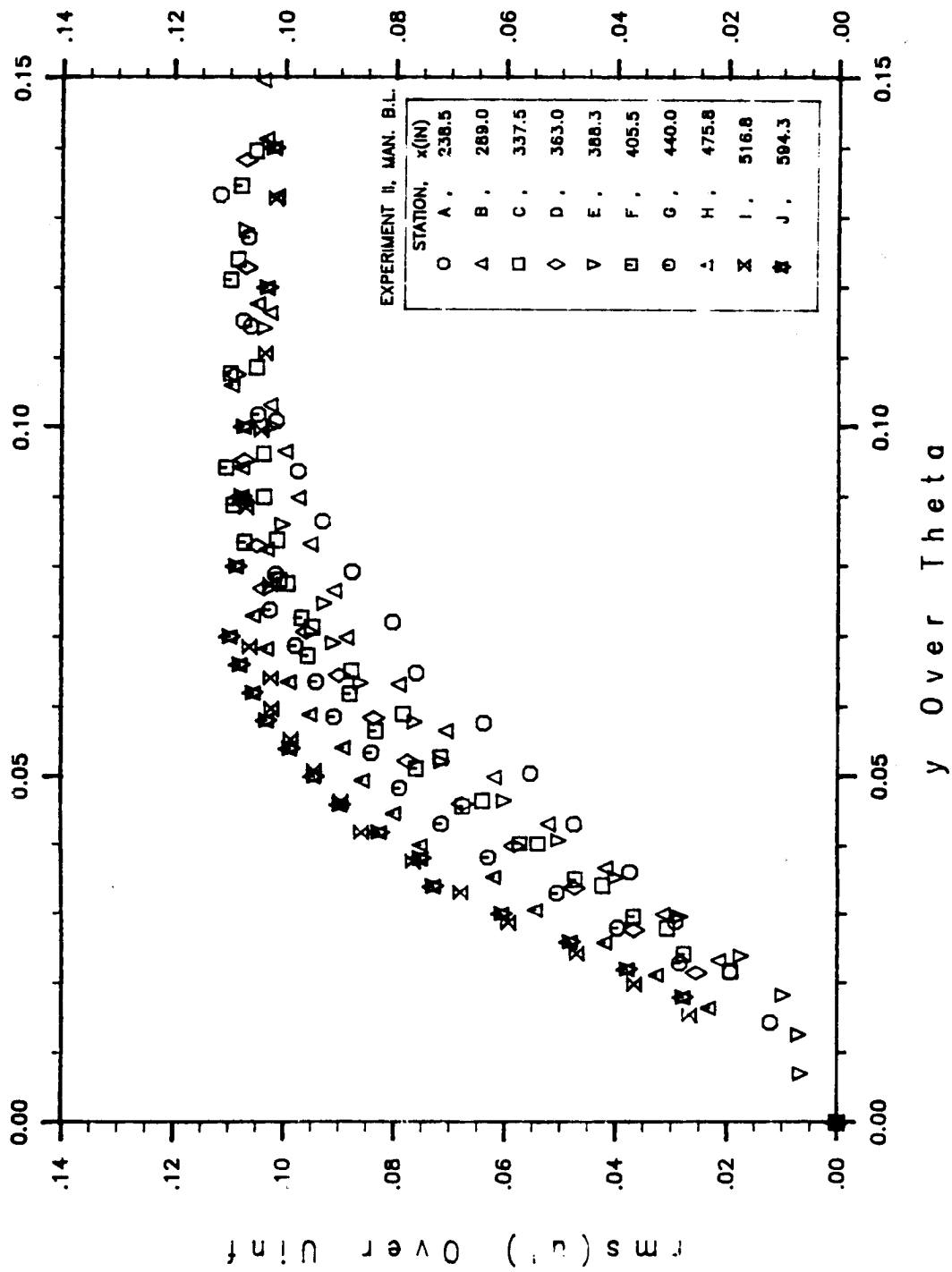
Figure 3.25 Near wall variation of rms(u')/U∞ vs y/θ at various streamwise stations in regular boundary layer from experiment II.

128
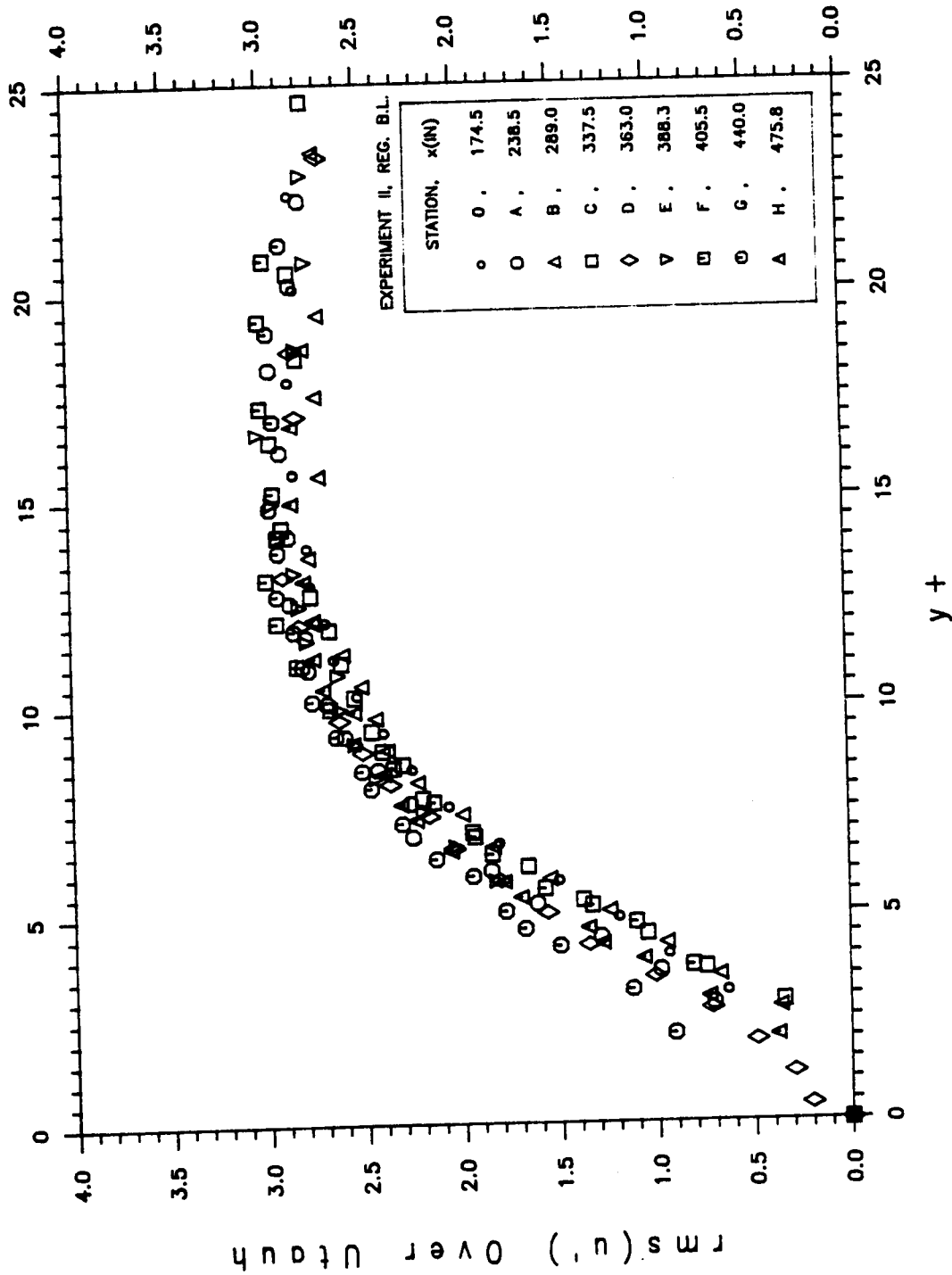
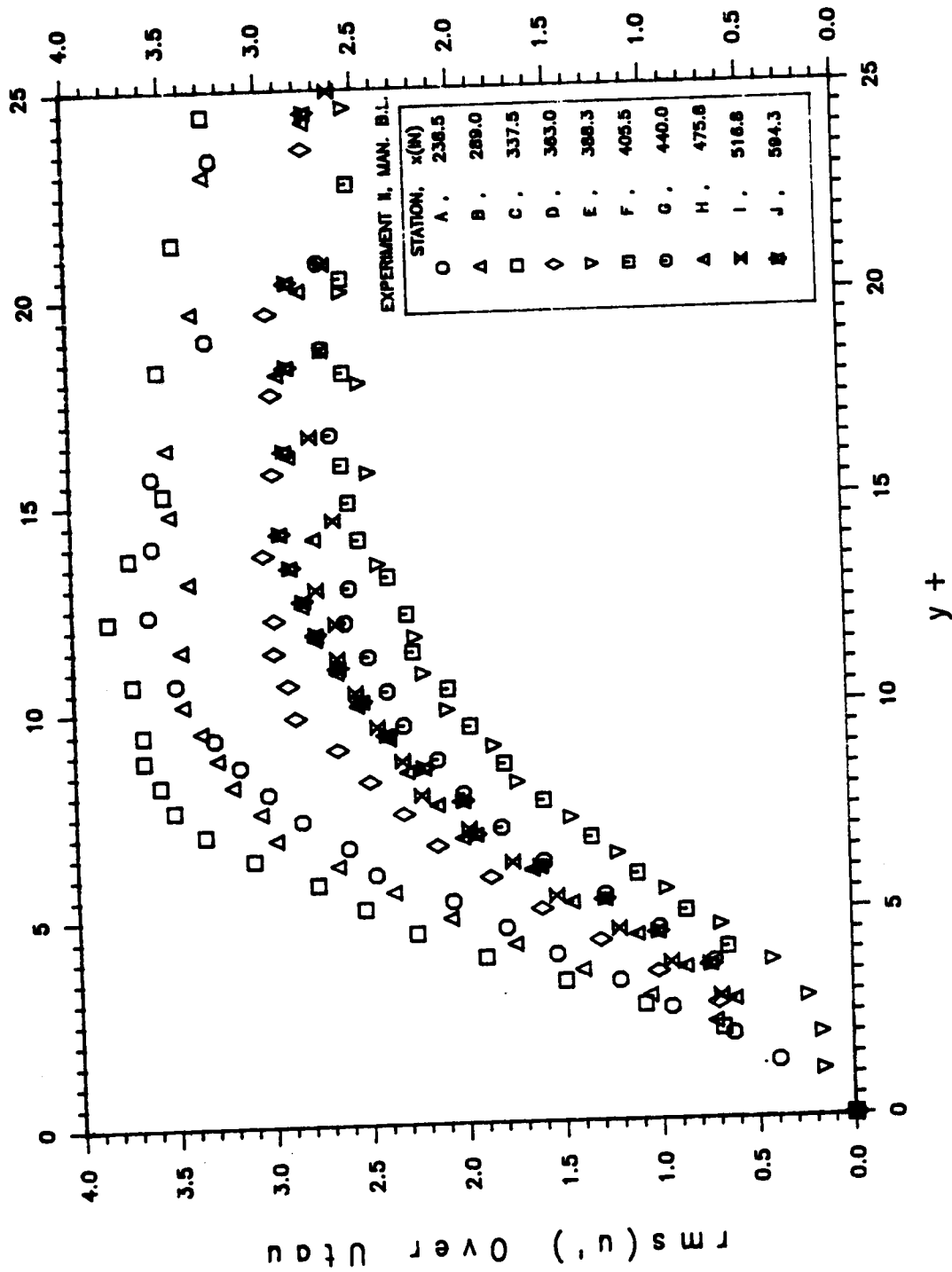Figure 3.26 Near wall variation of $rms(u')/u_{\tau\theta}$ vs $\rho y u_{\tau\theta}/\mu$ at various streamwise stations in regular boundary layer from experiment II.
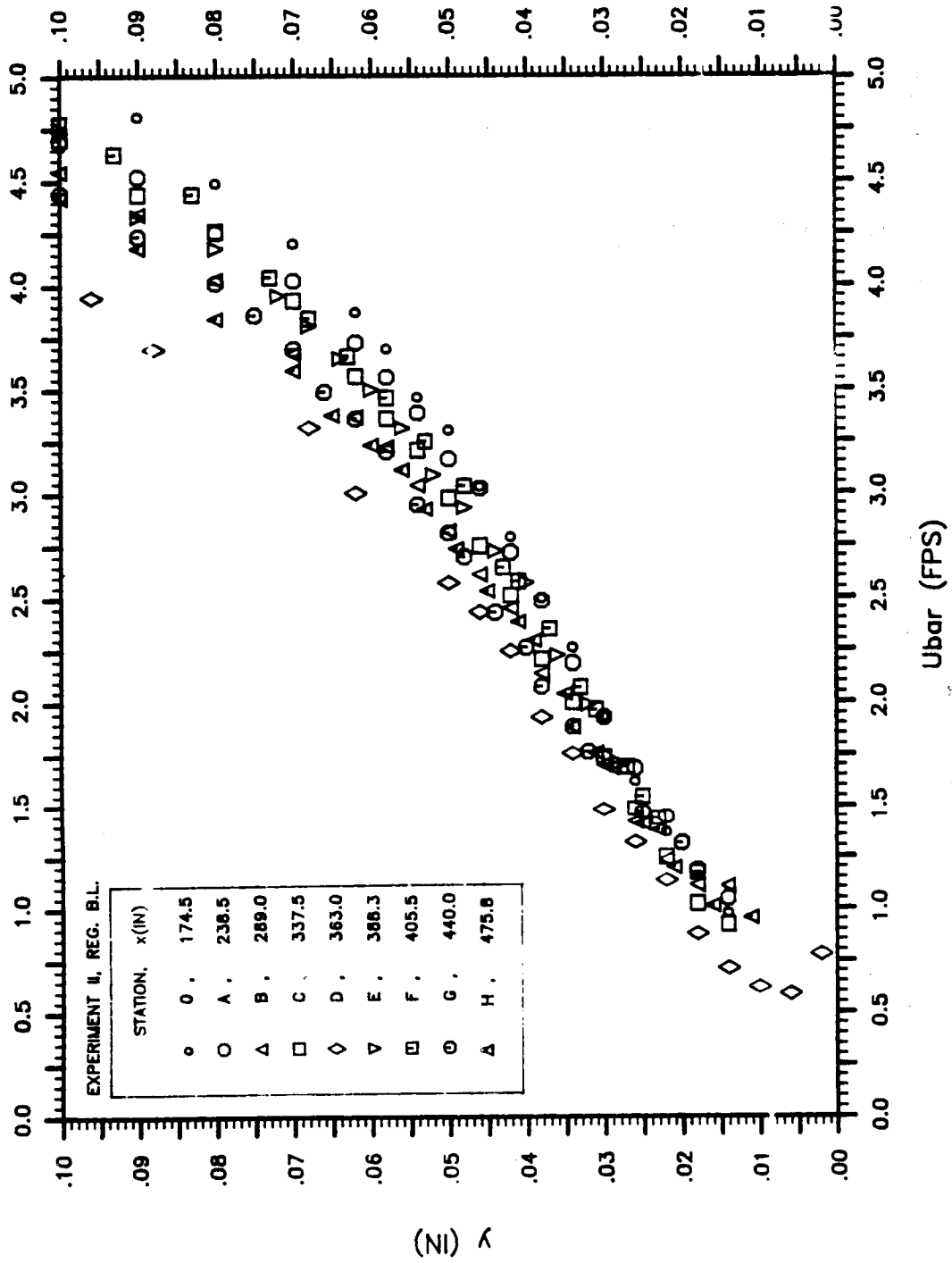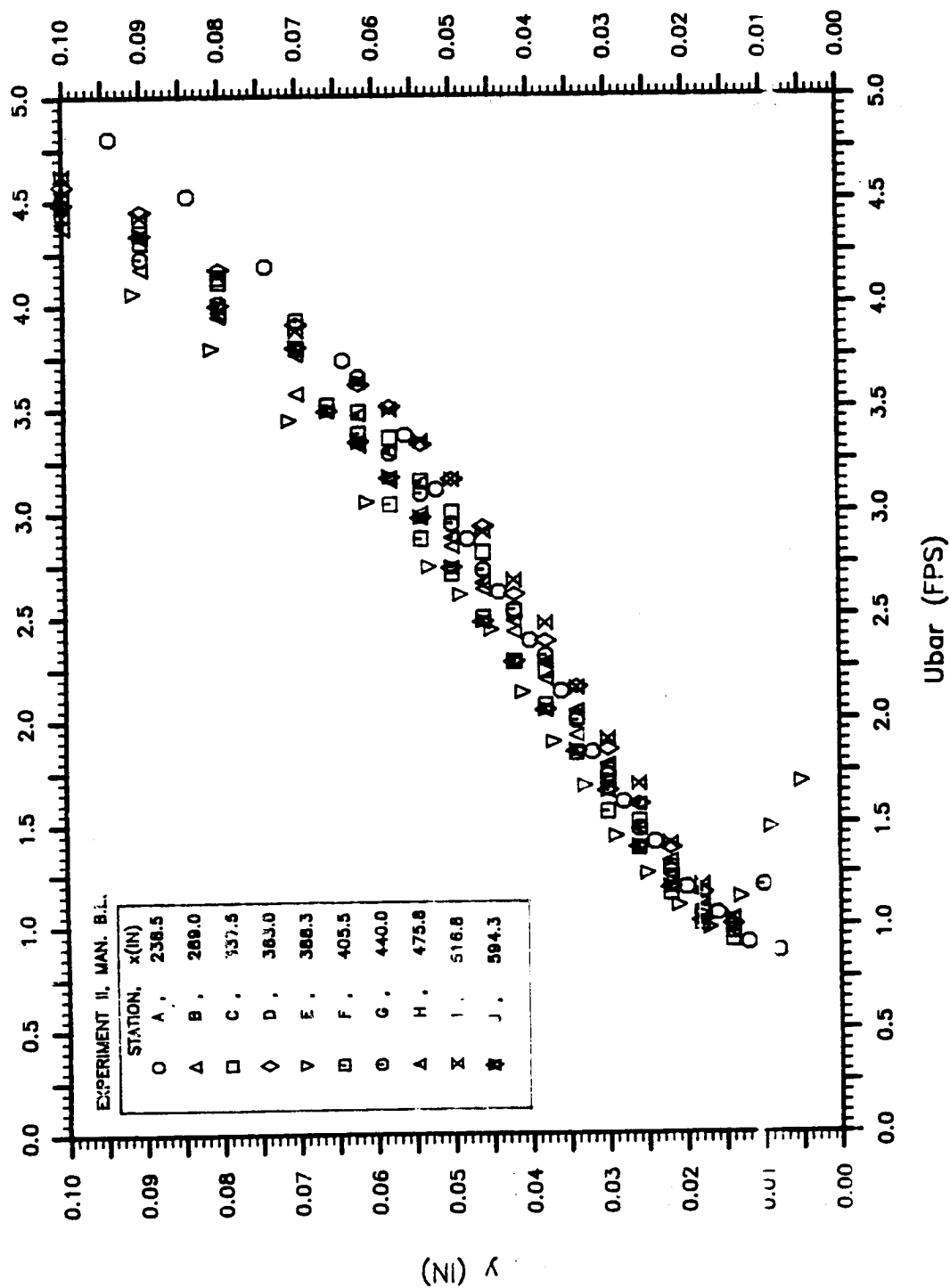
Figure 3.27 Near wall mean velocity profile (y vs U) at various streamwise stations in regular boundary layer from experiment II.
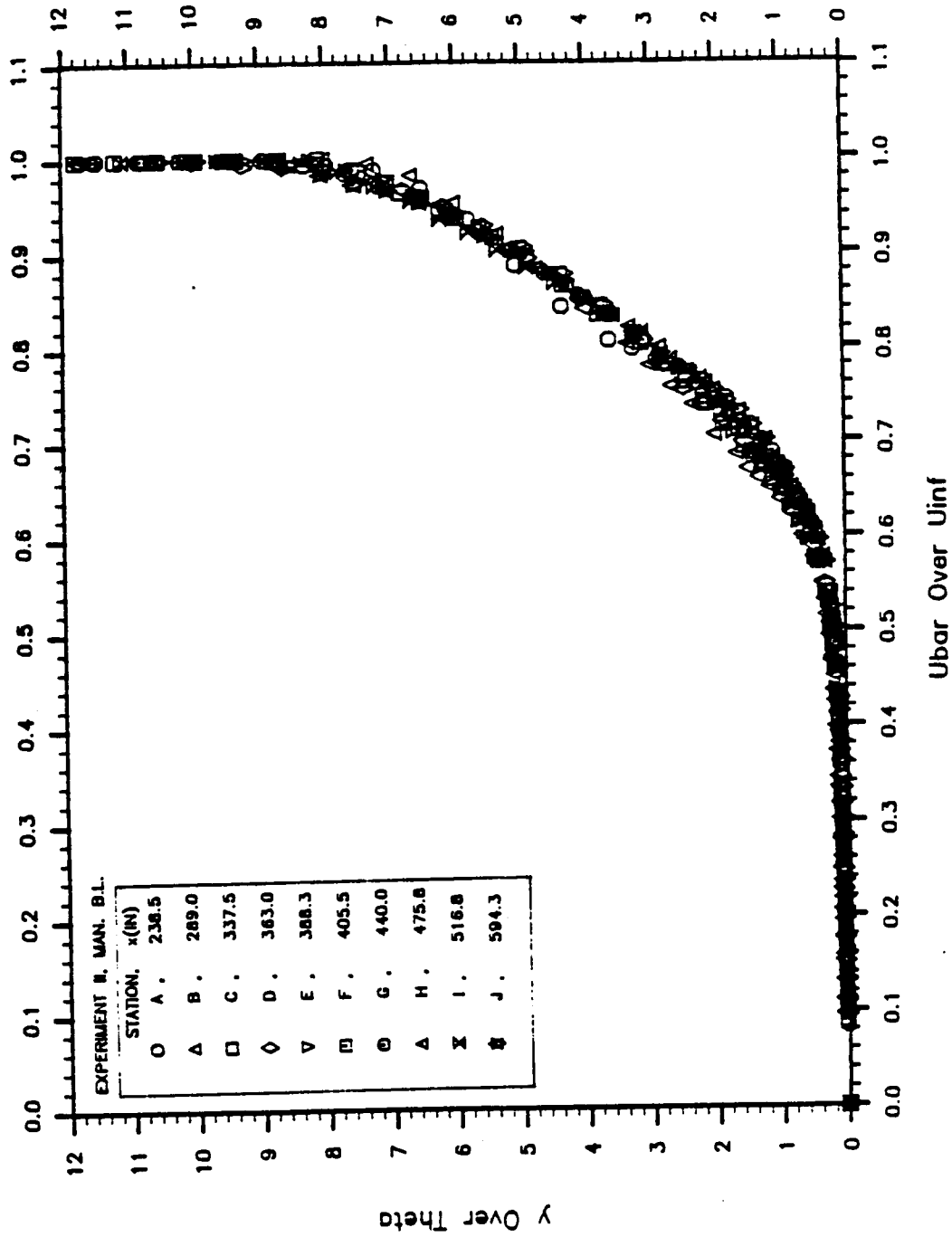
Figure 3.28 Non-dimensional mean velocity profiles (y/θ vs $\overline{U}/U_\infty$) at various streamwise stations in manipulated boundary layer from experiment 11.

Figure 3.29 Clauser plot for mean velocity profiles (U/U_∞ vs $\rho U_\infty y/\mu$) at various streamwise stations in manipulated boundary layer from experiment II.

132

Figure 3.30 Wall-unit non-dimensionalized mean velocity profiles ($\bar{U}/u_{\tau\theta}$ vs $\rho y u_{\tau\theta}/\mu$) at various streamwise stations in manipulated boundary layer from experiment II.

Figure 3.31 Variation of $(U_\infty - \bar{U})/u_{\tau\theta}$ vs $(yu_{\tau\theta}/\delta_d U_\infty)$ at various streamwise stations in manipulated boundary layer from experiment II.

134

Figure 3.32 Wake function profile (W vs y/δ) at various streamwise stations in manipulated boundary layer from experiment II. (Solid line : $W = 2Sin^2 (\pi y/2\delta)$)

Figure 3.33 Wall-unit non-dimensionalized fluctuating velocity profile (rms(u')/$u_{\tau\theta}$ vs $\rho y u_{\tau\theta}/\mu$) at various streamwise stations in manipulated boundary layer from experiment II.

Figure 3.34 Variation of rms(u')/U∞ vs y/θ at various streamwise stations in manipulated boundary layer from experiment II.

Figure 3.35 Near wall variation of rms(u')/U∞ vs y/θ at various streamwise stations in manipulated boundary layer from experiment II.

138

Figure 3.36 Near wall variation of rms(u')/u_τθ vs ρyu_τθ/μ] at various streamwise stations in manipulated boundary layer from experiment II.

Figure 3.37 Near wall mean velocity profiles (y vs U) at various streamwise stations in manipulated boundary layer from experiment II.
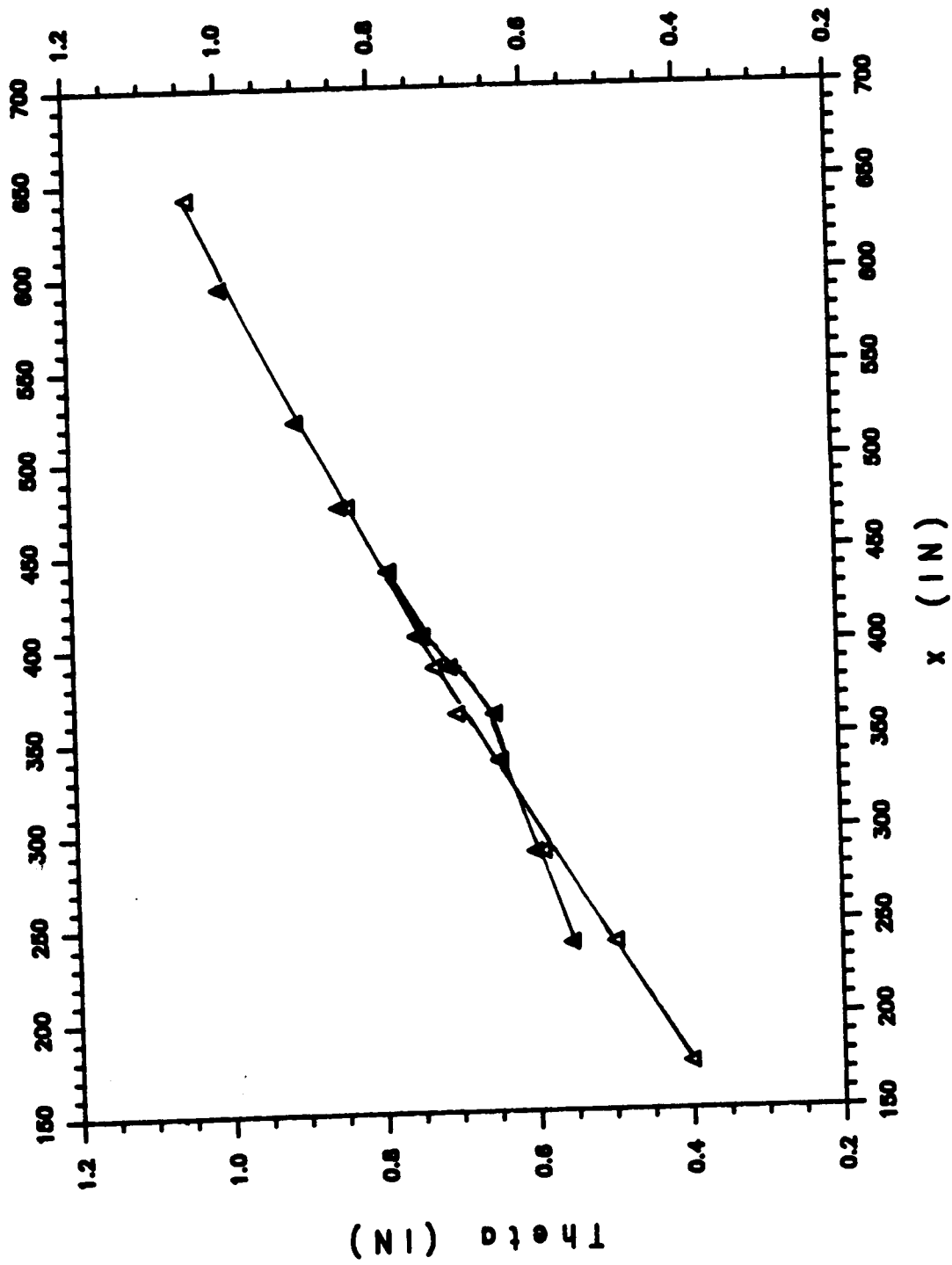
Figure 3.38 Comparison of streamwise momentum thickness distributions (θ vs x) for regular (open) and manipulated (filled) boundary layers from experiment II.
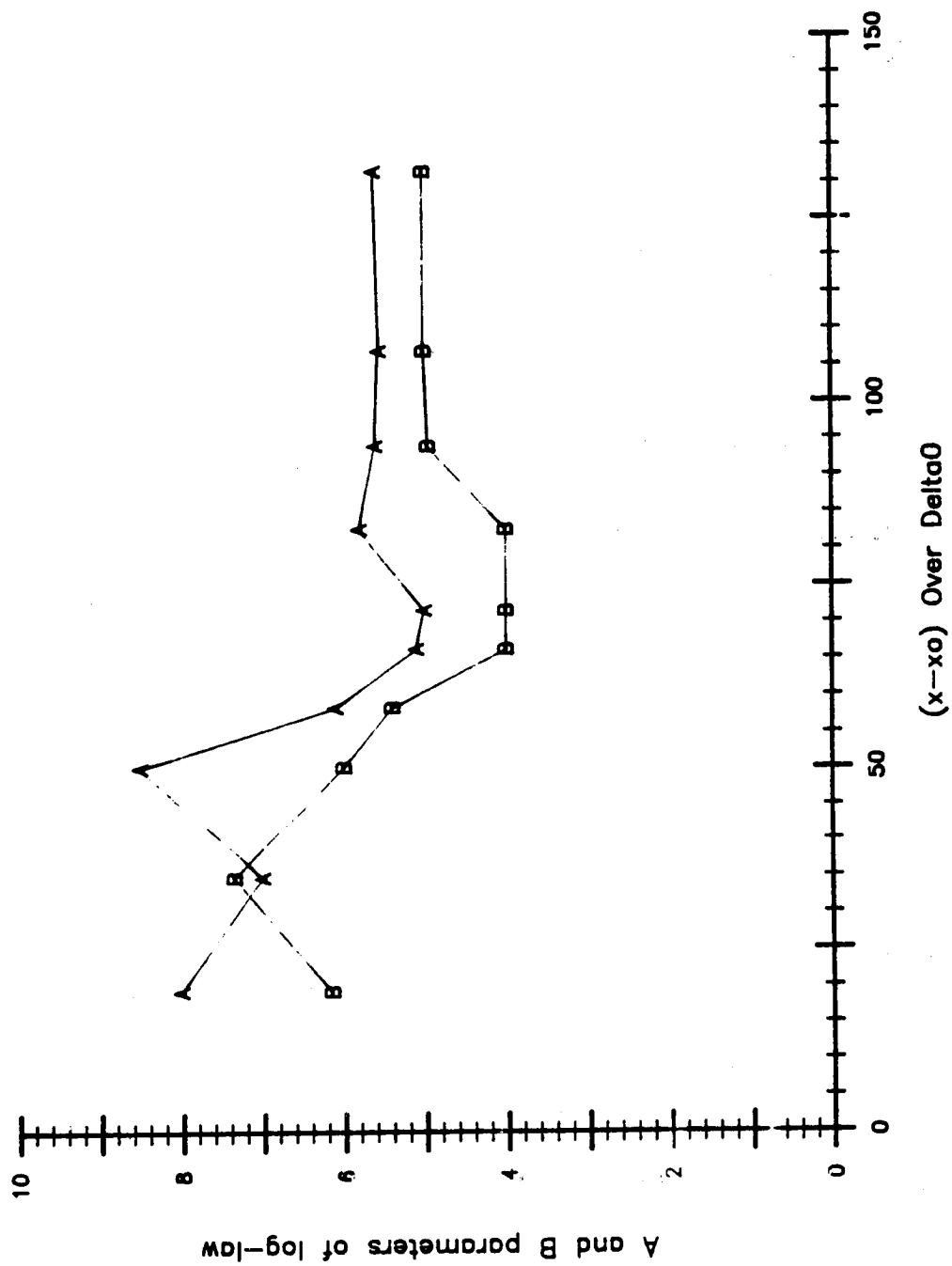
Figure 3.39 Streamwise variation of "law of the wall" ($u^+ = A\log_{10}(y^+) + B$) parameters (A and B) in manipulated boundary layers from experiment II.
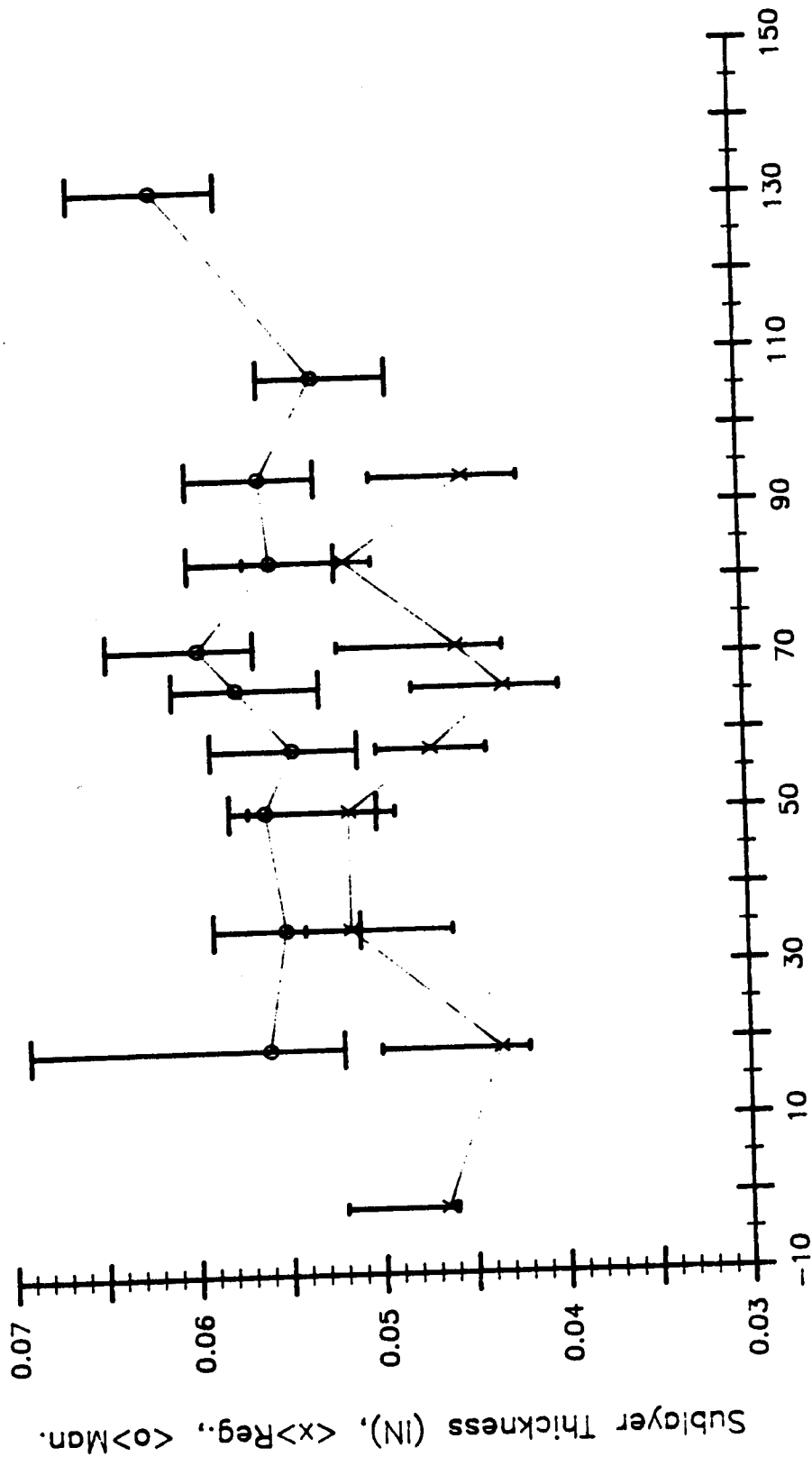
Figure 3.40 Comparison of streamwise sublayer thickness distribution (δ_{sl} vs ξ) in regular (x), and manipulated (o) boundary layers.
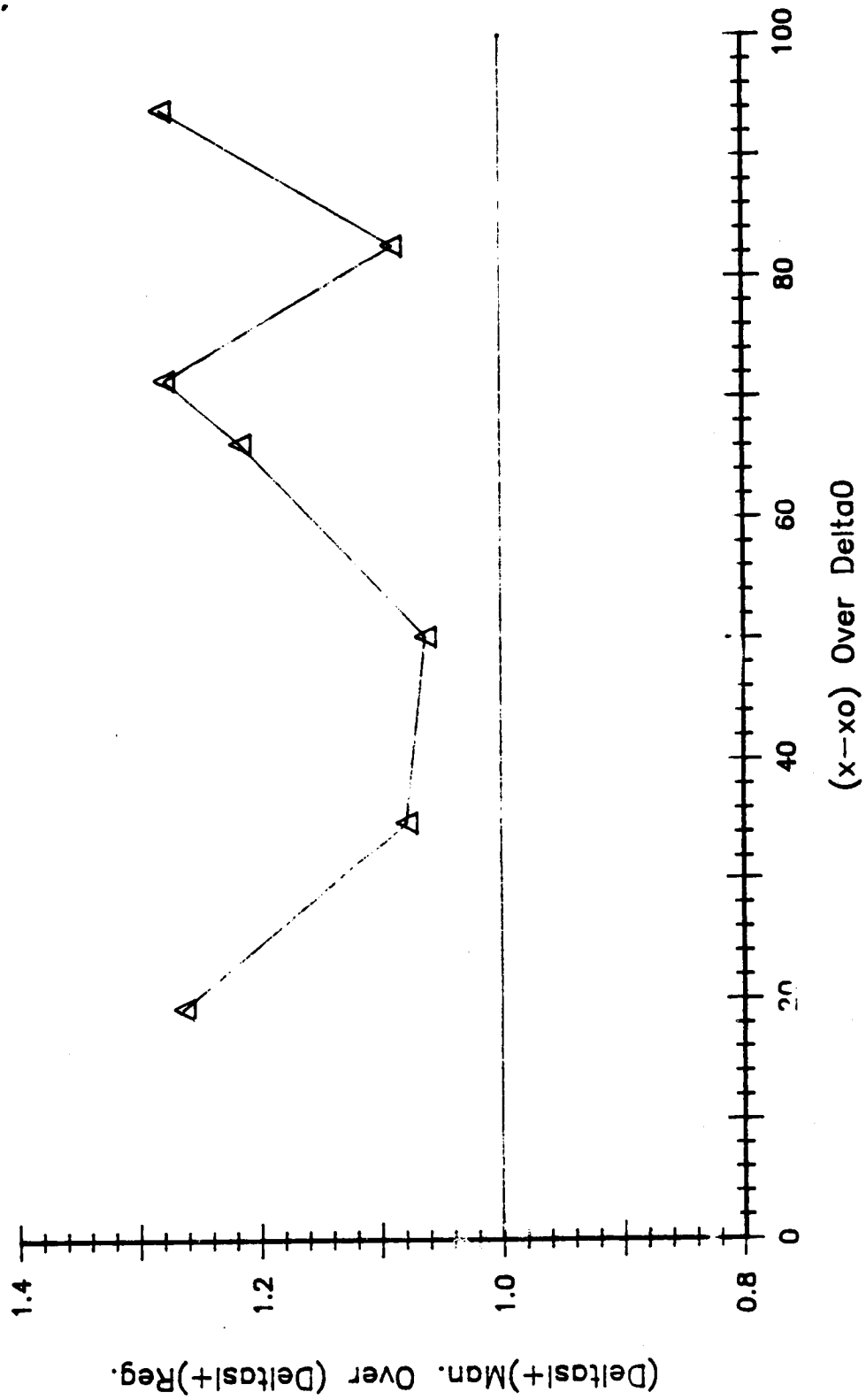
Figure 3.41 Wall-unit non-dimensionalized ratio of sublayer thickness
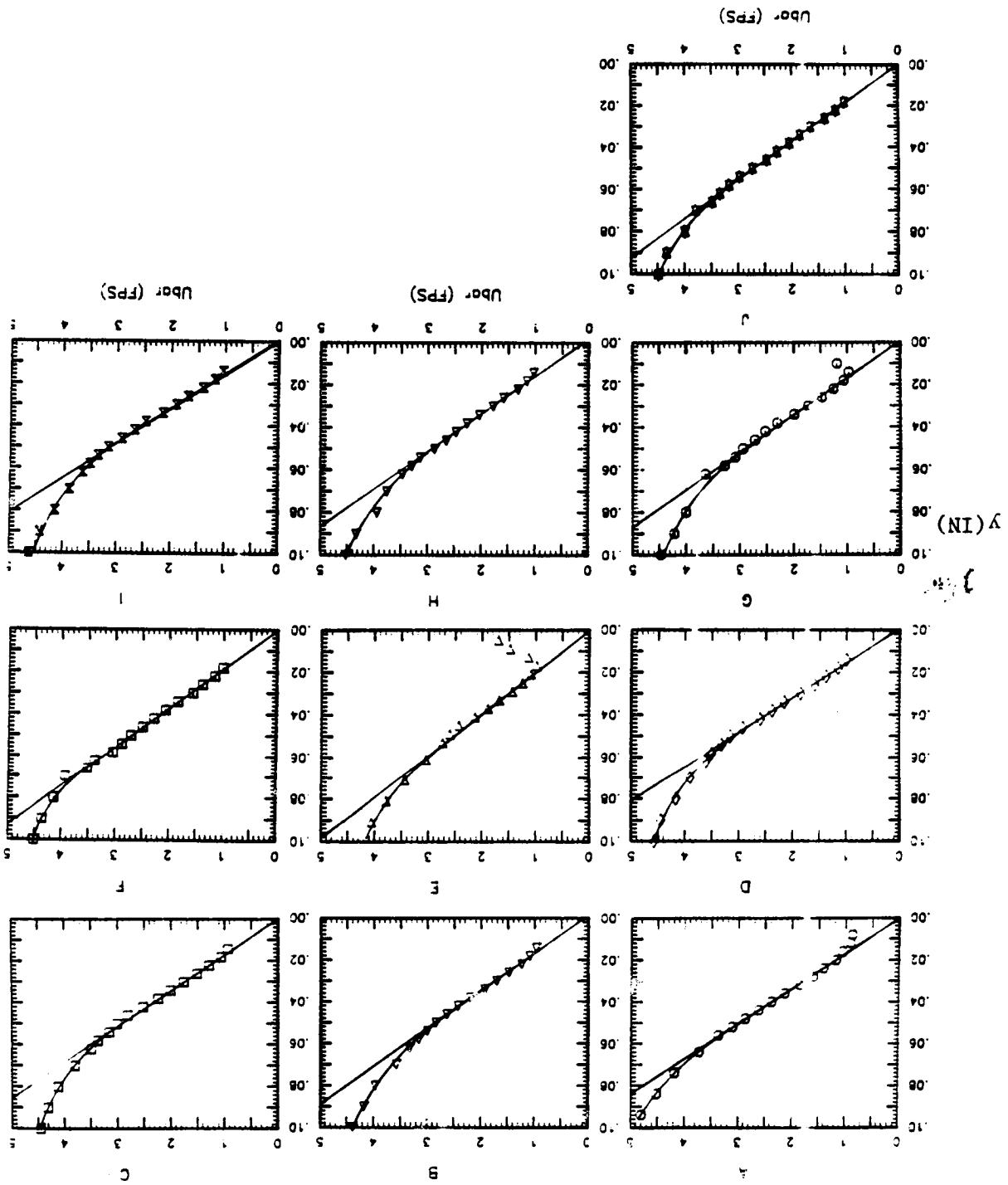$[\rho\delta_{sl}u_{\tau n}/\mu]_{man.}/[\rho\delta_{sl}u_{\tau n}/\mu]_{reg.}$ vs ξ.

144
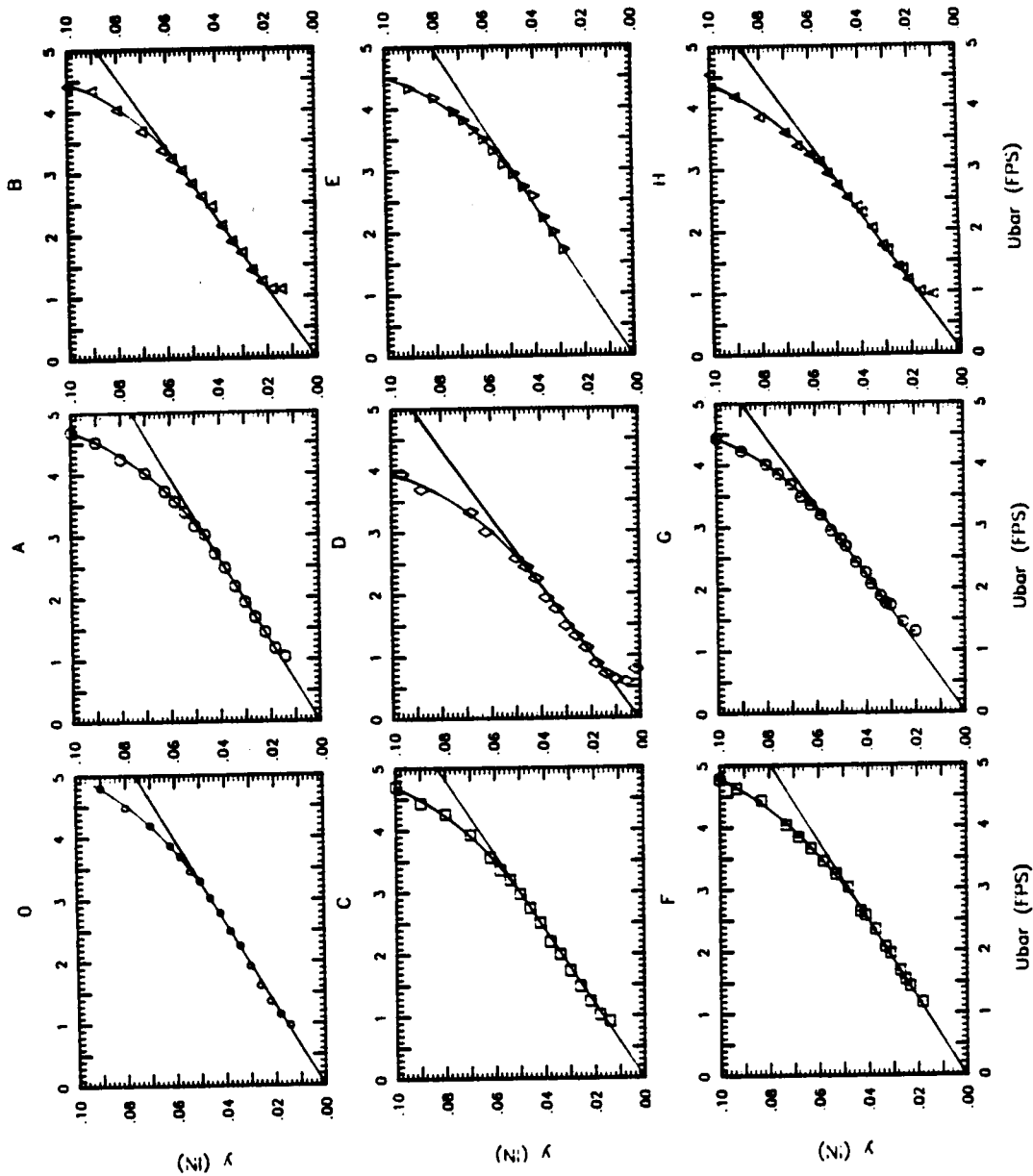
Figure 3.42 Near wall mean velocity profile (y vs U) at various streamwise stations (O, A–H) used to measure the $d\bar{U}/dy_w$ and the sublayer thickness in regular boundary layer from experiment II.
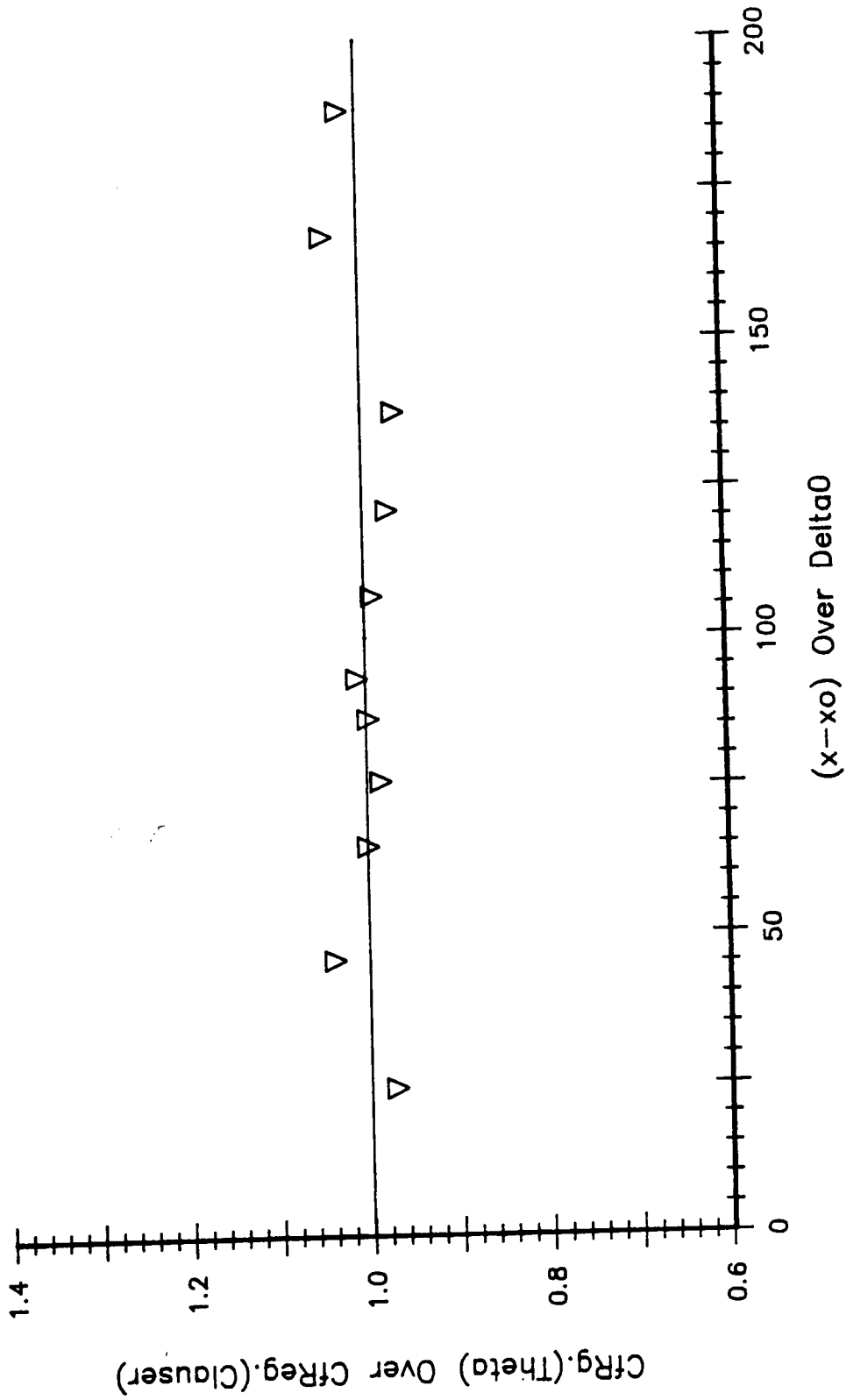
145

Figure 3.43 Near wall mean velocity profile (y (In.) vs vs U) at various streamwise stations (A-J) used to measure the $d\overline{U}/dy_w$ and the sublayer thicknes in manipulated boundary layer from experiment II.

Figure 3.44 Streamwise variation of the $C_{f\theta}/C_{fc}$ in regular boundary layer for experiment I.
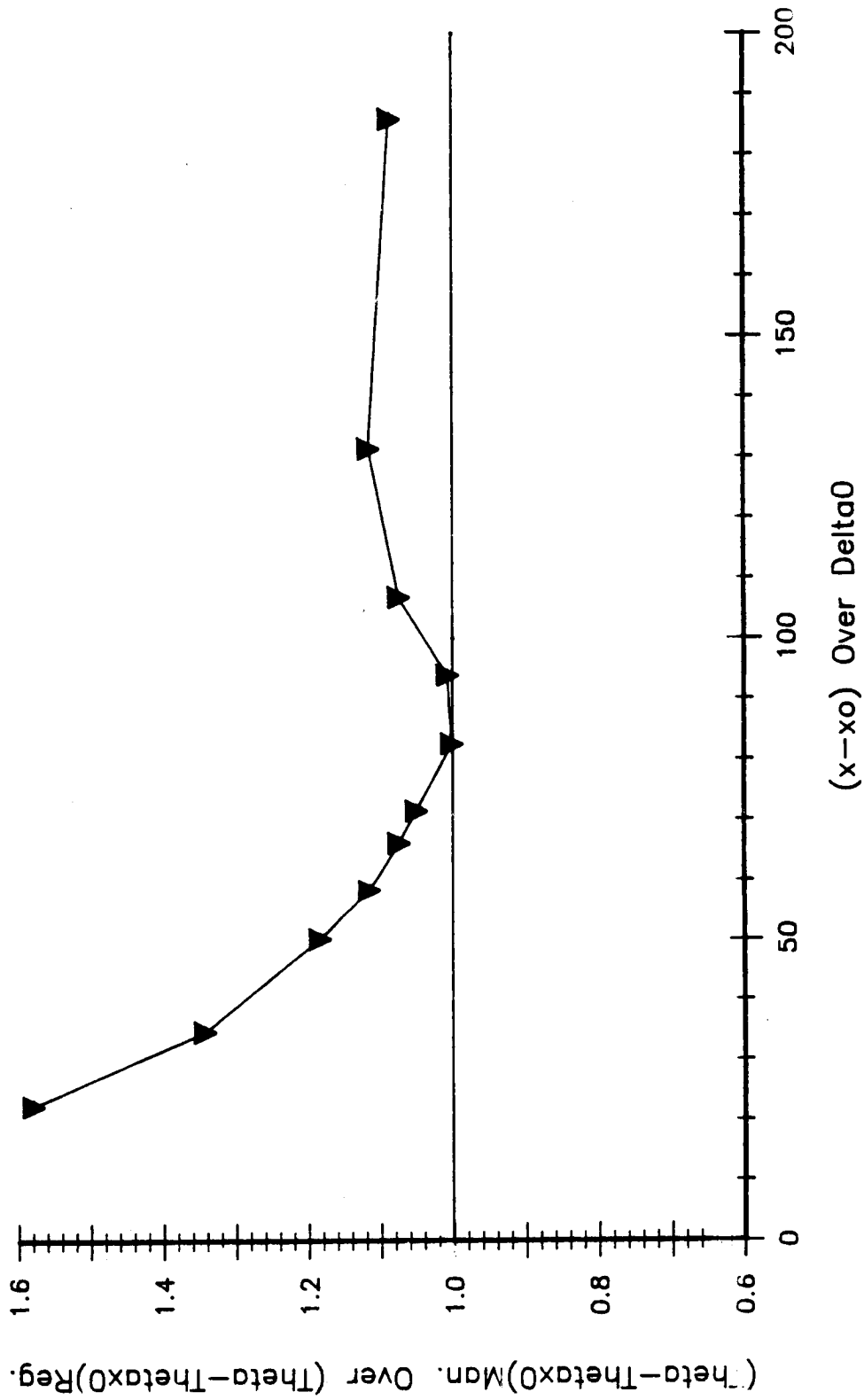
Figure 3.45 Streamwise variation of the non-dimensional net drag ratio (NDR) $(\Theta - \Theta_0)_{Man.}/(\Theta - \Theta_0)_{Reg.}$, for experiment I.
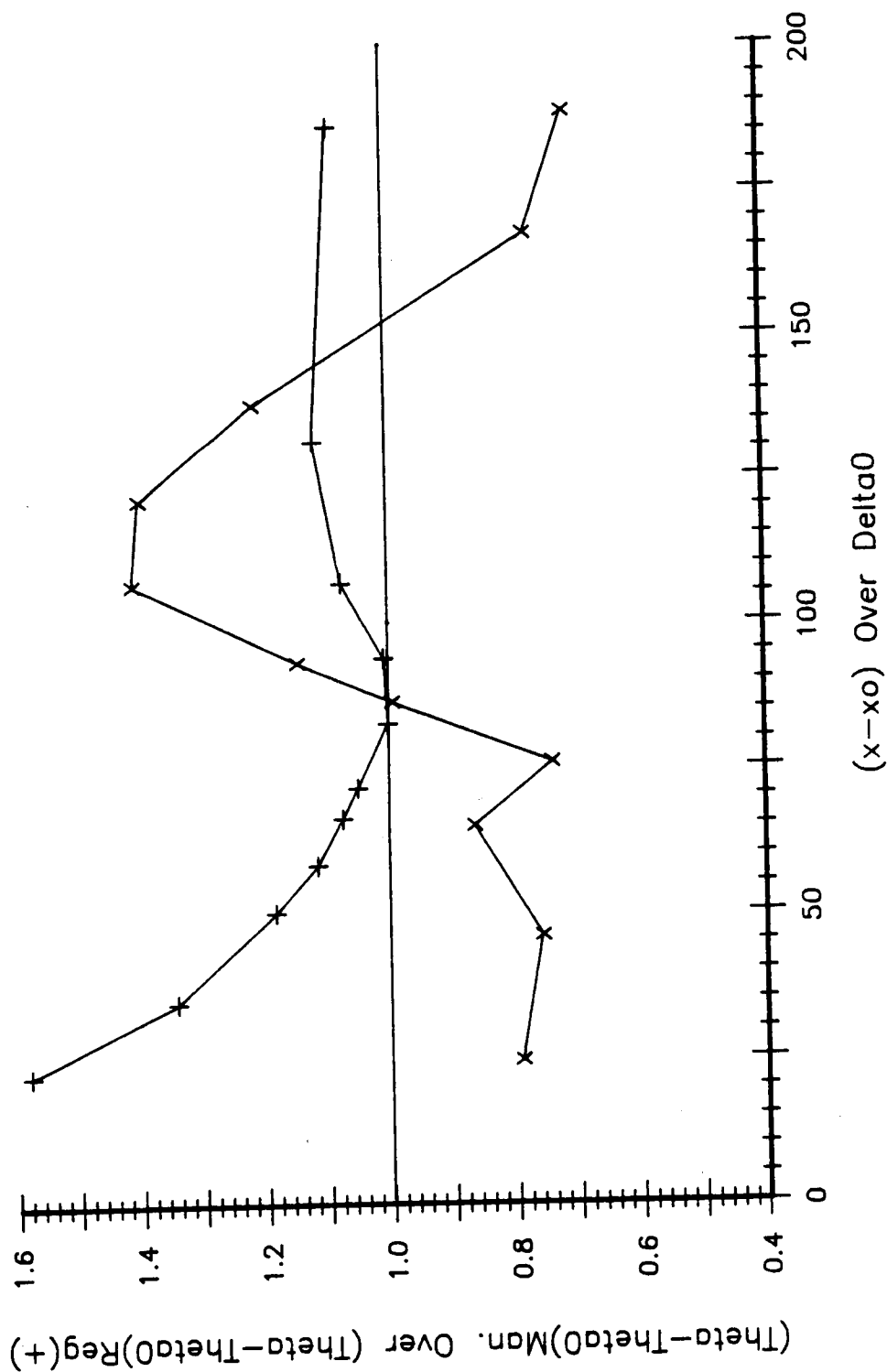
Figure 3.46 Comparison between streamwise variation of the non-dimensional net drag ratio (NDR) $(\Theta - \Theta_o)_{Man.}/(\Theta - \Theta_o)_{Reg.}$ (+), and the local skin friction ratio $(C_{f\Theta})_{Man.}/(C_{f\Theta})_{Reg.}$ (x) both obtained from momentum balance in experiment I.
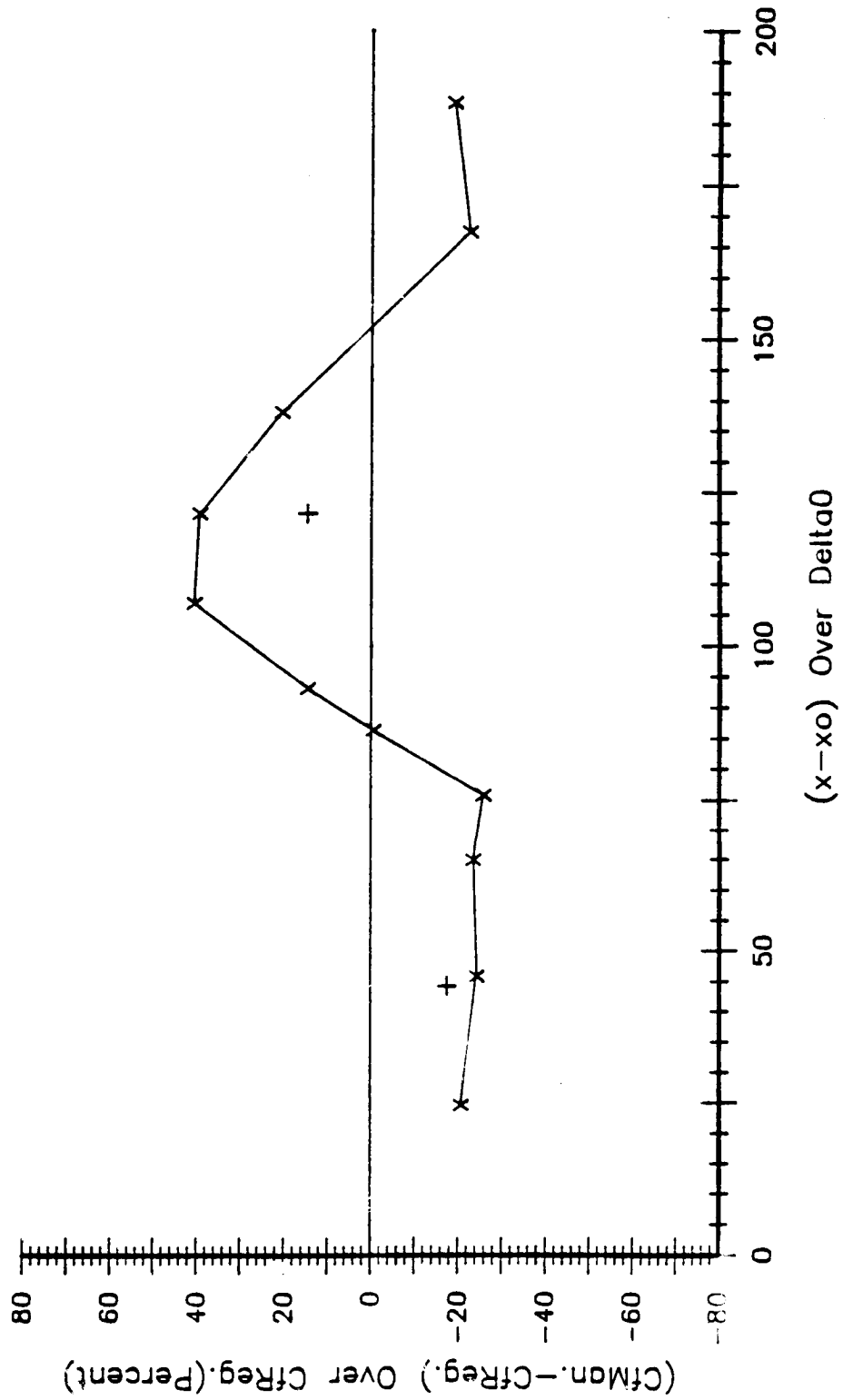
Mom. Bal. (x), dUdy at Wall (+)

(x-xo) Over Delta0

Figure 3.47 Comparison between streamwise percent variation of $(C_{fMan.} - C_{fReg.}) / C_{fReg.}$ from momentum balance (x), and from slope of mean velocity pofile at the wall $(d\bar{U}/dy_w)$ (+) in experiment I.
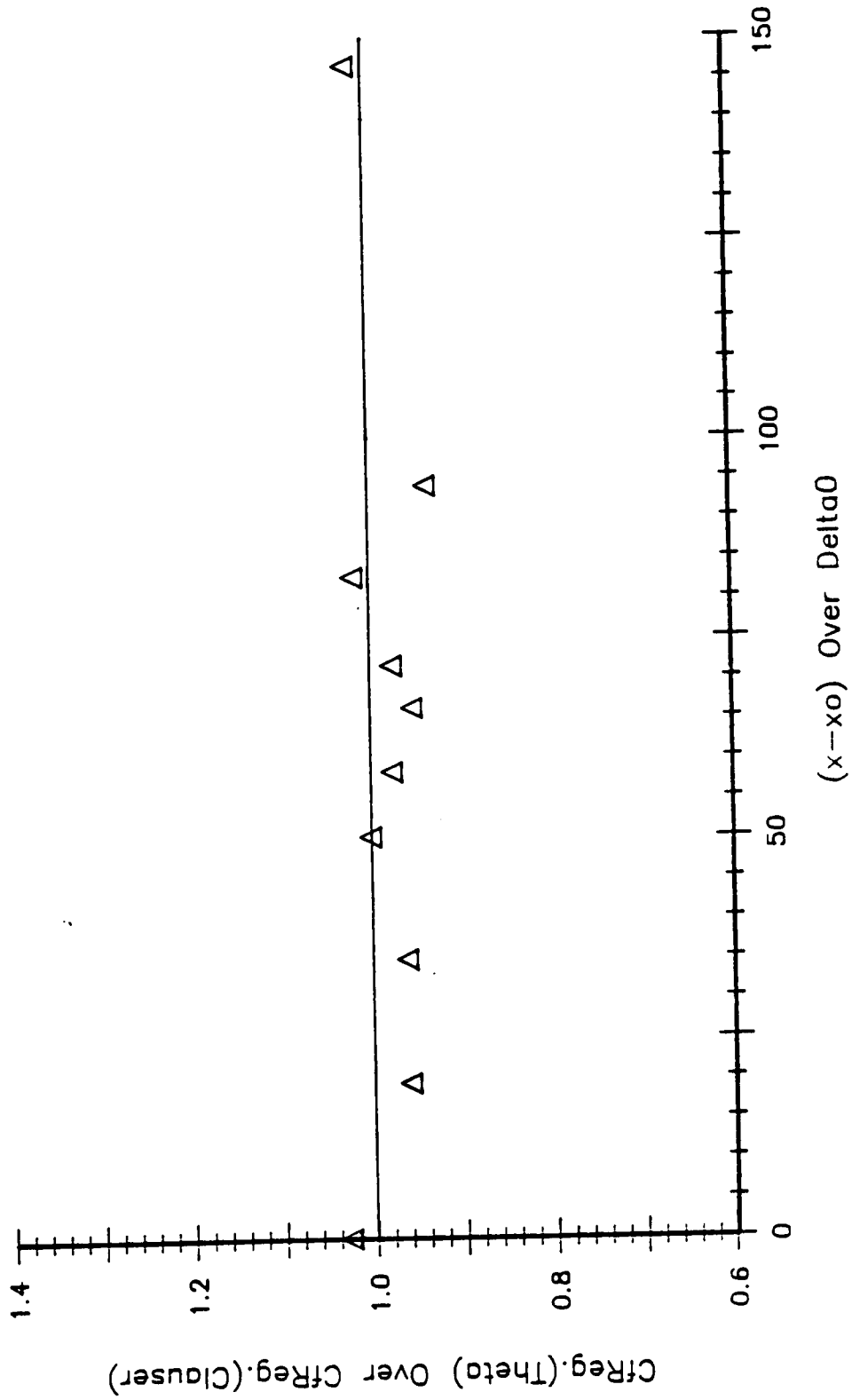
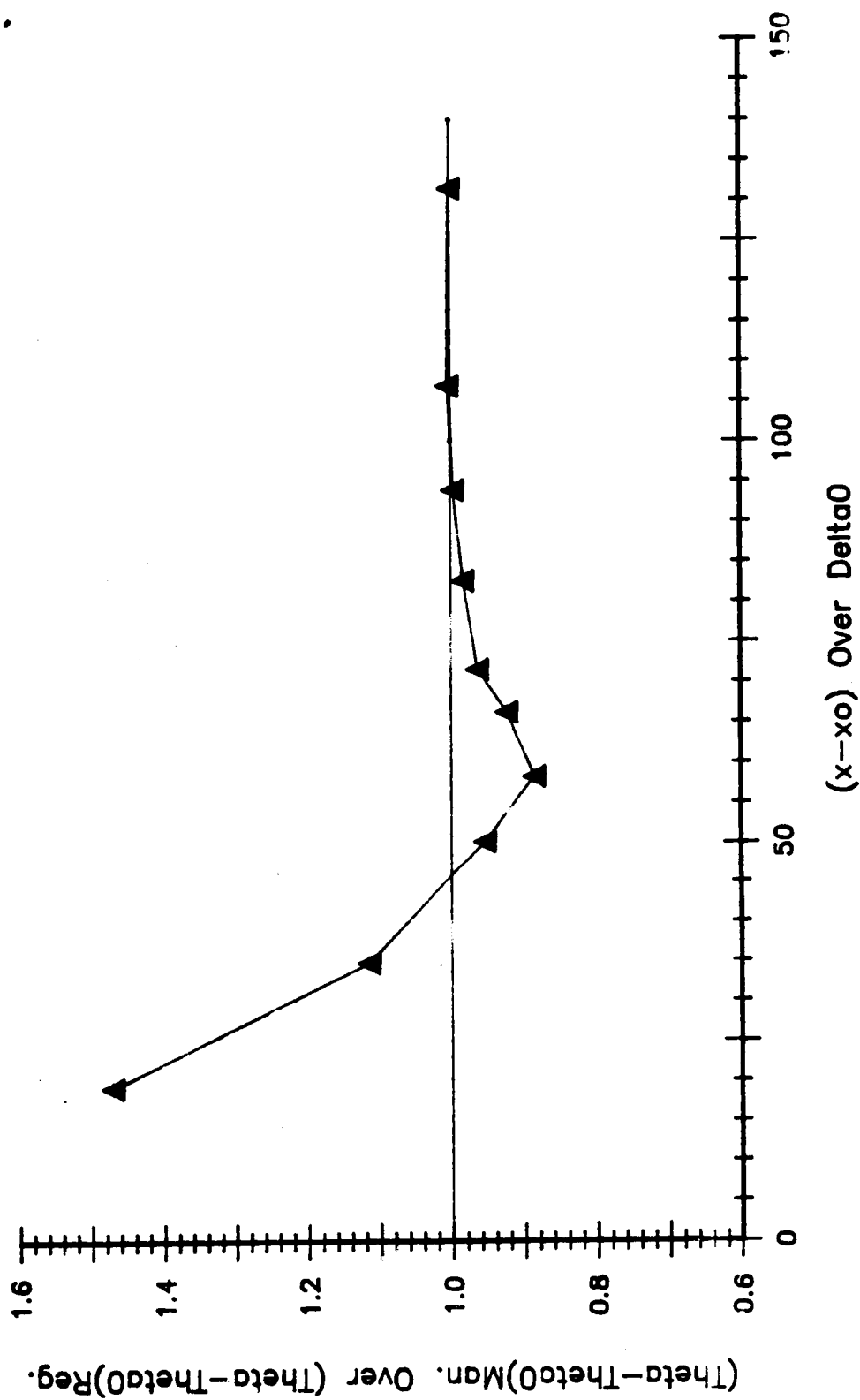Figure 3.48 Streamwise variation of the $C_{f\theta}/C_{fc}$ in regular boundary layer for experiment II.

Figure 3.49 Streamwise variation of the non-dimensional net drag ratio (NDR) $(\theta - \theta_o)_{Man.}/(\theta - \theta_o)_{Reg.}$ for experiment II.
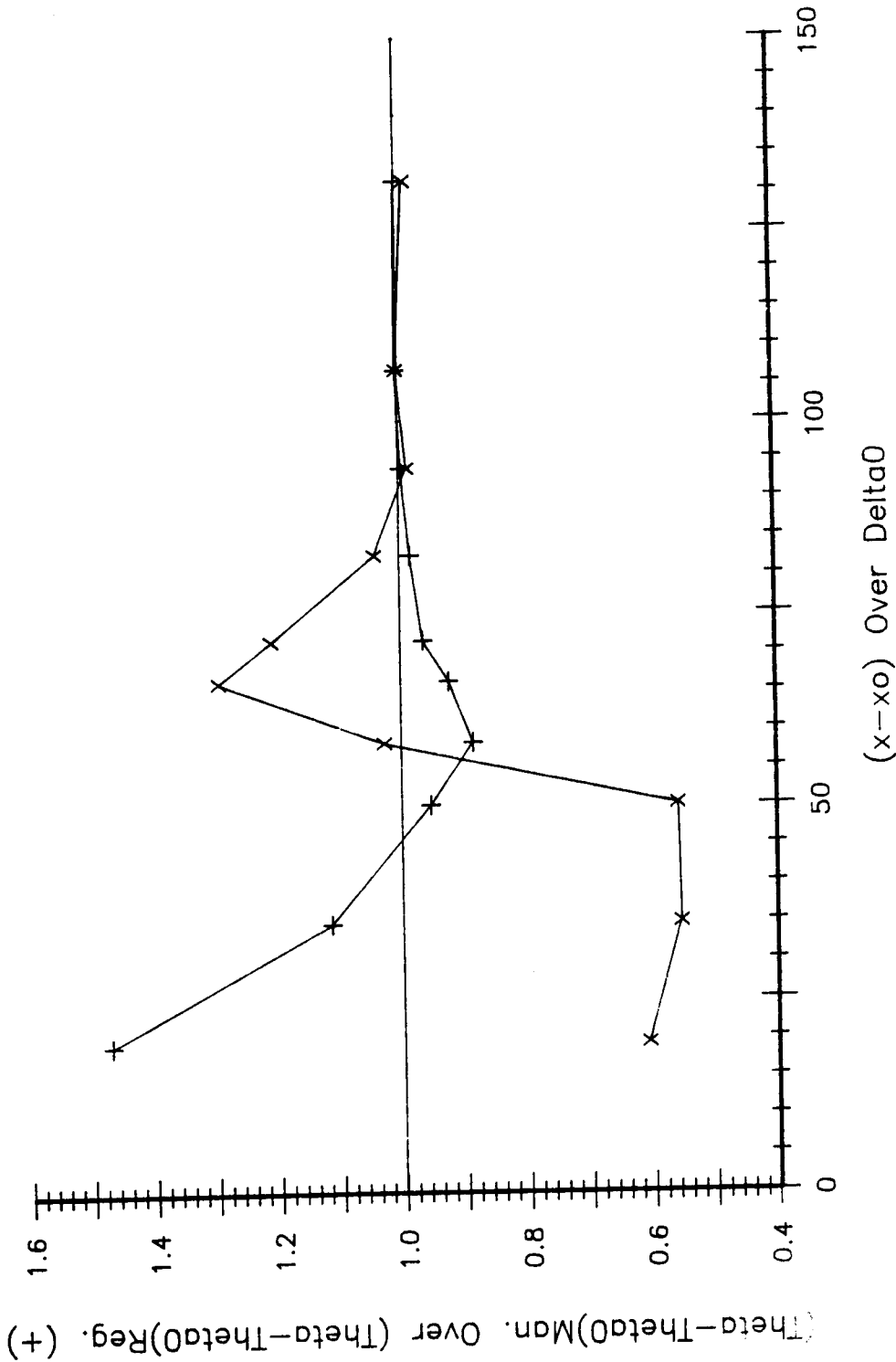
Figure 3.50 Comparison between streamwise variation of the non-dimensional net drag ratio (NDR) $(\theta - \theta_0)_{Man.}/(\theta - \theta_0)_{Reg.}$ (+), and the local skin friction ratio $(C_{f\theta})_{Man.}/(C_{f\theta})_{Reg.}$ (x) both obtained from momentum balance in experiment II.
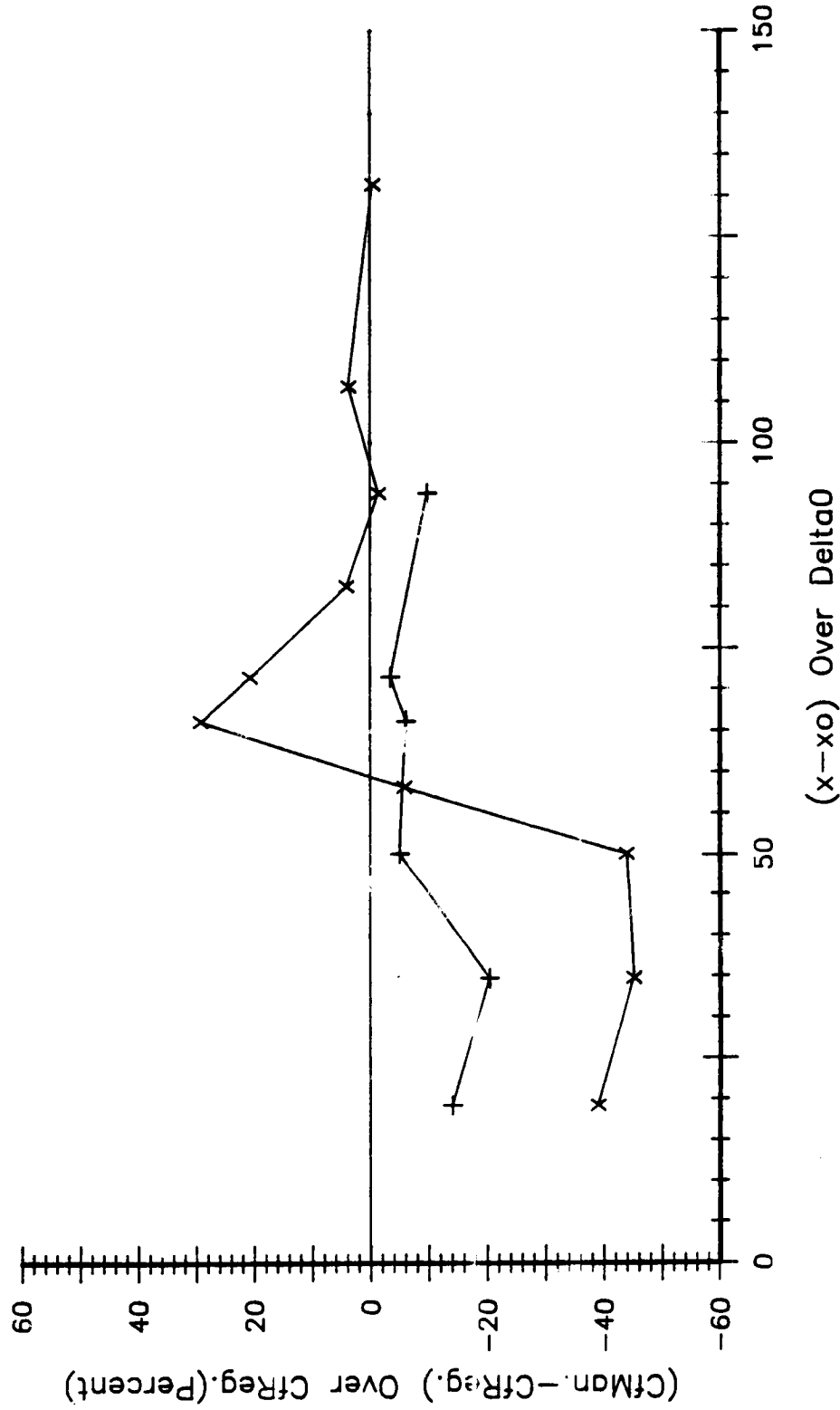
Figure 3.51 Comparison between streamwise percent variation of $(C_{fMan.} - C_{fReg.}) / C_{fReg.}$ from momentum balance (x), and from slope of mean velocity at the wall $(d\bar{U}/dy_w)$ (+) in experiment II.

154
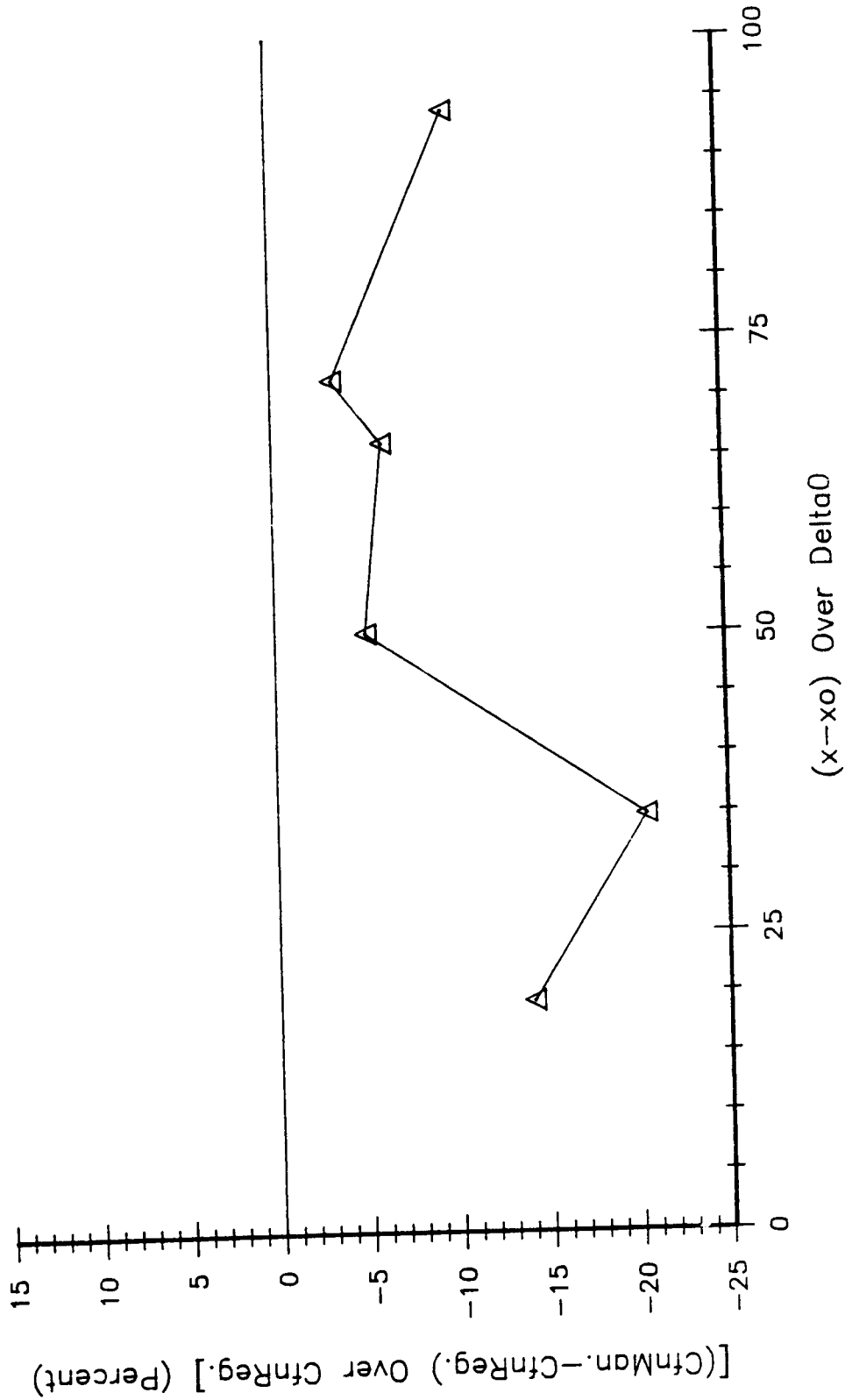
Figure 3.52 Streamwise percent variation of $(C_{fnMan.} - C_{fnReg.}) / C_{fnReg.}$ obtained from slope of mean velocity at the wall $(d\bar{U}/dy_w)$s in experiment II.
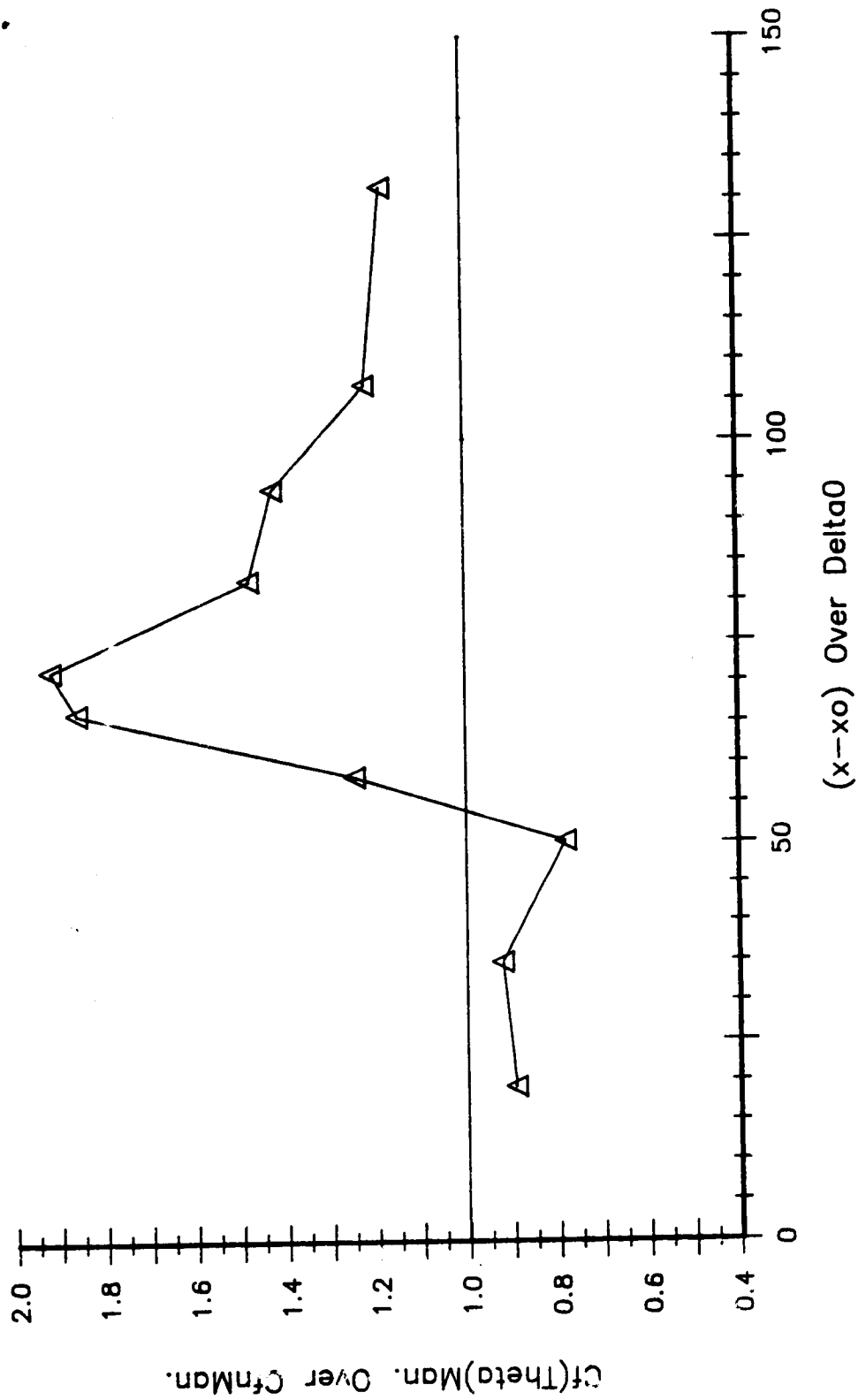
Figure 3.53 Streamwise variation of ratio $(C_{f\theta})_{Man.} / (C_{fn})_{Man.}$ obtained in manipulated boundary layer in experiment II.

FLOW

Figure 3.54   A snap-shot of the turbulent boundary layer downstream of the second manipulator plate.   (Flow is from right to left).

←FLOW
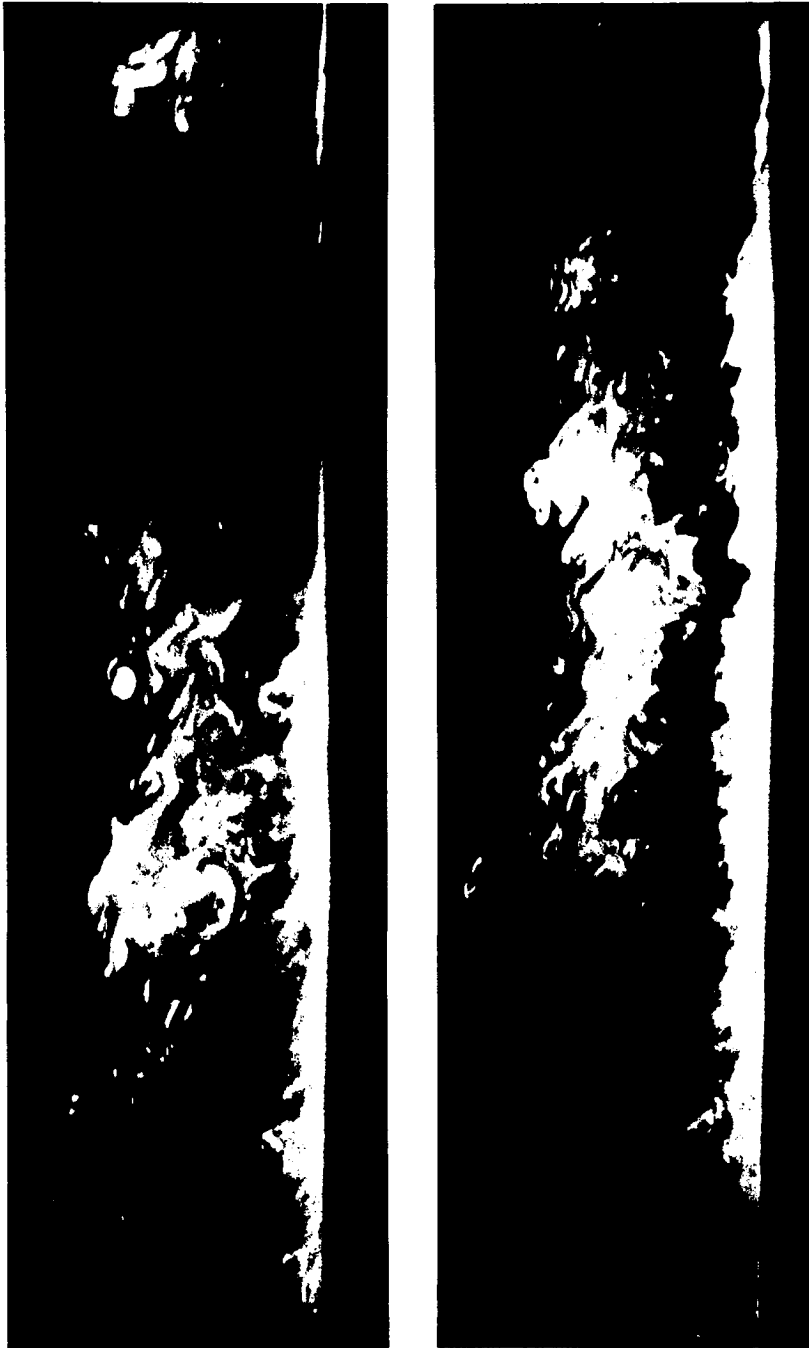
Figure 3.55 Snap-shots of manipulators wake interaction with wall-layer fluid upstream plate in place (top), and both plates in place (bottom) at $S = 20$ (center of the pictures).

← FLOW
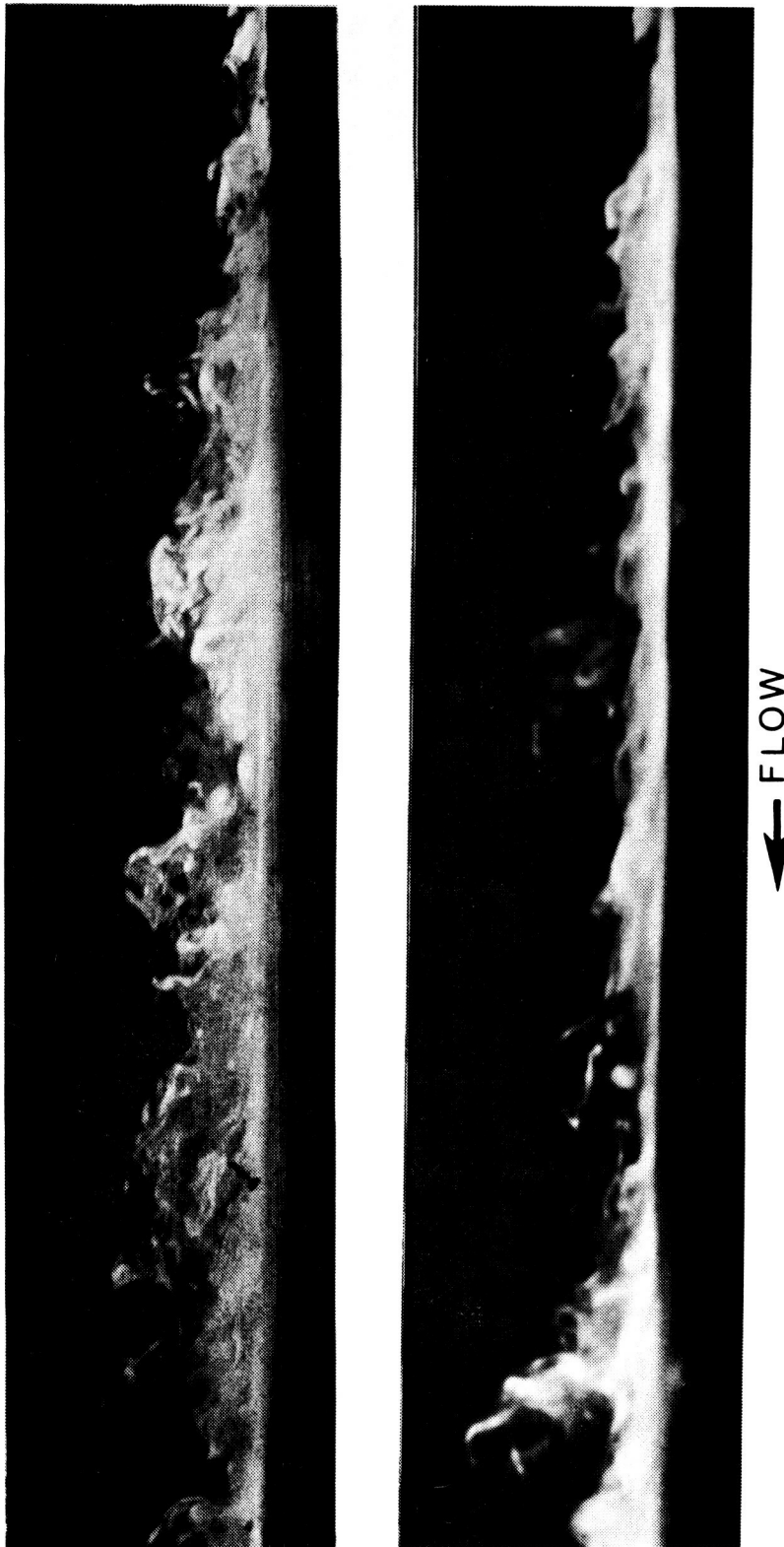
Figure 3.56 Snap-shots of wall-layer normal transport of fluid marker (TiCl$_4$) into outer region at ξ = 20 (center of the pictures), regular (top), and manipulated (bottom) boundary layers.
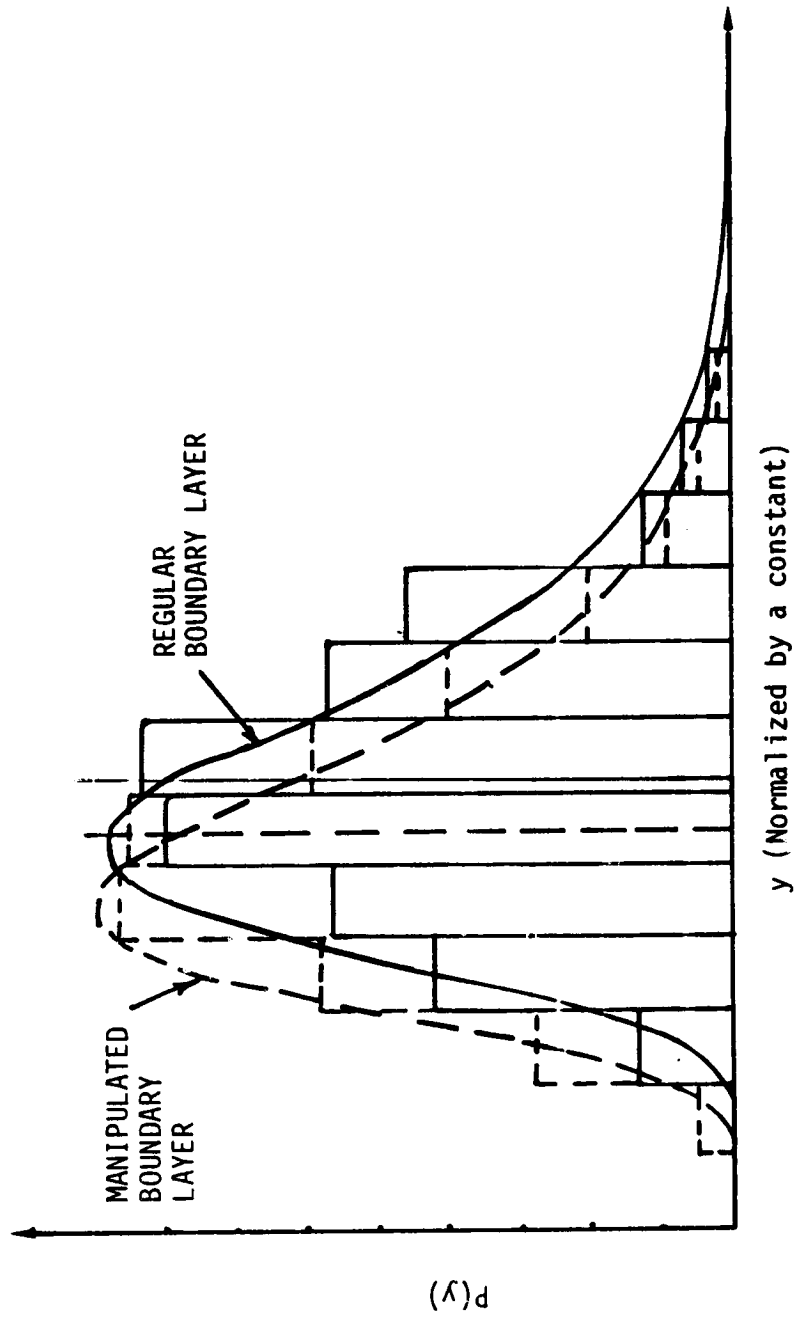
Figure 3.57 Probability distribution of normal transfer of flow marker (TiCl$_4$) into the wall region measured over ±3.3δ, around ξ = 20 for regular and manipulated boundary layers.

POCKETS
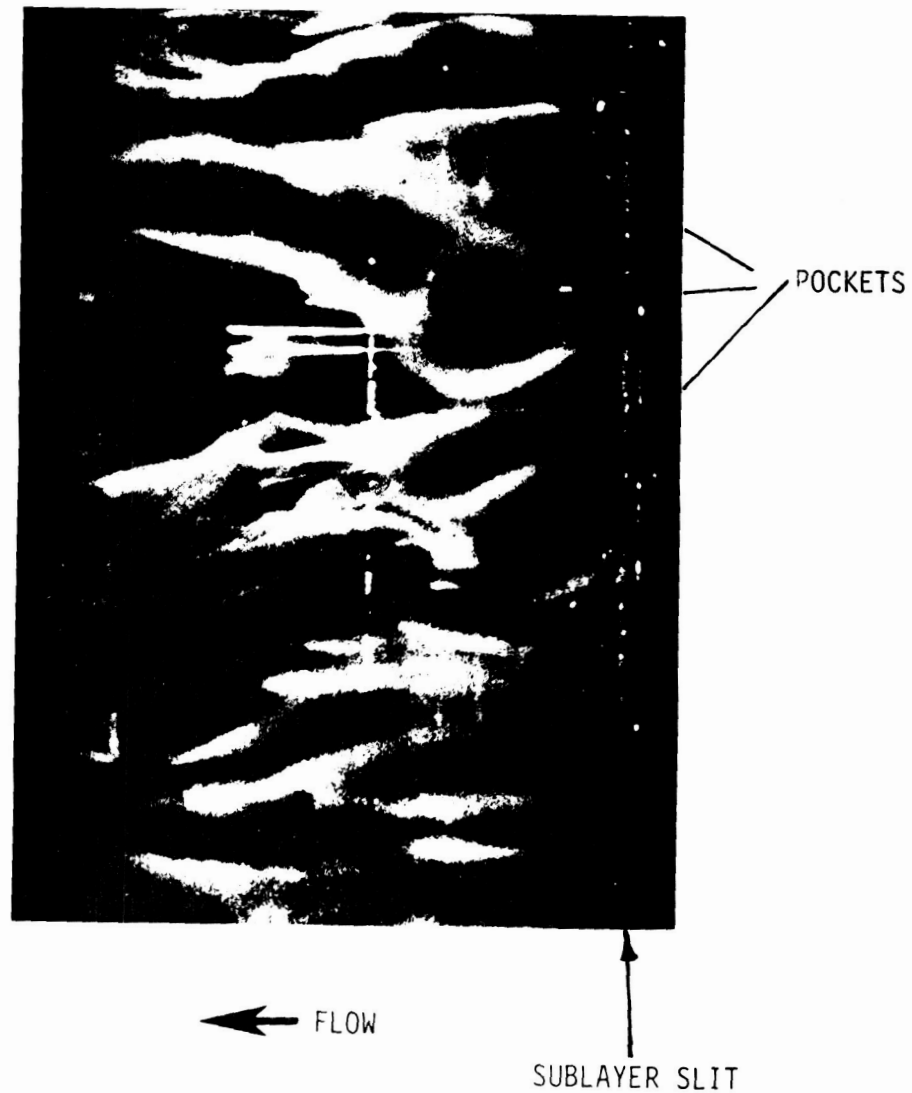
← FLOW

SUBLAYER SLIT

Figure 3.58 Plan view of smoke-filled turbulent sublayer showing the "pocket" flow modules, which result from the interaction of outer layer typical eddies with the sublayer region.

Tau. = dt*Uinf Over (Local Reg. Delta)
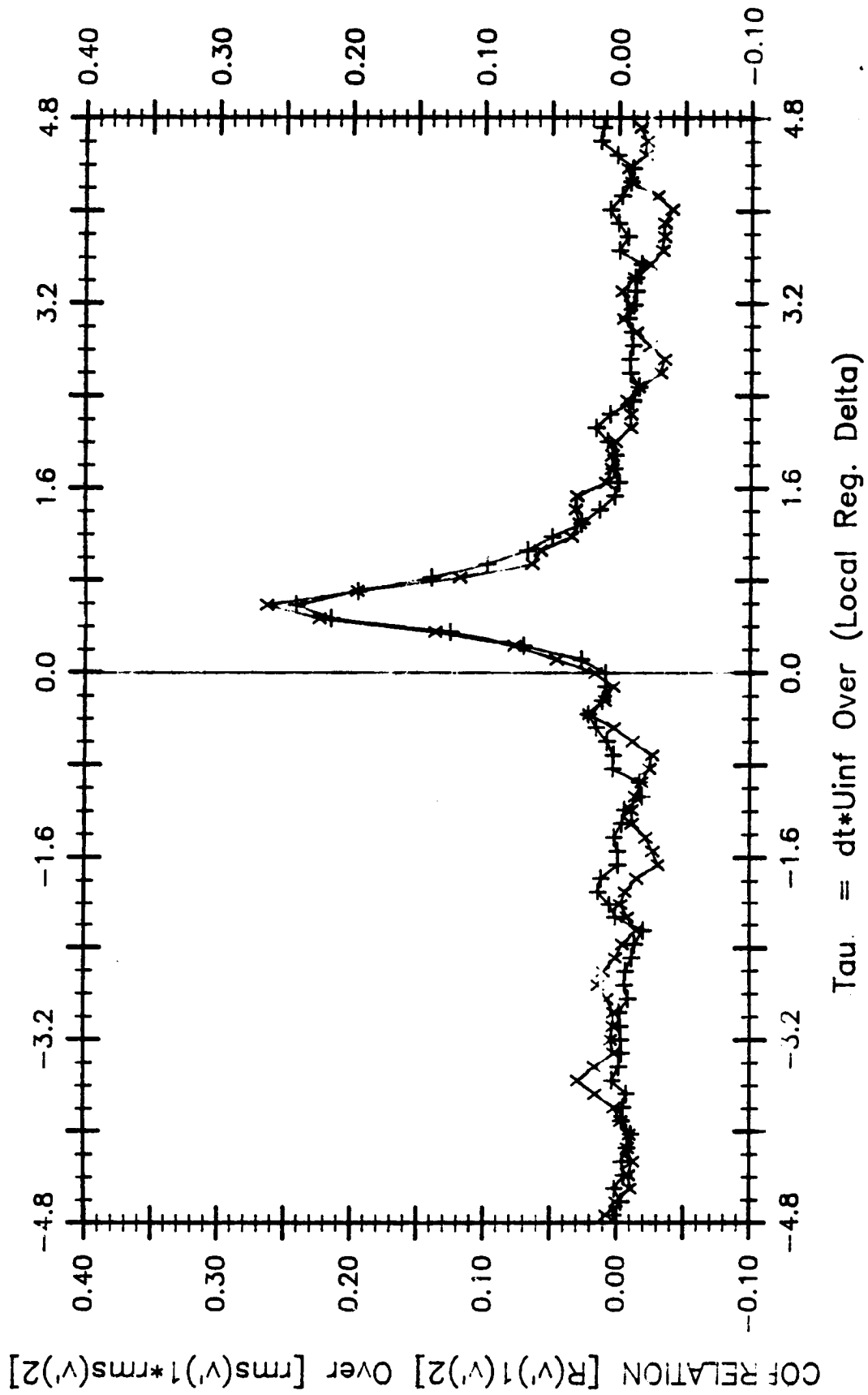
Figure 3.59 Variation of $R_{v'_1 v'_2} / rms(v'_1) rms(v'_2)$ versus τ for regular (x), and manipulated (+) boundary layers at $\xi = 51$.

162
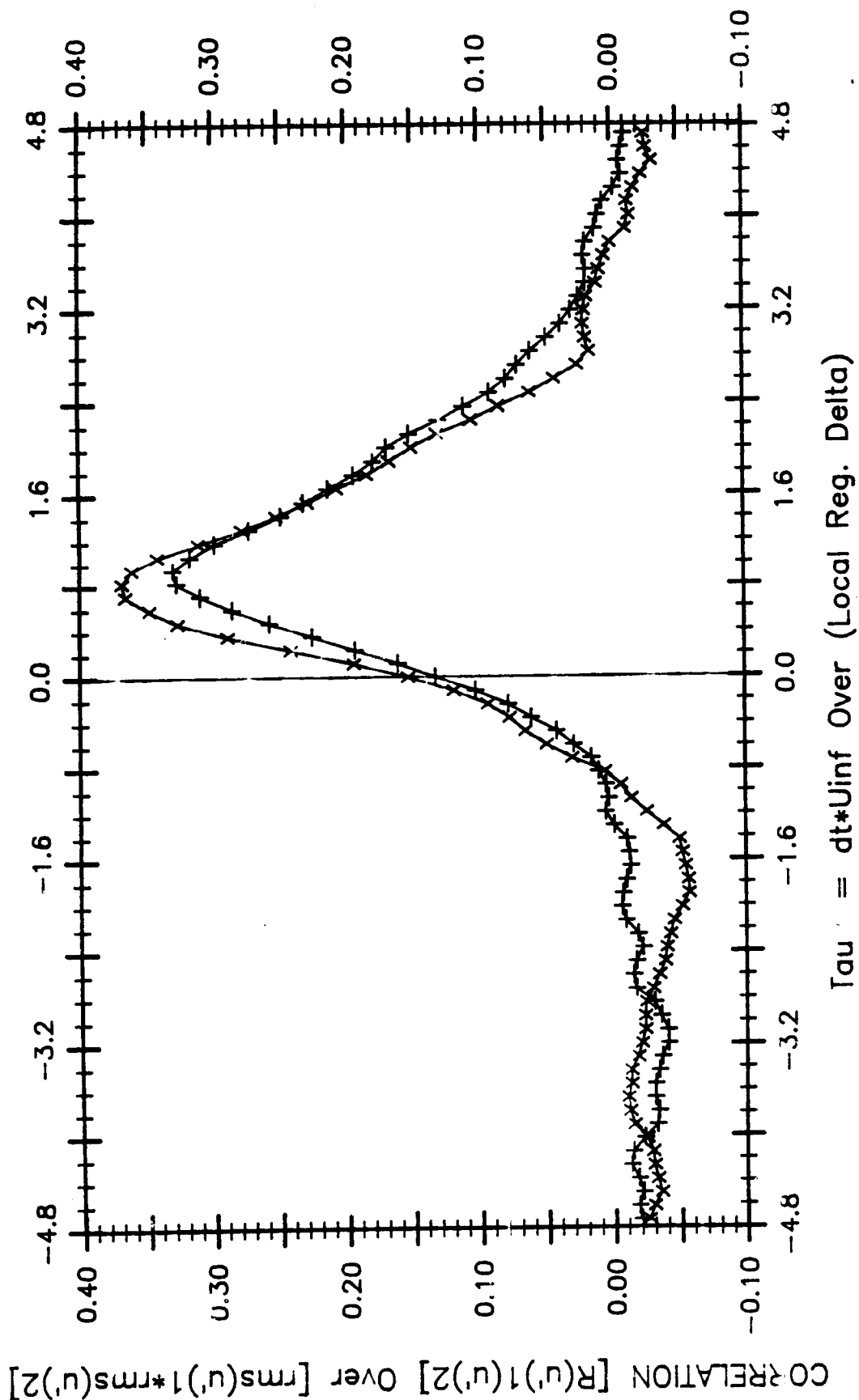
Figure 3.60 Variation of $R_{u'_1 u'_2}$ /rms(u'$_1$)rms(u'$_2$) versus τ for regular (x), and manipulated (+) boundary layers at $\xi = 51$.

Tau' = dt*Uinf Over (Local Reg. Delta)

CORRELATION [R(u')1(u')2] Over [rms(u')1*rms(u')2]

Tau = dt*Uinf Over (Local Reg. Delta)

CORRELATION [R(u')1(v')2] Over [rms(u')1*rms(v')2]
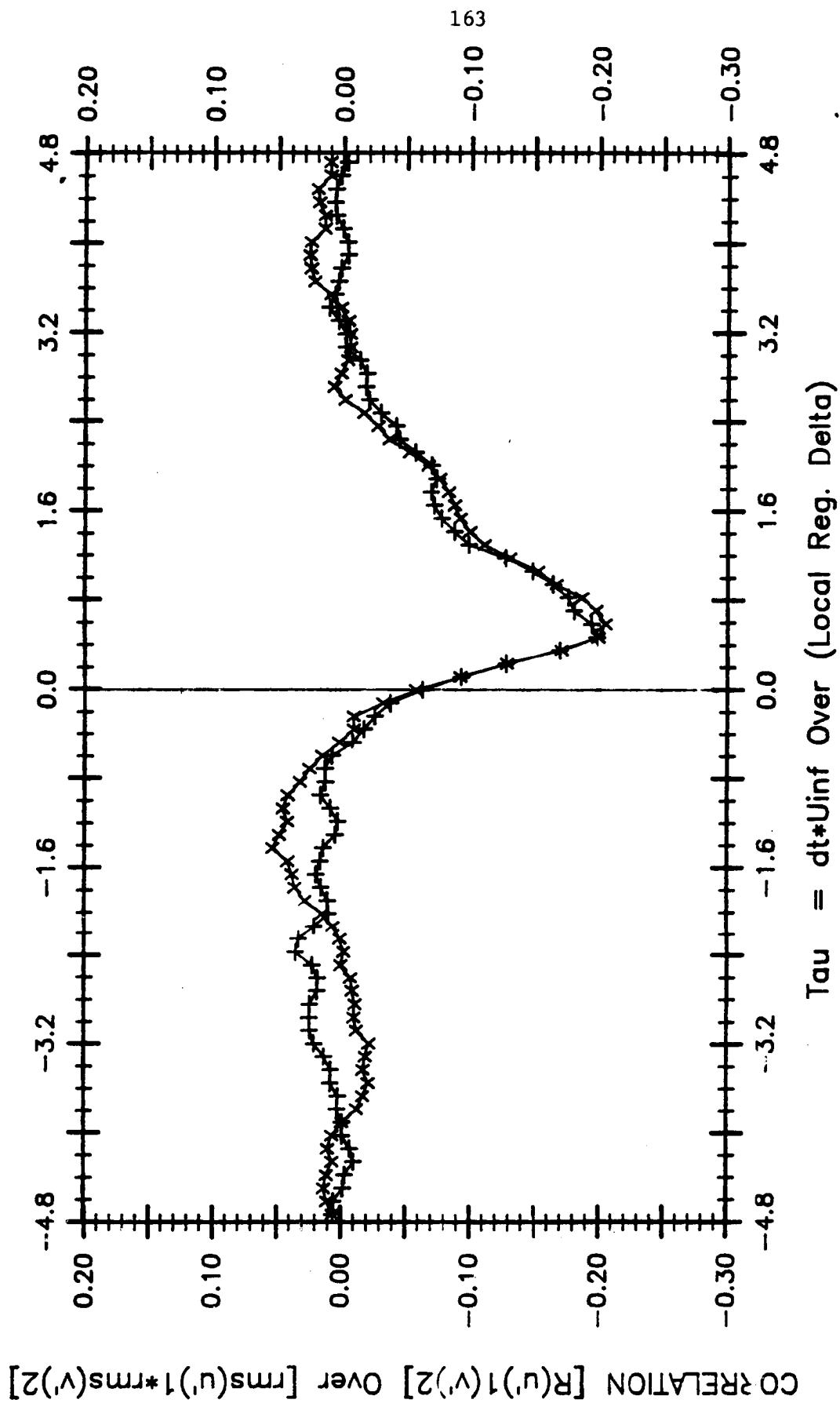
Figure 3.61 Variation of $R_{u_1'v_2'}/rms(u_1')rms(v_2')$ versus τ for regular (x), and manipulated (+) boundary layers at $\xi = 51$.

164

Tau'' = dt*Uinf Over (Local Reg. Delta)

CORRELATION [R(u'v')1(u'v')2] Over [rms(u'v')1*rms(u'v')2]

Figure 3.62 Variation of $R_{(u'v')_1(u'v')_2}/rms((u'v')_1)rms((u'v')_2)$ versus τ for regular (x), and manipulated (+) boundary layers at ξ = 51.
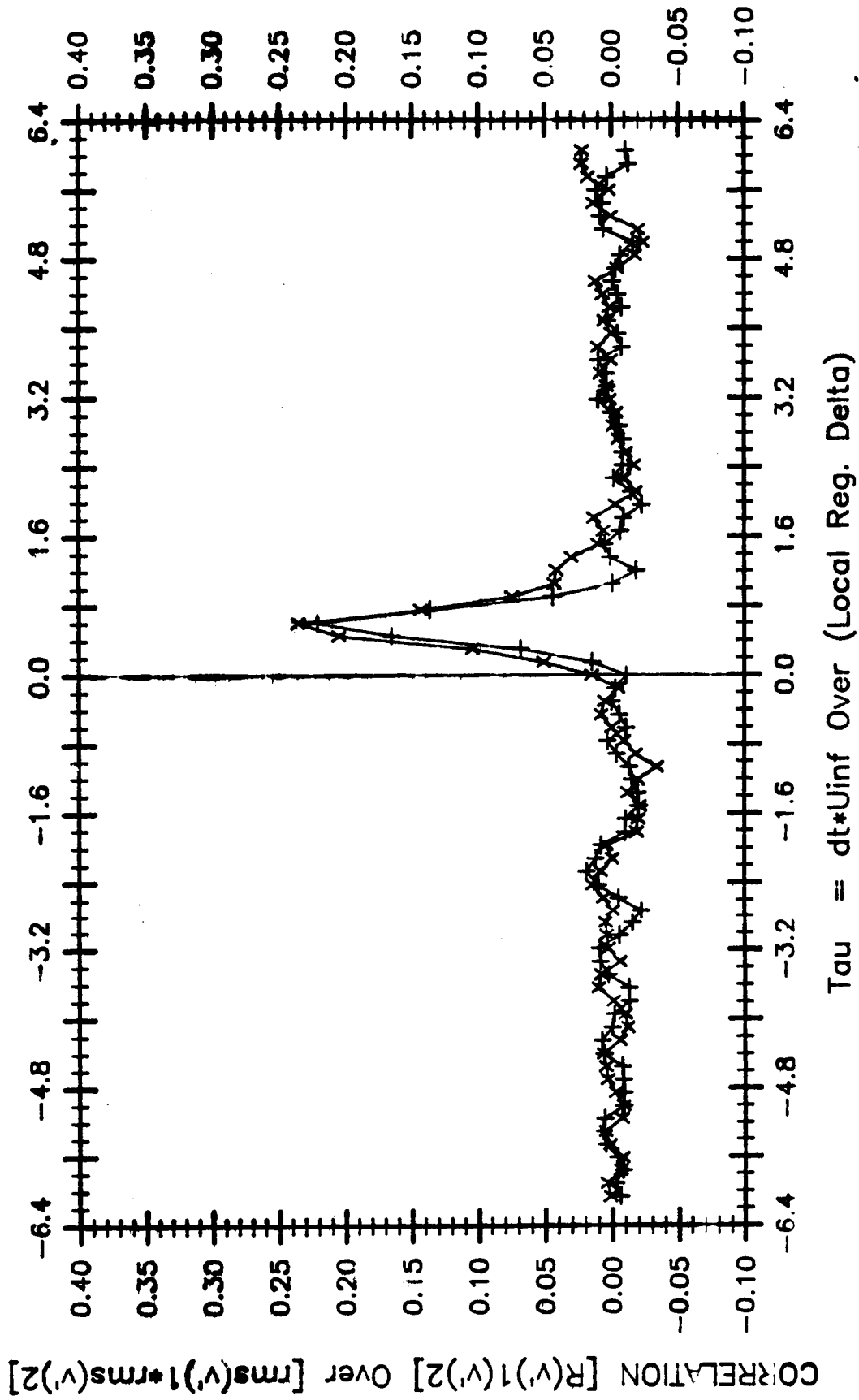
Figure 3.63 Variation of $R_{v'_1 v'_2}/rms(v'_1)rms(v'_2)$ versus τ for regular (x), and manipulated (+) boundary layers at $\xi = 20$.
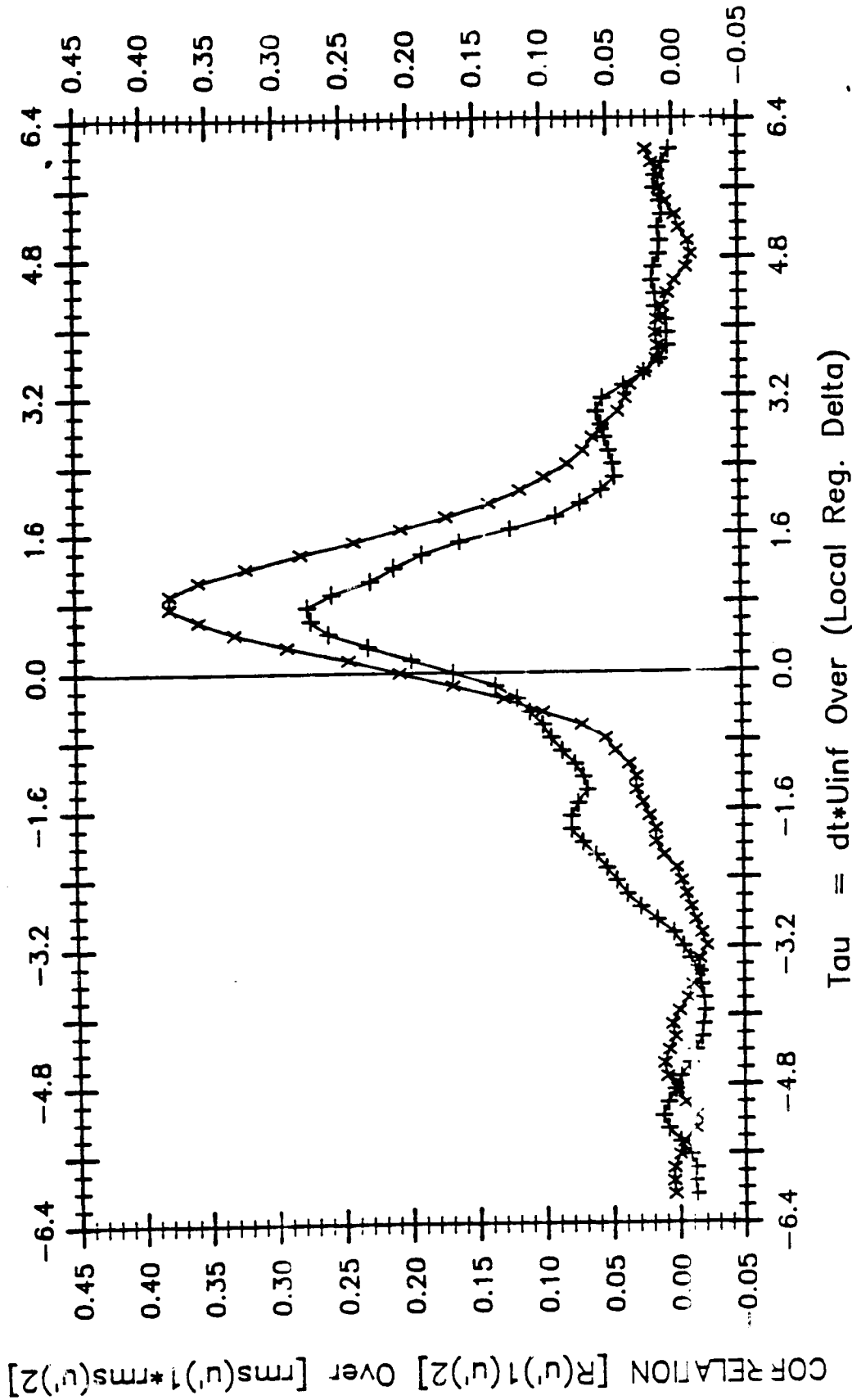
Figure 3.64 Variation of $R_{u'_1u'_2}/rms(u'_1)rms(u'_2)$ versus τ for regular (x) and manipulated (+) boundary layers at $\xi = 20$.

Tau = dt*Uinf Over (Local Reg. Delta)

CORRELATION [R(u')1(u')2] Over [rms(u')1*rms(u')2]

Tau = dt*Uinf Over (Local Reg. Delta)

CORRELATION [R(u')1(v')2] Over [rms(u')1*rms(v')2]
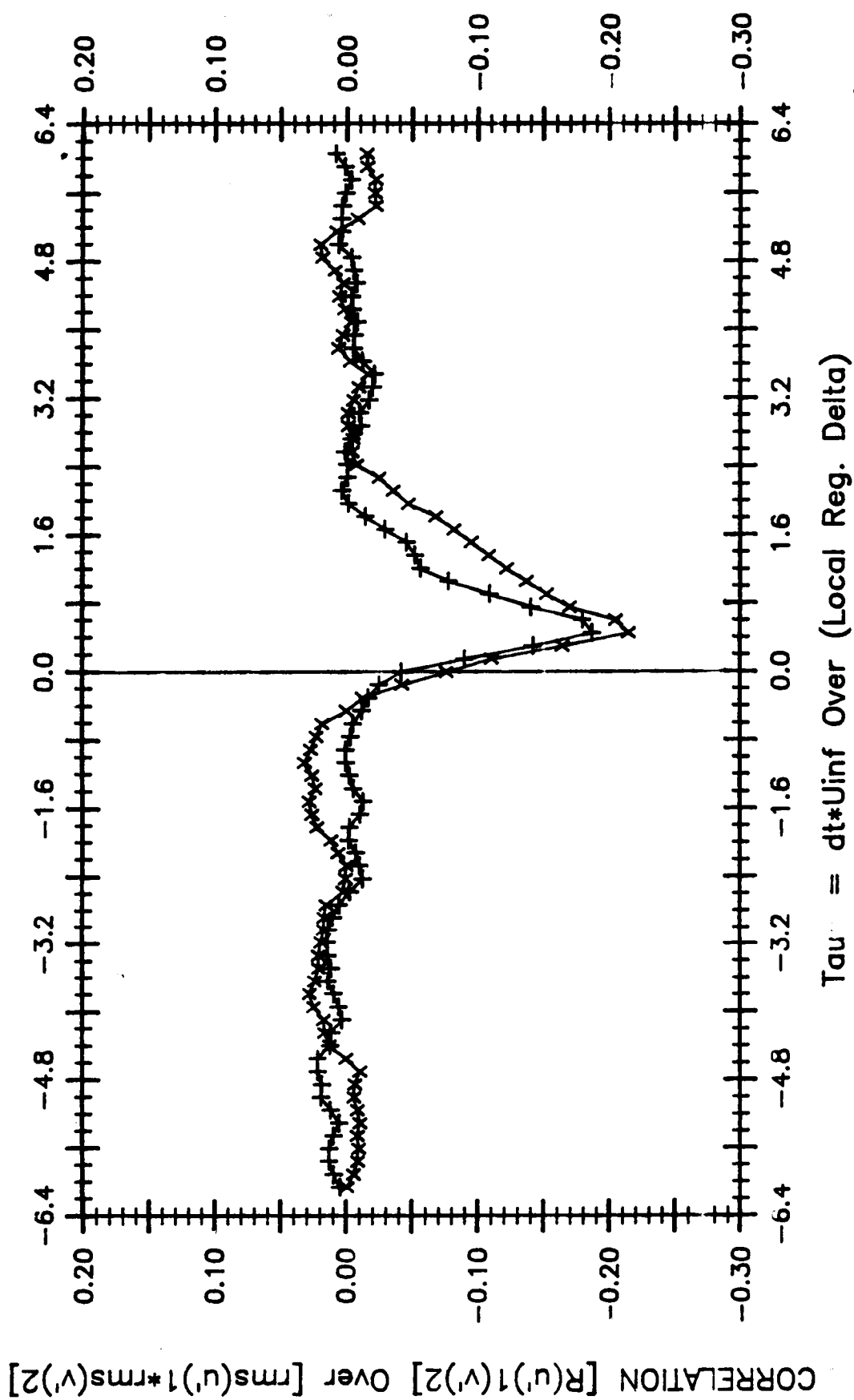
Figure 3.65 Variation of $R_{u_1' v_2'} / rms(u_1') rms(v_2')$ versus τ for regular (x). and manipulated (+) boundary layers at $\xi = 20$.
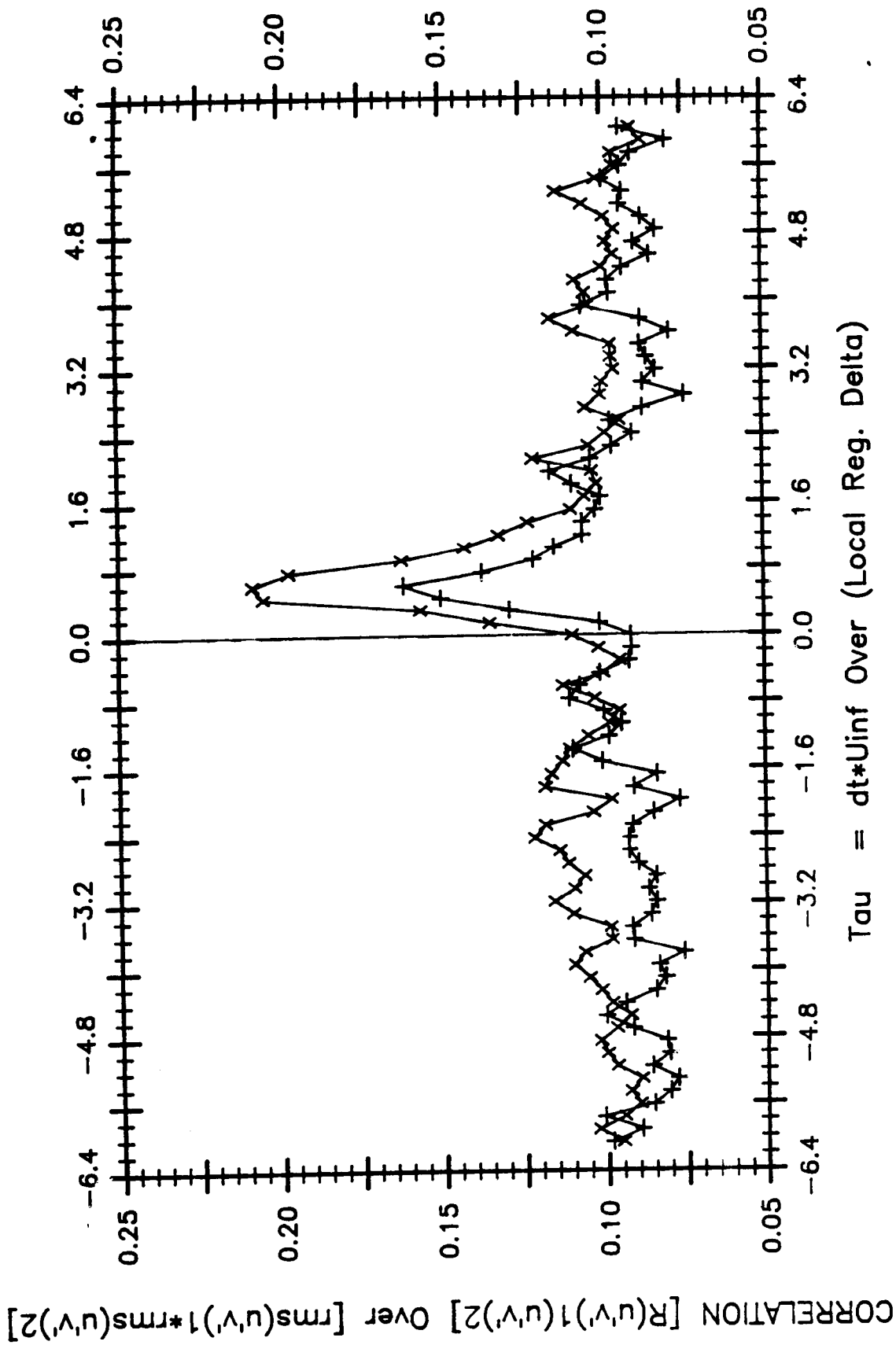
Figure 3.66 Variation of $R_{(u'v')_1(u'v')_2}/rms((u'v')_1)rms((u'v')_2)$ versus τ for regular (x), and manipulated (+) boundary layers at $\xi = 20$.

CORRELATION $[R(u'v')1(u'v')2]$ Over $[rms(u'v')1*rms(u'v')2]$

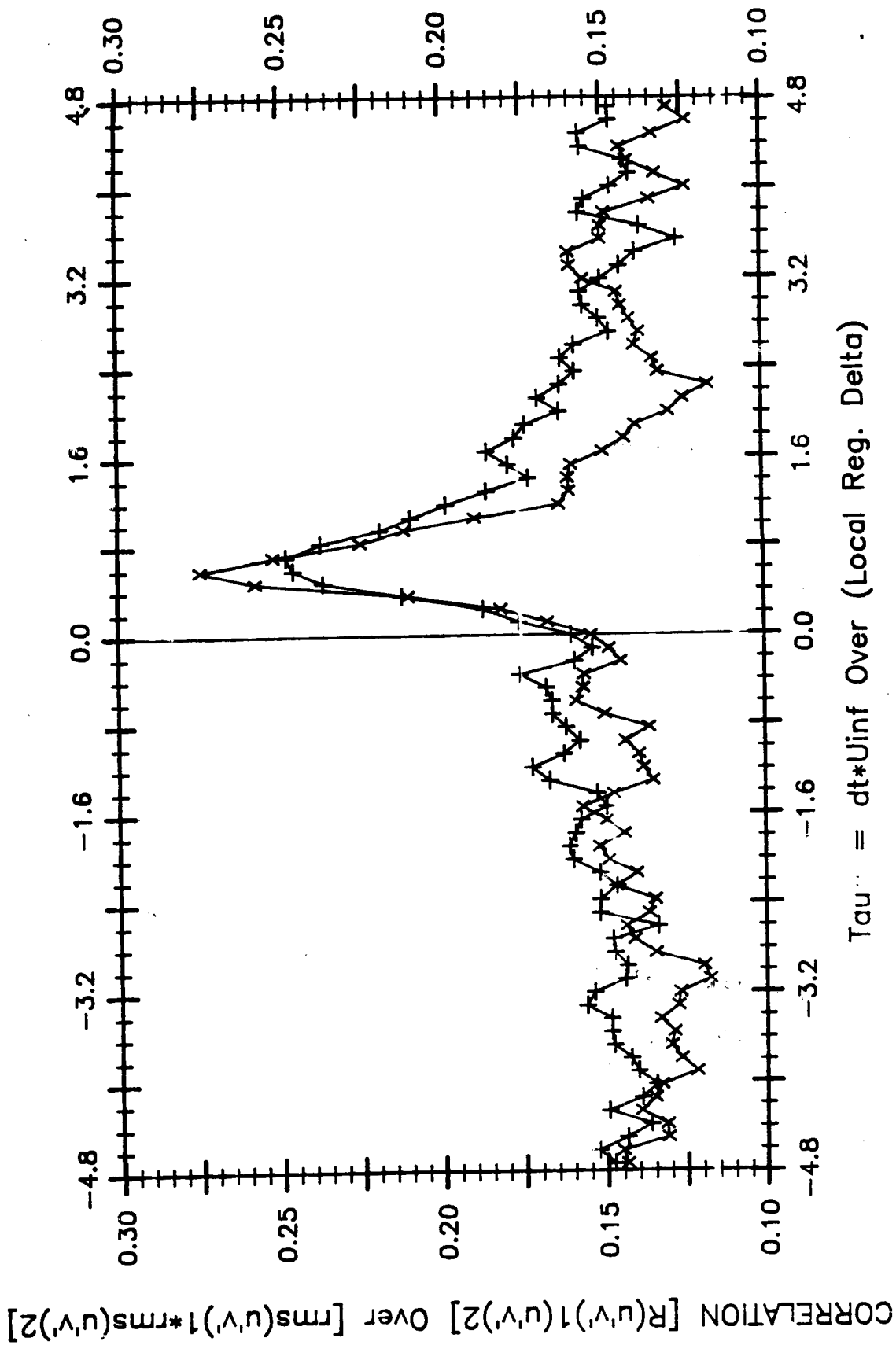Tau $= dt*Uinf$ Over (Local Reg. Delta)
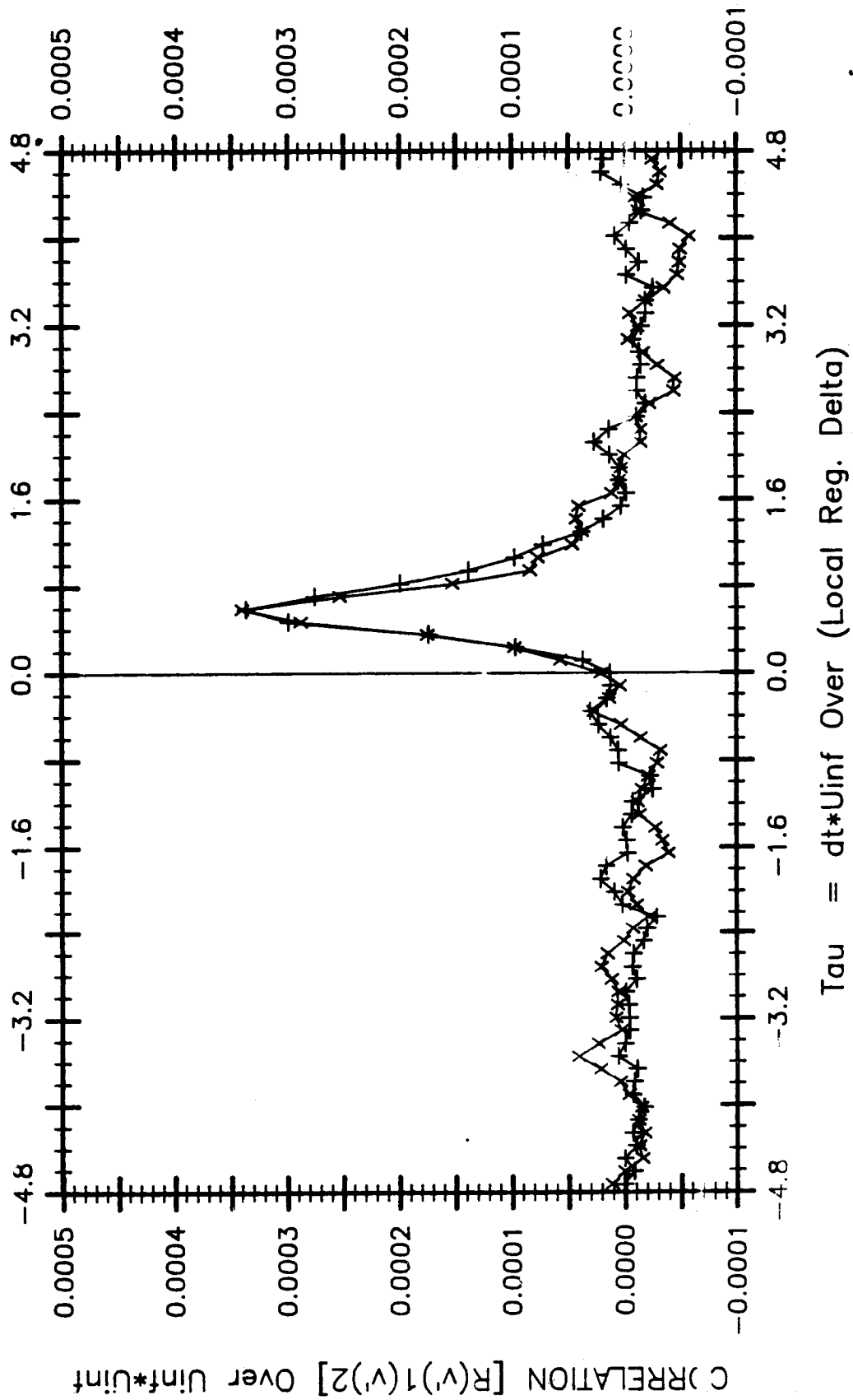
Figure 3.67 Variation of R_y, $v'v'/U_\infty^2$ versus τ for regular (x), and manipulated (+) boundary layers at ξ = 51.
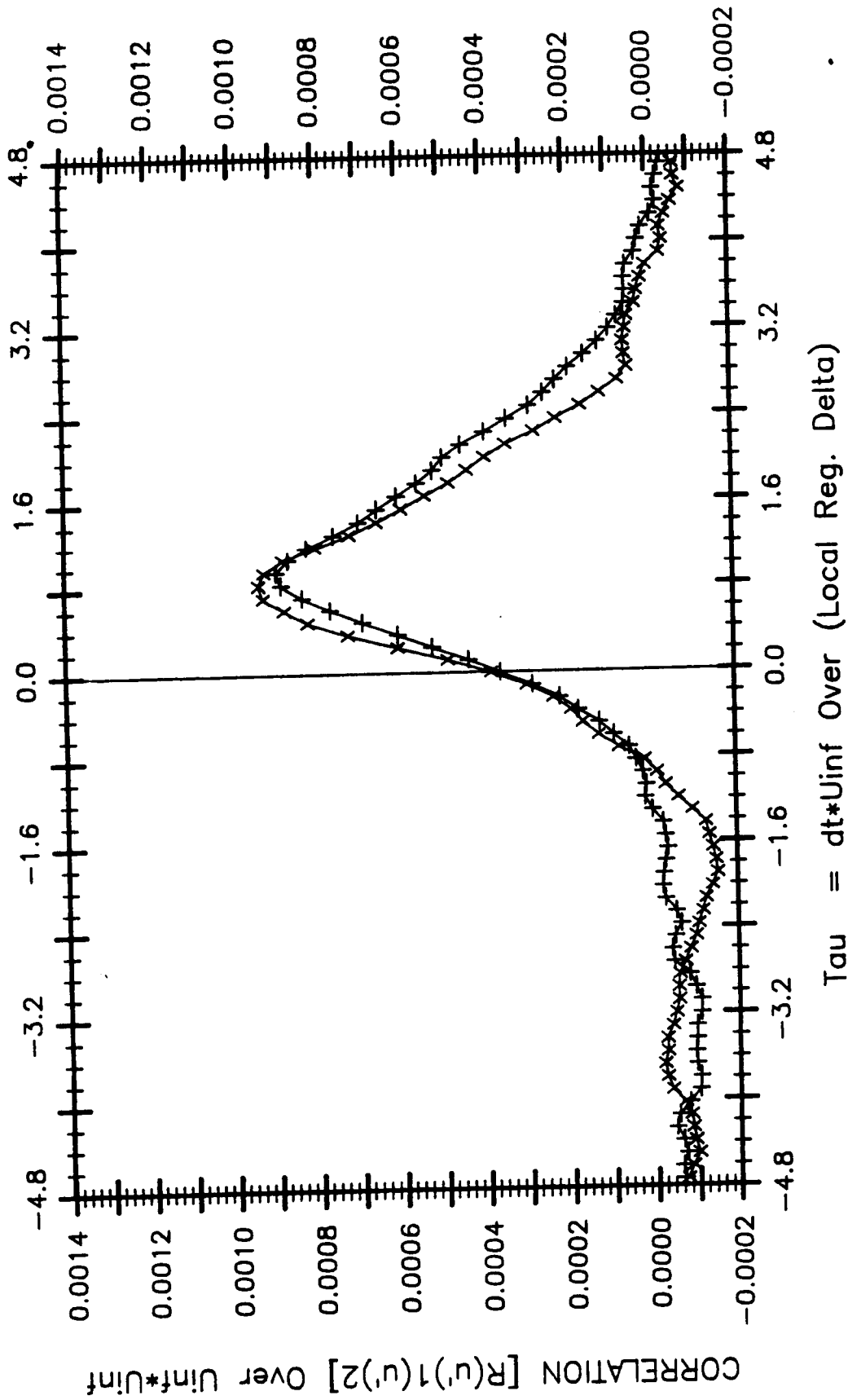
Figure 3.68 Variation of R_{ij} u_i' u_j'/u_∞^2 versus τ for regular (x), and manipulated (+) boundary layers at $\xi = 51$.

CORRELATION [R(u')1(u')2] Over Uinf*Uinf

Tau = dt*Uinf Over (Local Reg. Delta)
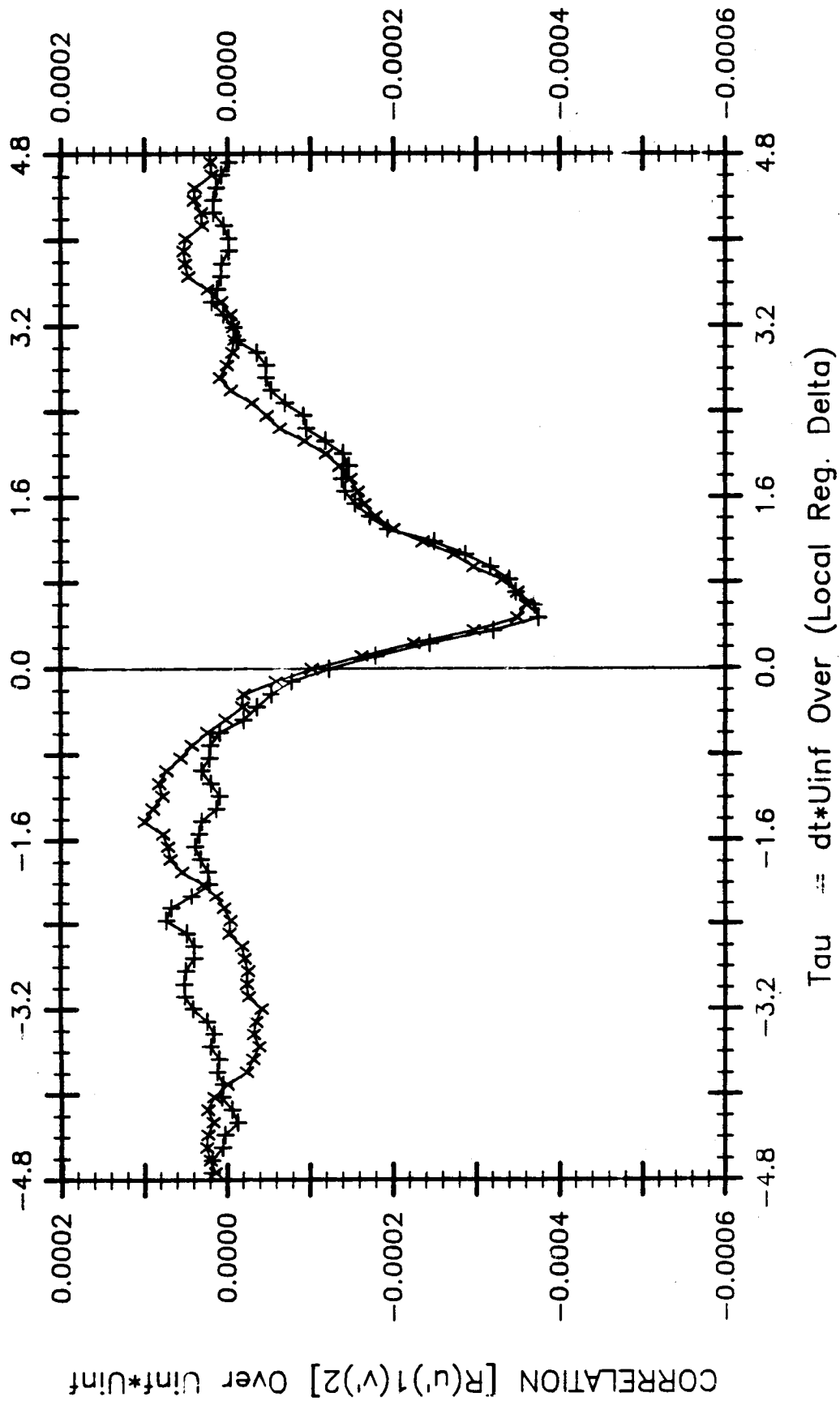
Figure 3.69 Variation of R_p, $u'_1 v'_1 / U_\infty^2$ versus τ for regular (x), and manipulated (+) boundary layers at $\xi = 51$.
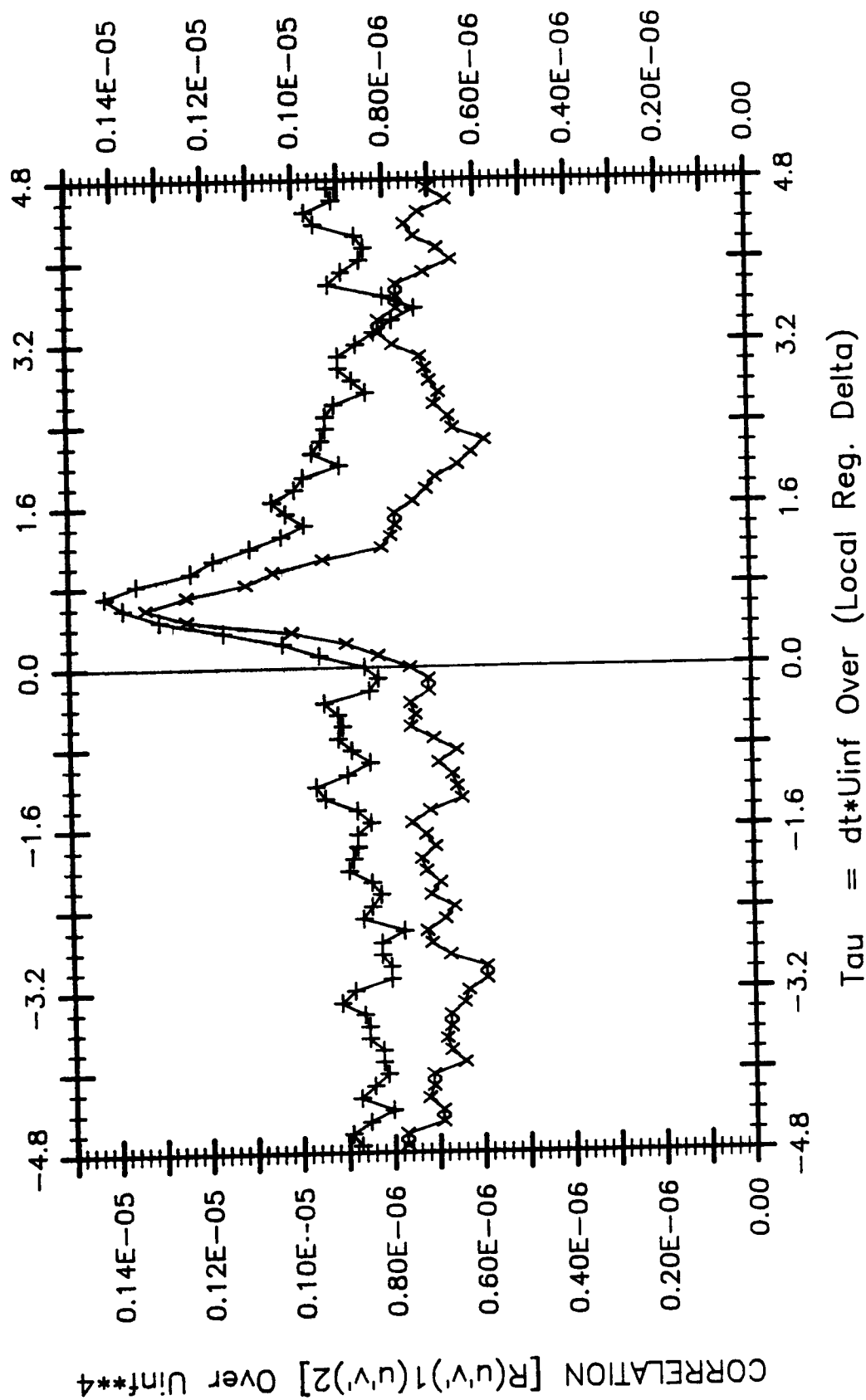
Figure 3.70 Variation of $R_{(u'v')1(u'v')2}(u'v')/U_\infty^4$ versus τ for regular (x), and manipulated (+) boundary layers at $\xi = 51$.

Tau = dt*Uinf Over (Local Reg. Delta)
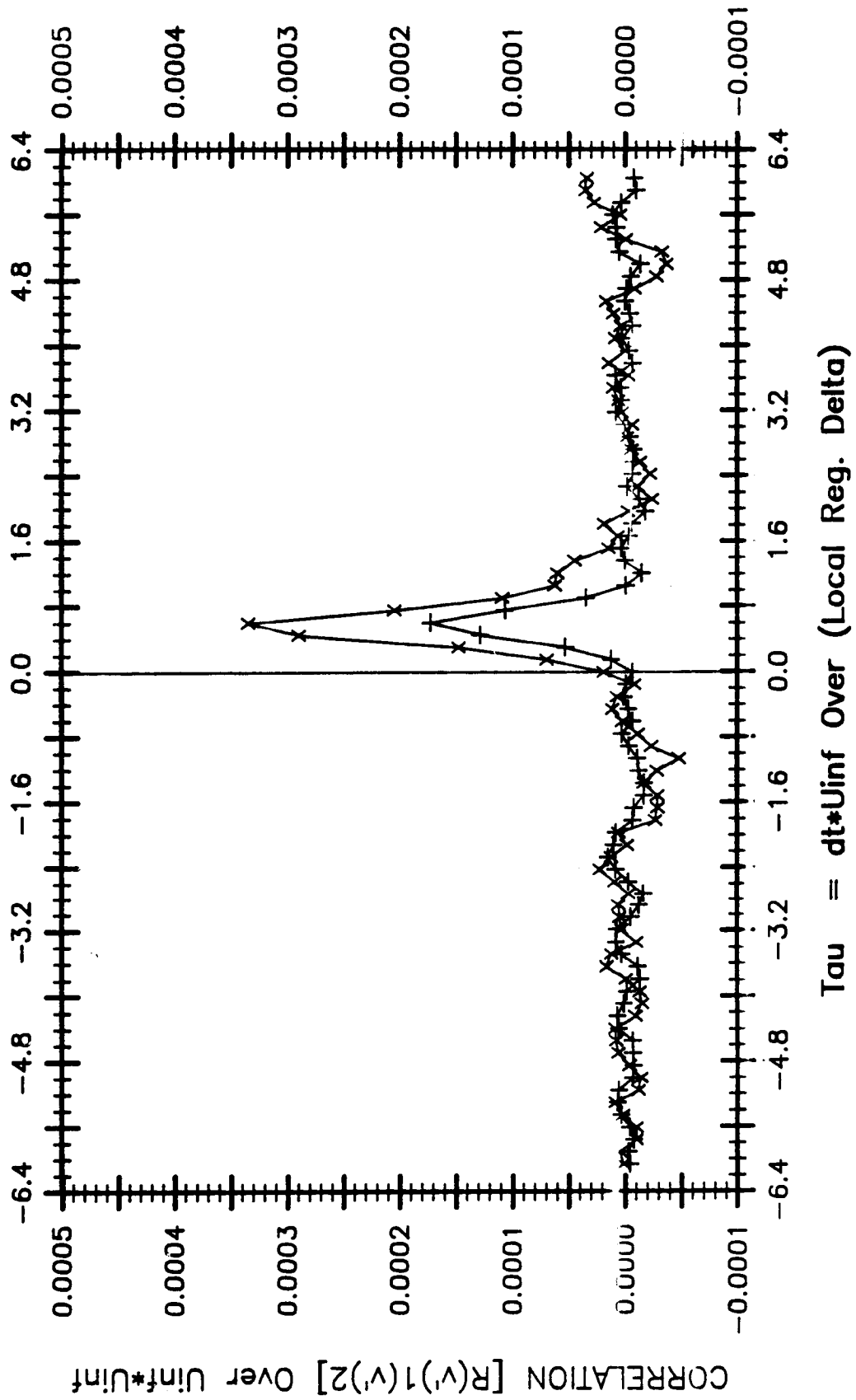
Figure 3.71 Variation of $R_{v'_1 v'_2}/U_\infty^2$ versus τ for regular (x), and manipulated (+) boundary layers at $\xi = 20$.

CORRELATION [R(v')1(v')2] Over Uinf*Uinf
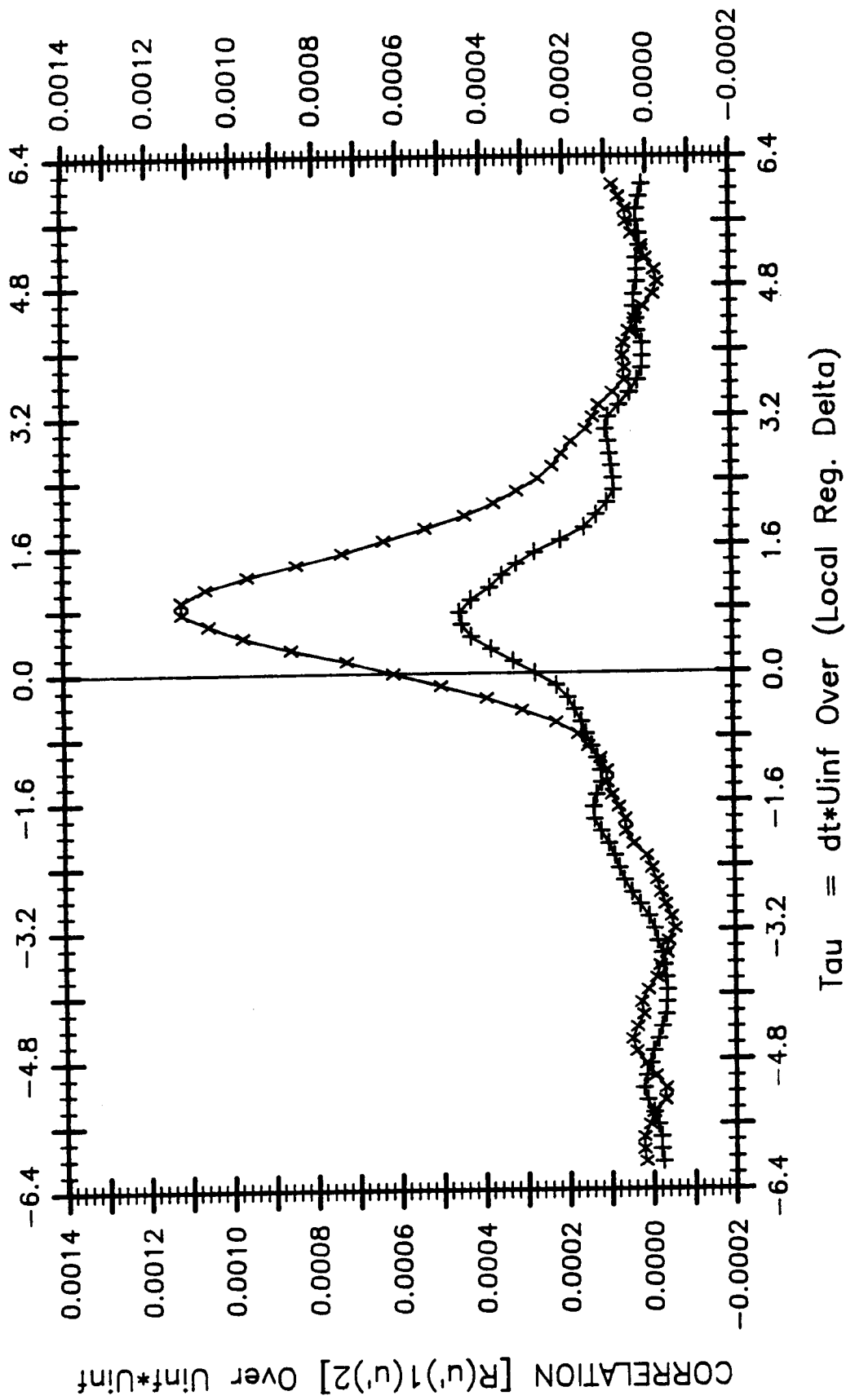
Figure 3.72 Variation of $R_{u'_1 u'_1}/U_\infty^2$ versus τ for regular (x), and manipulated (+) boundary layers at $\xi = 20$.

Tau = dt*Uinf Over (Local Reg. Delta)
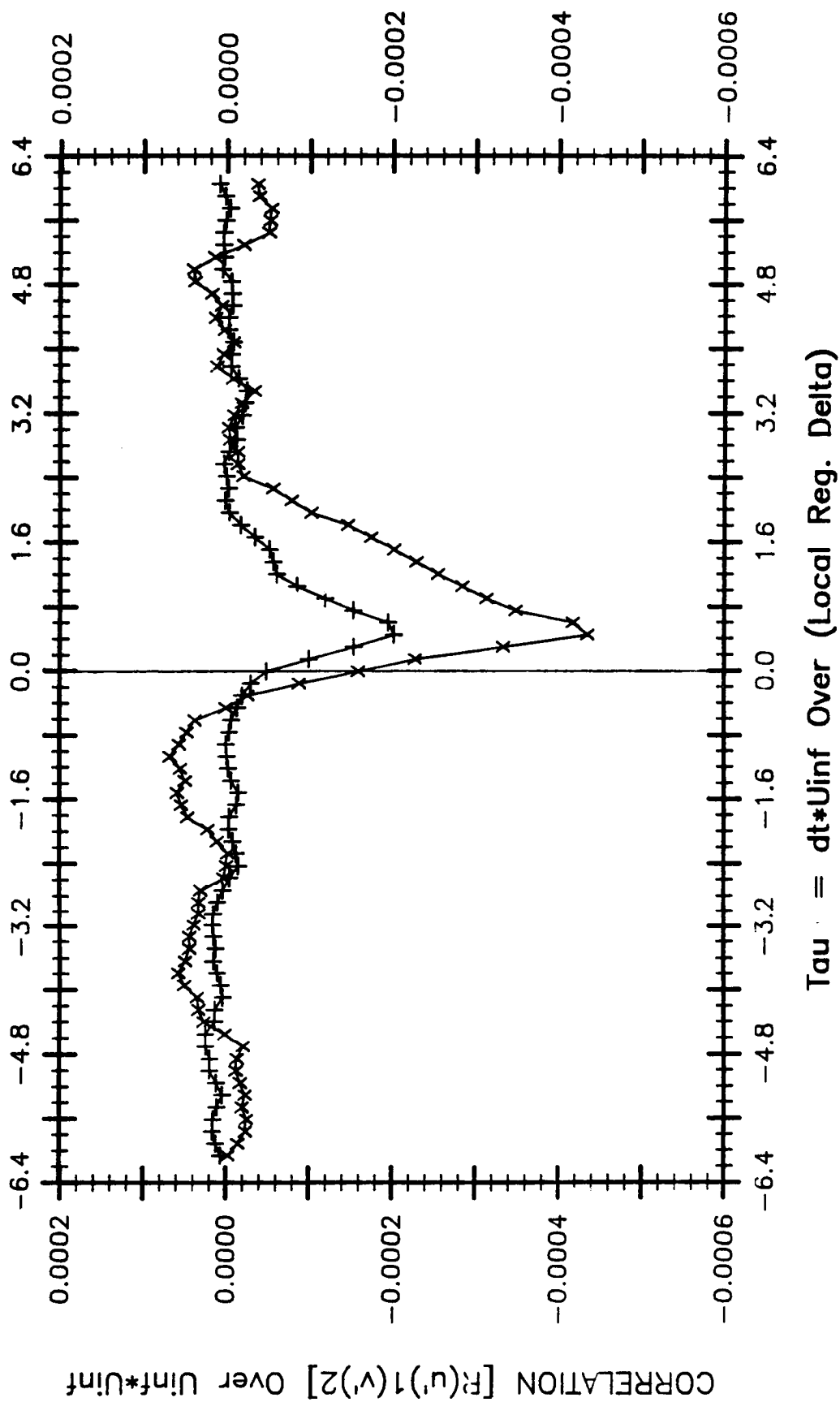
Figure 3.73 Variation of R_n, u' v' / U_∞^2 versus τ for regular (x), and manipulated (+) boundary layers at $\xi = 20$.

CORRELATION [R(u')1(v')2] Over Uinf*Uinf
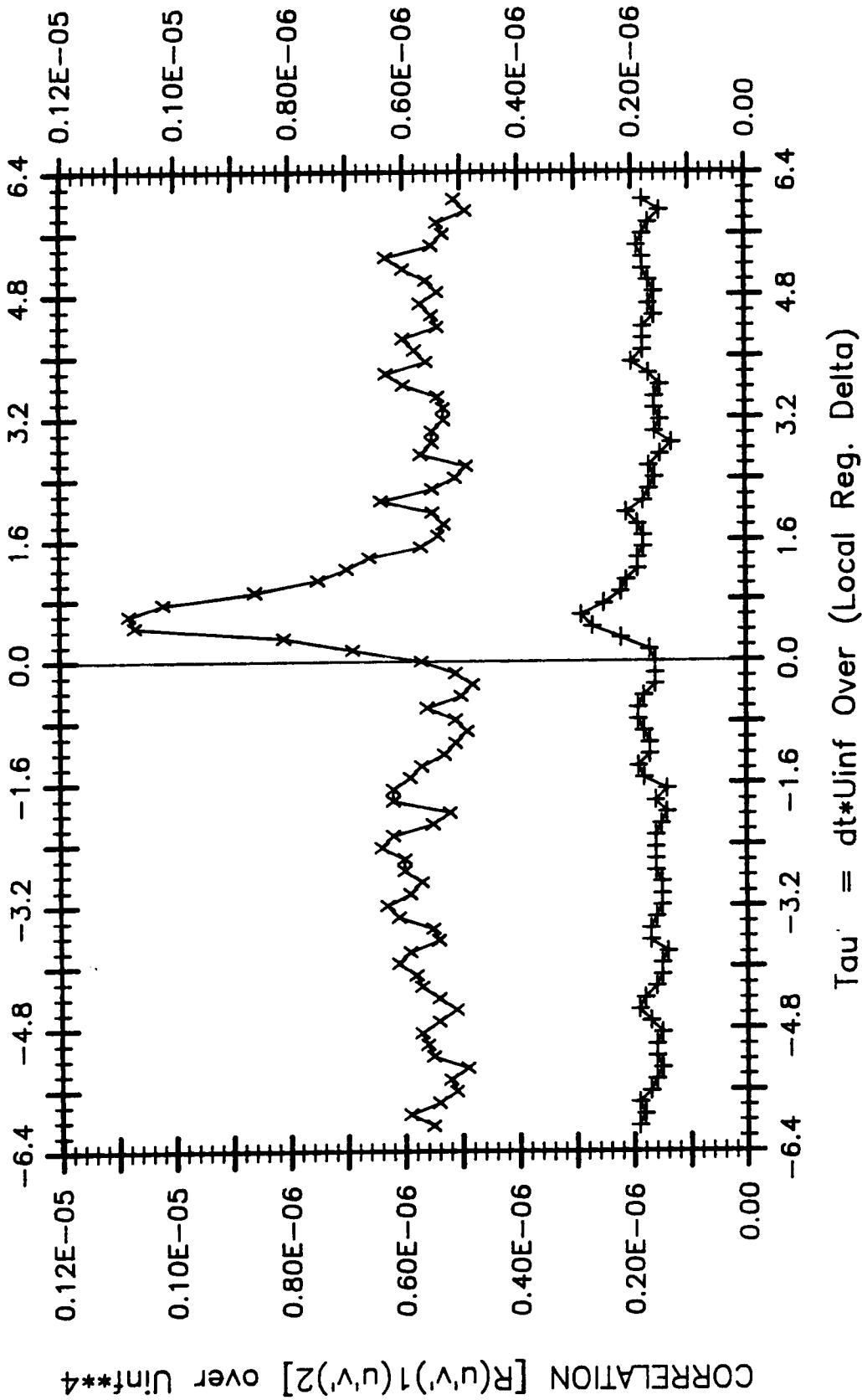
Figure 3.74 Variation of $R_{(u'v')_1(u'v')_2}/U_\infty^4$ versus τ for regular (x), and manipulated (+) boundary layers at $\xi = 20$.
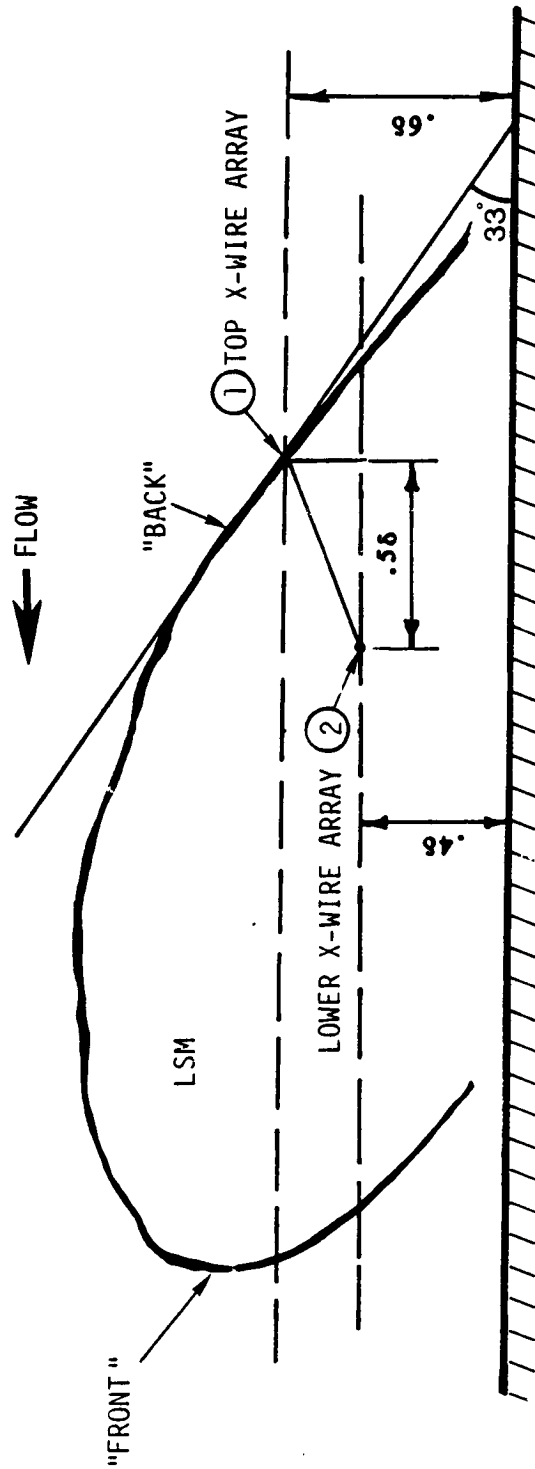
Figure 3.75 Schematic of an ideal large-scale motion in turbulent boundary layer.
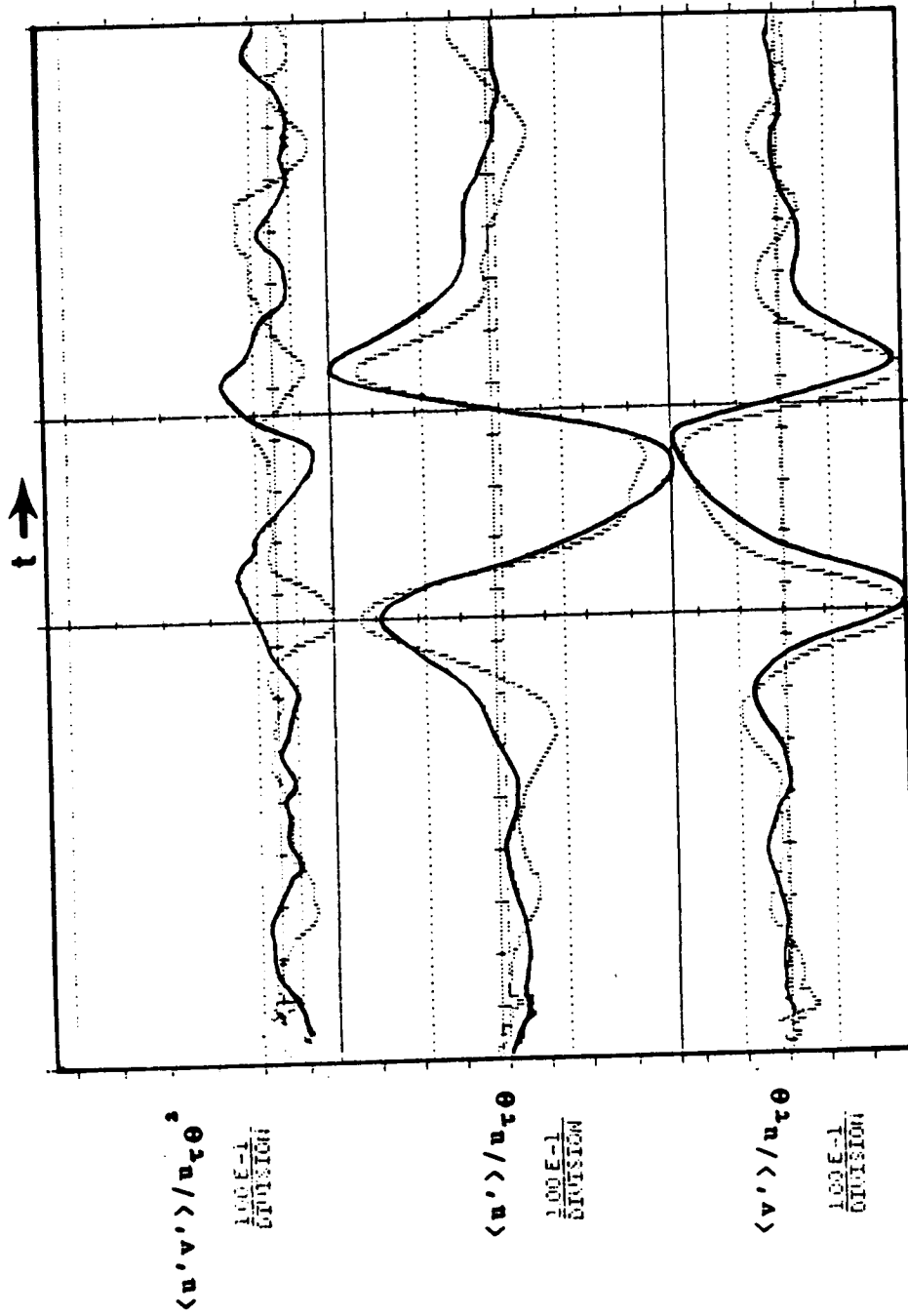
Figure 3.76 Ensemble averaged v', u', and u'v' signals conditionally sampled to large scale motions and normalized by $u_{\tau\theta}$ in regular (solid line signals) and manipulated (light dashed line signals) boundary layers at y = .66δ_{local}.
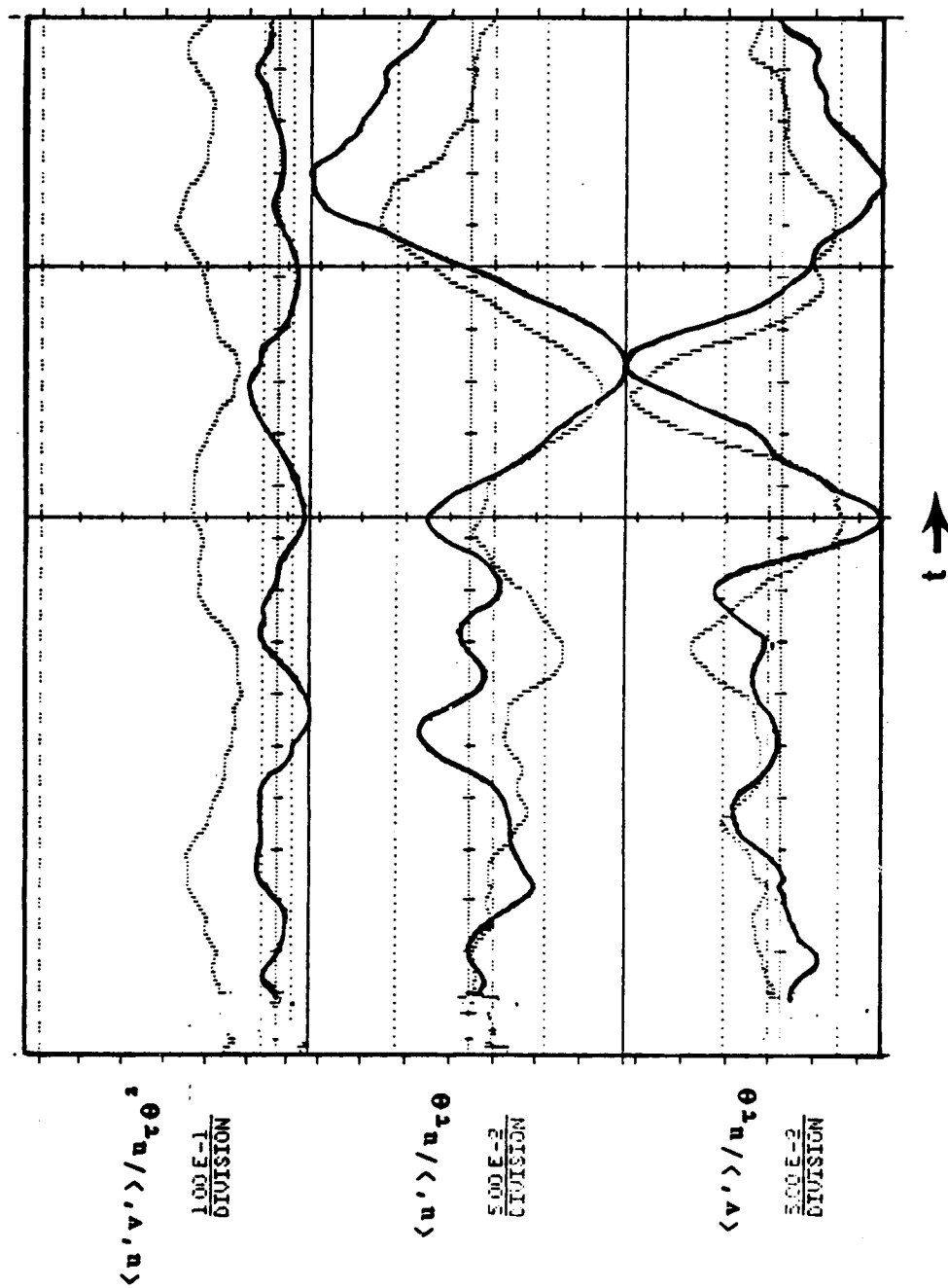
Figure 3.77 Ensemble averaged v', u', and u'v' signals conditionally sampled to large scale motions and normalized by $u_{\tau\theta}$ in regular (solid line signals) and manipulated (light dashed line signals) boundary layers at y = .4δ.

180
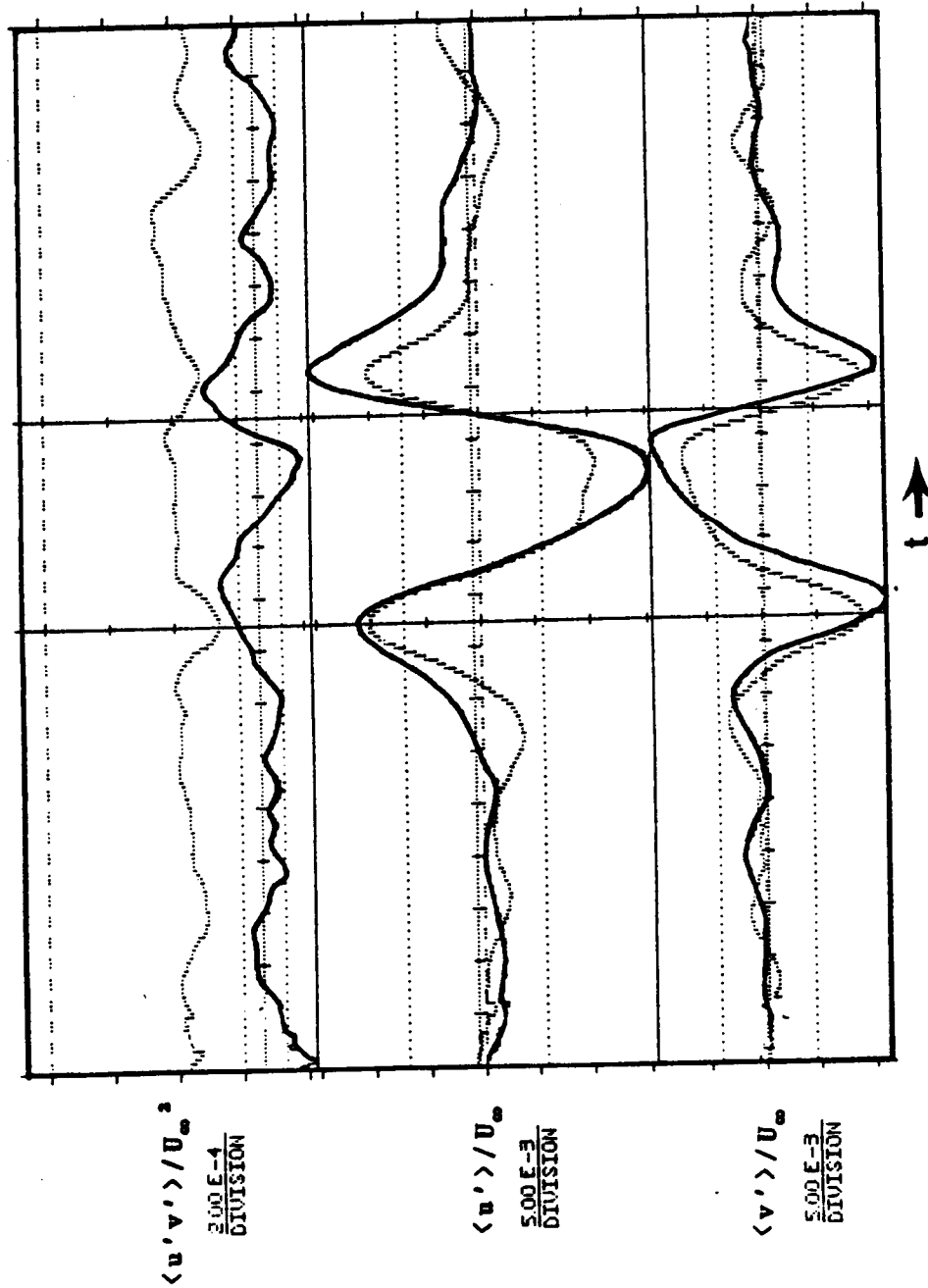
Figure 3.78 Ensemble averaged v', u', and u'v' signals conditionally sampled to large scale motions and normalized by U_∞ in regular (solid line signals) and manipulated (light dashed line signals) boundary layers at y = .66.
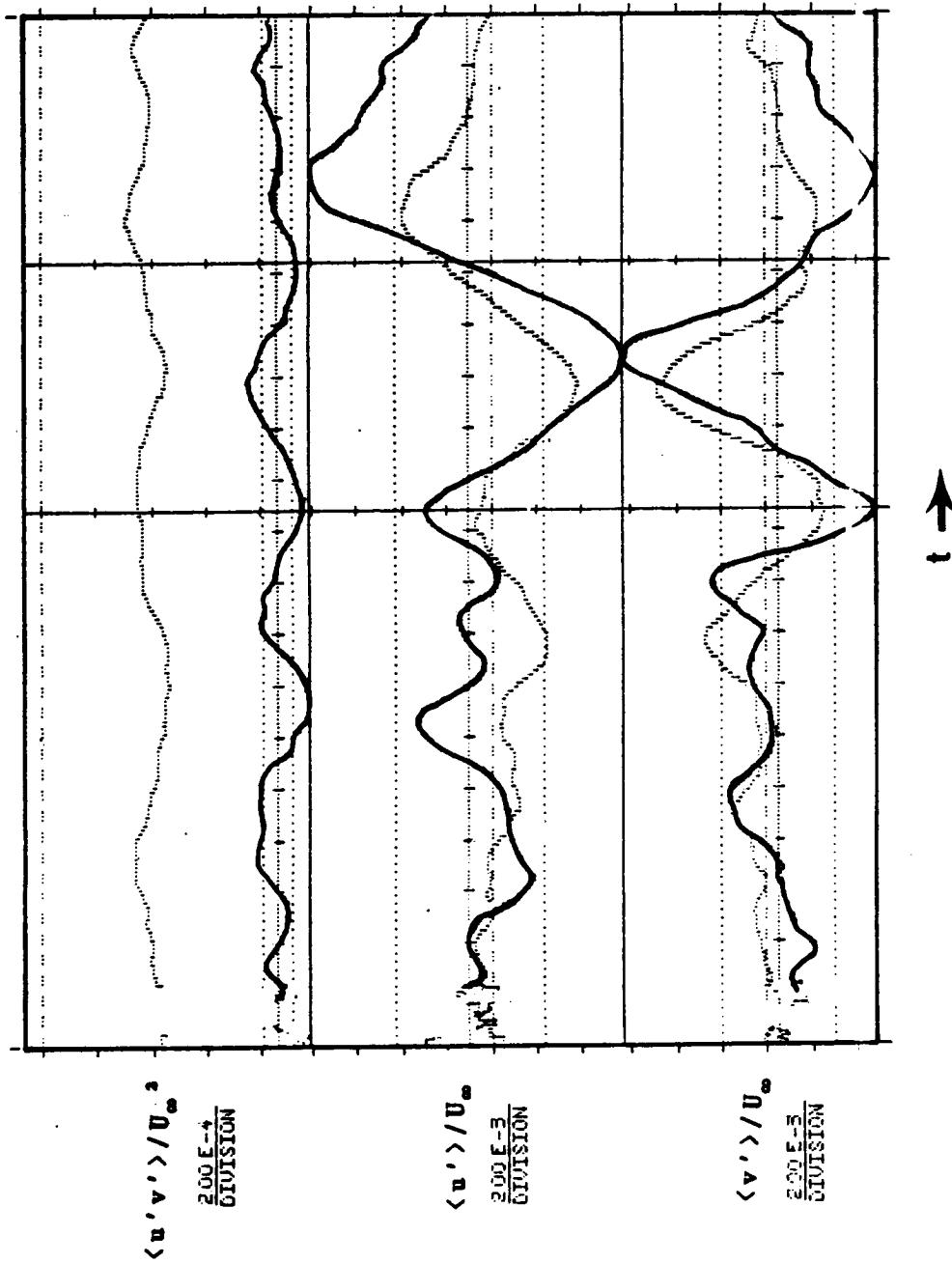
Figure 3.79 Ensemble averaged v', u', and $u'v'$ signals conditionally sampled to large scale motions and normalized by U_∞ in regular (solid line signals) and manipulated (light dashed line signals) boundary layers at $y = .46$.

182
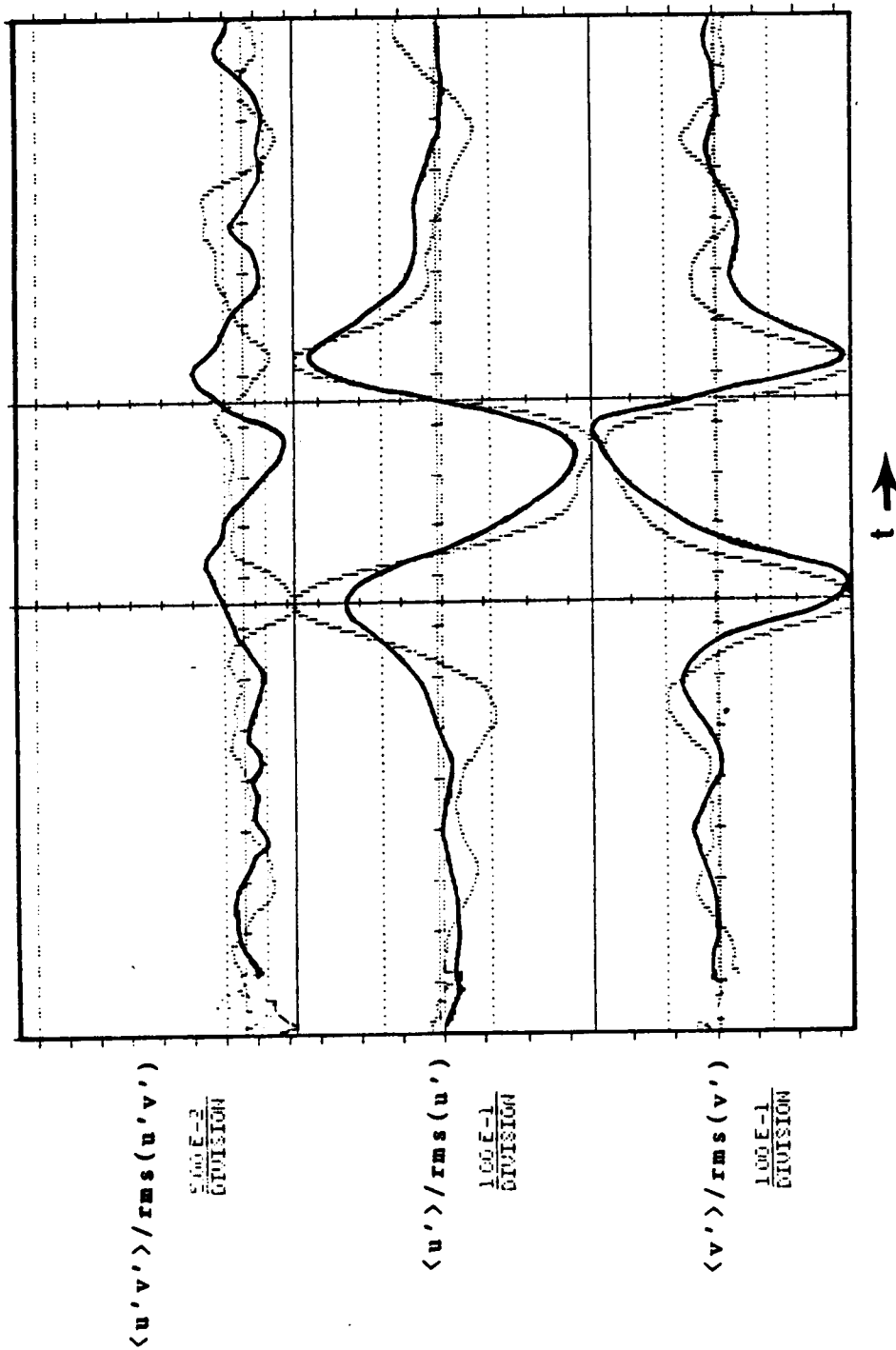
Figure 3.80 Ensemble averaged v', u', and u'v' signals conditionally sampled to large scale motions and normalized by their respective rms values in regular (solid line signals) and manipulated (light dashed line signals) boundary layers at y = .68.
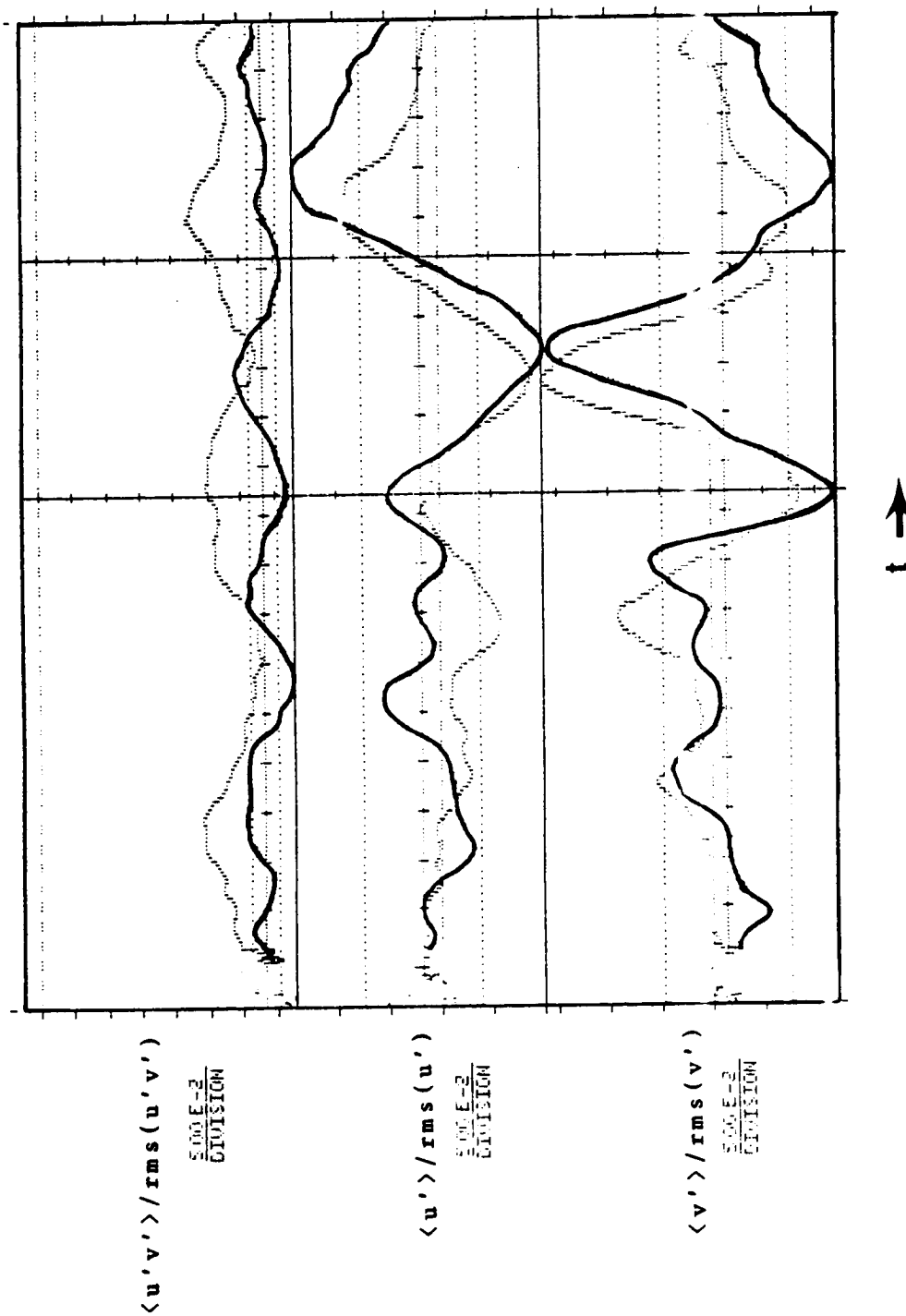
Figure 3.81 Ensemble averaged v', u', and u'v' signals conditionally sampled to large scale motions and normalized by their respective rms values in regular (solid line signals) and manipulated (light dashed line signals) boundary layers at y = .46.
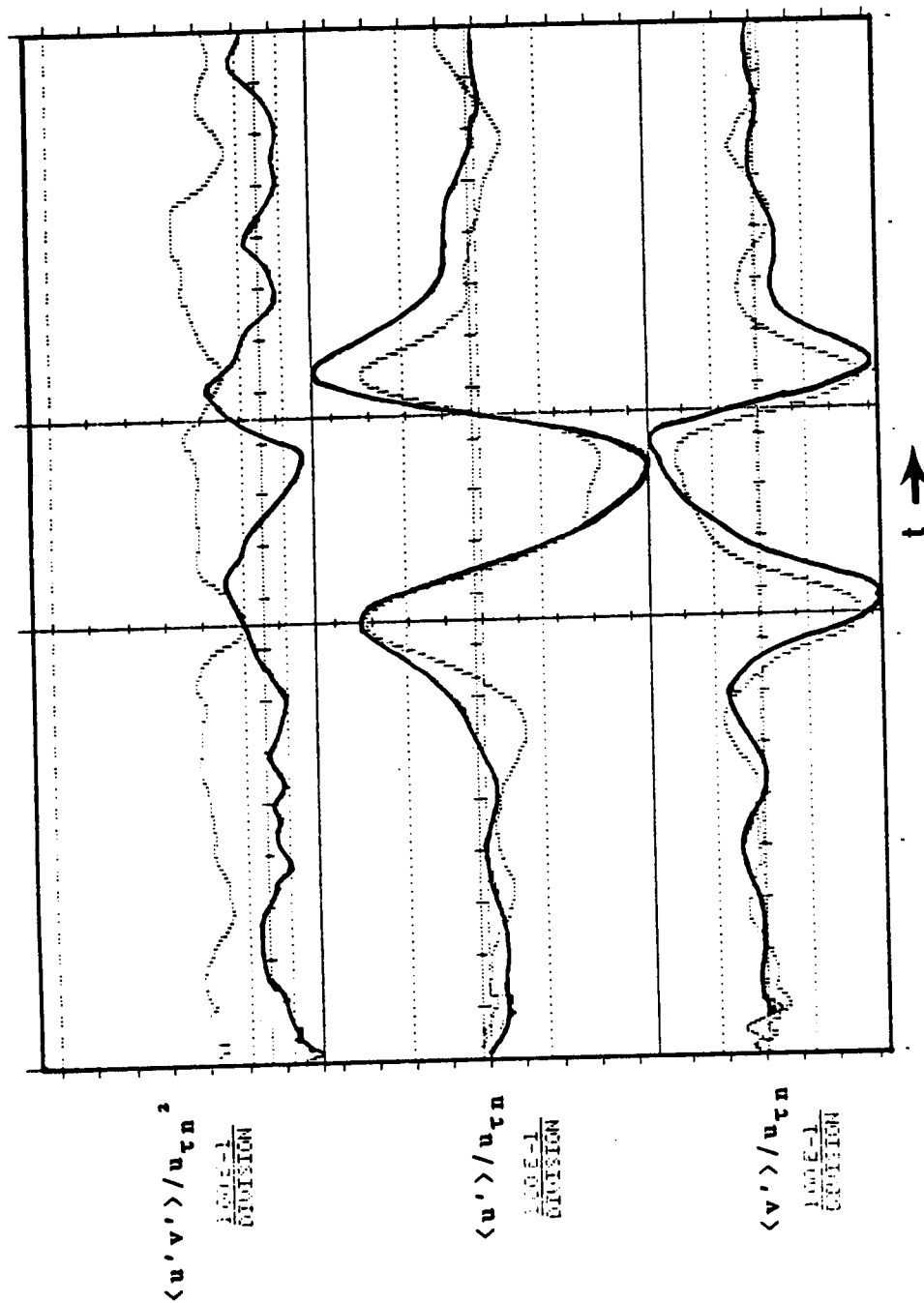
Figure 3.82 Ensemble averaged v', u', and u'v' signals conditionally sampled to large scale motions and normalized by $u_{\tau n}$ in regular (solid line signals) and manipulated (light dashed line signals) boundary layers at y = .6δ.

ORIGINAL PAGE IS
OE POOR QUALITY
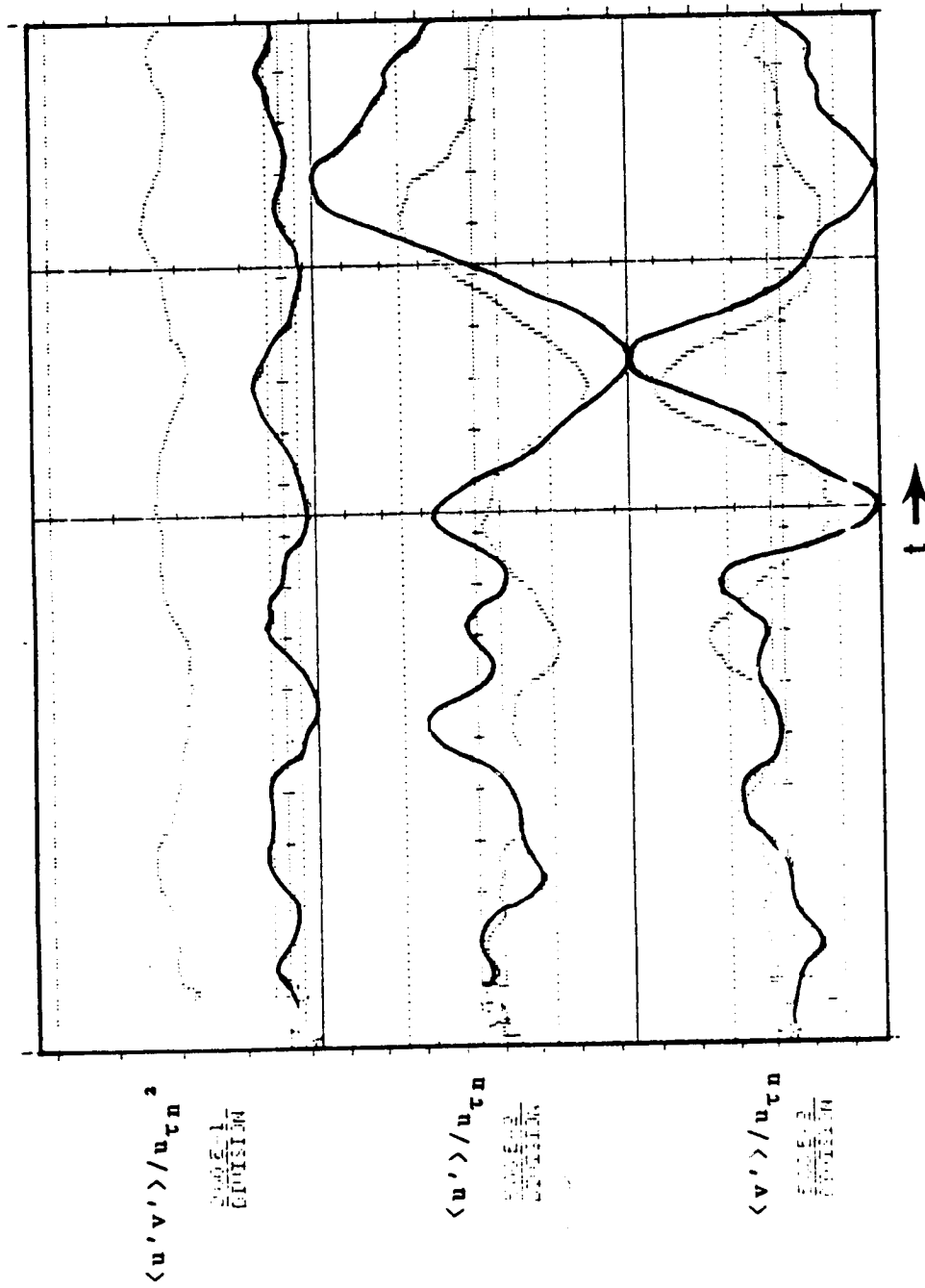
Figure 3.83 Ensemble averaged v', u', and u'v' signals conditionally sampled to large scale motions and normalized by $u_{\tau n}$ in regular (solid line signals) and manipulated (light dashed line signals) boundary layers at y = .4δ.
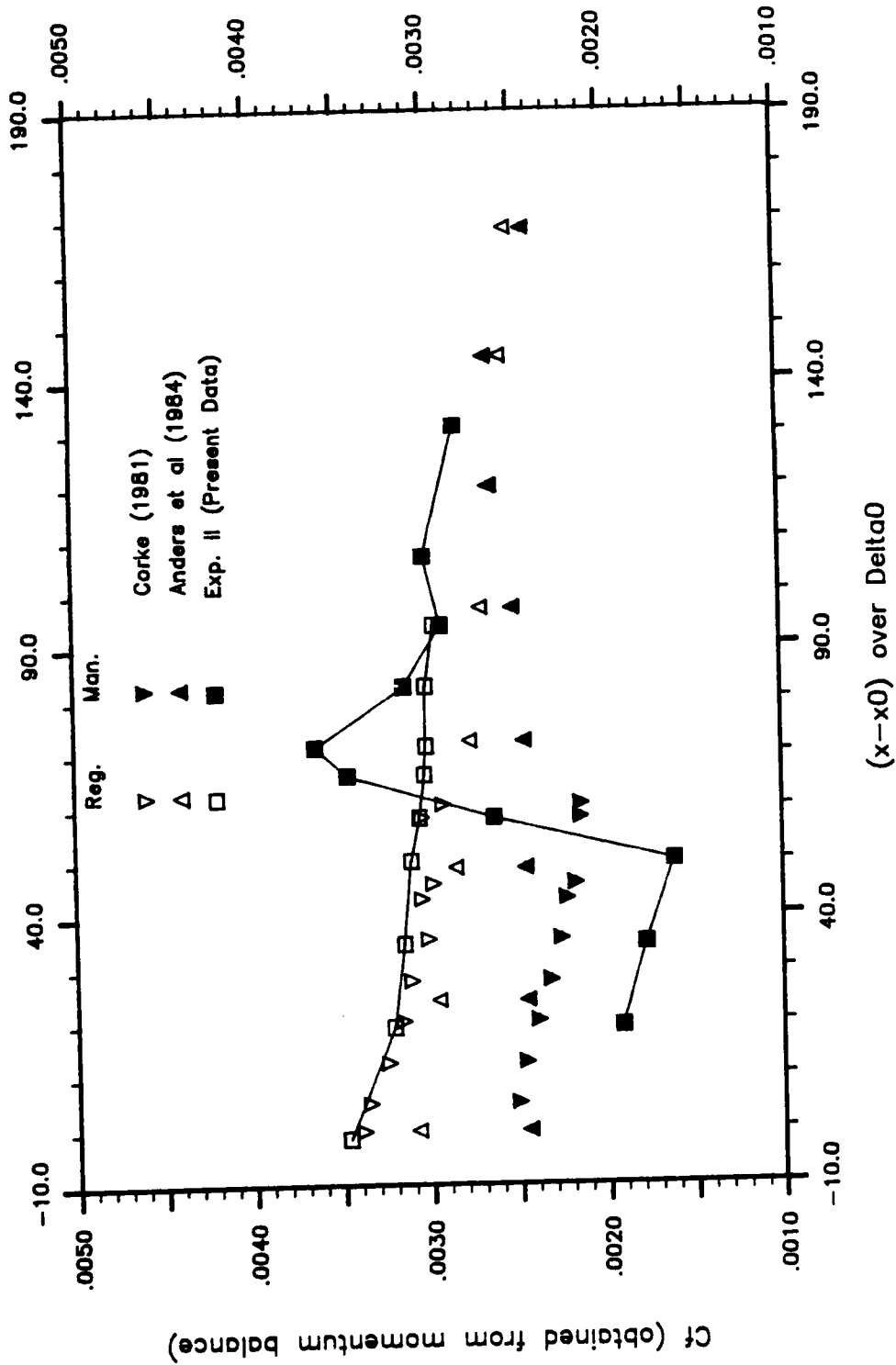
Figure 4.1 Variation of $C_{f\theta}$ versus $(x-x_\theta)/x_\theta$ for regular and manipulated boundary layers and comparison with other investigators' results.
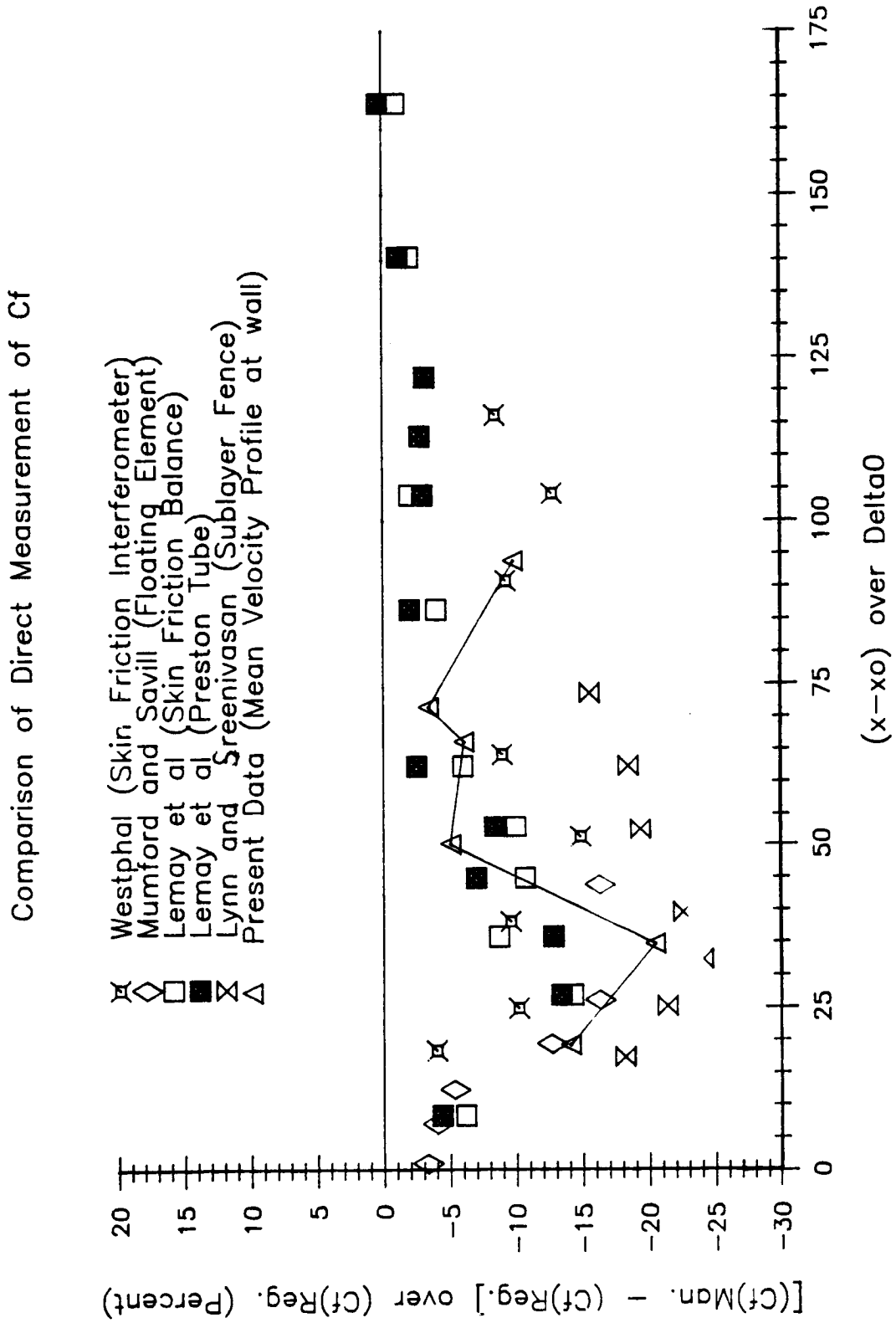
Figure 4.2 Variation of $[C_{fMan} - C_{fReg.}]/C_{fReg.}$ versus $(x-x_o)/x_o$ obtained via different techniques.

Net Drag (Obtained from Cfn Integration [*])
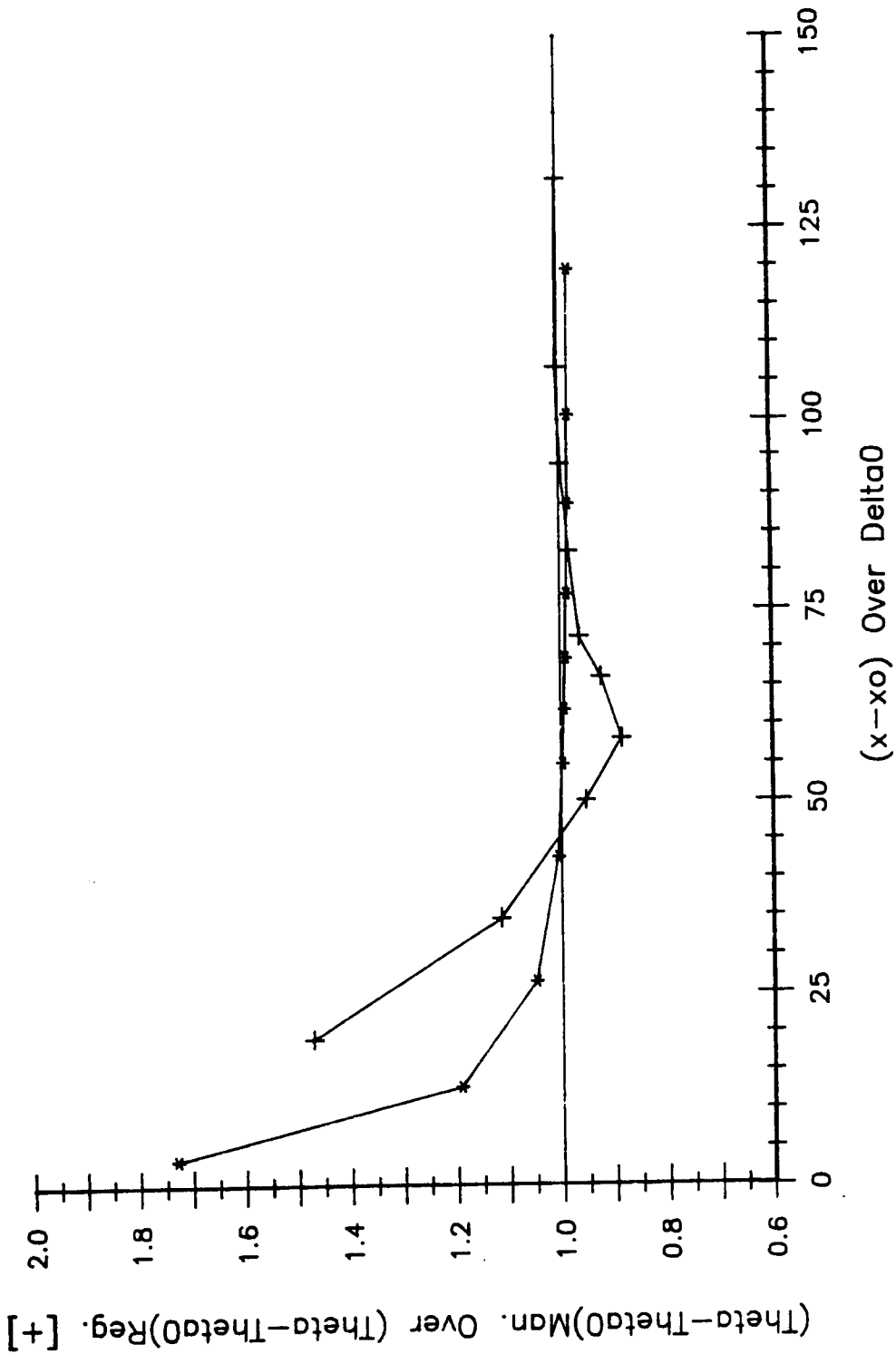
Figure 4.3 Streamwise comparison between non-dimensional net drag ratio (NDR) $(\Theta_x - \Theta_o)_{Man.}/(\Theta_1 - \Theta_o)_{Reg.}$ obtained from momentum balance, and direct measurement of $d\overline{U}/dy_w$ in experiment II.

Table 3.1 Mean boundary layer characteristics and wall-layer statistical information of visualization experiment at ξ = 20.

B. L. Parameters		Regular	Manipulated
δ	(IN)	4.16	4.17
θ	(IN)	0.4988	0.5550
H		1.4116	1.3594
R_θ		2542	2991
$C_{f\theta}$		0.003144	0.001914
C_{fn}		0.002473	0.002125

Statistical information of outward normal travel (y^+) of fluid corresponding to the figure 3.56.

	Regular	Manipulated
Mean (y^+)	240.3	179.1
Std. Dev. (y^+)	72.4	62.1
Skewness Factor	0.2525	0.5517
Flatness Factor	2.9477	3.3372

DATA FOR EXPERIMENT NO. 2

Table 3.2 Mean Boundary Layer Integral Characteristics for Experiment No. 2

REGULAR

STATION	O	A	B	C	D	E	F	G	H
δ (IN)	3.16	4.16	5.16	5.33	5.52	5.79	6.11	6.65	7.46
δ_d (IN)	0.5494	0.7166	0.8102	0.7864	0.9640	1.0718	1.0409	1.0904	1.1491
θ (IN)	0.4011	0.4986	0.5905	0.6459	0.7286	0.7509	0.7511	0.7867	0.8382
H	1.3698	1.4373	1.3722	1.2175	1.3230	1.4274	1.3859	1.3860	1.3709
R_θ	2152.50	2540.42	2872.19	3484.51	3946.77	4263.80	4028.71	4296.31	4143.06
$C_{f\theta}$	0.003467	0.003144	0.003206	0.002887	0.002560	0.002672	0.003008	0.003007	0.002855
C_{fn}	.002421	.002413	.002370	.002169	.001964	.001998	.002266	.001884	.002267

MANIPULATED

STATION	A	B	C	D	E	F	G	H	I	J
δ (IN)	4.17	4.26	4.91	5.38	5.45	5.69	6.30	6.62	7.15	8.31
δ_d (IN)	0.7544	0.8630	0.8591	0.8630	0.9496	1.0596	1.1007	1.1886	1.2541	1.3818
θ (IN)	0.5550	0.6011	0.6445	0.6507	0.7088	0.7429	0.7858	0.8490	0.9037	0.9996
H	1.3594	1.4357	1.3328	1.3262	1.3399	1.4264	1.4008	1.4000	1.3877	1.3823
R_θ	2991.30	3305.84	3460.18	3525.61	3773.07	3958.86	4141.76	4564.90	4848.87	5415.91
$C_{f\theta}$	0.001914	0.001779	0.001615	0.002631	0.003456	0.003636	0.003130	0.002818	0.003011	0.002828
C_{fn}	.002125	.001884	.002059	.002105	.001875	.002188	.002064	.002044	.001759	.001893

APPENDIX

Formulation of Direct Net Skin Drag Calculation

In order to calculate the net skin drag ratio of manipulated to regular turbulent boundary layers, the following formulation was used: When the manipluator was present in the boundary layer, the device drag D (neglecting pressure drag) was obtained. Assumin a two-dimentional incompressible flow, a control volume is drawn as sho n in the following figure.
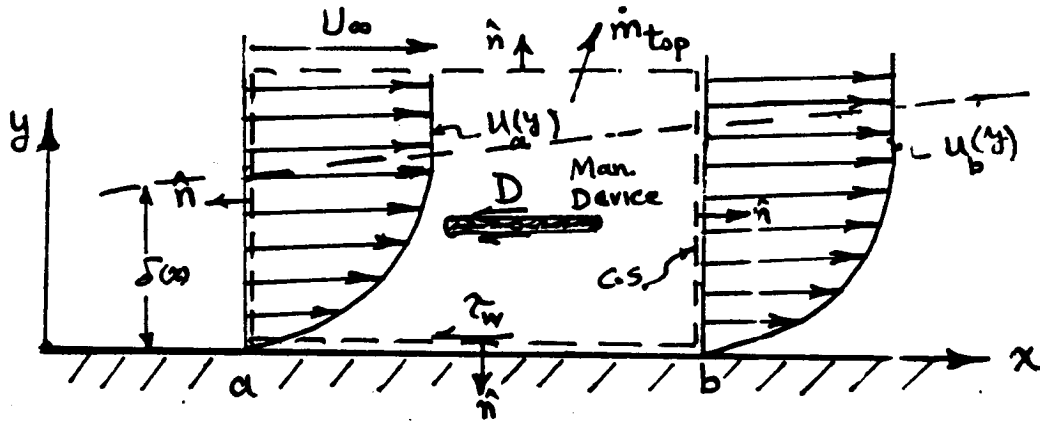
Using the control volume (surface) concept, one may write:

$$-\int_{a}^{b} \tau_w dx - D = \int_{front} \rho V_x \vec{V} \cdot \hat{n} dA + \int_{rear} \rho V_x \vec{V} \cdot \hat{n} dA + \int_{top} \rho V_x \vec{V} \cdot \hat{n} dA + \int_{bottom} \rho V_x \vec{V} \cdot \hat{n} dA$$

where τ_w = Wall shear stress
ρ = air density
V_x = streamwise component of the velocity vector $\hat{V}$
$\vec{V}$ = velocity vector
$\hat{n}$ = normal unit vector.

Substituting for the velocity, rearranging and assuming a unit width for the flow, one may simplify the above equation to:

$$(1) \qquad -\int_{a}^{b} \tau_w dx - D = -\int_{0}^{\infty} \rho u_a^2 dy + \int_{0}^{\infty} \rho u_b^2 dy + U_\infty \dot{m}_{top}$$

where $\dot{m}$ is mass flux from the top surface of the control volume and 1dy = dA

Continuity equation is written as

$$\int_{C.S.} \rho \vec{V} \cdot \hat{n} dA = 0$$

or

$$(2) \quad \int_0^\delta \rho u_a dy - \int_0^\delta \rho u_b dy = \dot{m}_{top}$$

Substitute (2) into (1) and rearrange:

$$D = -\int_0^\delta \rho u_a (U_\infty - u_a) dy + \int_0^\delta \rho u_b (U_\infty - u_b) dy - \int_a^b \tau_w dx \quad (3)$$

Define $\theta = \int_0^\delta (u/U_\infty)[1 - u/U_\infty] dy$ and substitute into (2) to obtain the device drag:

$$(3) \quad D = \rho U_\infty^2 (\theta_b - \theta_a) - \int_a^b \tau_w dx$$

The net drag ratio (NDR) at any station along the test wall can be calculated by substition of the wall shear stress (τ_w obtained from slope of mean velocity profile near wall) into the following equation:

$$(4) \quad NDR = [D + (\int_{x_b}^x \tau_w dx)_{man.}]/(\int_{x_a}^x \tau_w dx)_{reg.}$$

BIBLIOGRAPHY

Anders, J. B., Hefner, J. N. and Bushnell, D. M. 19 4, "Performance of Large Eddy Breakup Devices at Post-Transitional Reynolds Numbers", Presented at the AIAA 22nd Aerospace Sciences Meeting, Reno, Nevada, AIAA-84-0345.

Anders, J. B., and Watson, R. D., 1985, "Airfoil Large-Eddy Breakup Devices for Turbulent Drag Reduction", Presented at the AIAA Shear Flow Conference March 12-14, 1985/Boulder, Colorado, AIAA-84-0345.

Bhatia, J. C., Durst, F., and Jovanovic, J., 198 , "Corrections of Hot-wire Anemometer Measurements Near Walls." _J. Fluid Mechanics_, Vol. 122, pp. 411-431.

Bertelrud, A., Troung, T. V., and Avellan, F., 1982, "Drag Reduction in Turbulent Boundary Layers Using Ribbons", _AIAA Paper N_ . 82-1370.

Bradshaw, P. 1965, "The Effect of Wind Tunnel Screens on Nominally Two-Dimensional Boundary Layers", _J. Fluid Mech. Vol. 22_, p. 679.

Bushnell, D. M., 1983, "Turbulent Drag Reduction for External Flows", _AIAA Paper_ No. 83-0227.

Clauser, F. H., 1954, "Turbulent Boundary Layers in Adverse Pressure Gradients", _J. Aeronautical Science_, 21, 92. 108.

Coles, D. 1956, "The Law of the Wake in the Turbulent Boundary Layer", _J. Fluid Mech. Vol. 1_, pp. 191-226.

Coles, D. 1968, "Young Person's Guide to Data", _Proceedings of Computation of Turbulent Boundary Layers_, Stanford University, California.

Collis, D. C. and Williams, M. J., 1959, "Two-dimensional Convection from Heated Wires at Low Reynolds Numbers." _J. Fluid Mechanics, Vol. 16_, pp. 357-358.

Corke, T. C., Guezenec, Y., Nagiv, H. M., 1980, "Modification in Drag of Turbulent Boundary Layers Resulting from Manipulation of Large-Scale Structures, Viscous Drag Reduction", G. R. Hough, Ed. Vol. 72. _Progress in Astronautics and Aeronautics_, pp. 128-143.

Corke, T. C., 1981, "A New View on Origin, Role and Manipulation of Large Scales in Turbulent Boundary Layers", Ph.D. Thesis, Illinois Institute of Technology, Chicago, Illinois, Dec. 1981.

Corke, T. C., Koga, D., Drubka, R., and Nagiv, H. 197 , "A New Technique for Introducing Controlled Sheets of Smoke Streaklines in Wind Tunnels", _IEEE Publication_ 77-CH 1251-8 AES.

de Bray, B. G., 1967, "Some Investigation Into the Spanwise Non-Uniformity of Nominally Two-Dimensional Incompressible Boundary Layers Downstream of Gauze Screens", *British Aeronautical Research Council, Report* No. 29-271.

Falco, R. E. 1974, "Some Comments on Turbulent Boundary Layer Structure Inferred from the Movements of a Passive Contaminant", *AIAA Paper* No. 74-99.

Falco, R. E. 1977, "Coherent Motions in the Outer Region of Turbulent Boundary Layers", *Phys. Fluids, Vol. 20,*No. 10, Part II, pp. S124-S132.

Falco, R. E. 1978, "The Role of Outer Flow Coherent Motions in the Production of Turbulence Near a Wall", *Coherent Structure of Turbulent Boundary Layers,* ed. C. R. Smith and D. E. Abbott, AFOSR/Lehigh, pp. 448-461.

Falco, R. E. 1980, "Combined Simultaneous Flow Visualization/Hot-wire Anemometry for the Study of Turbulent Flows", *J. of Fluid Engr. Vol. 102,* pp. 174-183.

Falco, R. E. 1982, "A Synthesis and Model of Wall Region Turbulence Structure", in *The Structure of Turbulence, Heat and Mass Transfer,* ed. by Z. Zoric, pp. 124-135, Hemisphere Press.

Falco, R. E. 1983, "New Results, a Review and Synthesis of the Mechanism of Turbulence Production in Boundary Layer and its Modification", *AIAA Paper* No. 83-0377.

Favre, A. J., 1965, "Review of Space-Time Correlations in Turbulent Fluids", *J. Applied Mech.,*June 1965, p. 241.

Freymuth, P., Bank, W. and Palmer, M. 1983, "Use of titanium tetrachloride for visualization of accelerating flow around airfoils", presented at Third International Symposium on Flow Visualization, Ann Arbor, Michigan, USA, September 6-9, 1983.

Guezenec, Y. G. and Nagib, H. M. 1985, "Documentation of Mechanisms Leading to Net Drag Reduction in Manipulated Turbulent Boundary Layers", *AIAA Paper* No. 85-0519.

Hefner, J. N., Weinstein, L. M. and Bushnell, C. M. 1980, "Large-Eddy Breakup Scheme for Turbulent Viscous Drag Reduction, Viscous Flow Drag Reduction", *Progress in Astronautics and Aeronautics, Vol. 72,* pp. 110-127, 1980.

Hefner, J. N., Anders, J. B. and Bushnell, C. M. 1983, "Alteration of Outer Flow Structures for Turbulent Drag Reduction", AIAA 21st Aerospace Science Meeting, Jan. 1983, *AIAA Paper* No. 83-0293.

Kovasnay,L. S. G., Kibens, V., and Blackwelder, R. F., 1970, "Large-Scale Motion in the Intermittent Region of a Turbulent Boundary Layer", *J. of Fluid Mech., Vol. 41,* pp. 283-387.

Laufer, J., Narayanan, M. A. B., 1971, "Mean Period of the Turbulent Production Mechanism in a Boundary Layer", <u>Phys. Fluids. Vol. 14</u>, pp. 182-83.

Lemay, J., Provencal, D., Gourdeau, R., Nguyen, V. D., Dickinson, J., 1985, "More Detailed Measurements Behind Turbulence Manipulators Including Tandem Devices Using Servo-Controlled Balances", Presented at the AIAA Shear Flow Control Conference, March 12-14, 1985, Boulder, Colorado. Paper AIAA-85-0521.

Liang, S. 1984, "Vortex Ring Moving Wall Interactions", M.S. Thesis, Department of Mechanical Engineering, Michigan State University.

Loehrke, R. I. and Nagib, H. M., 1977, "Experiments on Management of Free Stream Turbulence", <u>AGARD Report</u>, R-598, AD-749-891.

Lovett, J. A. 1982, "The Flow Fields Responsible for the Generation of Turbulence Near the Wall in Turbulent Shear Flows", M.S. Thesis, Department of Mechanical Engineering, Michigan State University.

Lynn, T. B. and Sreenivasan, K. R., 1985, "Correlation and Length Scale Measurements in Manipulated Boundary Layers", <u>Report</u> 85 FM 2, Department of Mechanical Engineering, Yale University, April 1985.

Mumford, J. C., and Savill, A. M., 1984, "Parametric Studies of Flat Plate Turbulence Manipulators Including Direct Drag Results and Laser Flow Visualization", Presented at the ASME symposium on turbulent and laminar boundary layers, their control and flow over compliant and other surfaces. ETCE New Orleans, Feb. 11-14, 1984.

Murlis, John, 1975, "The Structure of a Turbulent Boundary Layer at Low Reynolds Number", Ph.D. Thesis, Dept. of Aero., Imperial College of Science and Tech.

Murlis, J., Tsai, M. H., and Bradshaw, P., 1982, "The Structure of Turbulent Boundary Layers at Low Reynolds Numbers", <u>J. of Fluid Mech., Vol. 122.</u>

Nagib, H. M., Guezenec, Y. and Plesniak, M., 1984, "Management of Turbulent Flow Structures in Boundary Layers Aimed at Drag Reduction", Progress report to NASA Grant NSG 1591, Illinois Institute of Technology, Chicago, Illinois.

Patel, V. C., 1965, "Calibration of the Preston Tube and Limitations on its Use in Pressure Gradients", <u>J. Fluid Mechanics, Vol. 23,</u> part 1, pp. 185-208.

Patel, V. C., and Head, M. R., 1969, "Some Observations on Skin Friction and Velocity Profiles in Fully Developed Pipe and Channel Flows", <u>J. Fluid Mechanics, Vol. 38,</u> part 1, pp. 181-201.

Plesniak, M. W., 1984, "Optimized Manipulation of Turbulent Boundary Layers Aimed at Net Drag Reduction", M.S. Thesis, Illinois Institute of

Technology, Chicago, Illinois, Dec. 1984.

Plesniak, M. W., and Nagiv, H. M., 1985, "Net Drag Reduction in Turbulent Boundary Layers Resulting from Optimized Manipulation", AIAA Paper No. 85-0518.

Preston, J. H., 1958, "The Minimum Reynolds Number for a Turbulent Boundary Layer and the Selection of a Transition Device." J. Fluid Mechanics, Vol. 3, pp. 373-384.

Rao, K., Narasimha, R. and Narayanan, M. A. 1971, "The Bursting Phenomenon in a Turbulent boundary Layer", J. Fluid Mech. Vol. 48, Part 2, pp. 339-352.

Rashidnia, N., Falco, R. E., 1983, "Effects of Outer Layer Flow Manipulators on Turbulent boundary Layer Structures", Bull. Am. Phy. Soc., Series II, Vol. 28, pp. 1387.

Rotta, J. C. 1962, "Turbulence Boundary Layers in Incompressible Flow", Vol. 2, Pergamon, Oxford.

Schlichting, H. 1979, Boundary-Layer Theory. McGraw-Hill Book Company, New York.

Shaw, R., 1960, "The Influence of Hole Dimensions on Static Pressure Measurements", J. Fluid Mechanics, Vol. 7, part 2, pp. 550-564.

Signor, D. B., 1982, "A Study of Intermediate Scale Coherent Motions in the Outer Region of Turbulent Boundary Layers", M.S. Thesis, Department of Mechanical Engineering, Michigan State University.

Smith, A. M. O., 1955, "On the Growth of Taylor-Görtler Vortices Along Highly Concave Walls." Quarterly Applications of Math. Vol. XIII, No. 3, pp. 233-262.

Tennekes, H. and Lumley, J. L. 1972, A First Course in Turbulence. The MIT Press, Cambridge, Massachusetts.

Townsend, A. A., 1956, The Structure of Turbulent Shear Flow. Cambridge University Press.

Walsh, M. J., 1980, "Drag Characteristics of V-Groove and Tranverse Curvature Riblets", G. R. Hough, Ed., Vol. 72. Progress in Astronautics and Aeronautics, pp. 168-184.

Walsh, M. J., "Turbulent Boundary Layer Drag Reduction Using Riblets", Presented at the AIAA 20th Aerospace Science Meeting, Orlando, Florida, Jan. 11-14, 1982.

Westphal, R. V., 1986, "Skin Friction and Reynolds Stress Measurements for a Turbulent Boundary Layer Following Manipulation Using Flat Plates", presented at the AIAA 24th Aerospace Sciences Meeting, Reno, Nevada, January 6-8, 1986.

Yajnik, K. S. and Anchorya, M. 1977, "Non-equilibrium Effects in A Turbulent Boundary Layer Due to the Destruction of Large Eddies", National Aeronautical Lab, Bangalore, NAL-BL-7.

Standard Bibliographic Page

1. Report No. NASA CR-178152	2. Government Accession No.	3. Recipient's Catalog No.
4. Title and Subtitle Changes in the Turbulent Boundary Layer Structure Associated with Net Drag Reduction by Outer Layer Manipulators		5. Report Date September 1987
		6. Performing Organization Code TSL-86-1
7. Author(s) N. Rashidnia and R. E. Falco		8. Performing Organization Report No.
9. Performing Organization Name and Address Michigan State University Turbulence Structure Laboratory Department of Mechanical Engineering East Lansing, MI 48824		10. Work Unit No. 505-60-31-04
		11. Contract or Grant No. NAG1-302
12. Sponsoring Agency Name and Address National Aeronautics and Space Administration Washington, DC 20546		13. Type of Report and Period Covered Contractor Report
		14. Sponsoring Agency Code

15. Supplementary Notes
Langley Technical Monitor: Jerry N. Hefner
Final Report

16. Abstract

   A specially designed wind tunnel was used to examine the effects of tandemly-arranged parallel plate manipulators (TAPPMs) on a turbulent boundary-layer structure and the associated drag. Momentum balances, as well as measurements of the local shear stress from the velocity gradient near the wall, were used to obtain the net drag and local skin friction changes. Two TAPPM's, identical except for the thickness of their plates, were used in the study. Results with .003" plates were a maximum net drag reduction of 10% at $58\delta_0$ (using a momentum balance).

   At $20\delta_0$, simultaneous laser sheet flow visualization and hot-wire anemometry data showed that the Reynolds stress in the large eddies was significantly reduced, as were the streamwise and normal velocity components. Using space-time correlations the reductions were again identified. Furthermore, quantitative flow visualization showed that the outward normal velocity of the inner region was also significantly decreased in the region around $20\delta_0$. However, throughout the first $130\delta_0$, the measured sublayer thickness with the TAPPMs in place was 15-20% greater.

   On the whole, the data showed that the skin friction, as well as the structure of the turbulence, was strongly modified in the first $35\delta_0$, but that they both significantly relaxed toward manipulated boundary layer values by $50\delta_0$.

17. Key Words (Suggested by Authors(s)) Turbulent boundary layer Manipulator Skin friction drag Large eddy Momentum balance	18. Distribution Statement Unclassified – unlimited Subject Category 34

19. Security Classif.(of this report) Unclassified	20. Security Classif.(of this page) Unclassified	21. No. of Pages 215	22. Price A10